SOLAR-THERMOCHEMICAL HYDROGEN PRODUCTION USING THIN FILM ALD FERRITES AND OTHER METAL OXIDES

by

JONATHAN RICHARD SCHEFFE

B.S., North Carolina State University, 2005

A thesis submitted to the

Faculty of the Graduate School of the

University of Colorado in partial fulfillment

of the requirement for the degree of

Doctor of Philosophy

Department of Chemical and Biological Engineering

2010

This thesis entitled:

Solar-thermochemical Hydrogen Production Using Thin Film ALD Ferrites and Other Metal Oxides

written by Jonathan Richard Scheffe

has been approved for the Department of Chemical and Biological Engineering

_____

Alan W. Weimer (Chair)

_____

Mark Allendorf

Date_____

The final copy of this thesis has been examined by the signatories, and we

Find that both the content and the form meet acceptable presentation standards

Of scholarly work in the above mentioned discipline.

Scheffe, Jonathan Richard (Ph.D., Chemical and Biological Engineering)

Solar Thermochemical Hydrogen Production Using Metal Oxide-based Reactive Intermediates

Thesis directed by Professor Alan W. Weimer

Production of renewable hydrogen is achievable via two-step redox cycles using metal oxide-based intermediates. Concentrated solar energy is capable of decomposing the metal oxide in the first high temperature step, and in the second step water is reacted with the reduced metal oxide to produce H_2 and regenerate the starting material.

The thermodynamics of relevant ferrite-based water splitting cycles has been investigated using the thermodynamics software package FactSage. The effect of different metal substitutions in $M_xFe_{3-x}O_4$, has been explored, and indicates that Co and Ni based ferrites are both superior to Fe_3O_4. Additionally, it is shown that increasing the inert gas concentrations has a direct effect on the reduction temperature. Increasing the amount of cobalt results in lowering the thermal reduction requirements, but does not necessarily translate to more H_2 production. For values of $x > 1$, the amount of reducible iron decreases, and results in less H_2 production at elevated reduction temperatures. Oxidation of reduced species is shown to be achievable at temperatures greater than when $\Delta G_{rxn} > 0$ if large excesses of water are introduced. More H_2 is expected to be present at equilibrium for ferrite based reactions compared to ceria based water splitting cycles, because the degree of reduction is approximately three times greater.

Atomic layer deposition (ALD) has been used as a means to synthesize thin films of iron oxide, which can be used as reactive intermediates in solar redox cycles. Conformal films of amorphous iron(III) oxide and α-Fe_2O_3 have been coated on zirconia nanoparticles (26 nm) in a

fluidized bed reactor by atomic layer deposition. Ferrocene and oxygen were alternately dosed into the reactor at temperatures between 367 ^{o}C and 534 ^{o}C. Self-limiting chemistry was observed via *in situ* mass spectrometry, and by means of induced coupled plasma – atomic emission spectroscopy analysis. Film conformality and uniformity were verified by high resolution transmission electron microscopy, and the growth rate was determined to be 0.15 Å per cycle.

Iron oxide (γ-Fe_2O_3) and cobalt ferrite ($Co_xFe_{3-x}O_4$) thin films have also been synthesized via ALD on high surface area (50 m^2/g) m-ZrO_2 supports. The oxide films were grown by sequentially depositing iron oxide and cobalt oxide, and adjusting the number of iron oxide cycles relative to cobalt oxide to achieve desired stoichiometry. Samples were chemically reduced in a flow reactor equipped with *in situ* x-ray diffraction. They were also subjected to chemical reduction and oxidation in a stagnation flow reactor to test activity for use in chemical looping cycles to produce H_2 via water splitting. γ-Fe_2O_3 films chemically reduced in mixtures of H_2, CO, and CO_2 at 600 °C formed Fe_3O_4 and FeO phases, and exhibited a trend-wise decrease in H_2 production rates upon cycling. $Co_{0.85}Fe_{2.15}O_4$ films were successfully cycled without deactivation and produced four times more H_2 than γ-Fe_2O_3, principally due to the formation of a CoFe alloy upon reduction. For comparison, a mechanically milled mixture of α-Fe_2O_3 and ZrO_2 powders with similar iron loading to the thin films did not maintain high activity to water splitting due to sintering and grain growth.

Cobalt ferrites are deposited on Al_2O_3 substrates via ALD, and the efficacy of using these in a ferrite water splitting redox cycle to produce H_2 is studied. Experimental results are coupled with thermodynamic modeling, and results indicate that $CoFe_2O_4$ deposited on Al_2O_3 is capable of being reduced at lower temperatures than $CoFe_2O_4$ (200^{o}C-300^{o}C) due to a reaction between

the ferrite and substrate to form $FeAl_2O_4$. Significant quantities of H_2 are produced at reduction temperatures of only 1200 ^oC, whereas, $CoFe_2O_4$ produced little or no H_2 until reduction temperatures of 1400 ^oC. $CoFe_2O_4/Al_2O_3$ was capable of being cycled at 1200 ^oC reduction/ 1000 ^oC oxidation with no obvious deactivation.

Cobalt ferrite ($Co_{0.9}Fe_{2.1}O_4$) and iron oxide (Fe_3O_4) thin films deposited via ALD on m-ZrO_2 supports are utilized in a high temperature water splitting redox cycle to produce H_2. Both materials were thermally reduced at 1450 ^oC and oxidized with H_2O (20-40%) at temperatures between 900 ^oC and 1400 ^oC in a stagnation flow reactor. Oxidation of iron oxide was more rapid than the cobalt ferrite, and the rates of both materials increased with temperature, even up to 1400 ^oC. At elevated oxidation temperatures (T > 1250 ^oC) we observed simultaneous production of H_2 and O_2, due to both thermal reduction and water oxidation operating in equilibrium. A kinetic model was developed for the oxidation of cobalt ferrite from 900 ^oC to 1100 ^oC, in which there was an initial reaction order limited regime, followed by a slower diffusion limited regime characterized well by the parabolic rate law. The activation energy and H_2O reaction order during the reaction order regime were 119.76 ± 8.81 kJ/mole and 0.70 ± 0.32, respectively, and the activation energy during the diffusion limited regime was 191 ± 19.8 kJ/mol.

The feasibility of using commercially available, un-doped, ceria (CeO_2) felts in a thermochemical redox cycle to produce H_2 has been explored, and a detailed kinetic analysis of the oxidation reaction is discussed. Reduction is achieved at 1450 ^oC, and the subsequent H_2 producing step is studied from 700 to 1200 ^oC and H_2O mole fractions of 0.04 to 0.32. The O_2 and H_2 equilibrium compositions remain constant for up to 30 redox cycles, and sintering appears to be abated by microscopy analysis. The average amount of H_2 produced is 280.9 ± 45.8 μmoles/g CeO_2. The re-oxidation rates are faster on a per mass basis than similar ferrite

based-cycles because the surface area is largely unaffected by thermal cycling. The oxidation reaction is governed by a first order reaction mechanism ($1-\alpha$) at low temperatures and conversions, but at higher temperatures the mechanism transitions to a second order reaction $(1-\alpha)^2$. This is attributed to the onset of the thermodynamically favored reverse reaction at elevated temperatures. The activation energy is calculated between 700 and 900 ^{o}C from $0.2<\alpha<0.5$, and determined to be 35.5 ± 13.3 kJ/mol. An Arrhenius expression, coupled with a first order reaction mechanism is used to model the experimentally observed reaction rates where the forward reaction was predominant.

Acknowledgements

Throughout my five long years as a graduate student there is no question that the help and support of several people have contributed to the quality of my research and personal life, without which I am not sure that this work would have been possible.

Firstly, I would like to thank my advisor, Professor Al Weimer. Al has provided me with the opportunity to perform world class research, in a way that allowed me sufficient flexibility and control to direct the work as I saw fit. From the time I began working in the lab as an inexperienced researcher and wondering how the heck I could ever make an impact on the scientific community, Al trusted me enough to present my work to others as if I were a tried and true expert in my field. I have been fortunate enough to present my work at several DOE Hydrogen meetings all over the country, which have provided valuable presentation skills and an appreciation of the intricacies of networking, politics, and research funding. He has always supported and encouraged presenting at international conferences, which I have been privileged enough to do on eight separate occasions. Al's notoriety in the solar field has also introduced me to several new colleagues which have led to research opportunities at Sandia National Laboratories and a post-doctoral position at ETH Zurich in Switzerland with Professor Aldo Steinfeld. It is safe to say that, without Al and his support, these opportunities would not have been available to me and for that I offer my thanks.

I would also like to thank Anthony "Tony" McDaniel and Mark Allendorf for all of the work that was accomplished at Sandia National Laboratories for the better part of 1.5 years. Tony was largely responsible for the construction of the stagnation flow reactor in his laboratory, which was the driving force behind all of the high quality work that was conducted while I was there. He made himself available on almost a daily basis, leading to discussions about the

directions of the experiments we were performing, and made me think critically about the analysis and interpretation of our results. In the end, this resulted in a confidence of my experimental methods and analysis that I never knew I was lacking. Mark also provided valuable feedback during our many meetings, and always offered fresh insight into the interpretation and analysis of our experimental data. I also wish to thank Mark for the time he spent discussing thermodynamic modeling, and have learned nearly everything I know from him. This is greatly appreciated. Ben Jacobs (HRTEM analysis), Ethan Hecht (Labview and reactor construction), and Eric Coker (in situ XRD) also provided invaluable help during my time at Sandia.

The members of the Weimer group have also been especially helpful. Special thanks are due to David King, Hans Funke, Chris Perkins, and Luis Hakim who all have helped me in different ways. Dave was especially helpful in editing my first publication, which would have suffered greatly without his help. Chris and Luis also offered valuable discussions during my first year when my project was just beginning to develop. Hans was especially helpful in teaching me the how to use all of the relevant equipment in the lab, which I was severely lacking early on. Additional thanks are due to Casey Carney, Paul Lichty, Xinhua Liang, Melinda Channel, Oliver Kilbury, Bryan Woodruff, Alia Lubers, Victoria Aston, Todd Francis, and Jianhua “Helen” Li.

There have also been many valuable undergraduate and graduate students who have helped me in the lab. Gevorg Sargysan was especially helpful during my first couple of years, and was loyal enough to stick with it even when the research seemed to never make any progress. Andrea Frances and Brittany Branch were also very helpful with some of the early ALD experiments.

Special thanks are also due to my committee members for providing valuable feedback and suggestions: thank you Will Medlin, Steven George, Aaron Saunders and Mark Allendorf.

Also, department and university staff have been very helpful. Specifically, I would like to thank Dragan Mejic for his help with constructing lab equipment and Dana Hauschulz for his help with all things electrical. Dominique de Vangel has been fantastic helping me with everything related to graduate advising and travel, and Paul Boni and Fred Luiszer for XRD and ICP-AES analysis.

Finally, I would like to thank my family and friends who have helped and supported me throughout my life, and made it bearable through graduate school. I am reminded of all of the great weekends I spent in the mountains skiing and the fun times at Southern Sun, all sandwiched between study sessions and long days in the lab. Paul, I have thoroughly enjoyed living with you and observing the metamorphosis of your house. Both of my parents, Richard and Debbie, have provided me with the fortunate position which has allowed me to pursue my professional goals, and afforded me the foundation that has determined who I am today. My siblings, Rachel and Gretchen, have always provided encouragement for my endeavors, and a needed and enjoyable reprieve from my life in Colorado during the holidays. Lastly, I would like to thank Ellen, who has always provided support when I need it the most, and without her advice I may not be writing this thesis today. Thank you for being so understanding. I can’t wait to finally be able to spend more time with you.

TABLE OF CONTENTS

LIST OF FIGURES

LIST OF TABLES

CHAPTER 1 MOTIVATION AND SCOPE

1.1 Motivation

Historically, energy has played a large role in the development and growth of societies. Before the discovery and use of fossil fuels, “ancient civilizations, no matter how enlightened or creative, rested on slavery and on grinding human labor, because human and animal muscle power were the principal forms of energy available for mechanical work [1].” The advent of the industrial revolution was fueled in large part by cheap and plentiful fossil fuels, and the discovery and use of these ubiquitous energy sources have helped our society progress to the point where it is today. In fact, energy usage has been directly correlated to a society’s standard of living [2]. There is no question that these easily accessible and abundant fuels sources have contributed to a comfortable standard of living for nations across the globe. However, their supplies are finite and it is imperative that we develop a more modern energy infrastructure in the future. In the nearly three hundred years since the beginning of the industrial age, we have seen innumerable technological advances, yet our dependence on fossil fuels over this time span has not waned. Once their supply begins to dwindle, prices will become prohibitively expensive, and in order to maintain our standard of living we must be capable of cheaply exploiting other alternative energy sources.

Many assume that renewable energy sources will smoothly and seamlessly replace fossil fuels when they are needed, but in reality this is a process that will take decades to realize. The world’s entire energy infrastructure is based on fossil fuels, from the internal combustion engines in our cars and the pipelines their gas is transported in, to the electricity generated and sent to our homes via an electrical grid. Predictions indicate that peak oil production may be reached as

early as 2021, yet only 7% of the United States energy needs are derived from renewable resources [3, 4]. A transition to another energy infrastructure, like the often discussed “Hydrogen Economy”, will take years of research, planning, and development, and will not simply occur overnight. It is vital that we are not caught flat-footed and realize too late that we are dependent on an energy source that will not be available forever.

There are other equally important but less quantifiable costs associated with our dependence on fossil fuels use. The United States is slowly becoming more dependent on foreign sources of oil, which inevitably leads to uncertainty regarding its price and supply. For example, the Organization of the Petroleum Exporting Countries (OPEC) is able to artificially manipulate the price of oil simply by decreasing production. We are reminded of this dependence during times like the 1973 oil embargo, and as recently as 2008 when the crude oil prices rose to a record high of nearly $150 per barrel. Price fluctuations such as these are inevitable when such large percentages of this exhaustible commodity are controlled by a few. Although the United States is the third largest producer of crude oil, we are the world’s largest consumer, of which 57% is imported [4]. As recently as 1970 its production peaked, but demand is at an all time high [5].

Another inevitable byproduct resulting from fossil fuel consumption is the release of greenhouse gases into the earth’s atmosphere. These gases are believed to accentuate the “greenhouse effect”, effectively causing the atmosphere to act as an insulator and preventing some of the earth’s radiative energy from escaping the atmosphere and warming the planet. Over the past twenty years, 75% of the emitted greenhouse gases have been caused by the burning of fossil fuels. CO_2 concentrations have increased to nearly 385 ppm since the onset of the industrial revolution and it is believed that this increase is directly related to the earth’s climate

[6]. Surface temperatures have risen by 0.6 ^{o}C to 0.9 ^{o}C and are expected to keep rising as CO_2 concentrations continue to increase [7]. This will have a direct effect on plant and animal species, as their environments will be irreparably altered. The Arctic ice cap is melting at an annual rate of twenty four thousand square miles, and increasing CO_2 concentrations in oceans are turning them more and more acidic. Other more tangible but equally unavoidable environmental impacts associated with the extraction of fossil fuels include large-scale oil spills, such as the British Petroleum spill in the Gulf of Mexico that has caused severe environmental problems. Although the short term costs of ignoring these problems are certainly less than addressing them, we must not lose sight of our future. The long term economic and environmental costs of not investing in alternative energy technologies are too great. The simple fact is we are a nation and society that is completely dependent on a resource that will undoubtedly not be here forever.

Of all the known renewable energy sources, solar energy is the most abundant. As of 2006, the earth's energy requirements were approximately 16 Terrawatts, and about half of this is used by United States [4]. The incident sunlight on the earth's surface provides more than enough power to provide this energy. According to the amount of solar irradiation incident in the southwestern United States shown on Figure 1-1, the state of Arizona receives about 12 times more solar energy than the entire United States required in 2006 [8]. Therefore, if we could capture this at only 10% efficiency it would be possible to power the country with an area roughly the size of Arizona. Efficiencies such as these are achievable commercially today, but obviously if the efficiencies were increased the amount of land required would be decreased. The shear abundance of solar energy is enough motivation to consider this energy source a viable candidate to satisfy our needs.

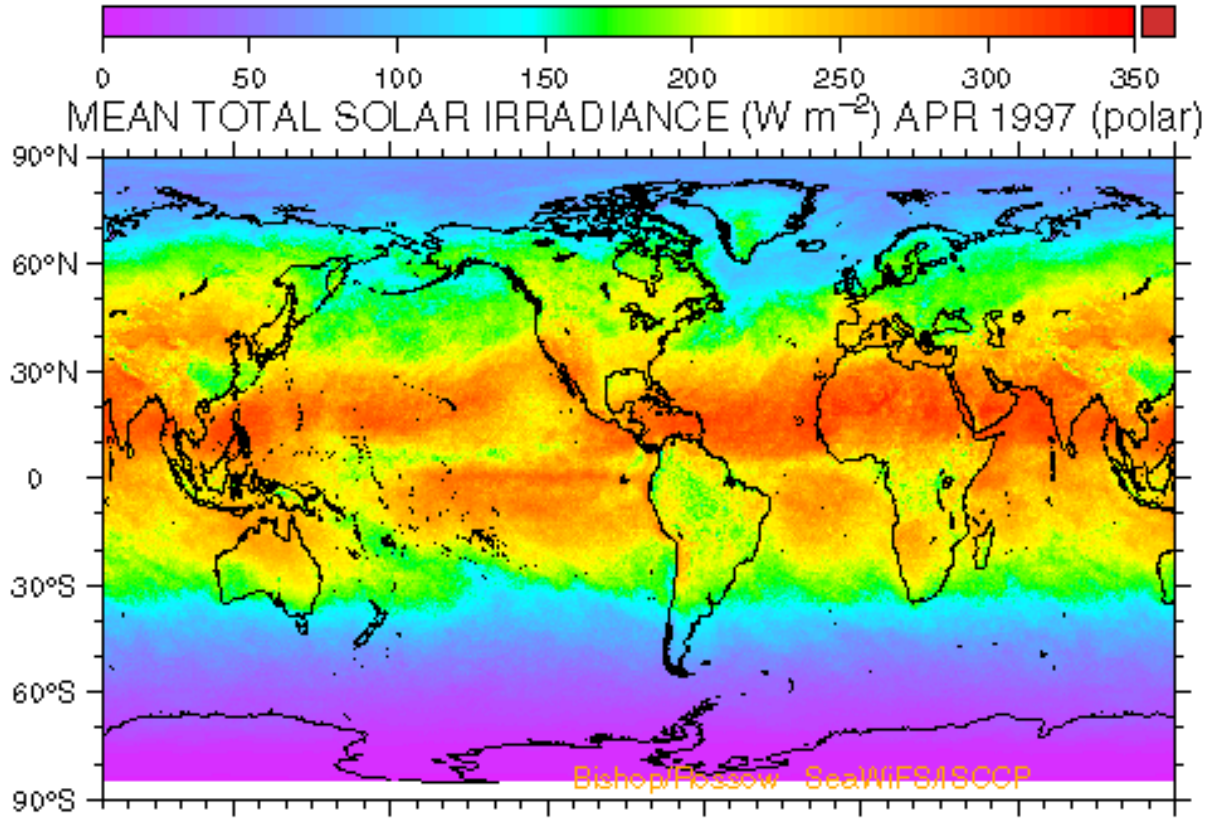

Figure 1-1: ISCCP Solar irradiance Data, April 1997. Bishop JKB. Surface Solar Irradiance from ISCCP data. Ocean Biogeochemical Processes Group at Lawrence Berkeley National Laboratory

Photovoltaic solar cells capable of generating electricity are perhaps the most ubiquitous of all solar technologies. This technology is practical at small scales where the generated electricity is used locally. However, it is not feasible to transport electricity over long distances due to resistive losses from the transmitting line. This problem is exemplified in the United States, where the highest concentrations of solar irradiance are generally located in areas of low population densities. Therefore, the conversion of solar energy to a fuel source that can be transported long distances would be ideal.

Hydrogen is a particularly promising solar derived energy carrier for several reasons, and talk of transition to a hydrogen fuel based economy has become so widespread that it is often

referred to as the “hydrogen economy” [9, 10]. It is possible that it could be transported in pipelines or on roads, not unlike how gasoline is transported today [11, 12]. Hydrogen is the most common element on the surface of the earth, and has the highest energy density of all conventional fuels [11]. It is capable of being utilized in fuel cells which are 2-3 times more efficient than traditional combustion engines and water is the only reaction byproduct. It is referred to as an energy carrier, rather than an energy source because it does not exist in its elemental form [11]. Rather it must be derived from other chemical species such as fossil fuels or water.

Currently, 98% of all hydrogen production comes from non-renewable fossil fuel based resources[10]. There are several renewable pathways for the production of hydrogen, many of which are solar-based[13], but most of these processes lack the ability to efficiently convert sunlight into hydrogen. This is largely because they rely on several steps to convert the sunlight/water into hydrogen, and with each step energy losses are incurred along the way. An example of this is photovoltaic (PV)/electrolysis in which sunlight is converted to electrical energy via PV cells, which subsequently power an electrolyzer to split water and generate H_2. An alternative to this is the solar-thermochemical production of hydrogen. This process avoids the inefficiencies of some of the other processes by thermally decomposing H_2O directly into H_2 and O_2, and has the potential to be the most efficient renewable H_2 production method [13]. It has theoretical maximum solar to heat efficiencies (LHV) of between 40 and 49% and solar to hydrogen efficiencies of about 20% [14, 15].

The production of hydrogen via solar-thermochemical cycles provides the motivation for this thesis [16]. The objective is to produce hydrogen or other related transportable fuels from renewable energy sources, particularly concentrated sunlight, as cheaply and efficiently as

possible in order to provide a fuel source which is capable of meeting the country's and world's future energy demands.

1.2 Scope

The ultimate objective of this research project is to produce hydrogen and/or other transportable fuels from water and carbon dioxide using concentrated solar energy. Specifically, possible materials will be explored, typically metal oxides, that are capable of operating in a two-step thermal-redox cycle to produce a useable fuel. The net reaction leaves the intermediate unchanged. The role of the intermediate is to reduce the energy requirements of the reaction, similar to the role of a catalyst. This process can be seen from the generic two-step water splitting process below to produce H_2.

$$MO + solar\ thermal\ energy \rightarrow MO_{1-x} + \frac{x}{2}O_2 \quad \textbf{1)}$$

$$MO_{1-x} + xH_2O \rightarrow MO + xH_2 \quad \textbf{2)}$$

$$Net\ Reaction: solar\ thermal\ energy + xH_2O \rightarrow \frac{x}{2}O_2 + xH_2 \quad \textbf{3)}$$

The first step involves the reduction of a metal oxide (MO) using solar thermal energy, and generally occurs at high temperatures (T > 1200 ^{o}C). The following step exposes the reduced MO to water, thereby re-oxidizing the MO and generating H_2. This results in a net reaction where the only feedstocks are solar thermal energy and water, and the net products are H_2 and O_2. The advantages of completing this reaction in two steps rather than one are twofold. First, the thermodynamic requirements to directly split water are extremely large (T> 4300 K), and this process acts to decrease the upper operating temperature required. Secondly, rather than dealing

with a potentially explosive mixture of H_2 and O_2 that needs to be separated, the H_2 and O_2 are generated independently.

There is a range of materials and/or feedstocks that have the potential to produce H_2 or other fuels by analogous 2-step processes. Perhaps the most ubiquitous materials include metal oxides of the form, $M_xFe_{3-x}O_4$, commonly referred to as ferrites or spinel oxides. M is generally a transition metal, and some of the most frequently explored metals include Co, Ni, Zn and Mn, all of which have advantageous properties. More recently, CeO_2 and metal doped CeO_2, have been utilized in these cycles due to their relative high temperature morphological stability.

In addition to H_2O, other feedstocks such as CO_2 have the potential to produce useable fuels via similar redox cycles. For example, when CO_2 is substituted for H_2O in the above reactions, the end product is CO rather than H_2. This can easily be converted into H_2 via the water gas shift reaction, or used in a syngas mixture to produce carbon based fuels. The temperature requirements can be lowered even further if a biomass source is incorporated in the first reaction. It is capable of chemically reducing the metal oxide at lower temperatures than would be possible from only thermal energy and the resulting second step would remain unchanged.

This thesis will focus primarily on the use of cobalt ferrites ($Co_xFe_{3-x}O_4$) to thermally split H_2O into H_2 according to the above redox cycle. It is well documented that this material has the potential to produce H_2 via these thermochemical cycles, and has distinct advantages compared to other ferrites. It has been shown to be promising from both an experimental and thermodynamic perspective. Previous research that has been conducted to focus on the kinetics and thermodynamics of the relevant reactions will be extended. Furthermore, the effect of synthesis procedures will be investigated. In addition to cobalt ferrites, the feasibility of other

promising metal oxide materials will be explored along with alternative routes to the production of renewable H_2 via similar, high temperature redox cycles.

More specifically, this research will focus on the synthesis of cobalt oxide and iron oxide thin films via atomic layer deposition (ALD) in order to synthesize samples of the form $Co_xFe_{3-x}O_4$. The purpose of this is twofold. Firstly, the influence of cobalt concentration on the thermodynamics and kinetics of the relevant reactions will be investigated. Secondly, ALD provides the ability to deposit well defined and homogenous films. It is an ideal platform in which to model and to study the reaction kinetics. A fundamental understanding of the reaction kinetics is essential for material and reactor design, but has largely been overlooked by the scientific community. Because ALD is independent of line of sight, it also provides the ability to deposit films on various types of substrates, ranging from highly porous high surface area materials to well-defined single crystals. This work will focus on depositing the ferrite on ZrO_2 and Al_2O_3 supports, because both are readily available and thermally stable at the high temperatures of interest.

Baseline testing of the ALD synthesized materials will be conducted in a high temperature horizontal furnace, which is equipped with a steam delivery system and a residual gas analyzer (RGA) to measure the product gases. The goal of these studies is to roughly compare the materials to one another in terms of their ability to produce H_2 repeatedly over many cycles. They will also be compared to powder-based samples that are known to work well from the literature. The relevant phases that are formed after reduction and oxidation will be studied via powder x-ray diffraction (XRD) and other applicable analysis techniques to determine what interactions, if any, there are between the ALD films and the underlying supports.

The kinetics of the water splitting reaction will be studied at Sandia National Laboratories in a high temperature stagnation flow reactor (SFR). The advantage of this reactor lies in its ability to ensure one-dimensional and homogeneous flow across the sample. Understanding the gas dynamics at the sample's interface is essential for developing relevant kinetic models. We are interested specifically in determining the role, if any, of diffusion, surface area, and cobalt stoichiometry of these materials. Additionally, we are concerned with reaction conditions such as reduction and oxidation temperature, water concentration, and pressure. This reactor is equipped with a modulated beam mass spectrometer to measure the reaction product species, and is capable of operating between 1 and 760 Torr.

Following this, the effect of syngas reduction will be studied in contrast to thermal reduction to produce H_2 at lower temperatures. The interest here lies in determining the optimal reduction conditions that limit the morphological evolution of the samples and provide the best conditions for cyclical repeatability. The number of possible species formed during syngas reduction is much greater than for thermal reduction, and is dependent on the concentration and composition of reduction gases and the reaction temperature. Because of this complexity, these experiments will be coupled with in-situ XRD experiments to determine the crystalline phases that are formed.

In addition to cobalt ferrites, the feasibility of using CeO_2 for both H_2O and CO_2 splitting reactions will be studied and compared to $Co_xFe_{3-x}O_4$. These materials have received recent interest due to their high temperature stability, but are even less understood than ferrites. Some baseline experiments using the SFR will be conducted to determine the temperatures required for thermal reduction and optimal oxidation temperatures. Their thermal stability will be studied, and the oxidation kinetics will be investigated.

For all of the experiments mentioned, equilibrium calculations using the thermodynamic software package, FactSage, will be utilized to help understand and predict equilibrium species that are formed during thermal reduction and oxidation. Ultimately, thermodynamic calculations will help to determine optimal conditions where one would expect these reactions to occur, and help to design experiments effectively and efficiently. Thermodynamic modeling can be used as a means to easily screen for "alternative" water splitting cycles without the need to perform costly experiments.

Additionally, material characterization is critical to interpreting the aforementioned experimental results. The performance of these materials ultimately depends on their ability to be cycled repetitively, up to thousands or even millions of times. Therefore, it is planned to characterize how these materials change, if at all, during cycling. By coupling experimental data with microstructural analysis, we hope to resolve the means by which the materials are changing. Analysis techniques planned to be utilized are high resolution transmission electron microscopy (HRTEM), scanning electron microscopy (SEM), x-ray photoelectron spectroscopy (XPS), Raman spectroscopy, powder XRD, induced coupled plasma – atomic emission spectroscopy (ICP-AES), and BET surface area analysis.

1.3 References

[1] Revelle R. ENERGY USE IN RURAL INDIA. Science 1976;192:969.

[2] Pasternak AD. Global Energy Futures and Human Development: A Framework for Analysis. vol. UCRL-ID-140773: United States Department of Energy, 2000.

[3] Wood JH, Long GR, Morehouse DF. Long-Term World Oil Supply Scenarios: The Future Is Neither as Bleak or Rosy as Some Assert. EIA, United States Department of Energy, 2004.

[4] EIA. Annual Energy Review 2008. United States Department of Energy, 2008.

[5] Mufson S. This Time, It's Different: Global Pressures Have Converged to Forge a New Oil Reality. The Washington Post. Washington DC, 2008.

[6] Neftel A, Friedli H, Moor E, Lötscher H, Oeschger H, Siegenthaler U, Stauffer B. Historical Carbon Dioxide Record from the Siple Station Ice Core. Carbon Dioxide Information Analysis Center Oak Ridge National Laboratory, 1994.

[7] IPCC Fourth Assessment Report. Intergovernmental Panel on Climate Change, 2007.

[8] Bishop JKB. Surface Solar Irradiance from ISCCP data. Ocean Biogeochemical Processes Group at Lawrence Berkeley National Laboratory, 2006.

[9] Balat M, Kirtay E. Major Technical Barriers to a "Hydrogen Economy". Energy Sources Part a-Recovery Utilization and Environmental Effects;32:863.

[10] Marban G, Vales-Solis T. Towards the hydrogen economy? International Journal of Hydrogen Energy 2007;32:1625.

[11] Ekins P, Hughes N. The prospects for a hydrogen economy (1): hydrogen futures. Technology Analysis & Strategic Management 2009;21:783.

[12] Balat M. Political, economic and environmental impacts of biomass-based hydrogen. International Journal of Hydrogen Energy 2009;34:3589.

[13] Turner J, Sverdrup G, Mann MK, Maness PC, Kroposki B, Ghirardi M, Evans RJ, Blake D. Renewable hydrogen production. International Journal of Energy Research 2008;32:379.

[14] Kodama T. High-temperature solar chemistry for converting solar heat to chemical fuels. Progress in Energy and Combustion Science 2003;29:567.

[15] Steinfeld A. Solar hydrogen production via a two-step water-splitting thermochemical cycle based on Zn/ZnO redox reactions. International Journal of Hydrogen Energy 2002;27:611.

[16] Perkins C, Weimer AW. Solar-Thermal Production of Renewable Hydrogen. Aiche Journal 2009;55:286.

CHAPTER 2 LITERATURE REVIEW

2.1 Traditional Methods of Hydrogen Production

Worldwide, about 0.1 Gton of H_2 is produced annually, 98% of which is the product of fossil fuel conversion [1]. Several processes are used to convert a variety of fossil fuels, included steam reforming of natural gas[2], partial oxidation and autothermal reforming of hydrocarbons and alcohols[2, 3], and coal gasification, and biomass gasification[4]. Both steam reforming of natural gas and partial oxidation involve reforming the fuel source with steam to produce a syngas mixture, which can be further converted to a H_2/CO_2 mixture via the water gas shift reaction. The difference between the two processes lies in how heat is provided to the reaction. In steam reforming heat is provided externally, whereas in partial oxidation the necessary heat is provided by burning a portion of the fuel. In their most basic forms, traditional coal and biomass gasification operate analogously to the aforementioned processes. The coal or biomass is gasified, reacted with air or steam at elevated temperatures to form a syngas mixture, and followed by the water gas shift reaction to generate more H_2. Due to the nature of these fuel sources, more CO_2 and impurities are generated compared to the aforementioned methods. Currently, all of these processes are a viable means to produce H_2, but they are not a solution to our energy problems. They all require the use of non-renewable fuel sources, and in all cases are inherently more energy intensive than the amount of useable energy acquired. However, because all of the CO_2 generated in these processes is centralized, sequestration is more viable than if it were generated elsewhere on a smaller scale (i.e. automobiles). Additionally, these processes would allow fuel sources to be used that are plentiful in the United States [5], rather than relying heavily on other nations for the country's energy needs. So, while these traditional H_2 production

methods are not an end solution to our energy concerns, they do provide a realistic means to transition from our current energy infrastructure to one based on hydrogen.

2.2 Carbon Neutral Hydrogen Production

A more efficient and renewable means of H_2 production from biomass[6-8], coal[9], natural gas[10], and even carbonaceous waste materials[11] using concentrated solar energy has been explored recently. Rather than burning a portion of the feedstock to provide the energy needed for heating the reactants, concentrated solar in the form of thermal energy is used. This has several distinct advantages compared to traditional gasification[12]. Firstly, the calorific value of the feedstock is increased because it is not used to provide energy for the reaction. Secondly, the products are not contaminated by the products of feedstock combustion and because the feedstock is not combusted, there are no greenhouse gases emitted. Additionally, the reactants are directly irradiated, resulting in rapid kinetics compared to indirect heating methods. Another distinct advantage of this process is the ability to efficiently operate at high temperatures. This results in less undesirable tar formation during biomass gasification, which is a concern when operating at lower temperatures[7]. Although all of these processes utilize carbon-based sources to generate H_2, some can be considered carbon neutral. Biomass gasification, for instance, can be considered a renewable process if there is as much biomass grown as is utilized. Others such as coal or natural gas driven processes, cannot be considered as such, but do represent a major step towards renewable H_2 production when compared to traditional gasification processes.

There are several other carbon neutral processes capable of producing renewable H_2 via water splitting methods, but most are considered to be more expensive than the aforementioned processes. As such, most are being investigated extensively in order to try and make them more

economically viable and competitive with traditional hydrogen production methods. These include, but are not limited to, electrolysis, photolysis via photoeletrochemistry, photolysis via photobiological water splitting, and solar-thermal water splitting [13, 14].

The electrolysis of water is perhaps the simplest of all water splitting technologies and was first discovered in the 1800's [13]. Water is split into H_2 and O_2 on opposing sides of an anode and cathode when a direct current is applied, and it is capable of producing ultra-pure H_2 without having to deal with gas separations. This technology is intriguing because it can be easily incorporated with wind, photovoltaic (PV), and nuclear systems which generate renewable electricity. The cost of this process is limited largely by the cost of electricity generated and the capital cost of the electrolyzer. Currently, the cost of producing H_2 via electrolysis using the wind, solar or nuclear is more expensive than steam methane reforming, coal gasification and biomass gasification[15]. However, by the year 2030, these are expected to be competitive with or cheaper than non-renewable processes because of projected increases in fossil fuel costs and decreased renewable energy costs [15]. Additionally, there is ongoing research to try and improve electrolyzer efficiencies, which could further decrease the cost of H_2 production[16].

Closely related to PV/electrolysis is the photoelectrochemical (PEC) production of H_2. Rather than generating electricity and subsequently generating H_2 with an electrolyzer, however, photoelectrochemistry is capable of splitting water in a single step. This process is based on the theory that water is capable of absorbing specific wavelengths of visible light that provide sufficient energy to split H_2O into H_2 and O_2 [17]. However, because water is not efficient at absorbing visible light (most is transmitted), this process is used in conjunction with a semiconductor that is capable of absorbing light. Water is decomposed on its surface [13]. In essence, a PV cell and electrolyzer are incorporated into a single device, rather than operated as

separate entities. The advantage of this compared to PV/electrolysis lies in the theoretical electrolyzer efficiencies of PEC. Lower current densities are required and thus lower voltages, resulting in theoretical electrolysis efficiencies of 91% [13]. Photolysis of H_2O is also capable of being achieved by microorganisms in a similar manner to photosynthesis[13]. Theoretical efficiencies are similar to those of PEC H_2 production (10-13% incident solar to H_2), but have not yet been realized for extended periods of time due to several factors including limited reaction rates, and O_2 intolerances.

2.3 Solar Thermal Hydrogen Production – Direct Water Splitting

Potentially the most efficient process to convert solar energy into hydrogen is via solar-thermal water splitting, rather than electricity (PV/electrolysis) or photons (photolysis) [13, 14]. This process avoids the inefficiencies of some of the other processes by thermally decomposing H_2O directly into H_2 and O_2. Solar energy is collected via arrays of mirrors (heliostats), which are capable of achieving concentration ratios of greater than 5000 suns and temperatures as high as 3000 K [18]. The absorption efficiency of a solar receiver is defined as the net rate at which energy is being absorbed, $Q_{absorption}$, divided by the solar power input, Q_{solar}, shown as

$$n_{absorption} = \frac{Q_{reactor}}{Q_{solar}} = 1 - \frac{\sigma T^4}{IC} \qquad \mathbf{2-1})$$

where σ is the Stefan-Boltzmann constant, T is the reactor temperature, I is the normal beam insolation, and C is the concentration ratio of the incident solar radiation [18]. The solar to thermal efficiency is the product of the absorption efficiency and optical efficiency of the solar concentrators, and has been calculated by Steinfeld *et. al.* to be 40% and 49% for solar concentration ratios of 5000 and 10,000 suns at 2300 K. There are several known solar thermal

processes which have reaction efficiencies greater than 40%, resulting in theoretical solar to H_2 efficiencies of 20% [14, 19].

The simplest and most direct method of solar-thermal water splitting is the direct splitting of H_2O, or thermolysis. Thermodynamically, the spontaneous decomposition of water at 1 atm occurs at temperatures greater than 4300 K [14], but it is possible to decompose a significant amount of water at temperatures as low as 2500 K [20]. In fact, this reaction has been performed at temperatures below 2000 K, and it was concluded that interactions with the reactor walls have a large effect on the decomposition rate [20]. Conceptually, this process is very simple, but realistically there are many difficulties which prohibit its practicality in the near future. There are very few materials capable of withstanding the high temperatures required. In fact, most experiments are performed at temperatures well below the spontaneous H_2O decomposition temperature because ZrO_2 reactor tubes are used. As a result, temperatures must be maintained below 2500 K to prevent the zirconia from melting [21]. At these temperatures, only about 4% of the water is expected to dissociate under atmospheric conditions, which severely limits the efficiency of this process. Furthermore, a potentially explosive mixture of H_2 and O_2 is generated if allowed to cool, and therefore must be separated either at high temperatures, or by rapid quenching [21]. Quenching must occur at rates of 1500 K – 2000 K per millisecond to prevent recombination of the products. This is capable of preventing 90% of the reactants from recombining, but it is a highly energy intensive process. High temperature refractory membranes, electrodiffusion membranes, metallic membranes, centrifugation, and supersonic jets are all being investigated as a means to separate the product gases as high temperatures [21]. Higher H_2 yields can be achieved by these methods, but over time extensive sintering and pore clogging

lead to decreases in the yields. Because of these difficulties, this process is not expected to be economically feasible in the near future.

2.4 Solar Thermal Hydrogen Production – Thermochemical Water Splitting Cycles

Solar thermochemical water splitting cycles have proven to be an attractive alternative to direct water splitting. The net result of these cycles is the same as direct water splitting ($heat + H_2O \rightarrow H_2 + \frac{1}{2}O_2$), but the reaction is split into two or more reactions using chemical reactant intermediates. Generally, these cycles are characterized by a high temperature step in which the chemical reactant is thermally reduced via solar energy, and one or more lower temperature water splitting steps which may or may not require a thermal input. Currently there are more than 350 known thermochemical cycles, many of which have theoretical efficiencies of greater than 40% [22]. Some of the most thermodynamically feasible and efficient cycles were established by the Solar Hydrogen Generation Research (SHGR) project sponsored by the United State's Department of Energy [22]. Among these, some of the promising and extensively investigated include "lower temperature" cycles such as the sulfur hybrid cycle[19], sulfur iodine[23], UT-3 cycle[24], hybrid copper chloride[25] and "high temperature" cycles such as iron oxide, sodium manganese, zinc oxide, and various ferrite cycles. Also, the recently investigated ceria water splitting cycle has received a tremendous amount of interest.

The "low temperature" cycles were originally developed to be used in conjunction with nuclear waste heat, and therefore have been investigated extensively by the nuclear industry. Generally, these are more complex (more reactions involved) than the "higher temperature" cycles and often involve fairly hazardous chemicals, such as sulfuric and hydrochloric acid. One of the most widely studied "lower temperature" cycles is the sulfur iodine cycle which was

developed and studied extensively by General Atomics from the late 1970's until today [23, 26]. Although complex, small scale pilot plants have demonstrated the scale-up feasibility of this cycle using nuclear waste heat [27, 28]. This cycle involves three separate steps, the first being an exothermic liquid phase reaction of I_2, SO_2, and H_2O to form hydrogen iodide and sulfuric acid. Each of these products is decomposed in separate endothermic reactions. The decomposition of sulfuric acid occurs at temperatures near 900 ^oC and requires and external heat source such as nuclear or solar energy. The net result of these three reactions is the decomposition of H_2O into $0.5O_2$ and H_2. The biggest advantage of these cycles compared to higher temperature cycles is the lower temperature requirement.

The "higher temperature" cycles are conceptually simpler than the "lower temperature" cycles, but do occur at much higher temperatures (T generally > 1400 ^oC). Because of this, reactor construction materials become a concern due to high temperature instability, and thermal shock issues arise because the non-oxide refractory materials that are stable at these temperatures cannot withstand rapid temperature changes that are inevitable when utilizing concentrated solar energy [14]. The most extensively studied high temperature cycles occur in two distinct steps and do not require any hazardous chemical intermediates, with the exception of the sodium manganese cycle. These all involve the high temperature endothermic decomposition of a metal oxide, and a lower temperature water splitting step to regenerate the metal oxide and produce H_2.

The first "high temperature" cycle was proposed by Nakamura. He concluded that the direct thermal splitting of H_2O was not feasible or economical due to the high temperature and separation requirements, and proposed a two-step process which utilizes magnetite (Fe_3O_4) as a chemical intermediate. The advantage of this compared to direct water splitting is that the highest temperature step proceeds spontaneously at 2500 K, rather than 4300 K for direct water

splitting [29]. The cycle comprises two separate reactions, namely a high temperature endothermic decomposition step and a lower temperature exothermic water splitting step, as shown below.

$$Fe_3O_4 + \ thermal\ energy \rightarrow 3FeO + \frac{1}{2}O_2 \quad \{T > 2500\ K\} \qquad \mathbf{2-2})$$

$$H_2O + 3FeO \rightarrow Fe_3O_4 + \ H_2 \quad \{T < 650\ K\} \qquad \mathbf{2-3})$$

The first high temperature step involves the decomposition of magnetite to FeO and the subsequent release of O_2. In the second, lower temperature step, the reaction of FeO and water proceeds exothermically below 650 K to produce H_2 and regenerate magnetite. Thus, the only reactants are H_2O and thermal energy, and the products are O_2 and H_2. The magnetite is regenerated at the conclusion of every cycle and never consumed. In addition to operating at lower temperatures, the H_2 and O_2 are generated in separate steps, so separation difficulties are avoided.

An even more thermodynamically attractive “high temperature” cycle is the zinc oxide cycle. Conceptually, it is very similar to the magnetite cycle and involves the decomposition of zinc oxide to zinc vapor, and the subsequent oxidation of Zn with water to produce H_2 and regenerate the ZnO [18]. The first high temperature step is endothermic and occurs spontaneously at temperatures greater than 2300 K and the water oxidation step is exothermic, occurring at 700 K. Perkins *et.al.* have studied the decomposition step in great detail in both a high temperature aerosol flow reactor and thermogravimetric analyzer (TGA) [30, 31]. The observed rates in the aerosol flow reactor were three orders of magnitude greater than those

observed in the TGA, and the maximum conversion of ZnO to Zn was about 18% for residence times of only 1.11 to 1.78s. It was concluded that the reaction could be characterized well by the L'vov theory, which describes a reaction limited by the evolution of species from a solid surface. In fact, the decomposition of ZnO proceeds via the dissociation of of Zn and O gas from the surface, which is remarkably different than the decomposition of Fe_3O_4, in which only O_2 is evolved. This results in a cycle that is inherently more complex than the Fe_3O_4 cycle because the addition of a phase change results in rapid gas phase recombination kinetics. Therefore, the decomposition reaction must be quenched rapidly which results in a large energy input and decreases the efficiency of the process. Also, material handling becomes more complex because the Zn vapor tends to nucleate on reactor walls. Steinfeld *at. al.* have investigated solutions to this problem and have developed a rotating reactor in which the ZnO particles are held to the reactor walls by centripetal force, thereby maximizing the reactor volume for efficient radiative heat transfer. The resulting Zn vapor is carried to the outlet of the reactor by rapidly quenching with Ar gas, resulting in Zn solid powder [32]. The oxidation of Zn has been investigated extensively, and proceeds via a fast interfacial reaction followed by a slower diffusion limited regime [33]. This is caused by a ZnO product layer formed around the Zn metal. Generally, this reaction is attempted at fairly low temperatures ($T < 683$ K) to prevent melting and sintering [34]. When conducted at higher temperatures, the Zn is capable of reacting with water in the vapor phase, resulting in higher conversions (70%) and faster kinetics, but much of the products are deposited on the reactor walls [35].

The sodium manganese cycle is another attractive "high temperature" cycle that operates in three separate steps. The first step involves the conversion of solar thermal energy to chemical energy via the decomposition of manganese(III) oxide at temperatures greater than 1835 K [36].

The second reaction is exothermic and proceeds at 900 to 1100 K via the reaction of MnO and sodium hydroxide to produce H_2 and $NaMnO_2$. The third step involves the reaction $NaMnO_2$ and water to reform manganese(III) oxide and NaOH. Francis *et. al.* have studied the high temperature decomposition step in a TGA and aerosol flow reactor at temperatures ranging from 1673 K to 1873 K, and conversions as high as 75% were achieved [37]. Although this cycle is conceptually simple, realistically there are many barriers that must be overcome before it is feasible. Material handling is difficult because the second step involves a reaction with liquid sodium hydroxide, which is highly corrosive. In fact, there has been only one published demonstration of the second and third steps of the cycle [38]. The hydrolysis reaction proved to be the most difficult to accomplish, because rather than the anticipated formation of Mn_2O_3 and NaOH, a Na-Mn-oxide was formed.

2.4.1 Ferrite-based Water Splitting Cycles

Although the temperature requirements for both the zinc oxide and sodium manganese cycles are less than the iron oxide cycle proposed by proposed by Nakamura in 1977, they are both more difficult to realize due to their associated phase transformations and material handling concerns. As a result, “ferrite” cycles were evolved, and incorporate the simplicity of the iron oxide cycle with the lower temperature requirements of the other cycles. By substituting transition metal oxides (M = Ni, Co, Mn) for Fe in Fe_3O_4 ($M_xFe_{3-x}O_4$), the decomposition temperature is lowered by destabilizing the spinel phase, but the reduced phase is still capable of being re-oxidized to reform the ferrite [39]. A simplified version of this process is shown below in equations 2-4 and 2-5.

$$M_xFe_{3-x}O_4 + \ thermal\ energy \rightarrow (3-x)FeO + xMO + \frac{1}{2}O_2 \quad \{T > 1673\ K\} \qquad \mathbf{2-4})$$

$$H_2O + (3-x)FeO + xMO \rightarrow M_xFe_{3-x}O_4 + \ H_2 \quad \{T < 1673\ K\} \qquad \mathbf{2-5})$$

The first, thermal reduction step proceeds via the decomposition of the ferrite to a solid solution of the transition metal oxide (e.g. Co^{2+}), Fe^{2+}, and a small amount of Fe^{3+} (not shown). The second water splitting step operates at lower temperatures to oxidize the solid solution to reform the ferrite and produce H_2. The advantage of the substitution of a transition metal can be clearly observed in Figure 2-1, from Allendorf *et.al.* [39]. The decomposition of Zn, Ni, and Co ferrites (x = 1 in $M_xFe_{3-x}O_4$) are compared to Fe ferrite (Fe_3O_4) and all three have an influence on the thermodynamically predicted reduction temperature. Both cobalt and nickel ferrites are expected to reduce at temperatures below 1700 K, whereas Fe_3O_4 does not reduce completely until below 1750 K. In addition, the reduction of Fe_3O_4 occurs at temperatures greater than its melting point, which leads to extensive sintering and slow reaction rates [39]. The addition of Co and Ni helps to mitigate this problem and the substituted-ferrite reduces at temperatures below its melting point. As such, Co and Ni ferrites have received the most interest in the literature. The biggest advantage of ferrite cycles compared to other "high temperature" redox cycles is their ability to be cycled with relative ease because the ferrites do not undergo any phase changes (i.e. solid to liquid) [40-43]. However, the theoretical amount of hydrogen generated is less than other higher temperature thermochemical cycles due to the fact that only Fe^{3+} is capable of being reduced to Fe^{2+} at the temperatures of interest[43]. Additionally, hydrolysis kinetics are relatively slow due to diffusion or surface area limitations created by near surface oxidation [43, 44]. This problem is exacerbated by high temperature sintering which occurs during thermal reduction. This often

leads to increasing the water oxidation temperature (Step 2) in order to increase reaction rates (generally T > 1000 ^{o}C), resulting in oxidation temperatures that are much higher than other analogous cycles [43, 45, 46]. Furthermore, vaporization of metals can lead to extensive metal loss over time.

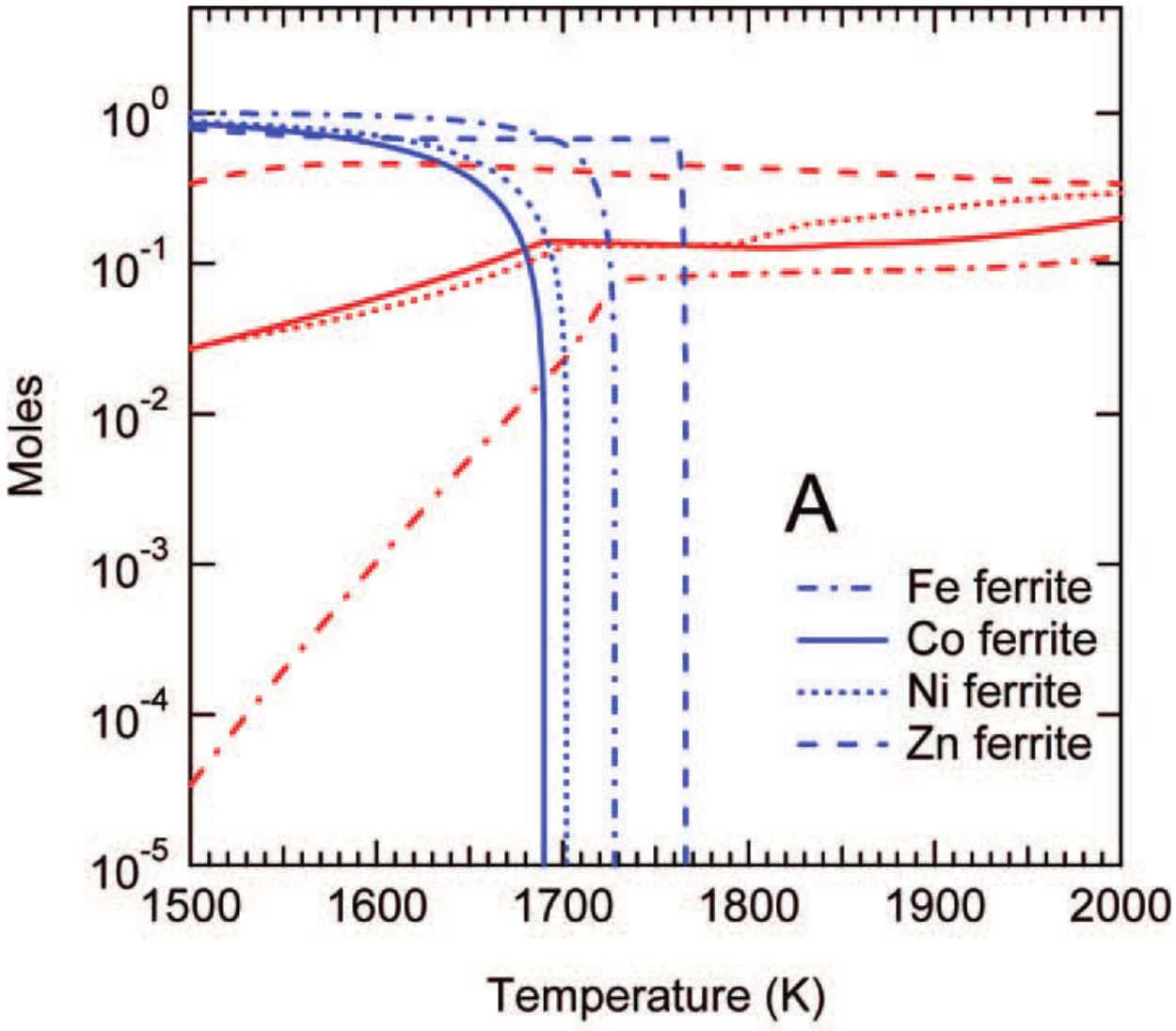

Figure 2-1. Equilibrium plot of the decomposition of various ferrites (blue) and subsequent evolution of O_2 (red), from Allendorf *et.al.* Energy & Fuels 2008;22:4115.

Ferrite water splitting cycles were first proposed by Tamaura *et. al.* in 1995 via the reduction of a Ni-Mn ferrite to a substoichiometric state [47]. Because the ferrite was only reduced to a substoichiometric state rather than the wustite (Fe^{2+}) phase, reduction was capable of being achieved at only 1373 K and the spinel phase was maintained. The reduced ferrite was capable of being re-oxidized with H_2O to form H_2 at 873 K. Although successful, it was concluded that the amount of H_2 generated was not enough to be economically feasible in a large scale process due to the small degree of reduction that was achieved. Nevertheless, this process opened the door for other ferrite cycles to be investigated, and resulted in a substantial amount of research around the globe devoted to its endeavor.

To date, most literature has been interested in the effects of the substituted metals in $M_xFe_{3-x}O_4$ and their stoichiometry [40, 41], synthesis methods[41, 48, 49], and various substrates[40, 43] on the total amount of H_2 produced and their ability to be cycled a number of times. For example, Allendorf *et. al.* recently reported on the thermodynamic effects of Fe, Co, Ni, and Zn substitution in $M_xFe_{3-x}O_4$, and observed that x and M greatly influence the equilibrium of this reaction for a given reduction temperature [39]. Co and Ni ferrites were both reduced to a greater extent at temperatures of interest (~1400 ^oC), and it was shown that Fe_3O_4 does not fully reduce until after the melting temperature of wustite. The addition of Zn actually resulted in a higher expected decomposition temperature, and is predicted to vaporize under these conditions. In fact, this has been observed experimentally and resulted in Zn deposition on reactor walls [50].

Kodama *et. al.* have observed greater cyclical stability and more H_2 production when depositing Ni, Co, and Fe ferrites on ZrO_2 and YSZ supports [40-42]. They observed that Fe^{2+} forms a solid solution with the substrate during thermal reduction and could be subsequently

oxidized to reform the ferrite. They also observed a decrease in sintering and attributed it to the presence of the substrate, which inhibits the reactive particles from interacting with one another. Because of this, they observed improved cyclical stability when compared to only physical particles, and the presence of a support is now ubiquitous for these types of high temperature cycles.

For these cycles to be a viable means of renewable H_2 production, the materials must be capable of being cycled thousands or millions of times in a repeatable and predictable manner, and therefore several different supports and synthesis methods have been investigated for their benefits. Following the work of Kodama *et.al.* Sandia National Laboratories (SNL) has investigated the influence of various types of supports on the production and repeatability of hydrogen using cobalt ferrites, including YSZ (3% Y_2O_3), Al_2O_3, TiO_2,HfO_2, and Y-doped HfO_2 [43]. They used a robocasting technique, developed at SNL, to fabricate monolith type structures directly from physically mixed ferrite and support particles. It was concluded that YSZ was the most promising support because more H_2 was produced than when using any of the other supports, and the materials remained active for tens of cycles. HfO_2 and Y-doped HfO_2 also produced hydrogen without signs of deactivation, but the yields were about half as much for the Y-doped HfO_2 and 25% for the HfO_2. The performance using Al_2O_3 and TiO_2 was much worse, as a small, decreasing amount of H_2 was produced for successive cycles. It was hypothesized that this was due to a solid state reaction between the support and the reactive ferrite [43]. Roeb *et.al.* have tested the effectiveness of recrystallized silicon carbide (ReSiC) and siliconized silicon carbide (SiSiC) monoliths as ferrite supports and were able to cycle the materials up to six times [51]. The ReSiC was concluded to be more suitable than the SiSiC due to its greater stability at higher temperatures and its lower resistance to reactivity with the ferrite.

Through thermodynamics, the effect of substituted metals and various substrates has been extensively studied. The kinetics and mechanisms of these reactions have yet to be explored in as much detail. Rapid hydrolysis kinetics is desired in order to facilitate high throughput of H_2 [43, 44]. Charvin *et. al.* observed a strong dependence of Fe_3O_4 particle size on the H_2 reaction rate during water oxidation experiments [52]. As the particle size was increased, slower rates were observed. It was hypothesized that this was due to an oxide barrier formed on the surface of the particles, hindering further oxidation of the bulk. Similar behavior has been observed for CO_2 splitting on chemically reduced $CoFe_2O_4$ nanoparticles [53]. Though it was hypothesized that this phenomena was due to bulk diffusion limitations, there was no evidence that it was not more dependent on surface area. Steinfeld *et.al.* have studied the oxidization kinetics of FeO particles using CO_2 [33]. They observed two distinct reaction limited regimes, namely an initially fast interfacial reaction which could be described by the power rate law, and a slower diffusion limited regime at longer reaction times. Experiments were conducted isothermally and non-isothermally in a TGA, and the calculated activation energies for the interfacial regime and diffusion limited regime were 70 kJ/mol and 106.4 kJ/mol, respectively. Go *et. al.* has studied the water oxidation of Zn, Mn, and Fe ferrite powders after chemical reduction using CH_4, and concluded that the reactions were diffusion limited [54]. It was apparent that the reaction models fit the data well for long reaction times, but the initial onset of the reaction was not captured well. The measured activation energies ranged from 57 kJ/mol to 110 kJ/mol, which are similar to Steinfeld *et.al.*'s value for FeO oxidation. Oxidation was studied using water concentrations ranging from 10% to 80% and no dependence on the reaction rates was observed. Because the materials were chemically reduced at low temperatures it is not clear how representative this study is of a true "high temperature" ferrite oxidation study. It is well documented that extensive

sintering occurs when ferrites are thermally reduced at higher temperatures, which has an effect on the material's morphology. Pitz-Paal *et. al.* have studied the water oxidation of zinc ferrite on SiC honeycomb supports and determined that the kinetics agreed well with the shrinking core model. The relevant kinetic parameters were calculated based on peak H_2 rates, and the activation energy was determined to be 110 kJ/mol [55]. Surprisingly, all of the calculated activation energies during the diffusion limited regimes for the above studies were less than those calculated for Fe diffusion in Fe_3O_4 [56-58]. This is unexpected because the diffusion of Fe through magnetite has been shown to be the rate limiting mechanism in Fe oxidation [59].

Presently, there have yet to be any kinetic studies of ferrite thermal decomposition reactions. It is well understood that the thermodynamics and kinetics improve as the temperature is increased, but obviously this is not a substitute for a fundamental understanding of reaction kinetics. Possibly, this step is less studied because the water oxidation reaction is even less understood, thereby garnering more attention from researchers. Ultimately, the economic viability of this thermochemical cycle is dependent on developing an understanding of the rate limiting mechanisms and kinetics of both the decomposition and oxidation reactions. This will prove to be important for engineering materials that are able to withstand the rigors of thermal stresses and high temperatures, while at the same time quickly and efficiently transporting oxygen through its lattice. Additionally, a fundamental understanding of the reaction kinetics is critical for designing reactors and solar fields that are able to operate under conditions that provide the most efficient pathway of converting incident solar radiation and water into hydrogen and oxygen.

2.4.2 Alternative Metal Oxide Cycles – Ceria

Perhaps the biggest barrier preventing ferrite water splitting cycles from being economical today is the slow rate of both decomposition and oxidation reactions. Because the oxidation reaction is limited by diffusion, one obvious solution to this problem would be to synthesize materials with larger surface area to volume ratios. However, this proves to be difficult to realize because of sintering that occurs at high temperatures. This compromises the material's integrity and results in a reduction of reactive surface area. To circumvent this problem, other materials are being investigated which have superior material properties at elevated temperatures compared to ferrites. One of these materials is ceria (CeO_2), which is capable of being cycled in an analogous manner to the ferrites [60]. Sintering is not as much of an issue because its melting temperature is much greater (2230 ^oC) [43]. Because of this, higher surface area materials can be utilized and the observed reaction rates are considerably faster than ferrite's [60].

In order to fully decompose CeO_2 to Ce_2O_3, very high temperatures are required (2000 ^oC), which is undesirable. Additionally, at these temperatures the ceria is highly volatile, leading to losses of reactive mass. However, it is capable of being reduced to a sub-stoichiometric state ($CeO_{2-\delta}$) at lower temperatures comparable to ferrite cycles [61]. The disadvantage of this is that the degree of reduction is less than ferrites, resulting in lower H_2 yields. Dopants are being investigated whose role is to increase the degree of nonstoichiometry and decrease the reduction temperature, but the degree of reduction will never equal that of ferrite cycles unless the ceria is reduced stoichiometrically to Ce_2O_3 [62]. In the end, there is a tradeoff between faster reactions or higher hydrogen yields when considering ceria and ferrite-based water splitting processes. However, ferrite rates have the possibility to improve with material design advances that limit the degree of sintering, whereas ceria yields are limited by thermodynamics and cannot be

improved. Currently, though, both cycles are the best candidates for “high temperature” solar water splitting applications, and as such each is receiving considerable interest from the scientific community.

2.5 References

[1] Marban G, Vales-Solis T. Towards the hydrogen economy? International Journal of Hydrogen Energy 2007;32:1625.

[2] Balat M. Possible Methods for Hydrogen Production. Energy Sources Part a-Recovery Utilization and Environmental Effects 2009;31:39.

[3] Hohn KL, Lin YC. Catalytic Partial Oxidation of Methanol and Ethanol for Hydrogen Generation. Chemsuschem 2009;2:927.

[4] Stiegel GJ, Ramezan M. Hydrogen from coal gasification: An economical pathway to a sustainable energy future. International Journal of Coal Geology 2006;65:173.

[5] Salameh MG. The new frontiers for the United States energy security in the 21st century. Applied Energy 2003;76:135.

[6] Hertwich EG, Zhang XP. Concentrating-Solar Biomass Gasification Process for a 3rd Generation Biofuel. Environmental Science & Technology 2009;43:4207.

[7] Lichty P, Perkins C, Woodruff B, Bingham C, Weimer A. Rapid High Temperature Solar Thermal Biomass Gasification in a Prototype Cavity Reactor. Journal of Solar Energy Engineering-Transactions of the Asme;132.

[8] Melchior T, Perkins C, Lichty P, Weimer AW, Steinfeld A. Solar-driven biochar gasification in a particle-flow reactor. Chemical Engineering and Processing 2009;48:1279.

[9] Piatkowski N, Steinfeld A. Solar-driven coal gasification in a thermally irradiated packed-bed reactor. Energy & Fuels 2008;22:2043.

[10] Dahl JK, Tamburini J, Weimer AW, Lewandowski A, Pitts R, Bingham C. Solar-thermal processing of methane to produce hydrogen and syngas. Energy & Fuels 2001;15:1227.

[11] Piatkowski N, Steinfeld A. Reaction kinetics of the combined pyrolysis and steam-gasification of carbonaceous waste materials. Fuel;89:1133.

[12] Trommer D, Noembrini F, Fasciana A, Rodriguez D, Morales A, Romero M, Steinfeld A. Hydrogen production by steam-gasification of petroleum coke using concentrated solar power - I. Thermodynamic and kinetic analyses. International Journal of Hydrogen Energy 2005;30:605.

[13] Turner J, Sverdrup G, Mann MK, Maness PC, Kroposki B, Ghirardi M, Evans RJ, Blake D. Renewable hydrogen production. International Journal of Energy Research 2008;32:379.

[14] Perkins C, Weimer AW. Solar-Thermal Production of Renewable Hydrogen. Aiche Journal 2009;55:286.

[15] Lemus RG, Duart JMM. Updated hydrogen production costs and parities for conventional and renewable technologies. International Journal of Hydrogen Energy;35:3929.

[16] Hauch A, Ebbesen SD, Jensen SH, Mogensen M. Highly efficient high temperature electrolysis. Journal of Materials Chemistry 2008;18:2331.

[17] Getoff N. PHOTOELECTROCHEMICAL AND PHOTOCATALYTIC METHODS OF HYDROGEN-PRODUCTION - A SHORT REVIEW. International Journal of Hydrogen Energy 1990;15:407.

[18] Steinfeld A. Solar hydrogen production via a two-step water-splitting thermochemical cycle based on Zn/ZnO redox reactions. International Journal of Hydrogen Energy 2002;27:611.

[19] Kolb GJ, Diver RB, Siegel N. Central-station solar hydrogen power plant. Journal of Solar Energy Engineering-Transactions of the Asme 2007;129:179.

[20] Etievant C. SOLAR HIGH-TEMPERATURE DIRECT WATER SPLITTING - A REVIEW OF EXPERIMENTS IN FRANCE. Solar Energy Materials 1991;24:413.

[21] Baykara SZ. Experimental solar water thermolysis. International Journal of Hydrogen Energy 2004;29:1459.

[22] McQuillan BW, Besenbruch GE, Brown LE, Rennels RA, Wong BY. Meal sulfate water splitting thermochemical hydrogen production cycles. The Second International Workshop on Hydrogen. Ghardaïa, 2007.

[23] Dokiya M, Fukuda K, Kameyama T, Kotera Y, Asakura S. STUDY OF THERMOCHEMICAL HYDROGEN PREPARATION .2. ELECTROCHEMICAL HYBRID CYCLE USING SULFUR-IODINE SYSTEM. Denki Kagaku 1977;45:139.

[24] Yoshida K, Kameyama H. THERMOCHEMICAL HYDROGEN PRODUCTION BY THE BR-CA-FE UT-3 CYCLE. Abstracts of Papers of the American Chemical Society 1979:21.

[25] Naterer GF, Gabriel K, Wang ZL, Daggupati VN, Gravelsins R. Thermochemical hydrogen production with a copper-chlorine cycle. I: oxygen release from copper oxychloride decomposition. International Journal of Hydrogen Energy 2008;33:5439.

[26] Wong B, Buckingham RT, Brown LC, Russ BE, Besenbruch GE, Kaiparambil A, Santhanakrishnan R, Roy A. Construction materials development in sulfur-iodine thermochemical water-splitting process for hydrogen production. International Journal of Hydrogen Energy 2007;32:497.

[27] Cerri G, Salvini C, Corgnale C, Giovannelli A, Manzano DD, Martinez AO, Le Duigou A, Borgard JM, Mansilla C. Sulfur-Iodine plant for large scale hydrogen production by nuclear power. International Journal of Hydrogen Energy;35:4002.

[28] Nakajima H, Ikenoya K, Onuki K, Shimizu S. Closed-cycle continuous hydrogen production test by thermochemical IS process. Kagaku Kogaku Ronbunshu 1998;24:352.

[29] Nakamura T. HYDROGEN PRODUCTION FROM WATER UTILIZING SOLAR HEAT AT HIGH-TEMPERATURES. Solar Energy 1977;19:467.

[30] Perkins C, Lichty P, Weimer AW. Determination of aerosol kinetics of thermal ZnO dissociation by thermogravimetry. Chemical Engineering Science 2007;62:5952.

[31] Perkins C, Lichty PR, Weimer AW. Thermal ZnO dissociation in a rapid aerosol reactor as part of a solar hydrogen production cycle. International Journal of Hydrogen Energy 2008;33:499.

[32] Schunk LO, Haeberling P, Wepf S, Wuillemin D, Meier A, Steinfeld A. A receiver-reactor for the solar thermal dissociation of zinc oxide. Journal of Solar Energy Engineering-Transactions of the Asme 2008;130.

[33] Loutzenhiser PG, Galvez ME, Hischier I, Stamatiou A, Frei A, Steinfeld A. CO2 Splitting via Two-Step Solar Thermochemical Cycles with Zn/ZnO and FeO/Fe3O4 Redox Reactions II: Kinetic Analysis. Energy & Fuels 2009;23:2832.

[34] Funke HH, Diaz H, Liang XH, Carney CS, Weimer AW, Li P. Hydrogen generation by hydrolysis of zinc powder aerosol. International Journal of Hydrogen Energy 2008;33:1127.

[35] Weiss RJ, Ly HC, Wegner K, Pratsinis SE, Steinfeld A. H-2 production by Zn hydrolysis in a hot-wall aerosol reactor. Aiche Journal 2005;51:1966.

[36] Sturzenegger M, Nuesch P. Efficiency analysis for a manganese-oxide-based thermochemical cycle. Energy 1999;24:959.

[37] Francis TM, Lichty PR, Weimer AW. Manganese oxide dissociation kinetics for the Mn2O3 thermochemical water-splitting cycle. Part 1: Experimental. Chemical Engineering Science;65:3709.

[38] Sturzenegger M, Ganz J, Nuesch P, Schelling T. Solar hydrogen from a manganese oxide based thermochemical cycle. Journal De Physique Iv 1999;9:331.

[39] Allendorf MD. Two-Step Water Splitting Using Mixed-Metal Ferrites: Thermodynamic Analysis and Characterization of Synthesized Materials. Energy & Fuels 2008;22:4115.

[40] Kodama T, Gokon N, Yamamoto R. Thermochemical two-step water splitting by ZrO2-supported NixFe3-xO4 for solar hydrogen production. Solar Energy 2008;82:73.

[41] Kodama T, Kondoh Y, Yamamoto R, Andou H, Satou N. Thermochemical hydrogen production by a redox system of ZrO2-supported Co(II)-ferrite. Solar Energy 2005;78:623.

[42] Kodama T, Nakamuro Y, Mizuno T. A two-step thermochemical water splitting by iron-oxide on stabilized zirconia. Journal of Solar Energy Engineering-Transactions of the Asme 2006;128:3.

[43] Miller JE, Allendorf MD, Diver RB, Evans LR, Siegel NP, Stuecker JN. Metal oxide composites and structures for ultra-high temperature solar thermochemical cycles. Journal of Materials Science 2008;43:4714.

[44] Gokon N, Hasegawa T, Takahashi S, Kodama T. Thermochemical two-step water-splitting for hydrogen production using Fe-YSZ particles and a ceramic foam device. Energy 2008;33:1407.

[45] Ernst FO, Steinfeld A, Pratsinis SE. Hydrolysis rate of submicron Zn particles for solar H-2 synthesis. International Journal Of Hydrogen Energy 2009;34:1166.

[46] Ma XF, Zachariah MR. Size-resolved kinetics of Zn nanocrystal hydrolysis for hydrogen generation. International Journal Of Hydrogen Energy;35:2268.

[47] Tamaura Y, Steinfeld A, Kuhn P, Ehrensberger K. PRODUCTION OF SOLAR HYDROGEN BY A NOVEL, 2-STEP, WATER-SPLITTING THERMOCHEMICAL CYCLE. Energy 1995;20:325.

[48] Agrafiotis C, Roeb M, Konstandopoulos AG, Nalbandian L, Zaspalis VT, Sattler C, Stobbe P, Steele AM. Solar water splitting for hydrogen production with monolithic reactors. Solar Energy 2005;79:409.

[49] Lorentzou S, Agrafiotis CC, Konstandopoulos AG. Aerosol spray pyrolysis synthesis of water-splitting ferrites for solar hydrogen production. Granular Matter 2008;10:113.

[50] Kaneko H, Kodama T, Gokon N, Tamaura Y, Lovegrove K, Luzzi A. Decomposition of Zn-ferrite for O-2 generation by concentrated solar radiation. Solar Energy 2004;76:317.

[51] Roeb M, Sattler C, Kluser R, Monnerie N, de Oliveira L, Konstandopoulos AG, Agrafiotis C, Zaspalis VT, Nalbandian L, Steele A, Stobbe P. Solar hydrogen production by a two-step cycle based on mixed iron oxides. Journal of Solar Energy Engineering-Transactions of the Asme 2006;128:125.

[52] Charvin P, Abanades S, Flamant G, Lemort F. Two-step water splitting thermochemical cycle based on iron oxide redox pair for solar hydrogen production. Energy 2007;32:1124.

[53] Khedr MH, Omar AA, Abdel-Moaty SA. Reduction of carbon dioxide into carbon by freshly reduced CoFe2O4 nanoparticles. Materials Science and Engineering a-Structural Materials Properties Microstructure and Processing 2006;432:26.

[54] Go KS, Son SR, Kim SD. Reaction kinetics of reduction and oxidation of metal oxides for hydrogen production. International Journal Of Hydrogen Energy 2008;33:5986.

[55] Neises M, Roeb M, Schmuker M, Sattler C, Pitz-Paal R. Kinetic investigations of the hydrogen production step of a thermochemical cycle using mixed iron oxides coated on ceramic substrates. International Journal of Energy Research;34:651.

[56] Dieckmann R, Schmalzried H. POINT-DEFECTS AND CATION DIFFUSION IN MAGNETITE. Zeitschrift Fur Physikalische Chemie-Frankfurt 1975;96:331.

[57] Dieckmann R, Schmalzried H. DEFECTS AND CATION DIFFUSION IN MAGNETITE .1. Berichte Der Bunsen-Gesellschaft-Physical Chemistry Chemical Physics 1977;81:344.

[58] Hendy SC, Laycock NJ, Ryan MP. Atomistic modeling of cation transport in the passive film on iron and implications for models of growth kinetics. Journal of the Electrochemical Society 2005;152:B271.

[59] Chen RY, Yuen WYD. Review of the high-temperature oxidation of iron and carbon steels in air or oxygen. Oxidation of Metals 2003;59:433.

[60] Abanades S, Flamant G. Thermochemical hydrogen production from a two-step solar-driven water-splitting cycle based on cerium oxides. Solar Energy 2006;80:1611.

[61] Kaneko H, Ishihara H, Taku S, Naganuma Y, Hasegawa N, Tamaura Y. Cerium ion redox system in CeO2-xFe(2)O(3) solid solution at high temperatures (1,273-1,673 K) in the two-step water-splitting reaction for solar H-2 generation. Journal of Materials Science 2008;43:3153.

[62] Kaneko H, Miura T, Ishihara H, Taku S, Yokoyama T, Nakajima H, Tamaura Y. Reactive ceramics of CeO2-MOx (M = Mn, Fe, Ni, Cu) for H-2 generation by two-step water splitting using concentrated solar thermal energy. Energy 2007;32:656.

CHAPTER 3 THERMODYNAMIC MODELING OF RELEVANT FERRITE-BASED WATER SPLITTING CYCLES

3.1 Abstract

The thermodynamics of relevant ferrite-based water splitting cycles has been investigated using the thermodynamics software package FactSage. The effect of different metal substitutions in $M_xFe_{3-x}O_4$, has been explored, and indicates that Co and Ni based ferrites are both superior to Fe_3O_4. Additionally, it is shown that increasing the inert gas concentrations has a direct effect on the reduction temperature. Increasing the amount of cobalt results in lowering the thermal reduction requirements, but does not necessarily translate to more H_2 production. For values of x > 1, the amount of reducible iron decreases, and results in less H_2 production at elevated reduction temperatures. Oxidation of reduced species is shown to be achievable at temperatures greater than when $\Delta G_{rxn} > 0$ if large excesses of water are introduced. More H_2 is expected to be present at equilibrium for ferrite based reactions compared to ceria based water splitting cycles, because the degree of reduction is approximately three times greater.

3.2 Introduction

Solar thermochemical production of H_2 by ferrite cycles was born out of the originally proposed Fe_3O_4 redox cycle, by Nakamura in 1977 [1]. By incorporating the advantages properties of Fe_3O_4 with those of other metal oxides by substituting them into its spinel structure, its ability to split water at relatively benign temperatures is maintained, but its decomposition temperature is lowered. Ferrites of the form $M_xFe_{3-x}O_4$ (where M is generally Co[2, 3], Ni[4-6],

Mn[7-9], Zn[10-12], or Fe[4, 13-15]) have all been shown to be capable of splitting water to generate hydrogen using solar thermal energy according to the redox reaction shown below:

$$M_xFe_{3-x}O_4 + \ thermal\ energy \rightarrow (3-x)FeO + xMO + \frac{1}{2}O_2 \quad \{T > 1673\ K\} \qquad \mathbf{3-1})$$

$$H_2O + (3-x)FeO + xMO \rightarrow M_xFe_{3-x}O_4 + \ H_2 \quad \{T < 1673\ K\} \qquad \mathbf{3-\ 2})$$

The ferrite is thermally reduced in the first, high temperature step (generally 1400 – 1600 ^{o}C), and oxygen is evolved. In the second lower temperature step (generally 900 – 1100 ^{o}C), the reduced ferrite is reacted with steam to generate H_2 and re-oxidize the ferrite to its original state. Thus, the only net inputs are H_2O and thermal energy, and the only net outputs are H_2 and O_2. This process is advantageous to direct water splitting as it operates at much lower temperatures and O_2 and H_2 are generated in separate steps, eliminating the need for high temperature separation of product gases[16].

Thermodynamic modeling of ferrite [17] and similar metal oxide redox cycles [16] has shown to be an effective method of predicting equilibrium species, as well as screening for other potentially relevant cycles. While these calculations can never take the place of experiments, their advantage lies in the ability to perform many calculations relatively easily, based on years of accumulated knowledge and experiments that have already been accomplished.

The objective of this work is to provide a theoretical framework, based on thermodynamic calculations, of ferrite water splitting cycles. Of particular interest is investigating the effects of various conditions on the overall performance of the ferrite. Specifically, the effects of different substituted metals (i.e. Ni, Co), their concentrations (M_xFe_{3-}

$_xO_4$), reduction and oxidation temperatures, and gas concentrations (both inert gas and oxidant). Additionally, a short amount of time will be devoted to the thermodynamics of ceria (CeO_2) water splitting cycles, which have received a tremendous amount of interest recently [18-21].

3.3 Methods

Thermodynamic calculations are performed using the thermodynamics software package, FactSage version 6.0. This software is equipped with extensive thermodynamic databases based on data from the literature. Equilibrium calculations are conducted by minimizing the total Gibbs energy, G, of the system, which is composed of all possible species formed based on the input species specified. These calculations have been shown to be an effective method for predicting phases and equilibrium H_2 generation of ferrites by Allendorf *et. al.* [17]. The inclusion of solution phases with species was shown to have a significant impact upon the equilibrium results. For all ferrite equilibrium calculations, we are including the species and solution phases shown in Table 3-1. Species included in the ceria calculations are shown in Table 3-2. All calculations are performed at 1 atm. Thermal reduction and oxidation calculations are performed with a dilution of 10000 moles of Ar and H_2O, respectively, unless specified otherwise.

Table 3-1: Species Included in Ferrite Equilibrium Calculations

Gases	Pure Liquids	Pure Solids	Solution Phases
Ar	FeO	FeO (wustite)	spinel
O_2	CoO	CoO	-$M_xFe_{3-x}O_4$
O	Fe_3O_4	NiO	-$M_xCo_{3-x}O_4$
Co	Co	Fe_3O_4 (magnetite)	-$M_xNi_{3-x}O_4$
Ni	Fe	Fe_2O_3 (hematite)	-MO_4
NiO	Ni	Co	metal oxides (MeO)
FeO		(CoO)(Fe_2O_3)	-FeO, Fe_2O_3,CoO, NiO
Fe		(NiO)(Fe_2O_3)	slag
O_3		Fe	- FeO, Fe_2O_3, CoO, NiO
		Co_3O_4	corundum (M_2O_3)
			-Fe_2O_3,
			M = Fe, Co, or Ni

Table 3-2: Species Included in Ceria Equilibrium Calculations

Gases	Pure Liquids	Pure Solids
Ar	Ce_2O_3	CeO_2
O_2	Ce	Ce_6O_{11}
O		Ce_2O_3
CeO		$Ce_{18}O_{31}$
O_3		
Ce		
Ce_2		

3.4 Results

3.4.1 *Gibbs Free Energy Analysis*

The effect of metal substitution, specifically cobalt, can be seen in Figures 3-1a and 3-1b, where the Gibbs free energy as a function of temperature is shown for decomposition and oxidation reactions using Fe_3O_4, Co_3O_4, and $CoFe_2O_4$ as intermediates. By definition, the reactions are spontaneous at temperatures where $\Delta G_{rxn} < 0$. Co_3O_4 (940 ^oC) is expected to decompose at lower temperatures than either Fe_3O_4 (2480^oC) or $CoFe_2O_4$ (2040 ^oC), but its re-

oxidation with water to produce H_2 is thermodynamically unfavorable. There are no temperatures where its Gibbs energy is less than zero. Fe_3O_4 is capable of decomposing at temperatures above 2480 ^oC, but this is very high considering that most reactor materials available today are not stable at temperatures greater than 2500 K [16]. Additionally, reradiation losses become significant due to their T^4 dependence, and above 1600 ^oC Fe_3O_4 exists as a liquid. The oxidation of its decomposition products to reform Fe_3O_4 and produce H_2 is exothermic and spontaneous at temperatures lower than 700 ^oC. However, this reaction is expected to be untenable if the liquid phase is formed due to diffusion limitations through its bulk. $CoFe_2O_4$, on the other hand, combines the advantages properties of both Co_3O_4 and Fe_3O_4. It is expected to decompose at temperatures greater than 2040 ^oC, about 450 ^oC lower than Fe_3O_4, due to its ability to destabilize the spinel structure [3]. Unlike Co_3O_4 however, it is still capable of reacting with water to re-oxodize and produce H_2. In fact, the Gibbs free energy of this reaction is nearly identical to Fe_3O_4's until temperatures greater than 1600 ^oC, which is well above realistic operating conditions.

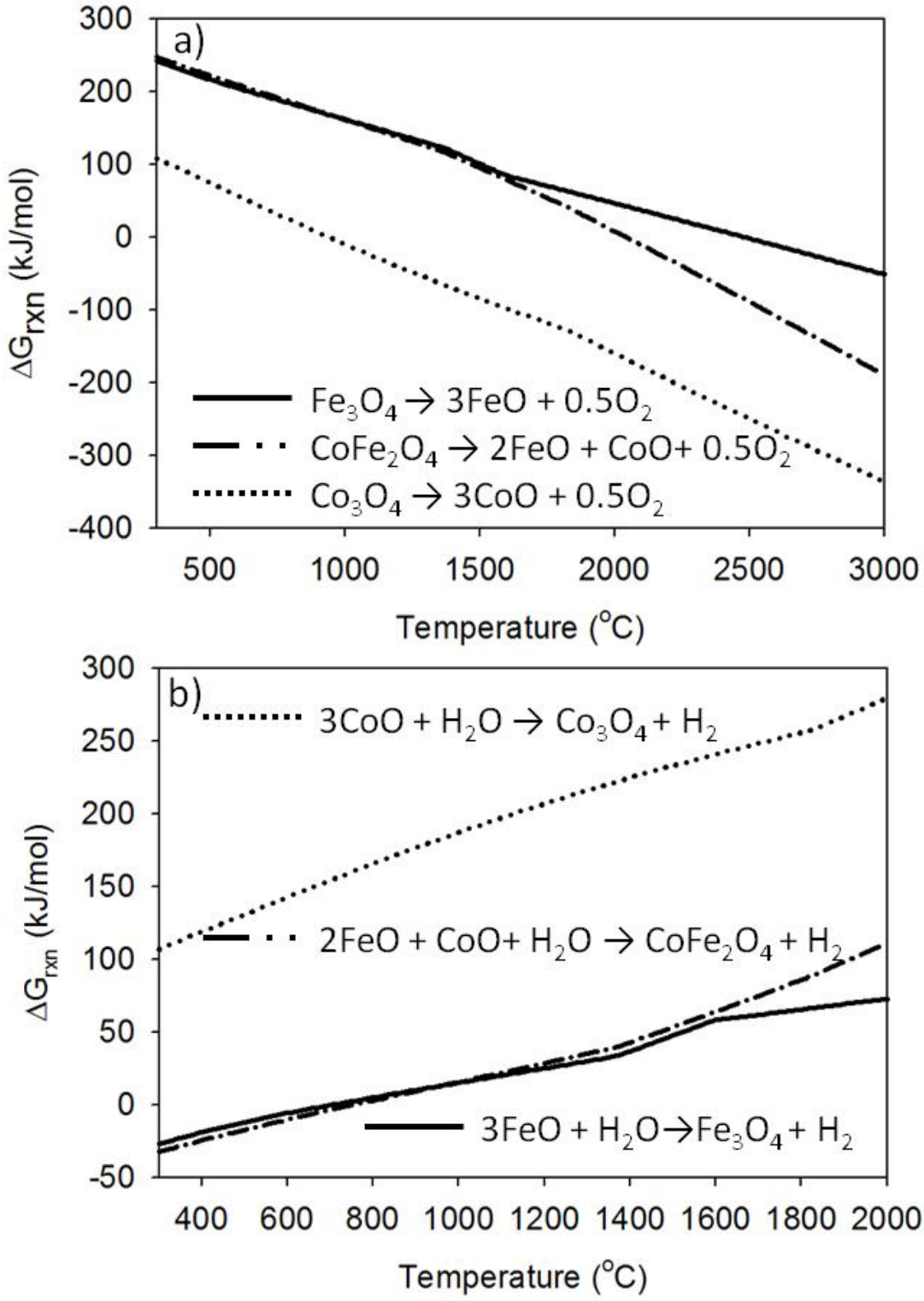

Figure 3-1: a) Gibbs free energy as a function of temperature for the decomposition of Fe_3O_4, Co_3O_4 and $CoFe_2O_4$. b) Gibbs free energy as a function of temperature for the water oxidation of Fe_3O_4, Co_3O_4 and $CoFe_2O_4$ decomposition products to produce H_2.

3.4.2 *Thermal Reduction – Equilibrium Calculations*

Although the Gibbs free energy plots discussed above provide a means to discuss the advantages of metal substitution of Fe in Fe_3O_4, they are not necessarily representative of results that would be expected experimentally. Firstly, ferrite redox cycles are generally not operated under equilibrium conditions. In most cases, the ferrite is held in a fixed position within a reactor and depending on the conditions an inert or oxidizing sweep gas flows over it [6, 7, 22]. As a result, the reaction products are carried away from the solid sample, driving the equilibrium of the reaction to lower temperatures. Secondly, the above calculations were achieved by assuming that the reactions shown in Figures 3-1a and 3-1b were only reactions that could occur. In reality, there are solution and slag phases which could form that may have an effect on the thermodynamics of the reaction [17]. A more realistic means to study the redox reactions is to perform equilibrium calculations which account for all of the possible species that may exist based on the input species. Additionally, introducing large concentrations of inert and oxidant gases into the calculations is capable of simulating experiments which do not operate under equilibrium conditions, by diluting the gas phase products (O_2 and H_2). Therefore, all of the remaining equilibrium calculations are performed in this manner to better replicate experimental scenarios.

Equilibrium calculations comparing the decomposition of two commonly used ferrites, $CoFe_2O_4$ and $NiFe_2O_4$, to Fe_3O_4 are shown in Figure 3-2. The ferrites (black line), and solid reduction products all exist as solution phases, which will hereby be referred to as spinel and MeO, respectively. The MeO solution phase is a combination of M^{2+} (where M is the substituted metal), Fe^{2+}, and Fe^{3+}. Both $CoFe_2O_4$ and $NiFe_2O_4$ begin to decompose at temperatures below 1200 ^oC, and are expected to be fully reduced by 1450 ^oC. The Fe_3O_4, on the other hand, does

not decompose completely until 1500 ^{o}C, and by this temperature exists as a slag phase which is undesirable. At the same time the Co and Ni spinel solutions decompose, O_2(g) is observed, corroborating that the ferrites are reducing rather than simply experiencing a change of phase.

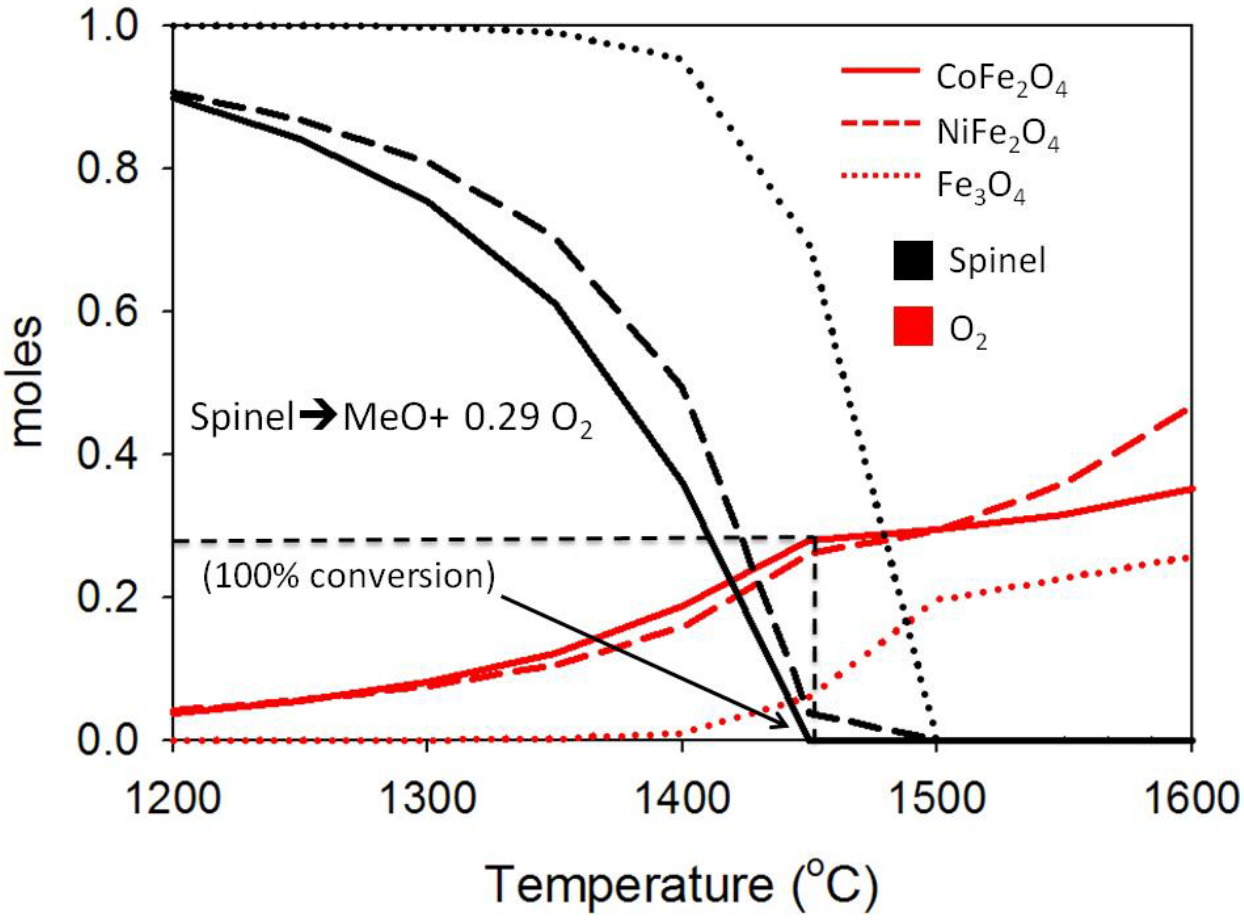

Figure 3-2: Equilibrium products as a function of temperature for the decomposition of Fe_3O_4, $CoFe_2O_4$ and $NiFe_2O_4$. Moles Ar:ferrite = 10000:1

Although the Fe_3O_4 decomposes by 1500 ^{o}C, it is not accompanied by large amounts of O_2, as the cobalt and nickel ferrites are. This is because this decomposition has largely proceeded via phase change to a slag, without the accompanying reduction of Fe^{3+} to Fe^{2+}. Surprisingly, at 1450 ^{o}C, when the cobalt ferrite is fully decomposed, only 0.29 moles of O_2 exists at

equilibrium, rather than 0.5, which would be present if all of the Fe^{3+} were reduced to Fe^{2+}. This is due to a significant portion of the Fe in the MeO phase existing as Fe^{3+}. Because conversions calculated in the literature assume that all of the Fe^{3+} is capable of reducing to Fe^{2+}, this observation may help to explain why some conversions are lower than expected [2, 4]. It is also apparent that all of these species are predicted to decompose at temperatures lower than the Gibbs free energy plots shown in Figure 3-1. This is due to the dilution of the gas phase products (O_2), with 10000 moles Ar:Ferrite.

The effect of dilution is further explored in Figure 3-3, and indicates that there is a direct relationship between expected decomposition temperatures of cobalt ferrite and inert gas concentration. Ratios of Ar:$CoFe_2O_4$ equaling 10000:1, 100:1, and 1:1 have been considered, and as expected, indicate lower predicted decomposition temperatures for higher dilutions. For a dilution of 10000:1 the ferrite is expected to decompose at 1450 ^oC, and the corresponding O_2 evolution is observed. The same trend is observed for a ratio of 100:1, but decomposition isn't expected to fully proceed until 1600 ^oC. By the time the spinel has fully decomposed with a 1:1 ratio, the slag phase has formed. As a result, less O_2 exists at this time compared to the other dilution conditions because the decomposition largely proceeded via the phase change to a slag, rather than to the reduced MeO phase. These observations also highlight a distinct advantage that ferrite cycles have over cycles such as the ZnO/Zn redox cycle. Because the ferrites remain a solid during decomposition, the reduction temperature can be manipulated easily by either flowing different concentrations of inert gas over a stationary sample, or simply operating under vacuum. ZnO/Zn cycles are not offered the same advantage however, because ZnO decomposes to Zn vapor during decomposition [16]. Therefore, a sweep gas would result in the gas phase products being swept away at the same time, which may be undesirable. As a result, ferrite

cycles are generally operated at lower temperatures than the ZnO/Zn cycle, even though the Gibbs free energy of its decomposition is every bit as favorable [16].

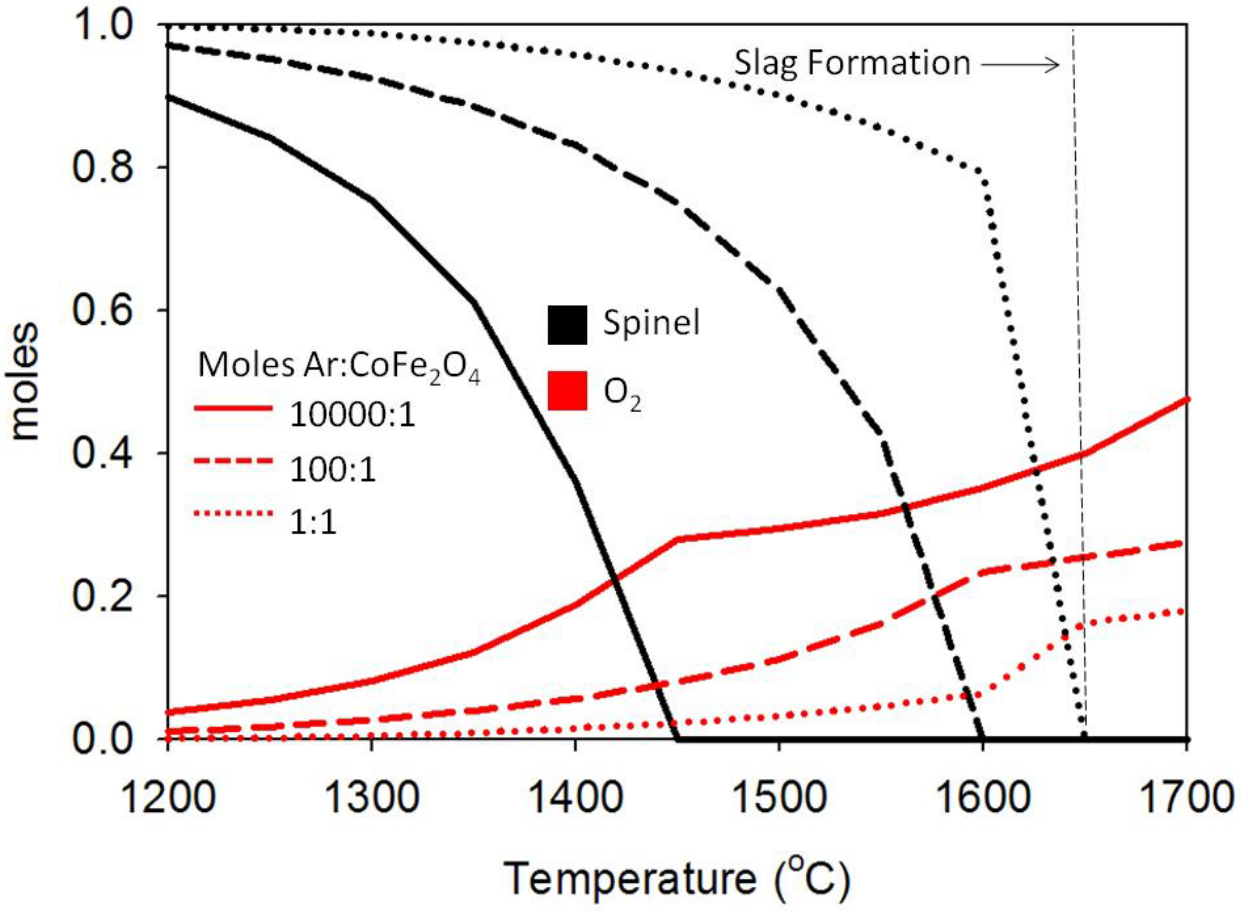

Figure 3-3: The effect of dilution on the equilibrium products as a function of temperature for the decomposition of $CoFe_2O_4$

The effect of the substituted metal concentration has also been debated in the literature, and to date, experimental results have largely been ambiguous [2, 3, 6]. Thermodynamic calculations indicate that, for the case of cobalt ferrite, the decomposition temperature is lowered as x, in $Co_xFe_{3-x}O_4$, is increased from 0.2 to 1.0, as shown in Figure 3-4. As already discussed, $CoFe_2O_4$ is completely decomposed by 1450 ^oC. The onset of decomposition of $Co_{0.6}Fe_{2.4}O_4$

begins at about 1250 ^{o}C, and does not decompose completely until 1500 ^{o}C. As x is decreased to 0.2, the decomposition does not begin until 1350 ^{o}C, and the slag phase is expected to form before it has fully decomposed. As x increases past 1, the behavior becomes more like Co_3O_4, which decomposes at low temperatures but is not capable of re-oxidizing to produce H_2. Larger cobalt concentrations did lead to even lower decompositions that for x=1, but are not considered here because the amount of active Fe decreases beyond this point.

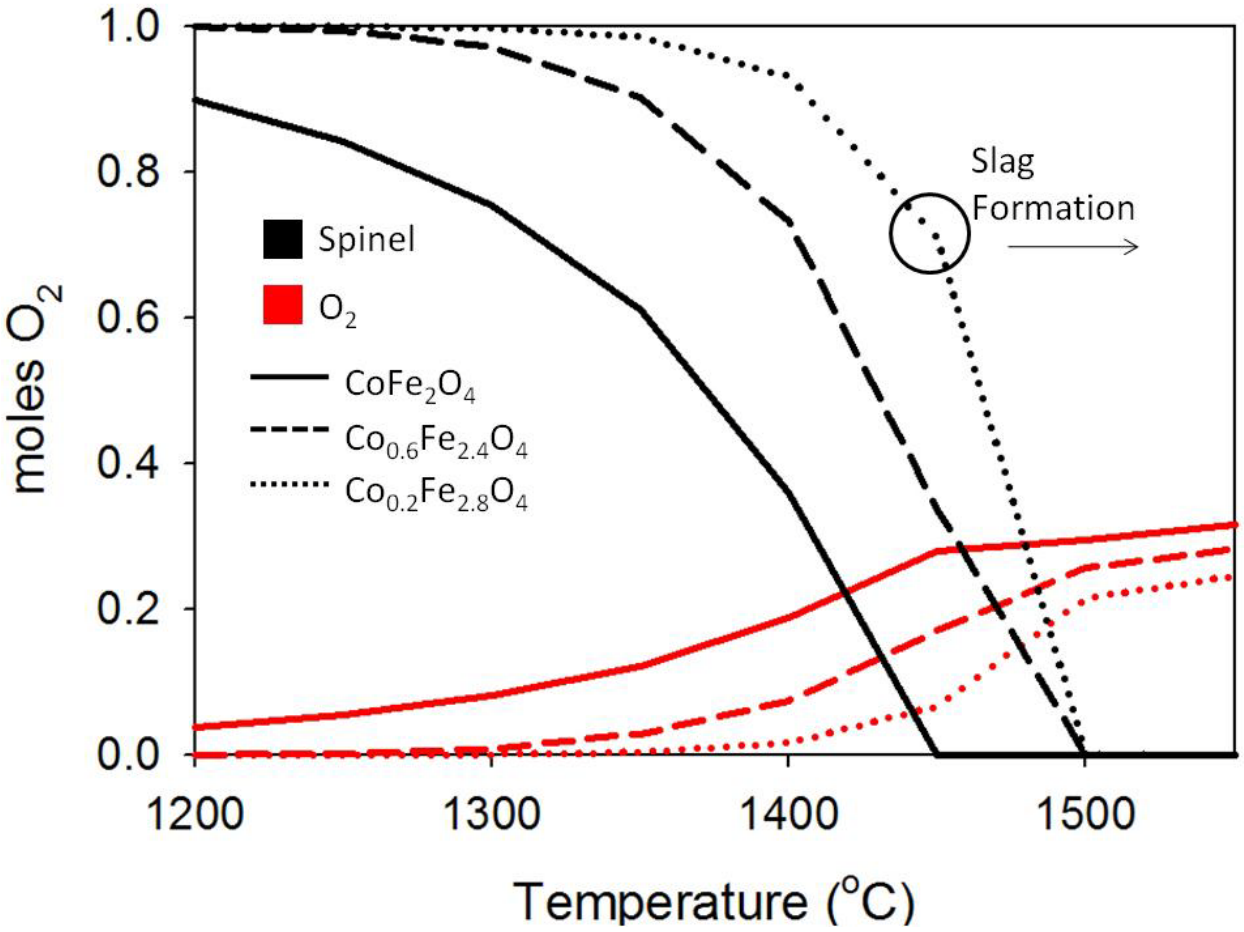

Figure 3-4: The effect of cobalt stoichiometry on the equilibrium products as a function of temperature for the decomposition of $Co_xFe_{3-x}O_4$. Moles Ar:ferrite = 10000:1

3.4.3 *Water Oxidation – Equilibrium Calculations*

Ferrite water oxidation experiments are generally operated at temperatures ranging from 900 to 1100 ^{o}C, although the reaction is thermodynamically spontaneous at temperatures much lower than these (see Figure 3-1b). This is partly due to the fact that lower oxidation temperatures result in sluggish observed reaction rates that result from sintering and diffusion limitations through the bulk particles [2, 23]. Also, analogous to the experimental reduction conditions, oxidation reactions are operated in a manner which allows the reaction to proceed at higher temperatures than thermodynamics would suggest. The effect of operating under non-equilibrium conditions can be seen in Figure 3-5, where we have considered the effect of three different H_2O:MeO ratios: 10000:1, 100:1, and 1:1. The MeO species in this case is the fully decomposed cobalt ferrite at 1500 ^{o}C and 10000 moles Ar:ferrite. With only a 1:1 ratio of H_2O:MeO, the reaction results predominantly in the formation of the spinel up to 800 ^{o}C. Beyond this temperature there is a sharp decrease in spinel formation, which is due to the transition to a positive ΔG_{rxn}. This is slightly higher than the initially stated 700 ^{o}C because of differences in the way the calculations were performed, as discussed previously. As the ratio of H_2O to MeO increases, the spinel is stable at even higher temperatures. Complete conversion to the spinel is achieved up to 500 ^{o}C for a dilution of 100:1, but even at 1200 ^{o}C, conversion is expected to be 70%. The spinel is stable to 1100 ^{o}C with a ration of 10000:1, with only a negligible decrease in fractional conversion to 1200 ^{o}C. Clearly the reaction to reform the ferrite to produce H_2 is more stable at higher temperatures when diluting the reaction products with an H_2O.

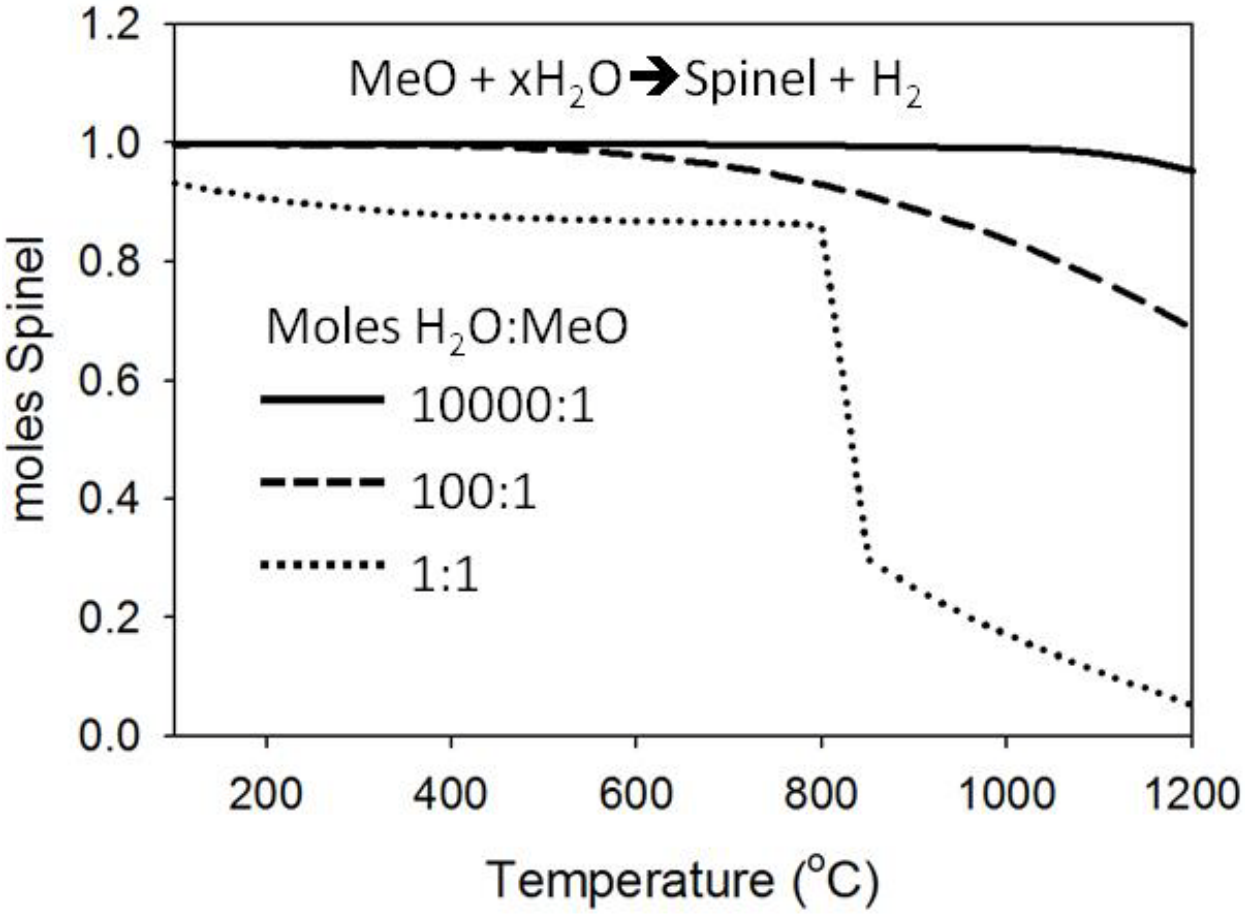

Figure 3-5: The effect of water concentration on the re-oxidation reaction to reform the spinel and H_2. MeO results from the decomposition of $CoFe_2O_4$ at 1500 ^oC, 10000 moles Ar

The effect of reduction temperature and x, in $Co_xFe_{3-x}O_4$ on the equilibrium H_2 production was considered in Figure 3-6. Calculations were performed by determining the equilibrium species of various cobalt substituted ferrites ($0<x<1.4$) from temperatures between 1300-1500 ^oC, and recycling these species (MeO and spinel) into another equilibrium calculation with 10000 moles H_2O at 1000 ^oC. As seen in Figure 3-5b, for all values of x, the amount of equilibrium H_2 increases as the temperature is increased due to an increase in reduced iron species (MeO). Also, for reduction temperatures up to 1400 ^oC, the amount of H_2 increases as the Co concentration increases. This was surprising, because for all values when $x > 1$, the amount

of reducible Fe is decreased. However, because full decomposition of the ferrites was not achieved by 1400 ^{o}C, the increased amounts of reducible iron for $x \leq 1$ did not contribute to greater amounts of equilibrium H_2 production. At higher reduction temperatures, the negative impact of $x > 1$ is realized because when $x \geq 1$ the ferrite is fully decomposed, resulting in decreased amounts of equilibrium H_2 beyond this point. For all of the conditions investigated at 1450 and 1500 ^{o}C, the most H_2 was produced for x=1.

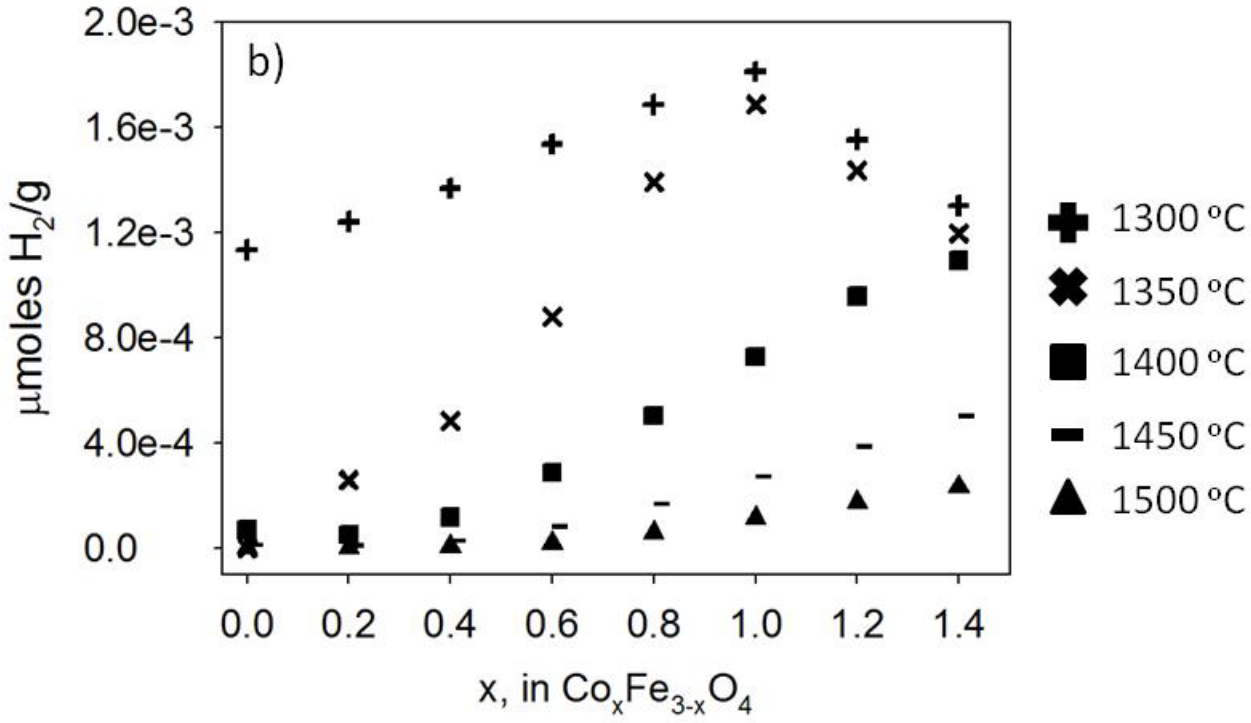

Figure 3-6: Equilibrium H_2 produced per gram of ferrite as a function of decomposition temperature and cobalt stoichiometry (x, in $Co_xFe_{3-x}O_4$).

3.4.4*Ceria-based Redox Cycles*

In addition to ferrites, ceria (CeO_2) and metal doped ceria have also received a tremendous amount of interest recently as “high temperature” solar thermochemical water

splitting candidates for renewable hydrogen production. They are capable of splitting water using solar energy according to the generic two step redox cycle shown below, where the only net inputs are solar energy and water and the outputs are O_2 and H_2.

$$CeO_2 + Solar\ Thermal\ Energy \rightarrow CeO_{2-\delta} + \frac{\delta}{2} O_2 \qquad \mathbf{3-3})$$

$$CeO_{2-\delta} + \delta H_2O \rightarrow CeO_2 + \delta H_2 \qquad \mathbf{3-4})$$

The first step proceeds via the thermal decomposition of CeO_2, usually to a non-stoichiometric state, and O_2 is evolved. The reduced ceria is then re-oxidized in the second lower temperature step using steam to produce H_2. The degree of reduction (Ce^{4+} to Ce^{3+}) is highly dependent on temperature, and complete reduction to Ce_2O_3 is only achieved at very high temperatures (≈2000 ^oC) [24]. The main advantage of ceria lies in its ability to be cycled at relatively high temperatures without sintering, resulting in faster observed reaction rates than ferrites [18, 25]. However, the degree of reduction is less than ferrites, which results in less H_2 production on a per mole bases.

As seen in Figure 3-7a, the decomposition of ceria results in several stable oxidation states, but complete reduction to Ce_2O_3 is not expected to occur until nearly 2000 ^oC. A more reasonable decomposition temperature of 1600 ^oC is required to reduce the ceria to Ce_6O_{11}. However, when compared to the decomposition of $CoFe_2O_4$, there are two glaring differences. First, the decomposition temperature is nearly 150 ^oC greater for ceria, and second, only about 1/3 of the oxygen is evolved. This is directly related to the amount of H_2 capable of being produced. Experiments have shown, however, that the decomposition of ceria generally proceeds

at temperatures similar to ferrite cycles. This is due to the addition of dopants, which increase the degree of reduction at low oxygen partial pressures compared to un-doped ceria [18, 25]. In effect, the dopants role is similar to that of cobalt in $CoFe_2O_4$, and aids in decreasing the reduction temperature. Although several dopants are being investigated, including Zr and Sm, the degree of reduction will never equal that of ferrite cycles unless the ceria is reduced stoichiometrically to Ce_2O_3 [18, 20, 25].

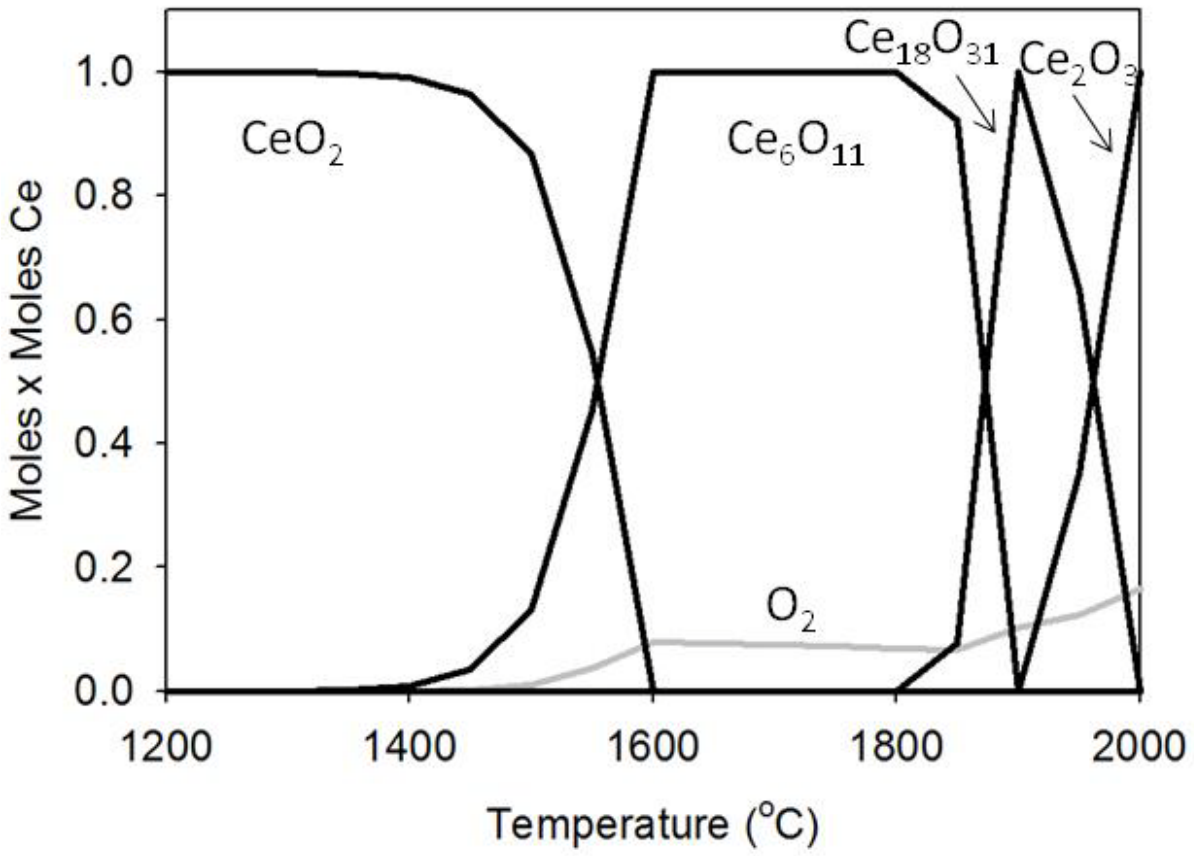

Figure 3-7: Equilibrium products for the decomposition of CeO_2. Ar:CeO_2 = 10000:1

The oxidation of Ce_6O_{11} with water to reform CeO_2 and produce H_2 is spontaneous below 880 ^oC, as seen in Figure 3-8. However, there is expected to be a tradeoff if dopants are introduced, resulting in water oxidation thermodynamics that are not as favorable as un-doped

ceria. This is because the role of dopants, like samarium, is to induce more oxygen vacancies at lower temperatures than un-doped ceria. As a result, doped ceria is thermodynamically more stable with higher oxygen vacancy concentrations than undoped, resulting in a larger energy barrier that needs to be overcome for re-oxidation.

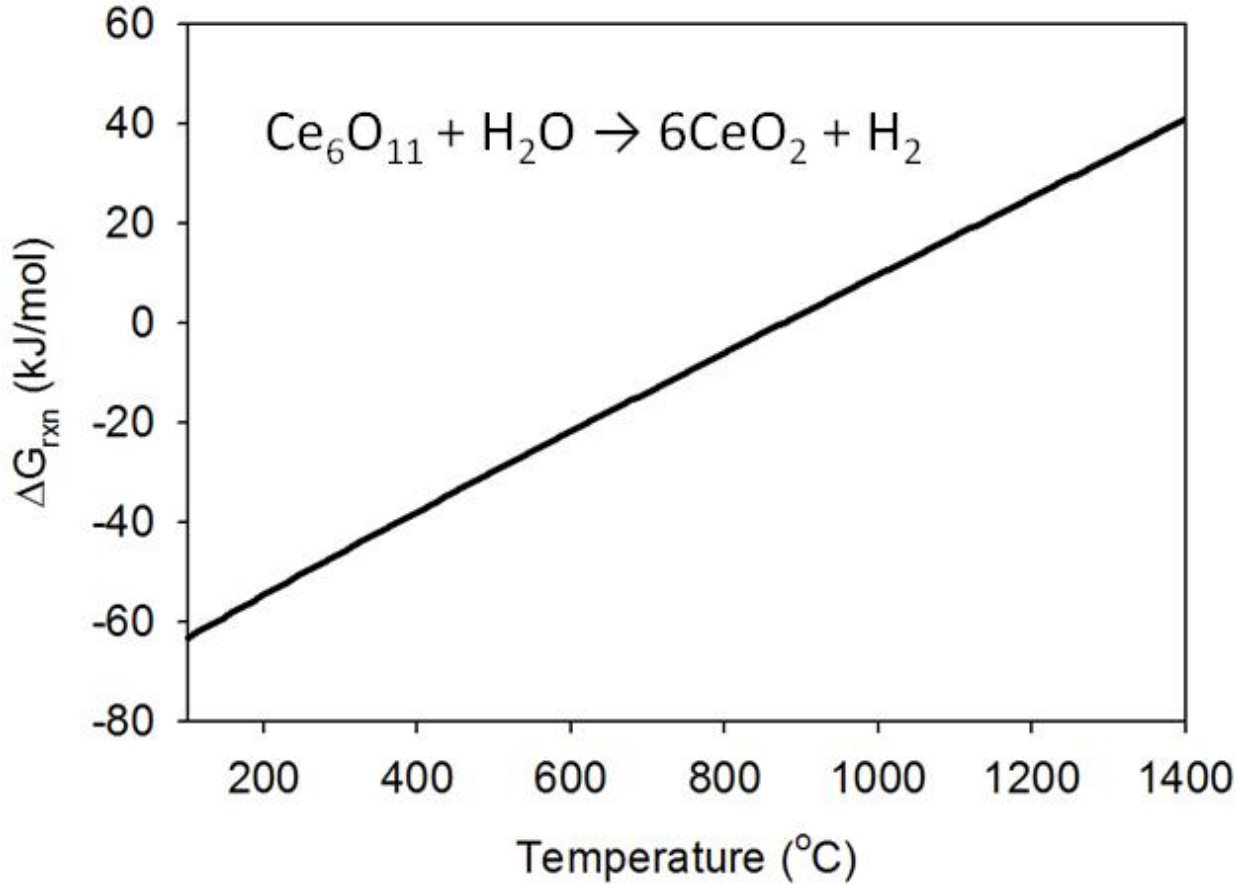

Figure 3-8: Gibbs free energy as a function of temperature for the water oxidation of Ce_6O_{11}

3.5 Conclusions

Equilibrium calculations have shown that the thermal reduction of metal substituted ferrites, such as Co and Ni, occurs at lower temperatures than un-substituted Fe_3O_4. Both are expected to decompose completely by 1450 ^{o}C, while Fe_3O_4 does not decompose completely

until its slag phase is expected to occur. Additionally, the decomposition temperature is directly related to the amount of inert gas present which acts to dilute the gas phase reaction products (O_2). As a result, the decomposition temperature can be manipulated experimentally by diluting the reactants with a sweep gas, or operating under vacuum. Also, the reduction temperature decreases as the amount of cobalt in $Co_xFe_{3-x}O_4$ is increased. The maximum amount of hydrogen is expected to be produced using $CoFe_2O_4$ reduced at temperatures greater than 1450 ^oC, and oxidized at temperatures less than 1100 ^oC. Below 1450 ^oC, ferrites with higher cobalt concentrations are expected to produce more H_2. Ceria is expected to decompose at higher temperatures than cobalt ferrites, unless doped with metals such as Sm or Zr. Additionally, complete reduction to Ce_2O_3 is not achievable until very high temperatures ($\approx$ 2000 ^oC), resulting in reduction to a non-stoichiometric state that has less potential for H_2 production than the complete decomposition of metal substituted ferrites.

3.6 References

[1] Nakamura T. HYDROGEN PRODUCTION FROM WATER UTILIZING SOLAR HEAT AT HIGH-TEMPERATURES. Solar Energy 1977;19:467.

[2] Kodama T, Kondoh Y, Yamamoto R, Andou H, Satou N. Thermochemical hydrogen production by a redox system of ZrO2-supported Co(II)-ferrite. Solar Energy 2005;78:623.

[3] Miller JE, Allendorf MD, Diver RB, Evans LR, Siegel NP, Stuecker JN. Metal oxide composites and structures for ultra-high temperature solar thermochemical cycles. 2008. p.4714.

[4] Gokon N, Murayama H, Nagasaki A, Kodama T. Thermochemical two-step water splitting cycles by monoclinic ZrO2-supported NiFe2O4 and Fe3O4 powders and ceramic foam devices. Solar Energy 2009;83:527.

[5] Hwang GJ, Park CS, Lee SH, Seo IT, Kim JW. Ni-ferrite-based thermochemical cycle for solar hydrogen production. Journal of Industrial and Engineering Chemistry 2004;10:889.

[6] Kodama T, Gokon N, Yamamoto R. Thermochemical two-step water splitting by ZrO2-supported NixFe3-xO4 for solar hydrogen production. Solar Energy 2008;82:73.

[7] Agrafiotis C, Roeb M, Konstandopoulos AG, Nalbandian L, Zaspalis VT, Sattler C, Stobbe P, Steele AM. Solar water splitting for hydrogen production with monolithic reactors. 2005. p.409.

[8] Alvani C, La Barbera A, Ennas G, Padella F, Varsano F. Hydrogen production by using manganese ferrite: Evidences and benefits of a multi-step reaction mechanism. International Journal of Hydrogen Energy 2006;31:2217.

[9] Roeb M, Sattler C, Kluser R, Monnerie N, de Oliveira L, Konstandopoulos AG, Agrafiotis C, Zaspalis VT, Nalbandian L, Steele A, Stobbe P. Solar hydrogen production by a two-step cycle based on mixed iron oxides. Journal of Solar Energy Engineering-Transactions of the Asme 2006;128:125.

[10] Aoki H, Kaneko H, Hasegawa N, Ishihara H, Suzuki A, Tamaura Y. The ZnFe2O4/(ZnO+Fe3O4) system for H-2 production using concentrated solar energy. Solid State Ionics 2004;172:113.

[11] Tamaura Y, Kaneko H. Oxygen-releasing step of ZnFe2O4/(ZnO+Fe3O4)-system in air using concentrated solar energy for solar hydrogen production. Solar Energy 2005;78:616.

[12] Kaneko H, Kojima N, Hasegawa N, Inoue M, Uehara R, Gokon N, Tamaura Y, Sano T. Reaction mechanism of H-2 generation for H2O/Zn/Fe3O4 system. International Journal of Hydrogen Energy 2002;27:1023.

[13] Kodama T, Nakamuro Y, Mizuno T. A two-step thermochemical water splitting by iron-oxide on stabilized zirconia. Journal of Solar Energy Engineering-Transactions of the Asme 2006;128:3.

[14] Gokon N, Murayama H, Umeda J, Hatamachi T, Kodama T. Monoclinic zirconia-supported Fe3O4 for the two-step water-splitting thermochemical cycle at high thermal reduction temperatures of 1400-1600 degrees C. International Journal of Hydrogen Energy 2009;34:1208.

[15] Charvin P, Abanades S, Flamant G, Lemort F. Two-step water splitting thermochemical cycle based on iron oxide redox pair for solar hydrogen production. Energy 2007;32:1124.

[16] Perkins C, Weimer AW. Likely near-term solar-thermal water splitting technologies. International Journal of Hydrogen Energy 2004;29:1587.

[17] Allendorf MD. Two-Step Water Splitting Using Mixed-Metal Ferrites: Thermodynamic Analysis and Characterization of Synthesized Materials. Energy & Fuels 2008;22:4115.

[18] Abanades S, Legal A, Cordier A, Peraudeau G, Flamant G, Julbe A. Investigation of reactive cerium-based oxides for H-2 production by thermochemical two-step water-splitting. Journal of Materials Science;45:4163.

[19] Chueh WC, Haile SM. Ceria as a Thermochemical Reaction Medium for Selectively Generating Syngas or Methane from H2O and CO2. Chemsuschem 2009;2:735.

[20] Kaneko H, Miura T, Ishihara H, Taku S, Yokoyama T, Nakajima H, Tamaura Y. Reactive ceramics of CeO2-MOx (M = Mn, Fe, Ni, Cu) for H-2 generation by two-step water splitting using concentrated solar thermal energy. Energy 2007;32:656.

[21] Miller JE, Allendorf MD, Diver RB, Evans LR, Siegel NP, Stuecker JN. Metal oxide composites and structures for ultra-high temperature solar thermochemical cycles. Journal of Materials Science 2008;43:4714.

[22] Gokon N, Takahashi S, Yamamoto H, Kodama T. Thermochemical two-step water-splitting reactor with internally circulating fluidized bed for thermal reduction of ferrite particles. International Journal of Hydrogen Energy 2008;33:2189.

[23] Neises M, Roeb M, Schmuker M, Sattler C, Pitz-Paal R. Kinetic investigations of the hydrogen production step of a thermochemical cycle using mixed iron oxides coated on ceramic substrates. International Journal of Energy Research;34:651.

[24] Abanades S, Flamant G. Thermochemical hydrogen production from a two-step solar-driven water-splitting cycle based on cerium oxides. Solar Energy 2006;80:1611.

[25] Chueh WC, Haile SM. A thermochemical study of ceria: exploiting an old material for new modes of energy conversion and CO2 mitigation. Philosophical Transactions of the Royal Society a-Mathematical Physical and Engineering Sciences;368:3269.

CHAPTER 4 ATOMIC LAYER DEPOSITION OF IRON(III) OXIDE ON ZIRCONIA NANOPARTICLES IN A FLUIDIZED BED REACTOR USING FERROCENE AND OXYGEN

4.1 Abstract

Conformal films of amorphous iron(III) oxide and α-Fe_2O_3 have been coated on zirconia nanoparticles (26 nm) in a fluidized bed reactor by atomic layer deposition. Ferrocene and oxygen were alternately dosed into the reactor at temperatures between 367 ^oC and 534 ^oC. Self-limiting chemistry was observed via *in situ* mass spectrometry, and by means of induced coupled plasma – atomic emission spectroscopy analysis. Film conformality and uniformity were verified by high resolution transmission electron microscopy, and the growth rate was determined to be 0.15 Å per cycle. Energy dispersive spectroscopy, X-ray diffractometry, and X-ray photoelectron spectroscopy were utilized as a means to determine film composition at each deposition temperature. Over all of the deposition temperatures investigated, films were deposited as amorphous iron(III) oxide. However, after heat treatment at 850 ^oC in air and N_2 atmospheres, α-Fe_2O_3 was the predominant species.

4.2 Introduction

Iron(III) oxide thin films have received significant attention in recent years due to their potential for use in catalytic, optical, electrical and magnetic applications. Iron oxide based Fisher-Tropsch synthesis catalysts, along with cobalt oxide based catalysts, are used industrially to convert synthesis gas to liquids with low H_2/CO ratios and have low CH_4 selectivities [1, 2]. Fe_2O_3 is used extensively to catalyze the dehydrogenation of ethylbenzene for styrene synthesis due to the intermediate adsorption strength of Fe^{3+} for ethylbenzene and styrene [3-6]. Iron(III)

oxide has a high propensity to transmit visible light while absorbing light in the infrared range, and as such can be used as a solar filter on windows to reduce radiative heat transfer [7, 8]. The band gap of iron (III) oxide is 2.0 eV, which allows for the capability of absorbing 38% of the solar spectrum. Relative to TiO_2, which typically only absorbs the ultraviolet portion of the solar spectrum (~ 5%) it is well suited to help improve the efficiency of photoelectrochemical hydrogen production [9, 10]. Additionally, there has been recent extensive research involving iron oxide nanoparticle synthesis, as the nanosized features exhibit different properties than the bulk material and have been used for several important magnetic applications [11-13]. The properties of iron (III) oxide thin films are highly dependent on thickness, morphology and chemical composition, and therefore it is advantageous to have precise control of these properties.

Currently, there are several methods employed for iron oxide thin film deposition, including chemical vapor deposition (CVD), sputtering, arc-plasma spray deposition, and various wet chemistry methods such as sol-gel deposition [7, 13-17]. However, there are disadvantages to these methods that limit their ability to precisely control film thickness, morphology and chemical composition. For example, sol-gel methods have the capability to deposit films as thin as 100 nm, but it can be difficult to control its chemical state, and many times films are not uniform and conformal[16-18]. Sputtering is able to deposit thinner films than those of wet chemistry methods, however due to the continuous bombardment of highly energetic species onto the film, the equilibrium state of the deposited oxide is very difficult to control [15, 16]. Perhaps the most common technique for iron oxide thin film deposition is CVD. This process involves vapor phase precursors reacting within a deposition chamber on a substrate surface, and as a result there are no geometrical limitations [19]. However, film thickness is difficult to

control because this process is not self-limiting, resulting in films that are generally micron-sized or thicker [20]. Films are typically non-conformal and granular due to the fact that excess vapor phase reactants may nucleate and precipitate on the substrate surface. Additionally, film stoichiometry is difficult to control, as the amount of precursor delivered into the deposition chamber is dependent on its vapor pressure [21].

Atomic layer deposition (ALD) is a self-limiting technique that is capable of depositing highly conformal films one molecular layer at a time [22-25]. Deposition is based upon the principle of splitting a binary reaction (typical of CVD) into two half- reactions and alternating the exposure of gas phase precursors of each half- reaction to a surface, as shown below:

Binary Reaction: $x \cdot M(L)_n + y \cdot H_2O \rightarrow M_xO_y + n \cdot (HL)$

Half-Reaction 1: $[S]:(OH)_y^* + x(ML_n) \rightarrow [S]:O_yM_x(L)_{n-y}^* + y(HL)$

Half-Reaction 2: $[S]:O_yM_x(L)_{n-y}^* + yH_2O \rightarrow [S]:(M_xO_y):(OH)_y^* + (n-y)(HL)$,

where M represents the metal species, n is the number of ligands (L), x:y is the metal to oxide ratio, [S] represents a surface site, and * represents an active surface species [26]. Operating conditions are controlled in such a way that the precursors of one half-reaction react only with the precursors of the other. This ensures atomic level control, since there is at most one sub-monolayer of added species per half-reaction [27].

Iron oxide ALD has been demonstrated on a wide array of crystalline surfaces using $Fe(thd)_3$ and $Fe(acac)_3$ as precursors [28, 29]. Recently, $Fe(C_5H_5)_2$ (ferrocene) and oxygen have been used to deposit iron oxide films onto Si(100) and anodic aluminum [30]. The growth rates on Si(100) and anodic aluminum were 0.14 nm and 0.06 nm per cycle, respectively. At deposition temperatures below 500 ^oC a mixture of hematite and an unidentified phase were present. In this work, ALD of iron oxide on zirconia nanoparticles using ferrocene and oxygen is

investigated. Films are deposited in a fluidized bed reactor (FBR) at temperatures ranging from 367 ^{o}C and 534 ^{o}C. They are shown to be highly conformal and uniform and can be controlled with angstrom level precision. As-deposited, the films are amorphous iron(III) oxide, but with heat treatment can be crystallized into α-Fe_2O_3.

4.3 Experimental Details

4.3.1 *Material Preparation*

A schematic representation of the FBR is shown in Figure 4-1. The reactor is 3.5 cm in diameter and includes a porous stainless steel (SS) distributor plate and filter at the inlet and outlet, respectively. These are used to prevent particles from leaving the reactor, while allowing gas to pass through freely. The details of this reactor configuration have been described elsewhere [26]. Product gases were measured using a Stanford Research Systems QMS series mass spectrometer.

Fluidization was accomplished at reduced pressure in conjunction with a mechanical vibration platform, as shown in Figure 4-1. Mechanical vibration has been shown to aid in overcoming interparticle forces present between nanoparticles, resulting in smaller aggregate sizes and a decreased minimum fluidization velocity [30]. The pressure drop across the bed was measured as a function of gas flow rate in order to maintain fluidization throughout the ALD cycle.

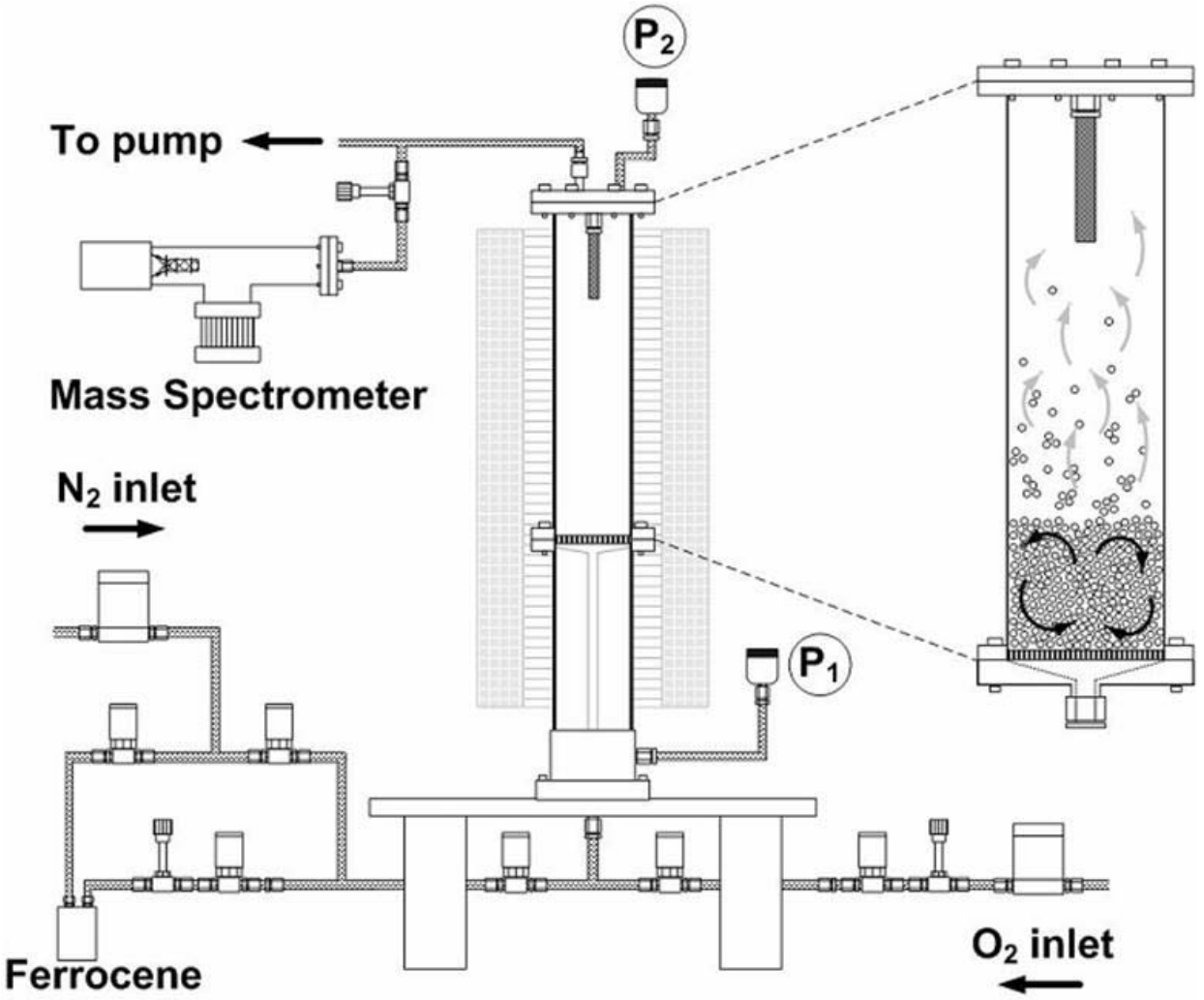

Figure 4-1: Schematic diagram of the ALD fluidized bed reactor.

The ALD cycle consisted of dosing ferrocene (99% purity acquired from Alfa Aesar®) and high purity oxygen (99.9%) in alternate doses into the reactor at temperatures ranging from 367 ^{o}C and 534 ^{o}C. Ferrocene was delivered into the reactor using a 200cc bubbler (Precision Fabricators Ltd.) heated to 60 ^{o}C and nitrogen was employed as a carrier gas. The reactor was then purged with nitrogen in order to remove any excess ferrocene and by-products. Once purged, oxygen was dosed, followed by another nitrogen purge. All lines were heated to 65 ^{o}C in order to prevent any ferrocene vapor from depositing. A three factor central composite

experimental design, shown in Figure 4-2, was carried out with temperature, ferrocene dosing time, and oxygen dosing time all varying accordingly.

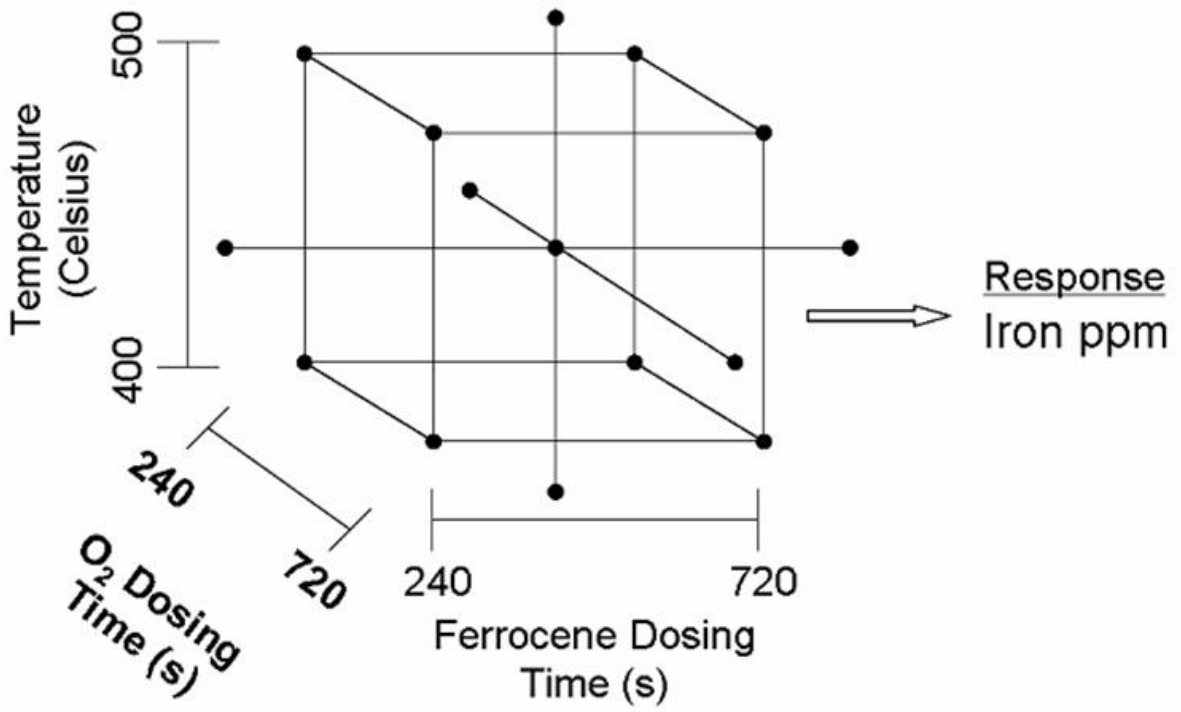

Figure 4-2: Experimental design used to study factors affecting iron oxide growth rate.

4.3.2 *Material Characterization*

Visual inspection of the films was carried out using a 200 kV JEOL 2010F Schottky field emission high resolution transmission electron microscope (HRTEM). Film composition was determined via energy dispersive spectroscopy (EDS), X-ray diffraction (XRD, Scintag PAD5 Powder Diffractometer, CuKα radiation, λ = 1.5406Å), and X-ray photoelectron spectroscopy (XPS, PHI 5600, Physical Electronics Inc., Al Kα). EDS results were obtained from a spectrometer that was coupled with the Schottky field emission TEM. XRD analysis was performed using a scan rate of 2 degrees/minute and step size of 0.2 degrees. A pass energy of

58.7 eV and step size of 0.2 eV was used during XPS analysis. The resulting scans were internally calibrated by shifting the C 1s peak to 285.0 eV. Induced coupled plasma – atomic emission spectroscopy (ICP-AES) was used as means to quantify the mass percent of iron in the film.

4.4 Results and Discussion

4.4.1 *Fluidization*

The main advantage of an FBR compared to other reactor configurations is the benefit of constant particle recirculation, resulting in excellent fluid-solid contact and increased heat and mass transfer coefficients [22, 31]. In an ALD reactor, this would result in the active surface sites reacting quickly with the reactant due to continuous exposure to the gas phase precursors. Therefore, it is imperative that the particles remain in a fluidized state during the entire ALD process. In order to ensure this, a fluidization curve was generated to verify that the particles could be fluidized, and to determine the appropriate superficial gas velocity used throughout the reaction. Incipient fluidization occurs when the pressure drop as a function of superficial fluid velocity remains constant [32]. The fluidization curve shown in Figure 4-3 verifies that the particles become fluidized at a superficial gas velocity of 0.015 cm/s.

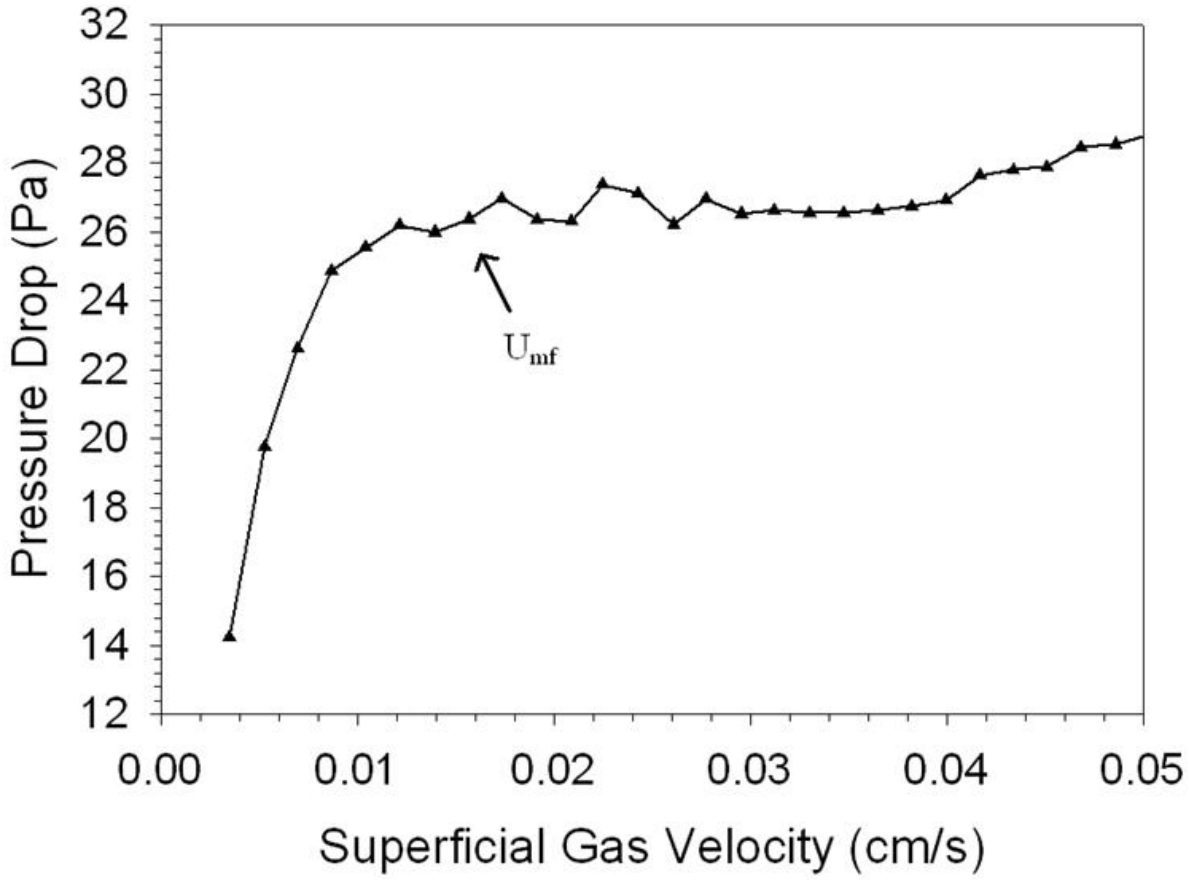

Figure 4-3: Pressure drop across the bed as a function of superficial gas velocity. Incipient fluidization occurs at 0.015 cm/s.

4.4.2 *In Situ Mass Spectroscopy*

Residual gas analysis (RGA), which has been shown to be an effective method to observe the termination of ALD half reactions on various substrates, was used to observe the ALD reaction *in situ* [23, 26]. The RGA plot of one complete cycle is shown in Figure 4-4 at a temperature of 450 ^{o}C. Each half-reaction was clearly observed and indicated that the chemistry was self-limiting. When ferrocene was dosed into the reactor ('Ferrocene Dose'), there was an increase in the partial pressure of CO_2. Soon after, the partial pressure of ferrocene began to increase, which signified precursor breakthrough, and eventually reached a maximum. The CO_2

subsequently decreased, which indicated that the surface was saturated and the reaction had reached completion. After the reactor was purged, oxygen was dosed ('O_2 Dose') and the partial pressure of both CO_2 and oxygen increased. As oxygen continued to be dosed, the reaction product began to decrease, which signifying that the reaction was approaching completion. In the first half reaction, CO_2 is attributed to chemisorbed oxygen reacting with ferrocene ligands adsorbed on the surface. As O_2 is dosed in the second half reaction, it reacts with the remaining chemisorbed ferrocene ligands to evolve CO_2, and oxidizes the iron. This mechanism has been observed during ALD of metals and metal oxides using metallocene precursors with oxygen, such as for Ru and RuO_2 using $Ru(C_5H_5)_2$ [33, 34].

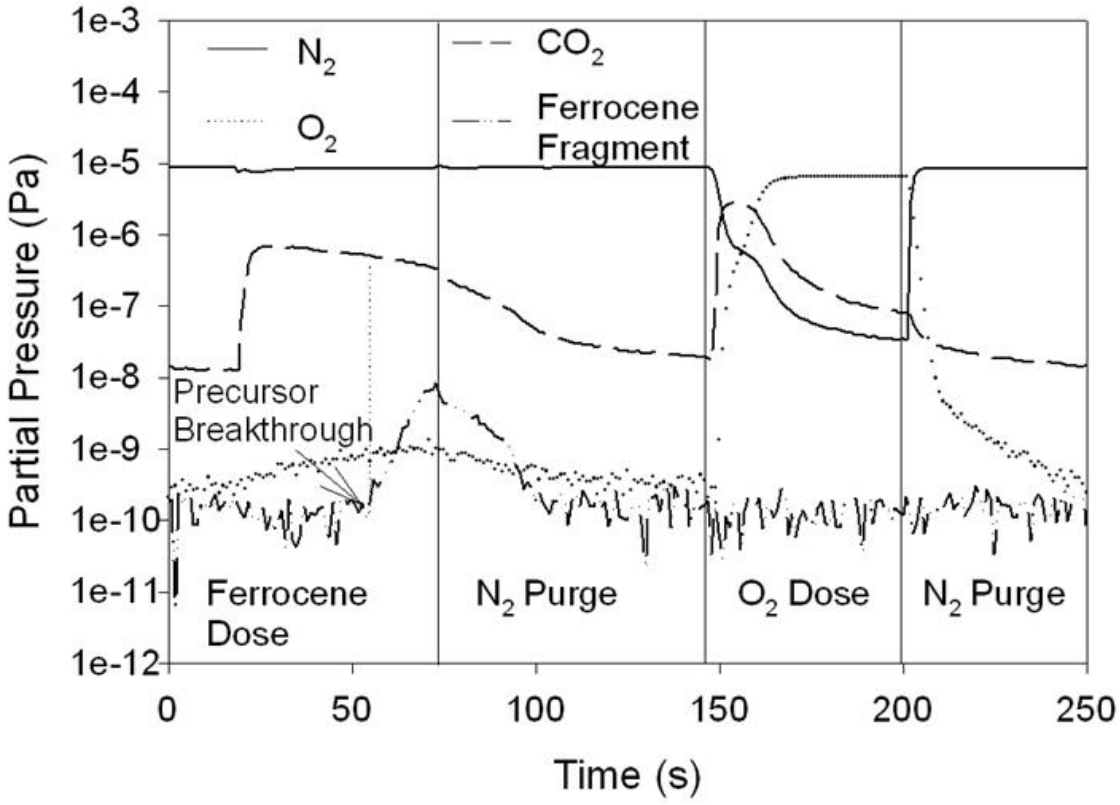

Figure 4-4: In situ mass spectrometry results during one complete ALD cycle.

4.4.3 *Film Characterization*

HRTEM images after 200 coating cycles at 450 ^{o}C are shown in Figures 4-5a and 4-5b. These images clearly indicate that the films are conformal and uniform around the particles. From visual inspection, the films are about 3 nm thick, corresponding to a growth rate of 0.15 Å per cycle, which is comparable to other metal oxide ALD growth rates [29, 35, 36]. Additionally, there is a clear differentiation between films around individual particles. This is observed in Figure 4-5b, where films around two individual particles can be observed, indicating that particles have not been glued together. EDS results, shown in Figure 4-5c, confirm the presence of iron. C and Cu peaks result from the grid that particles were analyzed on and are not representative of the particle surfaces. The only remaining peaks were Zr, Fe and O, which clearly indicated that iron had been deposited on the ZrO_2 particle substrates.

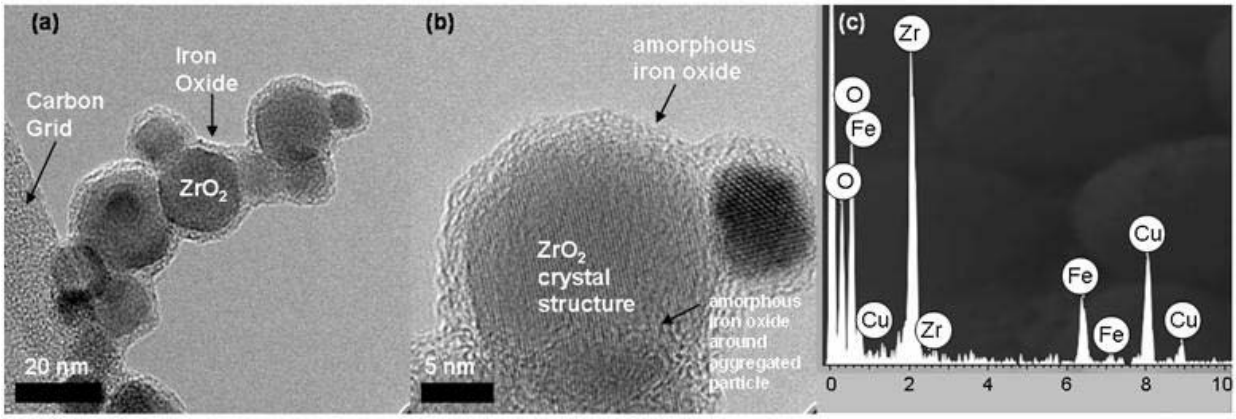

Figure 4-5: a) and b) HRTEM micrographs after 200 coating cycles. c) EDS spectrum confirms the presence of iron.

Two properties intrinsic to ALD, self-limiting chemistry and linear growth rate, are confirmed in Figures 4-6 and 4-7 by measuring iron mass percent as a function of ferrocene dosing time and number of ALD cycles at 450 ^{o}C, respectively. As ferrocene dosing time was increased from 67s to 480s, the iron mass percent in the film increased from about 1% to 11%.

However, as the dosing time was increased to 883 s, the amount of iron in the film did not significantly increase, confirming that ferrocene does not continue to react once all of the surface sites are saturated.

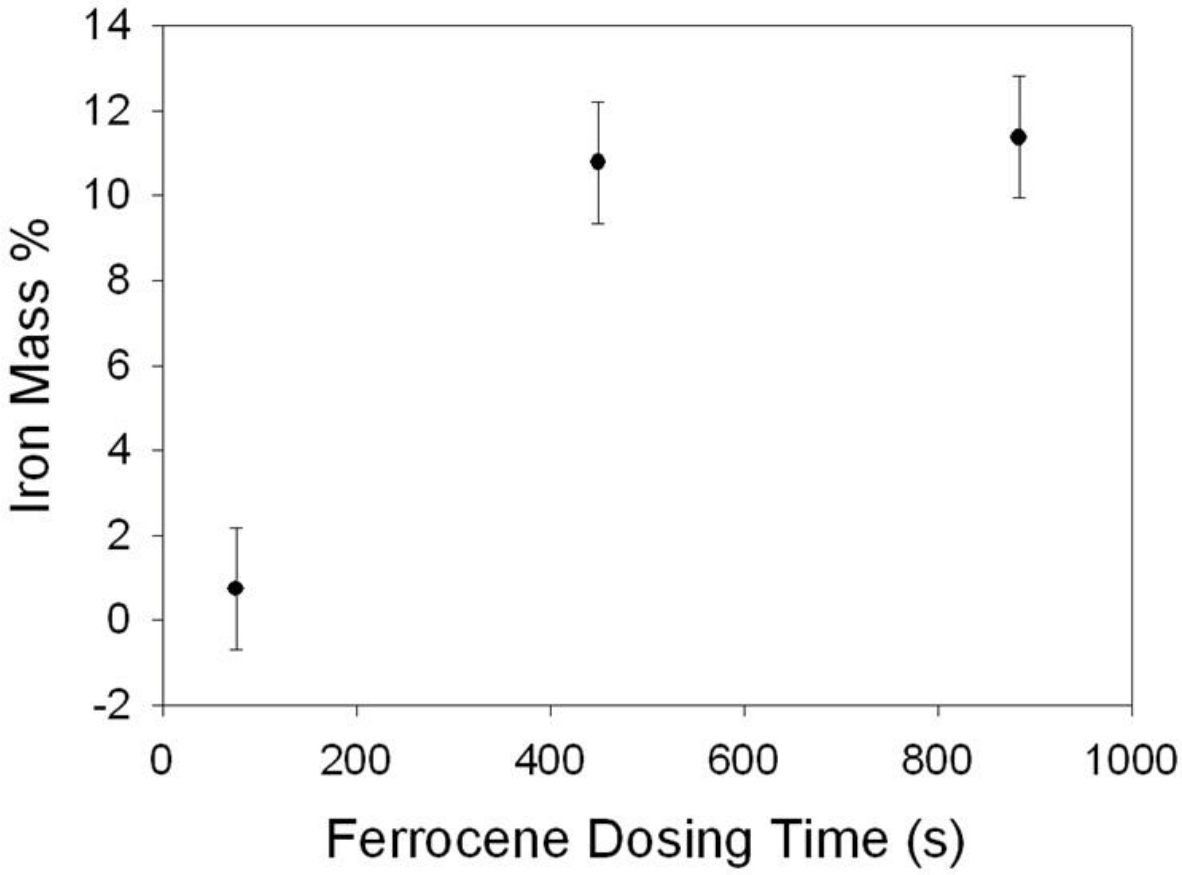

Figure 4-6: ICP-AES iron mass percent in the film as a function of ferrocene dosing time. Self-limiting chemistry is confirmed.

Nearly linear growth is observed in Figure 4-7 as the number of ALD cycles is increased from 50 to 200. The discrepancy between iron mass percent in Figure 4-6 and that of Figure 4-7 is due to the fact that zirconia nanoparticles were not used to study the growth of the films as a function of number of ALD cycles, but rather zirconia particles that had a mean diameter of 110 μm.

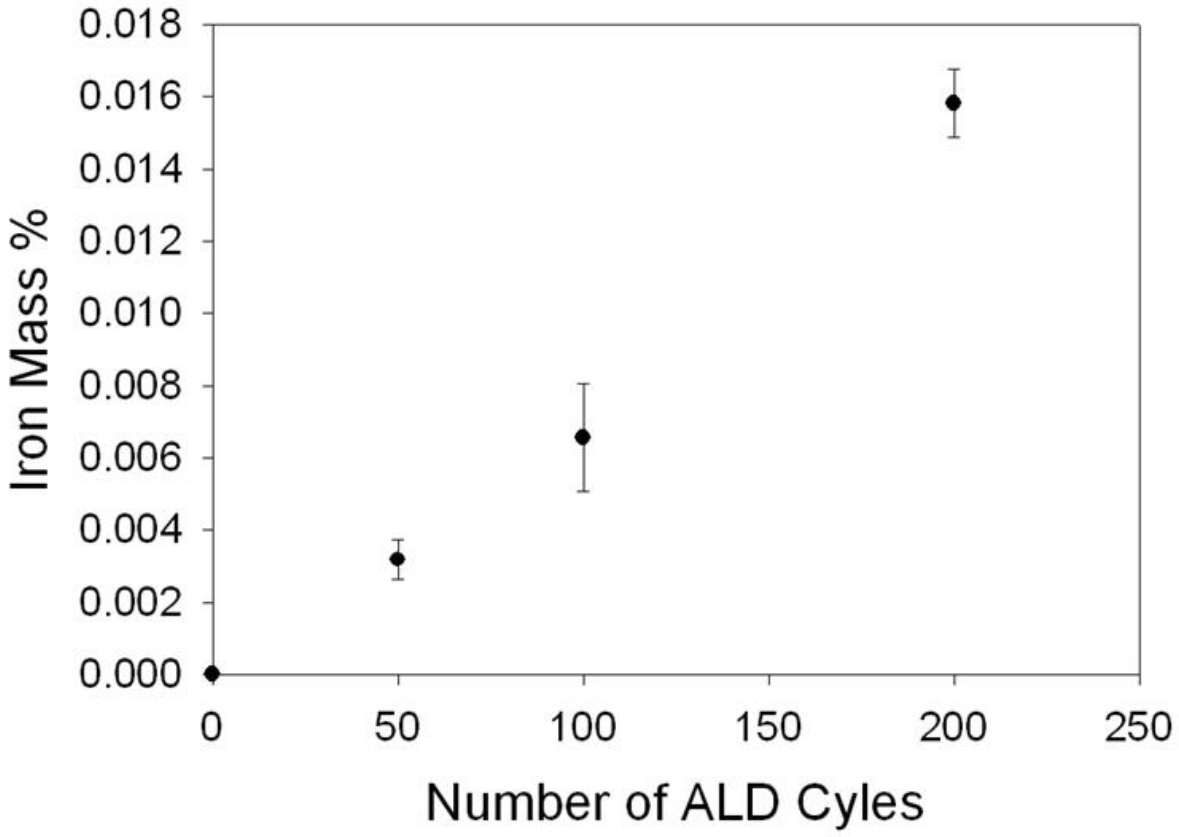

Figure 4-7: ICP-AES iron mass percent in the film as a function of the number of ALD cycles. Nearly linear growth is observed.

Contour plots shown in Figure 4-8 summarize how the mass percent of iron in the film varies with ferrocene dosing time, oxygen dosing time, and temperature. Each graphic depicts one factor (e.g. dosing time) as a function of another while holding the third factor constant at its center point (refer to Figure 4-2 for a schematic of the experimental design). Because the majority of change in iron mass percent was observed at short dosing times, each of these axes is shown only up to their center point. As seen in Figures 4-8a and 4-8b, the amount of iron in the film began to decrease as the temperature was raised beyond 500 ^{o}C. This is likely due to the thermal desporption of ferrocene, which has been shown to desorb molecularly intact [37].

Additionally, a greater dependence was observed for ferrocene dosing time than that of oxygen on the final iron mass percent in the films. As seen in Figure 4-8a, as ferrocene dosing time decreased below 200 s, the amount of iron in the film decreased rather dramatically, whereas the change was not nearly as significant for oxygen dosing time (Figure 4-8b). This was further corroborated in Figure 4-8c, where large changes in iron content were attainable even at very low oxygen dosing times. This can be explained by the fact that ferrocene was dosed into the reactor with the aid of a carrier gas (N_2) because of its low vapor pressure. Therefore, the mass of ferrocene available to react with the fluid bed per unit time was much smaller than that for oxygen.

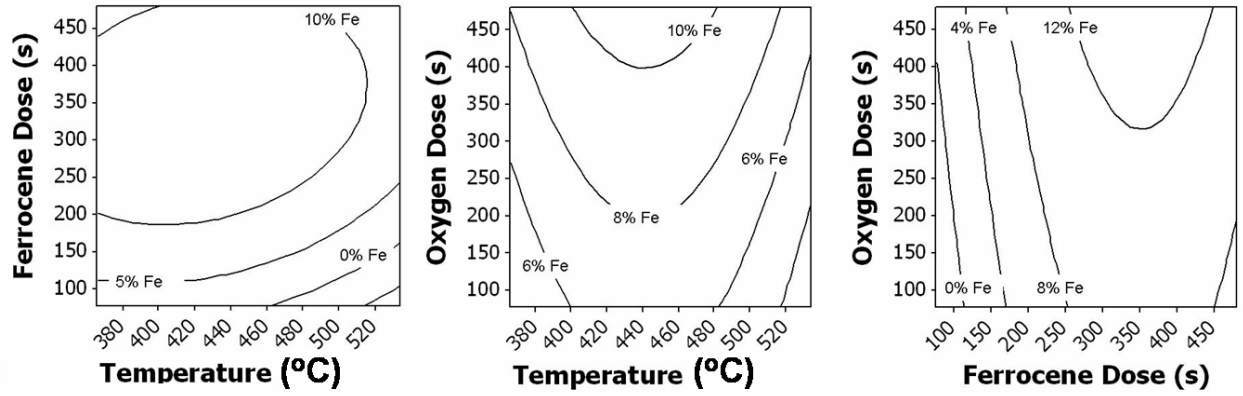

Figure 4-8: Countour plots of a) ferrocene dosing time vs. temperature at a constant O_2 dosing time of 480 s, b) O_2 dosing time vs. temperature at a constant ferrocene dosing time of 480 s, and c) O_2 dosing time vs. ferrocene dosing time as a constant temperature of 450 ^oC.

EDS results confirm the presence of iron but do not give any information regarding the oxidation state or crystalline nature of the films. Therefore, powder XRD was utilized in an effort to further understand the crystallininity of the film. XRD results of uncoated and coated particles after 200 cycles are shown in Figure 4-9. For both samples, only peaks representative of the ZrO_2 nanoparticles were evident, which suggests that the films were likely amorphous as

deposited. After 200 cycles it was apparent that the peaks were less sharp than uncoated particles, but the angle and relative intensity of the peaks remained unchanged. This can be observed visually in the high resolution TEM image in Figure 4-4b, where the crystalline and ordered nature can be clearly observed in the ZrO_2 particle, but not in the deposited film.

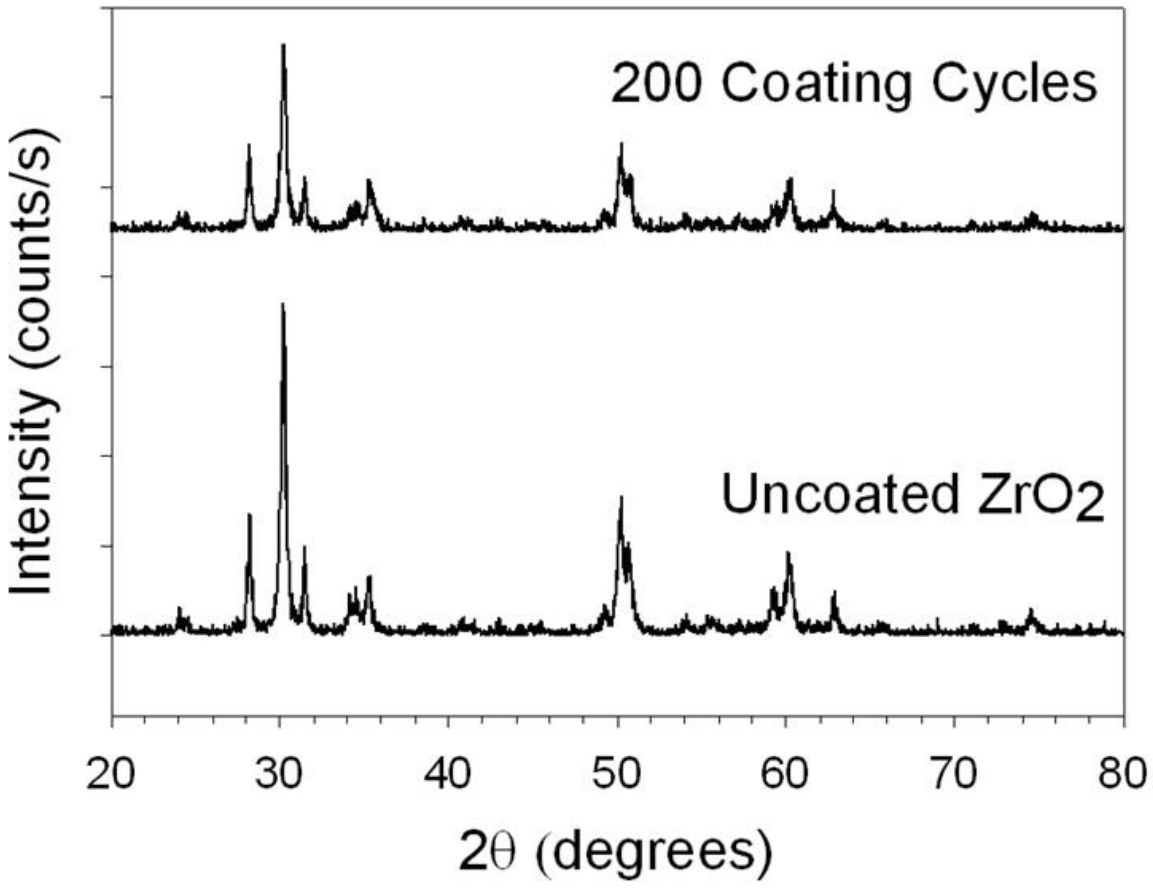

Figure 4-9: XRD spectrum of uncoated and coated ZrO_2 nanoparticles after 200 ALD cycles.

Because the coated film was amorphous, samples were thermally annealed in both air and an inert environment at 850 ^oC for four hours in an effort to crystallize the film and to help determine whether iron metal or amorphous iron oxide was deposited. At 850 ^oC in air, α-Fe_2O_3 is the thermodynamically favored state of iron oxide. In an inert environment, however, α -Fe_2O_3

would only be expected if the deposited film was amorphous iron(III) oxide, as it was not exposed to an oxidizing atmosphere during heat treatment. As seen in Figure 4-10, there are peaks representative of α-Fe_2O_3 for the sample heat-treated in air, which were not present in the sample measured in the as-deposited state. The crystal structure of the sample that was heat-treated in an inert environment was nearly identical to that of the sample thermally annealed in air, which indicated that amorphous iron(III) oxide was deposited on the particle surfaces by ALD using ferrocene and O_2 at a temperature of 450^{o}C.

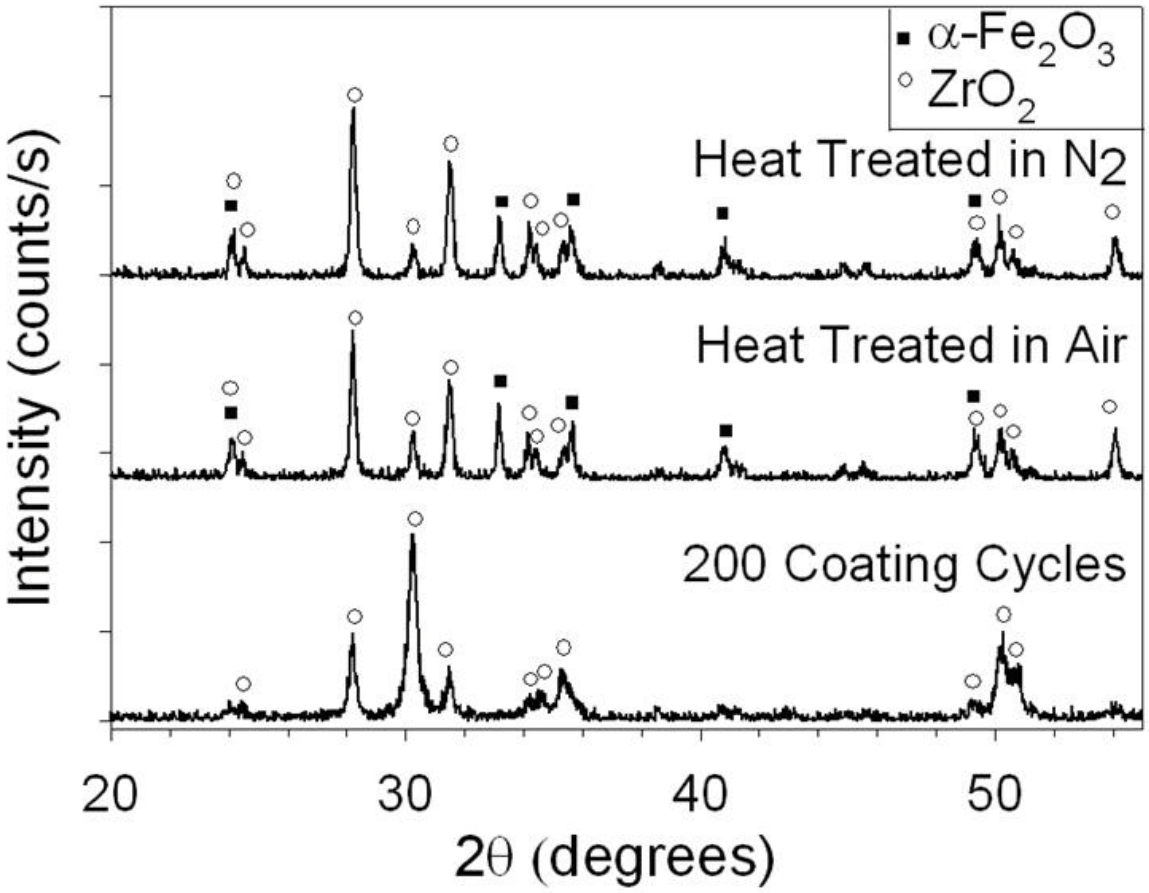

Figure 4-10: XRD spectrum of as-deposited and heat-treated samples after 200 ALD coating cycles.

In order to verify that the sample heat treated in an N_2 atmosphere was not oxidized from iron(II,III) oxide to iron(III) oxide due to oxygen or water adsorbed on its surface, XPS measurements were conducted for both the amorphous and heat-treated samples. These results confirmed that iron(III) oxide was deposited, as shown in Figures 4-11 and 4-12.

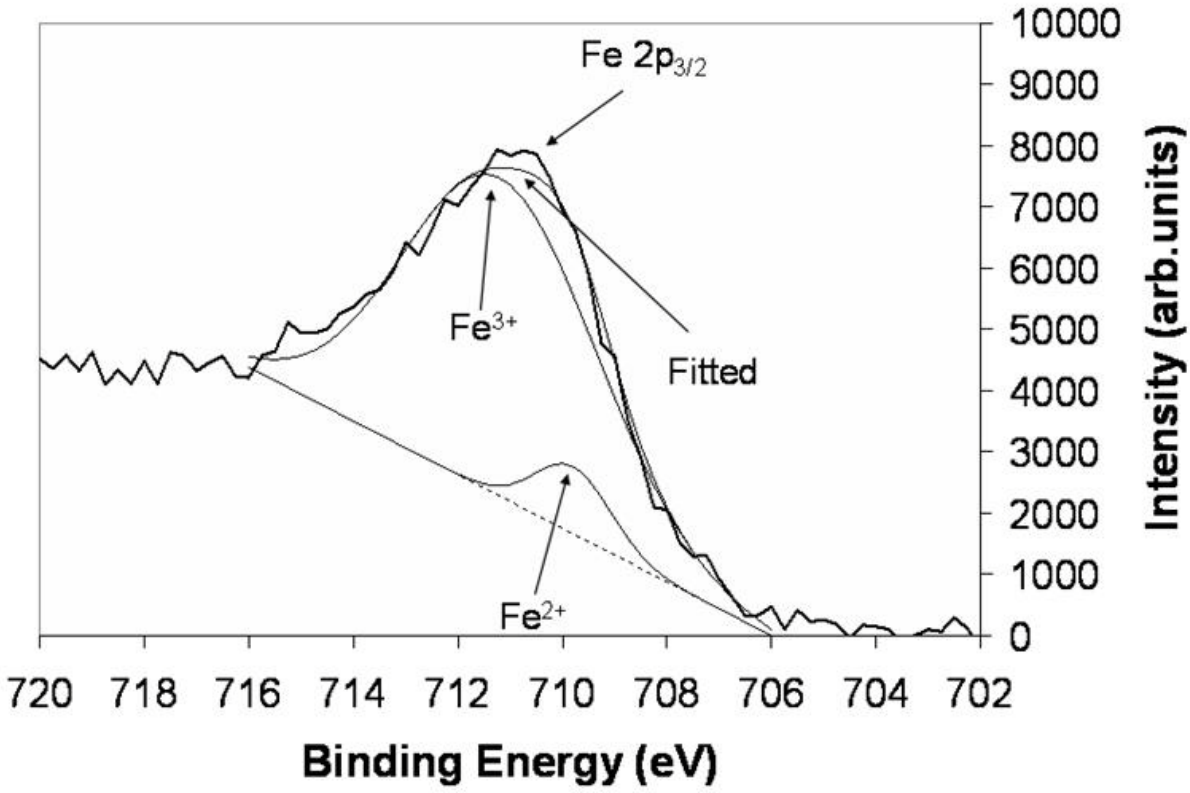

Figure 4-11: XPS spectrum of Fe 2p of amorphous iron oxide film.

The binding energy associated with electrons residing in the Fe $2p_{3/2}$ orbitals in both the amorphous and heat-treated samples was approximately 711.0 eV, which is in good agreement with previously reported literature values [38, 39]. Because the difference in binding energy between these orbitals for the Fe^{2+} and Fe^{3+} oxidation states is very small, it can be difficult to determine the relative amount of Fe^{2+} and Fe^{3+} in the sample [40]. Therefore, Gaussian curves

centered around Fe^{2+} (709.2eV – 709.8 eV) and Fe^{3+} (710.6eV - 711.2eV) were added and fit to the data using a sum of least squares approximation. The binding energy of metallic iron (707 eV) was not considered as it falls considerably away from the center of the Fe $2p_{3/2}$ peak. As seen in Figures 4-11 and 4-12, a majority of the contribution to the best fit line was due to the Fe^{3+} peak, while that of the Fe^{2+} was much smaller. Therefore it can be concluded that most of the iron was in the Fe^{3+} oxidation state, similar to the XRD results, but the presence of the Fe^{2+} state, albeit to a significantly lower degree, cannot be excluded.

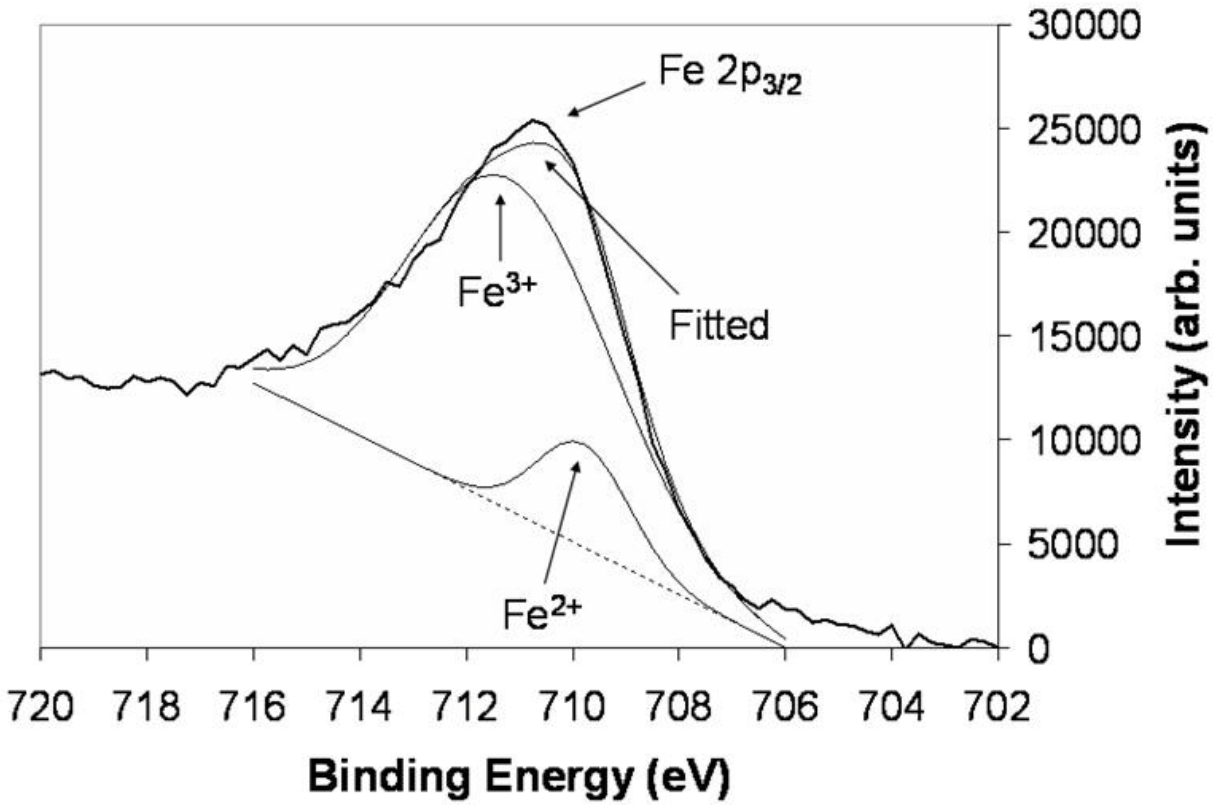

Figure 4-12: XPS spectrum of Fe 2p of iron oxide film heat treated at 850 ^{o}C.

4.5 Conclusions

ALD chemistry that combined ferrocene and oxygen as precursors was used to deposit ultrathin amorphous iron oxide layers on zirconia nanoparticles in a fluidized bed reactor. Self-limiting chemistry, characteristic of ALD, was observed via in situ mass spectrometry and ICP-AES studies. HRTEM images were used to show the conformal and uniform nature of the films on individual nanoparticles. XRD and XPS analyses established that essentially all of the iron oxide that was deposited was amorphous and in the +3 oxidation state. After heat treatment at 850 ^{o}C, it was shown that the films could be crystallized to form α-Fe_2O_3, even on the high radius of curvature substrates used here.

4.6 References

[1] Li SZ, Krishnamoorthy S, Li AW, Meitzner GD, Iglesia E. Promoted iron-based catalysts for the Fischer-Tropsch synthesis: Design, synthesis, site densities, and catalytic properties. Journal of Catalysis 2002;206:202.

[2] Li TZ, Yang Y, Zhang CH, An X, Wan HJ, Tao ZC, Xiang HW, Li YW, Yi F, Xu BF. Effect of manganese on an iron-based Fischer-Tropsch synthesis catalyst prepared from ferrous sulfate. Fuel 2007;86:921.

[3] Huang WX, Ranke W, Schlogl R. Molecular-level understanding of the catalytic cycle of dehydrogenation of ethylbenzene to styrene over iron oxide-based catalyst. Journal of Physical Chemistry B 2005;109:9202.

[4] Schule A, Nieken U, Shekhah O, Ranke W, Schlogl R, Kolios G. Styrene synthesis over iron oxide catalysts: from single crystal model system to real catalysts. Physical Chemistry Chemical Physics 2007;9:3619.

[5] Weiss W, Ranke W. Surface chemistry and catalysis on well-defined epitaxial iron-oxide layers. Progress in Surface Science 2002;70:1.

[6] Weiss W, Zscherpel D, Schlogl R. On the nature of the active site for the ethylbenzene dehydrogenation over iron oxide catalysts. Catalysis Letters 1998;52:215.

[7] Chavez-Galan J, Almanza R. Solar filters based on iron oxides used as efficient windows for energy savings. Solar Energy 2007;81:13.

[8] Dghoughi L, Elidrissi B, Bernede C, Addou A, Lamrani MA, Regragui A, Erguig H. Physico-chemical, optical and electrochemical properties of iron oxide thin films prepared by spray pyrolysis. Applied Surface Science 2006;253:1823.

[9] Ingler JWB, Khan SUM. Photoresponse of spray pyrolytically synthesized copper-doped p-Fe2O3 thin film electrodes in water splitting. International Journal of Hydrogen Energy 2005;30:821.

[10] Satsangi VR, Kumari S, Singh AP, Shrivastav R, Dass S. Nanostructured hematite for photoelectrochemical generation of hydrogen. International Journal of Hydrogen Energy 2008;33:312.

[11] Huang Y, Lin J, Ding XX, Tang C, Gu CZ, Qi SR. Coating carbon nanotubes with iron oxide using methanol-thermal reaction. Materials Letters 2007;61:697.

[12] Lee YJ, Jun KW, Park JY, Potdar HS, Chikate RC. A simple chemical route for the synthesis of gamma-Fe2O3 nano-particles dispersed in organic solvents via an iron-hydroxy oleate precursor. Journal of Industrial and Engineering Chemistry 2008;14:38.

[13] Park CD, Magana D, Stiegman AE. High-quality Fe and gamma-Fe2O3 magnetic thin films from an epoxide-catalyzed sol-gel process. Chemistry of Materials 2007;19:677.

[14] Glasscock JA, Barnes PRF, Plumb IC, Bendavid A, Martin PJ. Structural, optical and electrical properties of undoped polycrystalline hematite thin films produced using filtered arc deposition. Thin Solid Films 2008;516:1716.

[15] Mauvernay B, Presmanes L, Capdeville S, de Resende VG, De Grave E, Bonningue C, Tailhades P. Elaboration and characterization of Fe1-xO thin films sputter deposited from magnetite target. Thin Solid Films 2007;515:6532.

[16] Meille V. Review on methods to deposit catalysts on structured surfaces. Applied Catalysis a-General 2006;315:1.

[17] Park S, Lim S, Choi H. Chemical vapor deposition of iron and iron oxide thin films from Fe(II) dihydride complexes. Chemistry of Materials 2006;18:5150.

[18] Kester E, Gillot B. Cation distribution, thermodynamic and kinetics considerations in nanoscaled copper ferrite spinels. New experimental approach by XPS and new results both in the bulk and on the grain boundary. Journal of Physics and Chemistry of Solids 1998;59:1259.

[19] Fahlman BD. Recent advances in chemical vapor deposition. Current Organic Chemistry 2006;10:1021.

[20] Hakim LF, George SM, Weimer AW. Conformal nanocoating of zirconia nanoparticles by atomic layer deposition in a fluidized bed reactor. Nanotechnology 2005;16:S375.

[21] Barber ZH. The control of thin film deposition and recent developments in oxide film growth. Journal of Materials Chemistry 2006;16:334.

[22] Hakim LF, Blackson J, George SM, Weimer AW. Nanocoating individual silica nanoparticles by atomic layer deposition in a fluidized bed reactor. Chemical Vapor Deposition 2005;11:420.

[23] Leskela M, Ritala M. Atomic layer deposition (ALD): from precursors to thin film structures. Thin Solid Films 2002;409:138.

[24] George SM, Ott AW, Klaus JW. Surface chemistry for atomic layer growth. Journal of Physical Chemistry 1996;100:13121.

[25] Niinisto L, Paivasaari J, Niinisto J, Putkonen M, Nieminen M. Advanced electronic and optoelectronic materials by Atomic Layer Deposition: An overview with special emphasis on recent progress in processing of high-k dielectrics and other oxide materials. Physica Status Solidi a-Applied Research 2004;201:1443.

[26] King DM, Spencer JA, Liang X, Hakim LF, Weimer AW. Atomic layer deposition on particles using a fluidized bed reactor with in situ mass spectrometry. Surface & Coatings Technology 2007;201:9163.

[27] Han JH, Gao GL, Widjaja Y, Garfunkel E, Musgrave CB. A quantum chemical study of ZrO2 atomic layer deposition growth reactions on the SiO2 surface. Surface Science 2004;550:199.

[28] de Ridder M, van de Ven PC, van Welzenis RG, Brongersma HH, Helfensteyn S, Creemers C, Van Der Voort P, Baltes M, Mathieu M, Vansant EF. Growth of iron oxide on yttria-stabilized zirconia by atomic layer deposition. Journal of Physical Chemistry B 2002;106:13146.

[29] Lie M, Fjellvag H, Kjekshus A. Growth of Fe2O3 thin films by atomic layer deposition. Thin Solid Films 2005;488:74.

[30] Hakim LF, Portman JL, Casper MD, Weimer AW. Aggregation behavior of nanoparticles in fluidized beds. Powder Technology 2005;160:149.

[31] Wank JR, George SM, Weimer AW. Coating fine nickel particles with Al2O3 utilizing an atomic layer deposition-fluidized bed reactor (ALD-FBR). Journal of the American Ceramic Society 2004;87:762.

[32] Rhodes M. Introduction to Particle Technology: John Wiley and Sons, 2006.

[33] Aaltonen T. Atomic Layer Deposition of Noble Metal Thin Films. Department of Chemistry. Helsinki: University of Helsinki, 2005. p.71.

[34] Zhou M, Chen T, Tan JJ, Ru GP, Jiang YL, Ran L, Qu XP. Effect of pretreatment of TaN substrates on atomic layer deposition growth of Ru thin films. Chinese Physics Letters 2007;24:1400.

[35] Li ZW, Rahtu A, Gordon RG. Atomic layer deposition of ultrathin copper metal films from a liquid copper(I) amidinate precursor. Journal of the Electrochemical Society 2006;153:C787.

[36] Lim BS, Rahtu A, Gordon RG. Atomic layer deposition of transition metals. Nature Materials 2003;2:749.

[37] Welipitiya D, Dowben PA, Zhang JD, Pai WW, Wendelken JF. The adsorption and desorption of ferrocene on Ag(100). Surface Science 1996;367:20.

[38] Wandelt K. Photoemission studies of adsorbed oxygen and oxide layers. Surface Science Reports 1982;2:1.

[39] Yamashita T, Hayes P. Analysis of XPS spectra of Fe2+ and Fe3+ ions in oxide materials. Applied Surface Science 2008;254:2441.

[40] Yamashita T, Hayes P. Effect of curve fitting parameters on quantitative analysis of Fe0.94O and Fe2O3 using XPS. Journal of Electron Spectroscopy and Related Phenomena 2006;152:6.

CHAPTER 5 HYDROGEN PRODUCTION VIA CHEMICAL LOOPING REDOX CYCLES USING ALD SYNTHESIZED IRON OXIDE AND COBALT FERRITES

5.1 Abstract

Iron oxide (γ-Fe_2O_3) and cobalt ferrite ($Co_xFe_{3-x}O_4$) thin films have been synthesized via atomic layer deposition on high surface area (50 m^2/g) m-ZrO_2 supports. The oxide films were grown by sequentially depositing iron oxide and cobalt oxide, and adjusting the number of iron oxide cycles relative to cobalt oxide to achieve desired stoichiometry. The as-deposited films are shown to be crystalline by high resolution transmission electron microscopy and x-ray diffraction, with a thickness of approximately 2.5 nm. Raman spectroscopy was used to confirm the predominance of the spinel phase in the case of cobalt ferrite. Samples were chemically reduced in a flow reactor equipped with *in situ* x-ray diffraction. They were also subjected to chemical reduction and oxidation in a stagnation flow reactor to test activity for use in chemical looping cycles to produce H_2 via water splitting. γ-Fe_2O_3 films chemically reduced in mixtures of H_2, CO, and CO_2 at 600 °C formed Fe_3O_4 and FeO phases, and exhibited a trend-wise decrease in H_2 production rates upon cycling. $Co_{0.85}Fe_{2.15}O_4$ films were successfully cycled without deactivation and produced four times more H_2 than γ-Fe_2O_3, principally due to the formation of a CoFe alloy upon reduction. For comparison, a mechanically milled mixture of α-Fe_2O_3 and ZrO_2 powders with similar iron loading to the thin films did not maintain high activity to water splitting due to sintering and grain growth.

5.2 Introduction

Iron oxide and cobalt ferrites are receiving significant interest for their applications as catalysts and as intermediates in thermal redox cycles and chemical looping combustion processes. These materials have been shown to be effective catalysts for the decomposition of NO_x[1, 2], various organic contaminants[3, 4], decomposition of biomass tars[5], and for the production of H_2 via the water gas-shift reaction[6, 7]. They have also been used as a catalyst support to take advantage of their magnetic properties, which facilitates downstream separation unit operations, in large scale environmental catalysis applications[8]. Recently, iron oxide and mixed metal ferrites have been used as intermediates in chemical looping processes[9, 10] and thermal redox cycles for the renewable production of H_2 in concentrated solar power applications[11-13].

A high specific surface area is of particular importance for many catalytic applications and redox cycles because surface area has a direct affect on catalytic efficiencies[3] and oxidation kinetics of redox cycles. For example, Bleeker *et.al.* have used iron oxide particles in a fluidized bed, two-step redox cycle. In this work, pyrolysis oil was used to reduce the iron oxide and steam subsequently exposed to the reduced iron produced H_2[14, 15]. Grain growth of the iron oxide particles was observed with increased cycling, leading to a decrease in surface area and ultimately to decreased conversions. This behavior has also been observed by Bohn *et.al.* when reducing iron oxide particles all the way to metallic iron in a packed bed reactor[10]. However, deactivation was abated when the iron oxide was only reduced to the wustite phase (FeO).

High specific surface area is also essential in thermal gas splitting cycles operating at high temperature (1400-1600 ^oC) where the iron cation in a metal oxide ($M_xFe_{3-x}O_4$) is thermally reduced to $Fe^{2+}$and then oxidized by H_2O or CO_2 back to Fe^{3+} resulting in H_2 or CO formation.

Steinfeld *et.al.* observed a direct dependence on FeO surface area on the CO_2 oxidation rate. As larger surface to volume particles were used, the resultant initial reaction rates were more rapid[16]. Weidenkaff *at. al.* also observed a FeO particle size dependence on H_2O splitting, and attributed this to diffusion limitations through the bulk of the iron oxide [17]. Analogous to lower temperature chemical looping cycles, sintering and grain growth is also a problem for these high temperature gas splitting applications.

There are a variety of methods used to synthesis metal oxides of the form $M_xFe_{3-x}O_4$, including solution combustion synthesis[1], aerial oxidation of aqueous suspensions[13], sol-gel process[3], laser molecular beam epitaxy[18], sputtering[19], chemical vapor deposition[20], and atomic layer deposition (ALD)[21]. Deposition on porous supports, such as SiO_2, Al_2O_3, ZrO_2, and yttria stabilized zirconia (YSZ) has proven to be successful at limiting the amount of sintering and grain growth thereby maintaining active surface area and improving cycle stability[11, 12, 22, 23]. In addition, inorganic supports provide a platform in which specific surface area can be precisely controlled.

ALD is an especially attractive synthesis method for producing conformal thin films on high surface area, high porosity supports because nano-scale films of various materials can be deposited independent of line of sight. This cannot be done using physical vapor deposition or pulsed laser techniques. Due to the self-limiting nature of the deposition chemistry, precursors of one half-reaction react only on the surface with intermediate functional groups generated by the other precursor. This ensures atomic level control, since at most one sub-monolayer is deposited per each half-reaction. Cobalt oxide thin films can be grown on a wide array of surfaces using precursors such as bis(N,N -diisopropylacetamidinato)cobalt(II)[24], CoI_2[25], and $Co(thd)_2$[26, 27]. Additionally, iron oxide films have been deposited using bis(N,N -

diisopropylacetamidinato)iron(II)[24], $Fe(acac)_3$[28], $Fe(thd)_2$[29], $Fe(thd)_3$[30], iron(III) tert-butoxide[31], and ferrocene[32, 33]. Various stoichiometries of $Co_xFe_{3-x}O_4$ can also be deposited by combining selective organometallic precursors in alternating doses of correct proportions[21].

In this report, we describe the synthesis of nano-scale films of Fe_2O_3 and $Co_xFe_{3-x}O_4$ on high surface area m-ZrO_2 supports (50 m^2/g) using ferrocene and cobaltocene as the iron and cobalt sources, respectively, and O_2 as the oxidant. These materials can be used to study iron oxide and cobalt ferrite gas splitting kinetics in either a chemical combustion looping process or high temperature thermal redox. To evaluate the efficacy and activity of these materials for water splitting via chemical looping processes, we performed experiments in which supported ALD films are reduced in a synthesis-gas atmosphere, and subsequently oxidized by steam. Additionally, we compare these results to mechanically milled powders of bulk Fe_2O_3 and ZrO_2 mixtures (BET SA = 210 m^2/g).

5.3 Materials and Experimental Methods

5.3.1 ALD synthesis

Multilayers of iron(III) oxide and cobalt(II) oxide were deposited onto porous ZrO_2 substrates (BET surface area = 50 m_2/g, Alfa Aesar®) via ALD in alternating cycles according to the schematic shown in Figure 5-1. Details of the reactor configuration are described elsewhere[33]. The ZrO_2 supports were ground with a mortar and pestle and sieved to particle sizes ranging from 149 μm to 250 μm to facilitate gas diffusion through the entire porous structure and achieve conformal coverage of the deposit. Deposition conditions were 450 °C and 200 mTorr total pressure.

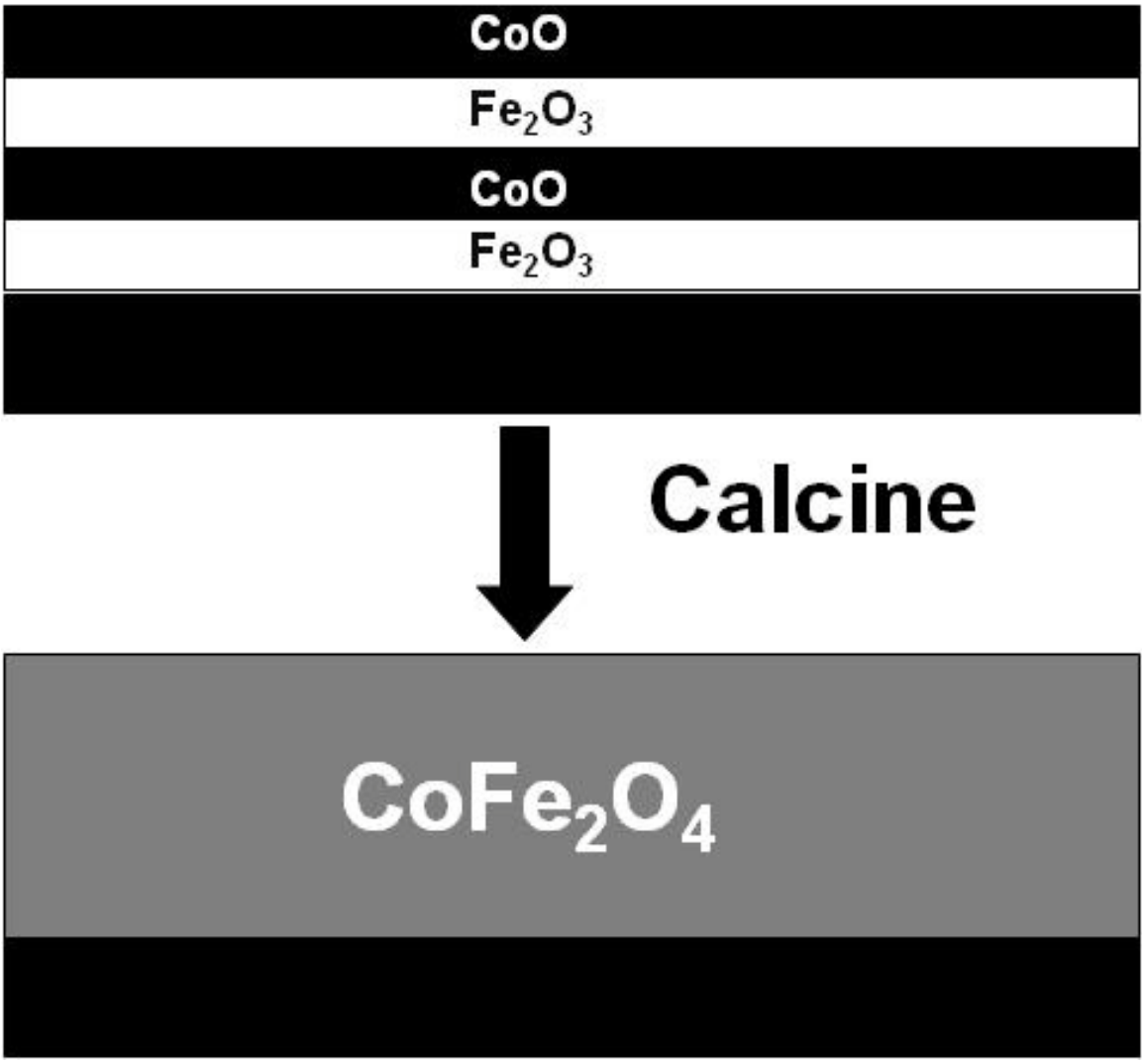

Figure 5-1: Schematic of $CoFe_2O_4$ synthesis by ALD.

Iron(III) oxide deposition consisted of flowing ferrocene (99% purity, Alfa Aesar®) or high purity oxygen (99.9%) into the reactor, with each dose representing one-half of the ALD cycle. A saturated vapor of ferrocene in nitrogen was delivered through a 200 cm^3 bubbler (Precision Fabricators Ltd.) heated to 60 ^oC. The reactor was then purged with pure nitrogen to remove any unreacted ferrocene and vapor phase byproducts of the ALD chemistry. Subsequently, oxygen was introduced into the reactor followed by another nitrogen purge.

Layers of Cobalt(II) oxide were deposited in an identical manner to that of iron(III) oxide using cobaltocene as the organometallic precursor.

In situ mass spectrometry is a reliable method for determining the termination of ALD half reactions on various substrates[34, 35] and was used here to monitor the extent of reaction. A plot illustrating the self-limiting nature of the ALD chemistry is shown in Figure 5-2. Each half reaction for both Fe_2O_3 and CoO deposition is clearly observed.

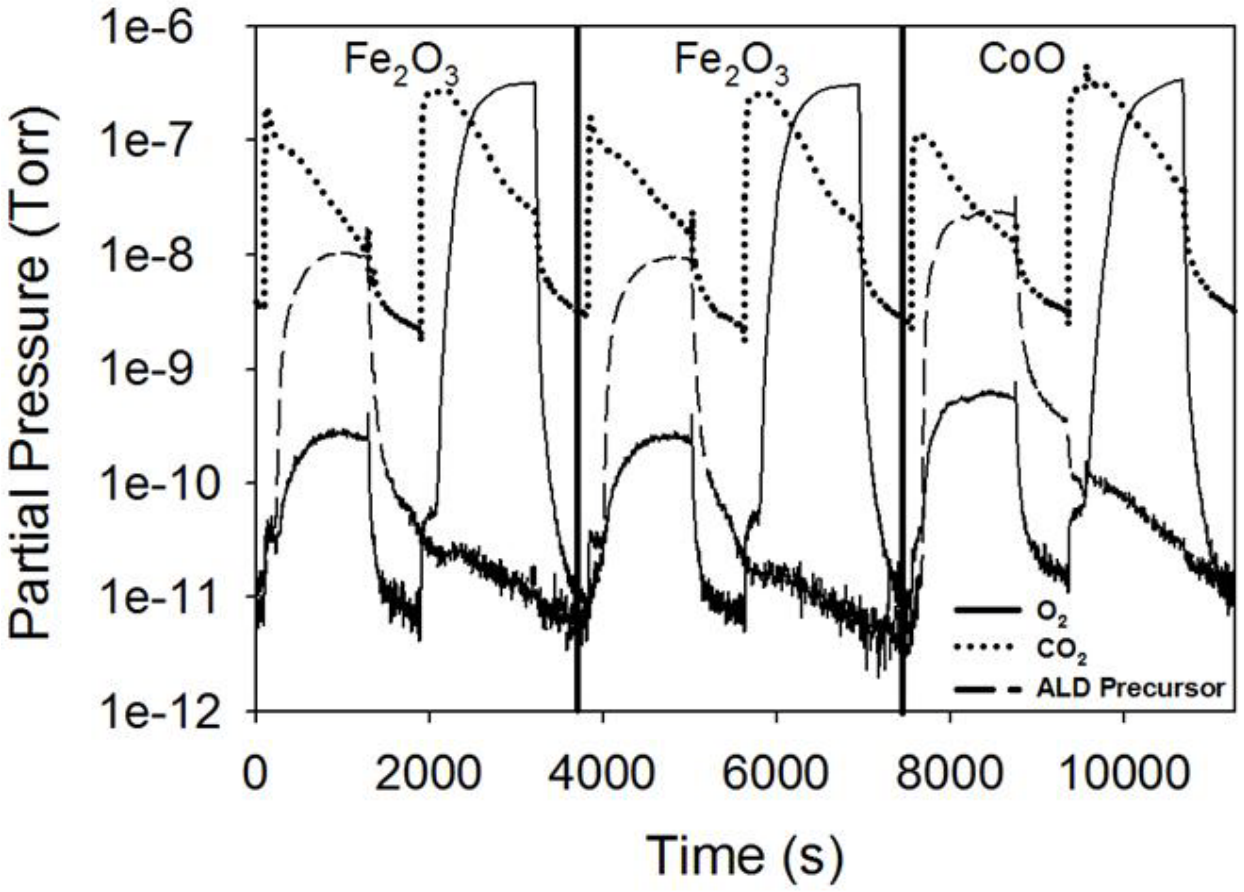

Figure 5-2: In situ mass spectrometry results showing Fe_2O_3 and CoO deposition.

Fe_2O_3 is deposited in the first two cycles and is characterized initially by an increase in the CO_2 partial pressure resulting from a reaction between ferrocene and the oxide surface. Once the

deposition nears completion, a mass spectral feature associated with the organometallic precursor at an m/e = 65 increases as the unreacted ferrocene breaks through the reaction zone. The partial pressure of CO_2 also starts to decrease at this point. Following a nitrogen purge the surface is oxidized with O_2 and an increase in CO_2 partial pressure, also a byproduct of this half reaction, is observed. Once O_2 breakthrough is achieved, indicating a termination of the half reaction, CO_2 again decreases. This process is repeated with ferrocene for one more cycle, shown in the center segment of Figure 5-1b, and then CoO is deposited using cobaltocene. The CoO ALD chemistry is nearly identical to that of ferrocene, evidenced by similar temporal behavior of the precursor and byproduct spectral patterns.

5.3.2 Material characterization

Electron microscopies were used to inspect morphology and crystallinity of the as-deposited ALD films. Elemental composition was determined via energy dispersive x-ray spectroscopy (EDS) and induced coupled plasma–atomic emission spectroscopy (ICP-AES). A Raman microscope was used to interrogate phonon modes in the films in order to fingerprint the chemical structure of the deposits. Surface area measurements were made with a Micrometrics Gemini V BET surface area analyzer.

Visual inspection of the films was carried out using a JEOL 2010F field-emission transmission electron microscope (HRTEM) operating at 200 kV. The material was lightly crushed using a mortar and pestle, and sonicated in ethanol. Copper TEM grids with a thin carbon support film were dipped into the suspension and allowed to dry. A JEOL 7600F field-emission scanning electron microscope (FESEM) operating at 4kV and 15kV was used to

examine surface morphology and local chemical variation. Here, samples were mounted on conductive tape and sputtered with carbon.

Raman spectra were acquired *ex situ* in a 180 degree-backscattering geometry using a 100× objective lens and 532-nm excitation from a frequency-doubled Nd:YAG laser. The scattered light was filtered by a film polarizer in crossed polarization with the incident, linearly polarized light to reduce the non-Raman background. A Semrock edge filter was used to reject the elastically scattered light. A spectrograph with a single 1200 groove/mm grating dispersed the light onto a CCD detector cooled by liquid nitrogen. The laser has a spot size of approximately 1 μm. The spectrometer was calibrated with a neon lamp. Raman spectra were collected at multiple locations on the sample surface.

5.3.3 In situ HT-XRD

High temperature XRD (HT-XRD) experiments were performed using a Scintag PAD X diffractometer (Thermo Electron Inc.; Waltham, MA). This diffractometer is equipped with a sealed-tube source (Cu Kα, $\lambda = 0.15406$ nm), an incident-beam mirror optic, a peltier-cooled Ge solid-state detector, and a Buehler hot-stage with Pt/Rh heating strip and surround heater. The hot stage lies within a sealed cell with x-ray-transparent beryllium windows, and is operable from ambient temperature to 1600 °C, and at gas pressures from 10^{-9} to 10^{3} Torr. A gas manifold was attached to the inlet of the reaction cell allowing the controlled flow of helium, hydrogen, and carbon dioxide through the cell. Suitable gas compositions were achieved by blending using mass flow controllers (Brooks Instruments).

Samples of typically 20 – 30 mg material were analyzed as thin films (ca. 50 – 100 μm) of powder on top of single-crystal <100> 9YSZ platelets (10mm x 10mm x 0.5mm, MTI

Corporation). *In situ* HT-XRD experiments were conducted at atmospheric pressure, under gas flow rates of 500 sccm. Experiments involved purging the reaction cell with He, then ramping the temperature to 600 °C before switching to a reducing gas mixture (2340 ppm H_2 and 2340 ppm CO_2). Diffraction patterns were recorded at room temperature under He, at 600 °C under He, and then continuously at 600 °C for 2 – 4 hours after introducing the reducing gas. A final XRD pattern was recorded after cooling the sample back to ambient temperature. Heating and cooling ramp rates were set to 20 °C min^{-1}. Using this experimental set-up, phase fractions as low as approximately 1 wt.-% could be reliably detected. The temperature calibration was performed using the thermal expansion behavior of known materials (e.g., alumina or Pt) to an accuracy of ±5 °C. Diffraction patterns were collected at 40 kV and 30 mA using fixed slits and a count time of 1 s.

5.3.4 Stagnation flow reactor

Samples were reduced and oxidized in a stagnation flow reactor (SFR) shown in Figure 5-3. The reactor consists of a stainless steel gas-handling manifold, ceramic reactor core, high temperature furnace (Carbolite STF16/180), and modulated effusive beam mass spectrometer. The ceramic reactor core is configured to allow inlet gases flowing downward towards the round-bottom, closed end of an Al_2O_3 tube (McDanel Advanced Ceramic Technologies) to impinge on a zirconia flat, turn 180 degrees, and exit through an annular space between the walls of two concentric tubes (see cross sectional view and flow stream lines in Figure 5-3). The distance between zirconia flat and bottom of inner tube wall was maintained at 8 mm to ensure ideal stagnation flow behavior as determined by 2-D computational fluid dynamic (CFD) calculations. Essentially the gas-phase region above the zirconia flat between centerline and

inner tube radius can be considered an ideal 1-D stagnation plane governed by diffusive transport. Shown in the inset to Figure 5-3 are plots of the surface velocity gradient as a function of inner tube radius for an ideal 1-D case, the best case CFD prediction used to fix the reactor geometry, and a worst case prediction. It is important to note that the SFR operates in a flow regime where velocity and thermal gradients are independent of tube radius so that materials sitting on the zirconia flat experience a uniform gas composition.

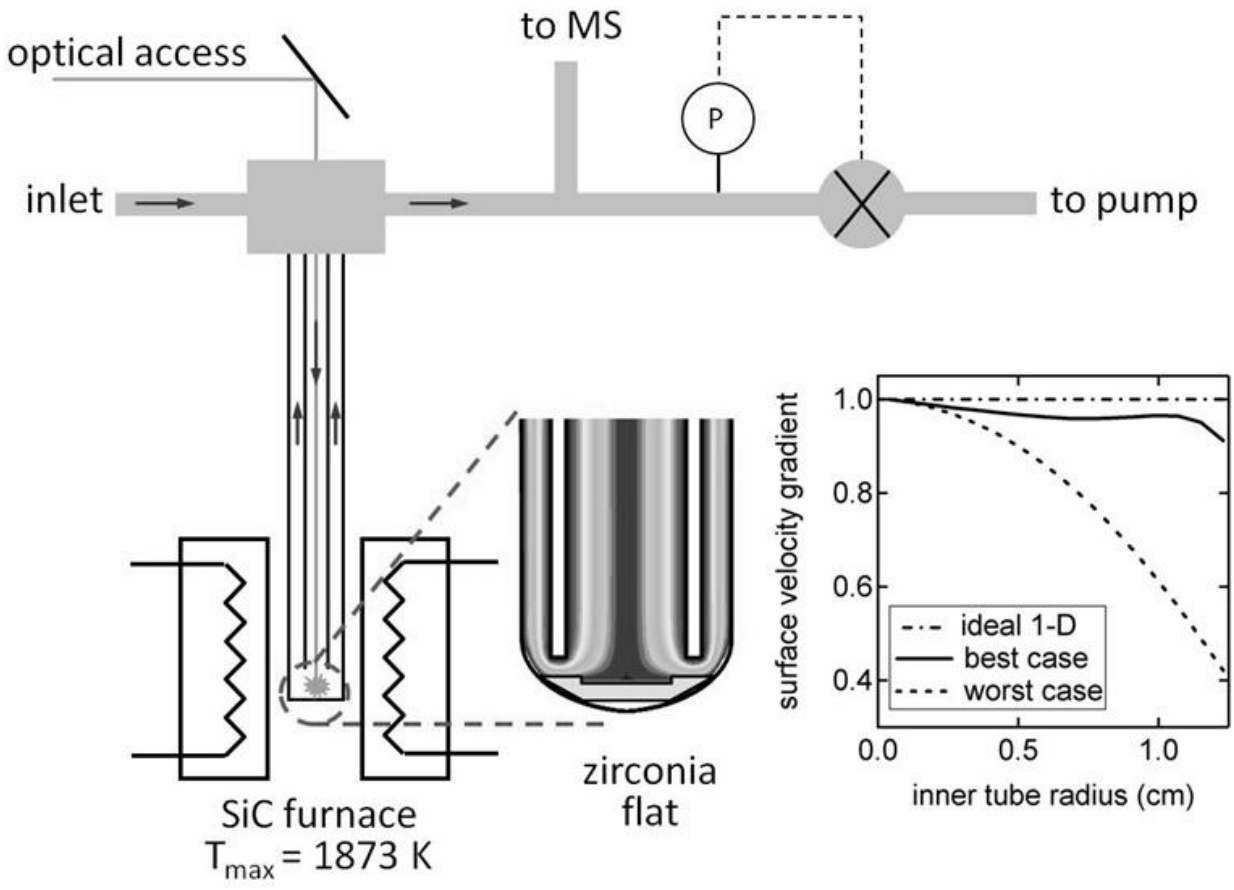

Figure 5-3: Stagnation flow reaction (SFR)

Gases exiting the flow reactor were sampled using a differentially pumped, modulated effusive beam mass spectrometer (Extrell C50, 500 amu). Upon expansion into the second of

three pumping stages, the molecular beam is chopped by a resonant modulator driven at 200 Hz and ionized by electron impact at 30 eV. Modulated ion current from the electron multiplier is routed through a lock-in amplifier and discriminated against DC background. This increases detector sensitivity and digitally filters out ion current resulting from gases that persist in the ionization volume thus enabling real-time baseline correction and a higher degree of precision for quantifying component partial pressures. A mixture of 5 vol.-% CO and 5 vol.-% H_2 in He was used to calibrate the detector.

Mass flow controllers were used to meter all gas feed rates. The reactor exhaust was throttled, allowing for feedback control of the reactor pressure to any desired setpoint within the range 1 to 760 Torr. Unless otherwise indicated, oxidation and reduction reactions were conducted at a temperature of 600 °C, a total flow rate of 500 sccm, using mixtures of H_2, CO, CO_2, H_2O, and He at a total pressure of 75 Torr. Water was delivered through an evaporator fed by micro-syringe pump. Liquid nitrogen traps were used to condense H_2O prior to sampling the reactor effluent with the mass spectrometer. Between 50 and 200 mg of sample material in the form of powder or ALD-coated ZrO_2 support were placed in the reactor. Chemical reduction was accomplished by exposing the sample to a gas mixture of 1 vol.-% H_2, 1 vol.-% CO, and 2 vol.-% CO_2 diluted in He for a total of 600 s. Water oxidation consisted of flowing H_2O and He in various proportions for 600 s.

5.4 Results and Discussion

5.4.1 ALD materials

ALD films with three representative cobalt stoichiometries (x = 0, 0.67 and 1 in $Co_xFe_{3-x}O_4$) were synthesized by appropriately adjusting the number and sequence of iron oxide and cobalt oxide deposition cycles (e.g., 1 cobalt oxide cycle for every 2 iron oxide cycles in $CoFe_2O_4$). The total number of ALD cycles was varied between 24 and 50 cycles. The corresponding mass loadings, as measured via ICP-AES analysis, varied from 20% to 37%. ICP-AES results showing the actual cobalt stoichiometry verses attempted are shown in Figure 5-4.

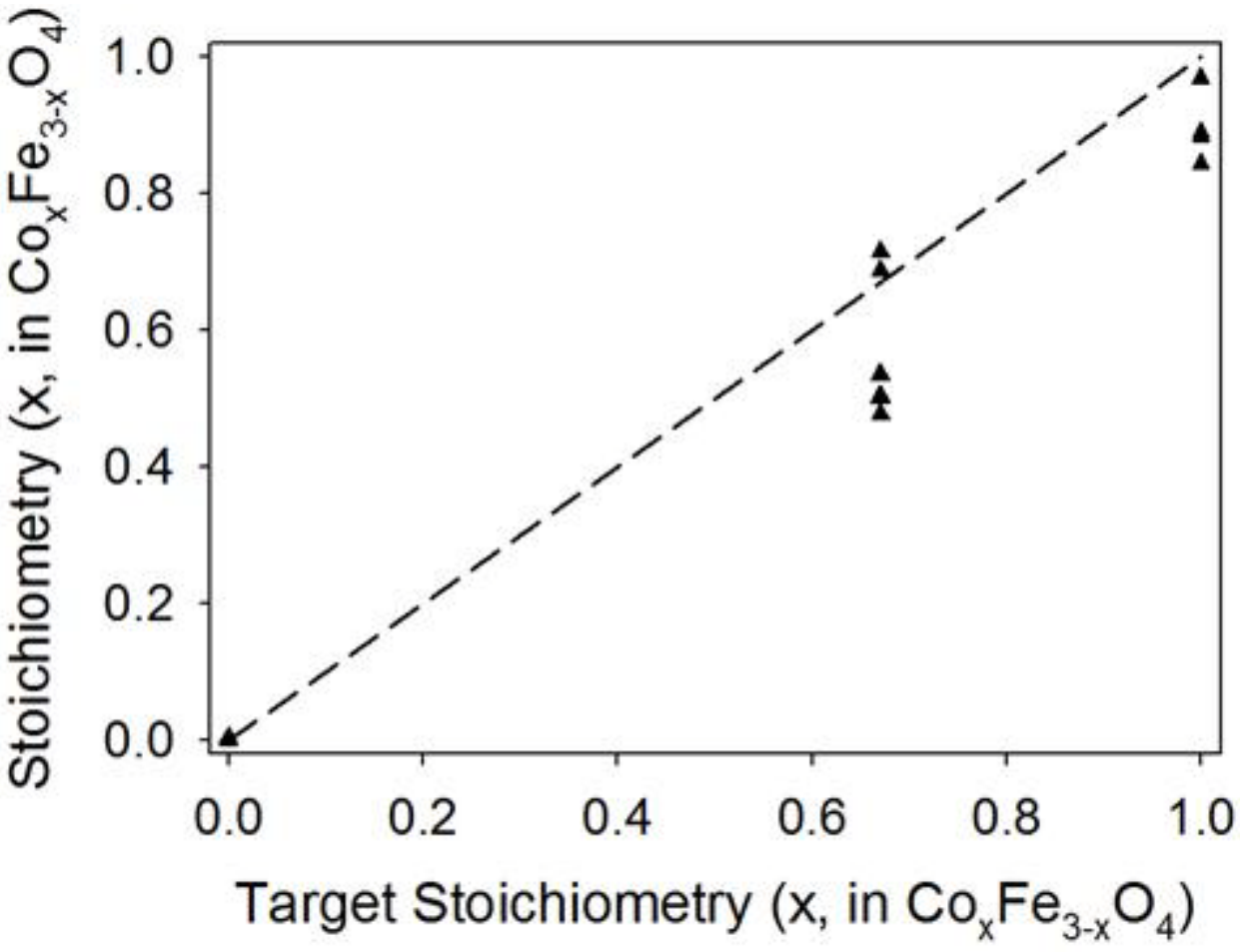

Figure 5-4: ICP-AES Results of the actual stoichiometry (x, in $Co_xFe_{3-x}O_4$) verses target stoichimetry

When flowing only ferrocene, the target and actual stoichiometries are identical because iron oxide is deposited. As higher cobalt concentrations are attempted, the actual stoichiometries agree well with the targeted stoichiometries, indicating that both iron oxide and cobalt oxide growth rates are similar. Variations in film stoichiometry are primarily due to gas diffusion limitations through the ZrO_2 support, but may also be due to cycle-to-cycle variability. As noted previously, the original ZrO_2 supports were ground to smaller particle sizes to decrease the reactant diffusion time, because the original supports were too large to allow for adequate diffusion through the pores.

FESEM images of $Co_{0.85}Fe_{2.15}O_4$ deposited on 50 m^2/g supports are presented in Figures 5-5a and 5-5b. The bulk support was ground and sieved prior to ALD and, at ×40 magnification, appears to have an average particle size of order 200 μm. The high surface area of these supports is the result of sintering ZrO_2 nanoparticles, which are nominally 50 nm in diameter as seen at higher magnification (×20000) in Figure 5-5b. Measurements of the specific surface area of the supports using BET methods confirm that significant sintering or grain growth did not occur during the deposition at 450 ^oC. After deposition of $Co_{0.85}Fe_{2.15}O_4$ (45% by mass), the surface area of the support decreased from 51 m^2/g to 28 m^2/g. This decrease agrees well with the increase in mass due to the addition of the ferrite film (45%), and also confirms that deposition did not result in pore clogging. EDS mapping of Zr and Fe (Figure 5-5c and 5-5d) confirm that iron is uniformly distributed throughout the support.

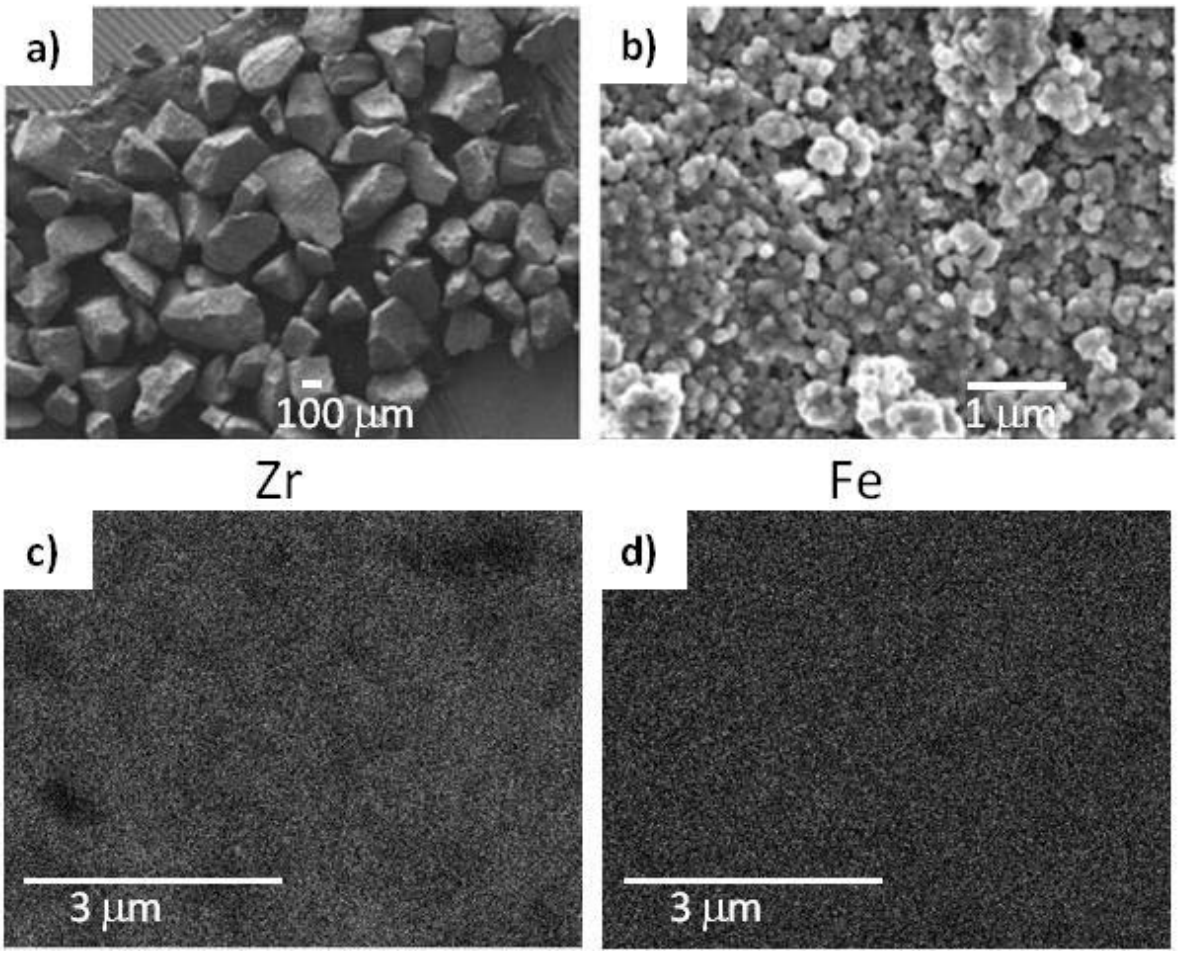

Figure 5-5: a) FESEM image of bulk ZrO2 supports, b)FESEM image of ZrO2 nanoparticles within the bulk, c) EDS Zr map after $Co_{0.85}Fe_{2.15}O_4$ deposition and d) EDS Fe map after $Co_{0.85}Fe_{2.15}O_4$ deposition

TEM analysis shows the crystalline nature of the ZrO_2 nanoparticles and the $Co_{0.85}Fe_{2.15}O_4$ coated nanoparticles after deposition at 450 ^oC. TEM and HRTEM images of the uncoated ZrO_2 support are shown in Figures 5-6a and 5-6b. The lattice fringes are clearly observed in Figure 5-6b, and the accompanying electron diffraction pattern (inset Figure 5-6a) confirms that the nanoparticles making up the support are m-ZrO_2. TEM images in Figures 5-6c and 5-6d show that a thin film surrounds the ZrO_2 nanoparticles after deposition. At higher magnification (Figure 5-6d) it is apparent that this 2 nm layer has a different crystolographic

orientation than the underlying support. This interface is not observed for the un-coated ZrO_2 support. Electron energy loss spectroscopy (EELS) also confirms that of cobalt and iron oxides were present throughout the surface of the ZrO_2.

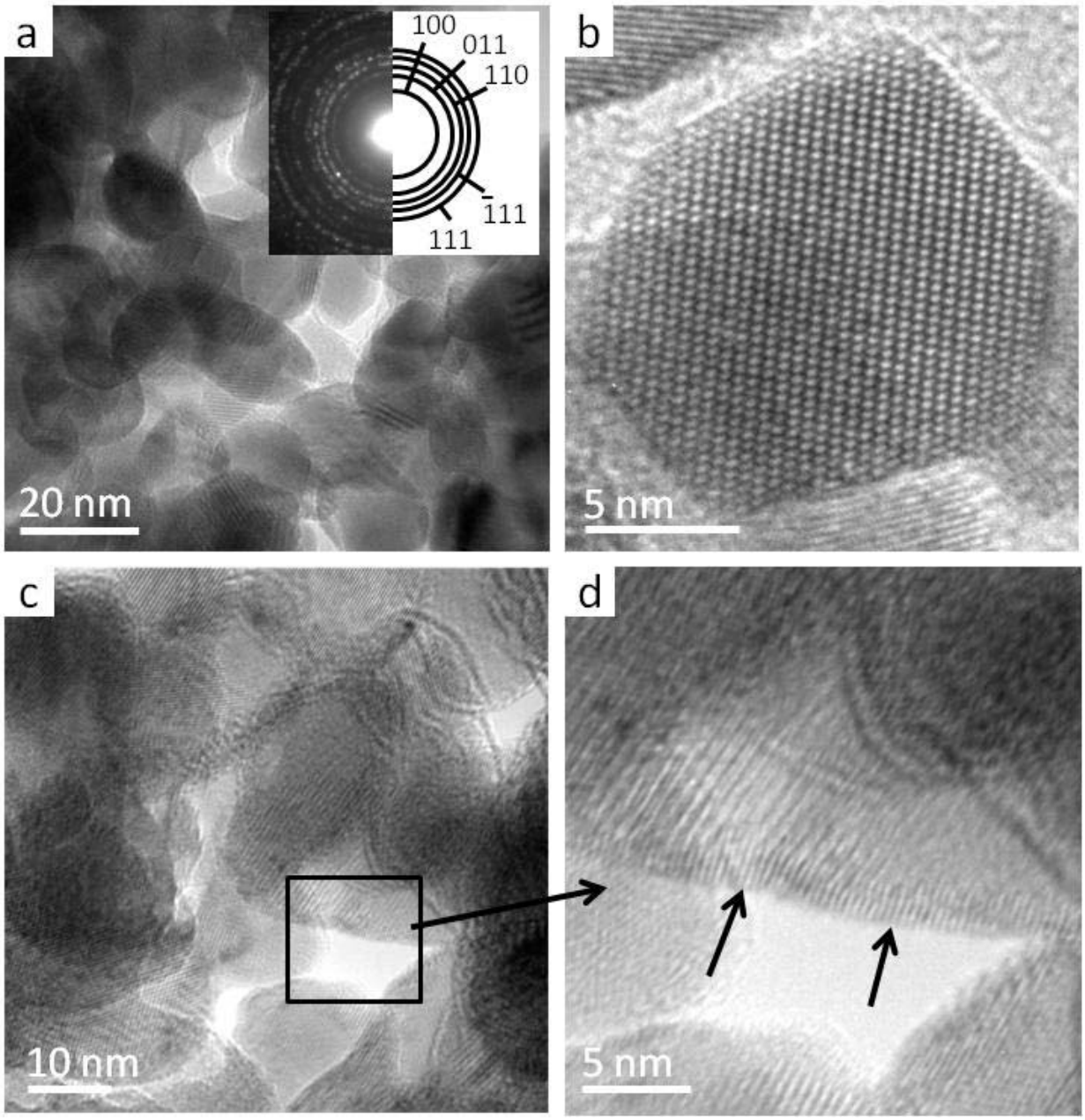

Figure 5-6: a) HRTEM image of m-ZrO_2 support and corresponding diffraction pattern, b)HRTEM image of m-ZrO_2 nanoparticle within support , c) HRTEM image after $Co_{0.85}Fe_{2.15}O_4$ deposition and d) HRTEM image showing crystalline $Co_{0.85}Fe_{2.15}O_4$ film on m-ZrO_2

The structural nature and homogeneity of the films were examined further by Raman spectroscopy. The strongest Raman modes we observe for ALD iron oxide films occur at 325, 370, 465, 495, 625, 650, and 710 cm^{-1}, as shown in Figure 5-7a. These modes are indicative of maghemite (γ-Fe_2O_3) and agree well with previous literature reports[36, 37]. This is also indirect confirmation for the presence of a nanoscale thin film as maghemite is the more thermodynamically favored phase of Fe^{3+} for small particle sizes (less than 16 nm) because it possesses a lower surface energy than hematite[36, 38, 39].

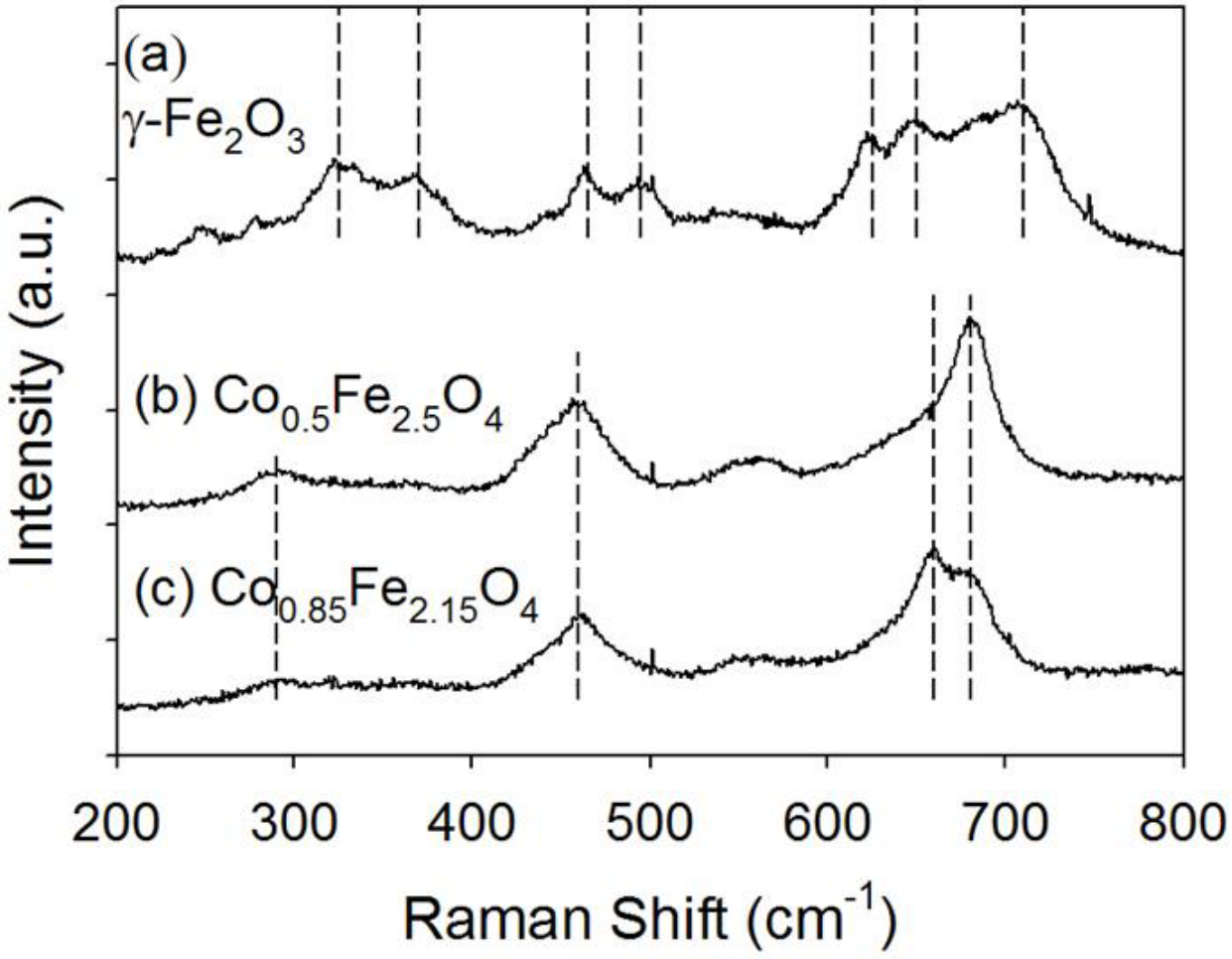

Figure 5-7: Raman spectra of a) g-Fe_2O_3 deposited on m-ZrO_2, b) $Co_{0.5}Fe_{2.5}O_4$ deposited on m-ZrO_2 and c) $Co_{0.85}Fe_{2.15}O_4$ deposited on m-ZrO_2

Substitution of cobalt for iron in the ALD film leads to a decrease in the Raman modes associated with maghemite, and a subsequent increase in the intensity of magnetite (Fe_3O_4) modes at 290, 460, and 680 cm^{-1} (Figure 5-7b)[36, 40]. In addition, the peak at 680 cm^{-1} is not symmetrical, which is expected for pure Fe_3O_4. The asymmetry is attributed to the presence of Co substituted for Fe. As the cobalt stoichiometry in the film increases from 0.5 to 0.85, a peak at 660 cm^{-1} grows in beside the peak at 680 cm^{-1}. This observation is consistent with literature reports of inverse spinel structures where Co substitutes for Fe in octahedral sites[20, 40]. The Raman spectra also reveal indirect evidence for conformal coverage of the ALD films on the support because no modes indicative of ZrO_2 are apparent.

5.4.2 Chemical reduction and HT-XRD

Iron oxide and cobalt ferrite samples were chemically reduced in either a 1:1 mixture of H_2:CO_2 diluted in He, or a 1:1:2 mixture of H_2:CO:CO_2 diluted in He. By including CO_2 in the reducing gas, the extent to which metallic iron (Fe^0) will form when starting from Fe_2O_3 (Fe^{3+}) can be suppressed such that the formation of FeO (Fe^{2+}) is thermodynamically favored. This is discussed in detail by Bohn et. al.[10] and we have confirmed this with calculations using the thermodynamics software package FactSage. Bohn et. al. observed better redox cycle repeatability when reducing iron oxide particles to FeO rather than metallic iron. They attributed this to the suppression of grain growth and sintering. Therefore, we chose to chemically reduce our materials in an atmosphere conducive to the formation of FeO in order to minimize cycle-to-cycle variability in H_2 production rates, as well as investigate water splitting chemistry that is comparable to thermal redox cycles in which iron oxide is cycled between Fe_3O_4 and FeO at high temperature. Phases formed during chemical reduction were monitored *in situ* by HT-XRD.

Chemical reduction of α-Fe_2O_3 nanoparticles physically mixed with m-ZrO_2 (25% α-Fe_2O_3 by mass) in 1 vol.-% H_2, 1 vol.-% CO_2 mixture resulted in the formation of FeO, but after prolonged reduction metallic Fe was formed, as shown in Figure 5-8. Prior to the addition of any reactants, only α-Fe_2O_3 is observed at room temperature. Once heated to at 600 ^oC, however, Fe_3O_4 is observed. After exposure to a reducing atmosphere, there is a rapid transition to FeO. Unexpectedly, however, the presence of metallic Fe is observed after only 15 minutes, and slowly increases in intensity until the sample is cooled to room temperature. This behavior is different from that of only α-Fe_2O_3 particles without m-ZrO_2. In fact, when we used only α-Fe_2O_3 we observed a clear transition from α-Fe_2O_3 to Fe_3O_4 to FeO only after the reducing gases were introduced. The presence of metallic Fe was observed, but after a much longer time (> 84 minutes). Because metallic Fe is not thermodynamically predicted to exist under either of these conditions, we attribute its formation to the grain growth of the iron oxide particles. This results in larger particles that can readily be reduced by the H_2, but the impact of CO_2 becomes kinetically limited due to diffusion limitations through the bulk of the particles. Bohn *et.al.* have performed similar experiments and did not observe any metallic Fe formation, but it should be noted that their experiments were much shorter (≤10 minutes). Only for longer reduction times than this did we witness any Fe [10]. Also, because of the differences observed with and without m-ZrO_2, it is clear that there is an interaction between the m-ZrO_2 and α-Fe_2O_3, which results in a more rapid reduction of iron to its reduced phases. Without further investigation, however, it is difficult to determine the nature of this observation. The rapid reduction may be in part due to the role that ZrO_2 plays in preventing grain growth of the Fe_2O_3 particles, and the reduction to Fe rather than FeO may be related to the solubility of iron in ZrO_2.

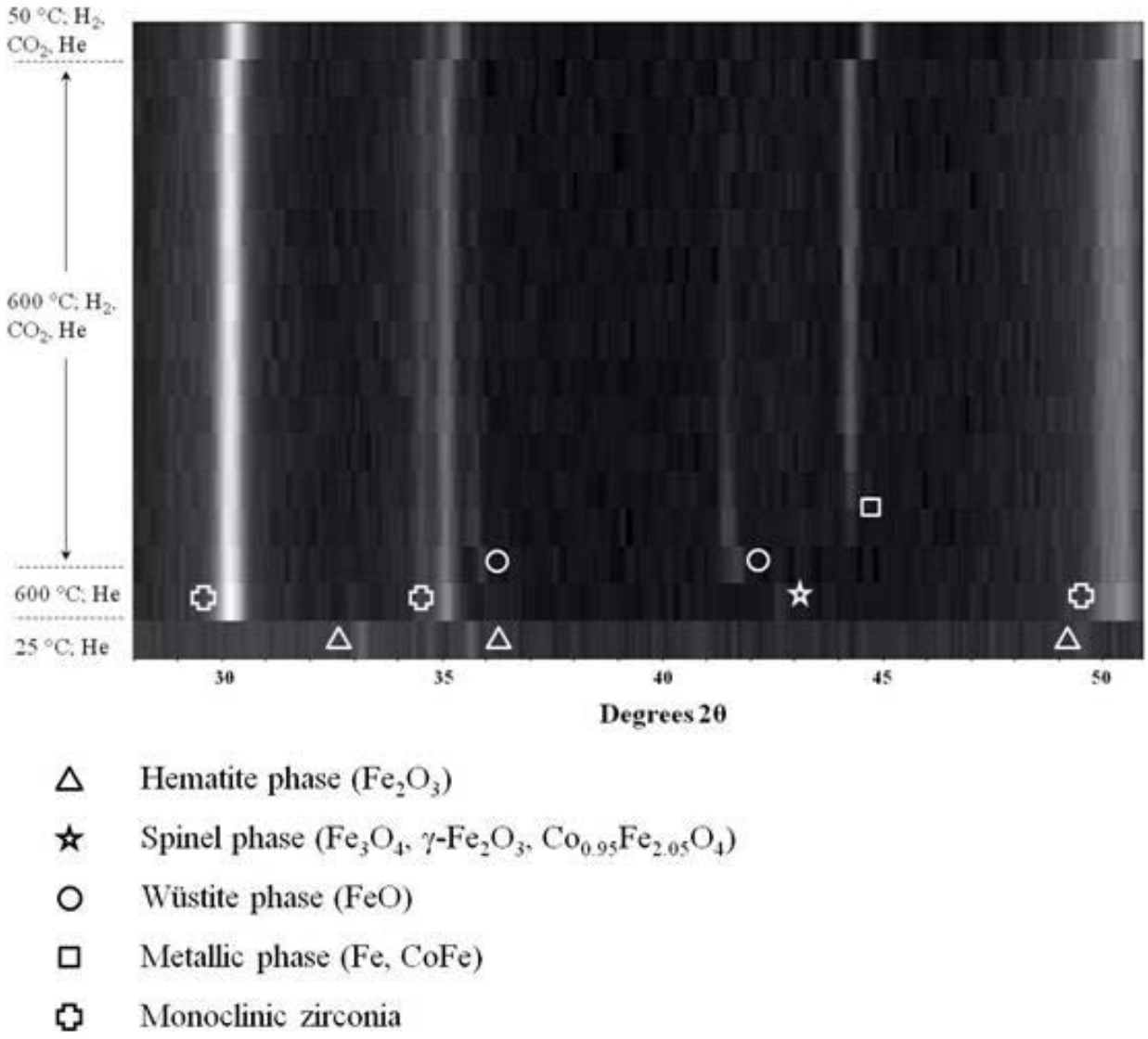

Figure 5-8: In situ XRD spectra of 25% α -Fe_2O_3 /75% m-ZrO_2 by mass reduced in 1% H_2 / 1% CO_2 in He (500 sccm total) at 600 ^oC

Metallic Fe is not observed during the chemical reduction of γ-Fe_2O_3 synthesized via ALD. Only FeO is observed after chemical reduction for up to 148 minutes. As seen in Figure 5-9, upon exposure to the reducing atmosphere, there is an immediate appearance of FeO (42^o) and the maghemtite (γ-Fe_2O_3, 35^o) decreases in intensity. By the end of the experiment, no changes in either γ-Fe_2O_3 or FeO intensity are observed, indicating that the reaction has completed. This

is in contrast to the α-Fe_2O_3/ZrO_2 powder in which the iron was reduced to metallic Fe. Because the γ-Fe_2O_3 synthesized via ALD was deposited on a stable ZrO_2 support, morphological changes are suppressed for the duration of the experiment. It is difficult to see the transition from γ-Fe_2O_3 to Fe_3O_4 because maghemtite and magnetite both have similar XRD patterns, and the resolution of our diffractometer is not capable of distinguishing between the two.

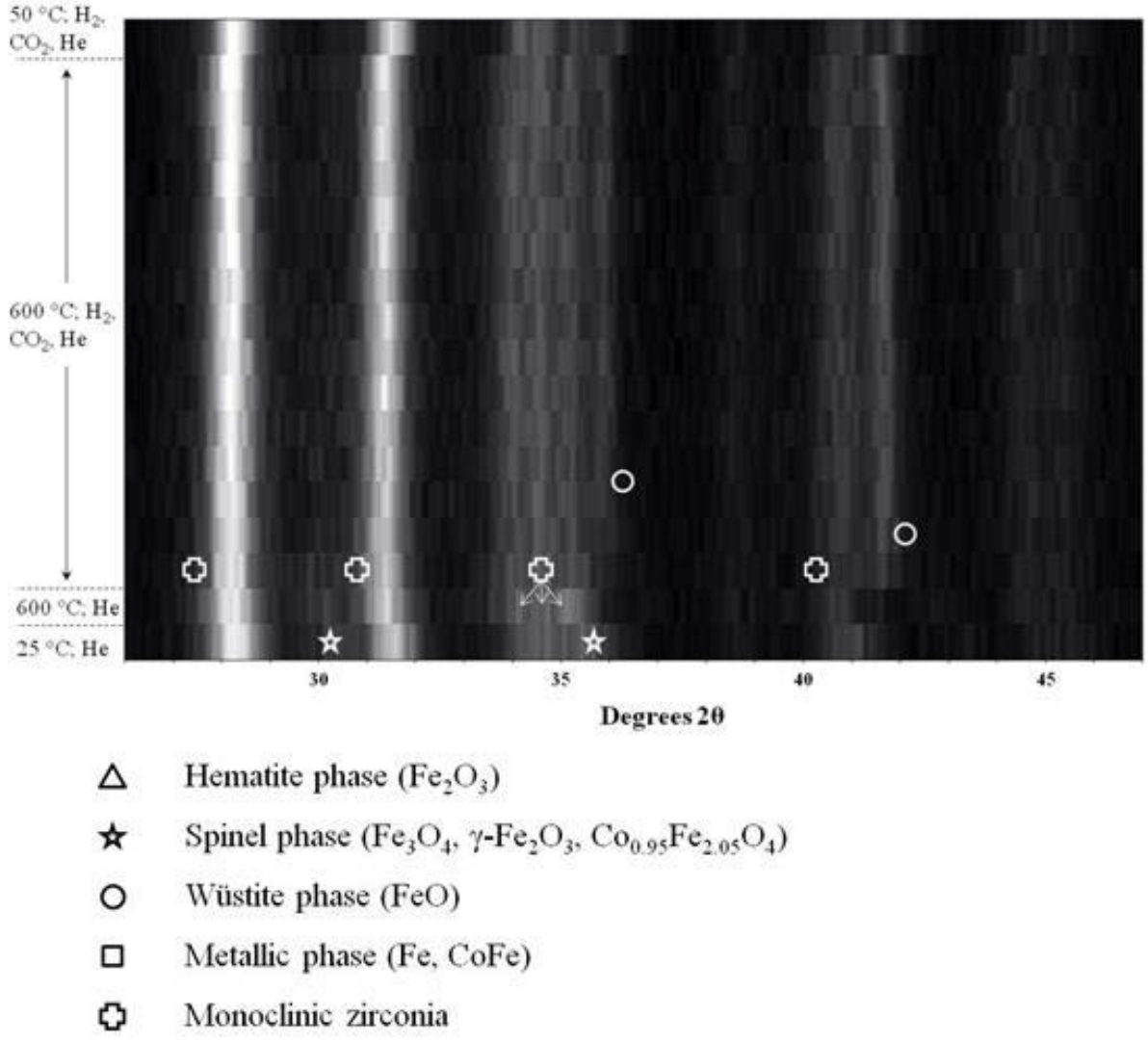

Figure 5-9: In situ XRD spectra of Fe_2O_3 on m-ZrO_2 (ALD/20.2% mass loading) reduced in 1% H_2 / 1% CO_2 in He (500 sccm total) at 600 ^oC

Additionally, many of the peaks due to m-ZrO_2 fall on or near the peaks of interest, making data interpretation more difficult. It is not yet clear why the α-Fe_2O_3 particles mixed with ZrO_2 reduce to metallic Fe and the ALD synthesized γ-Fe_2O_3 films on ZrO_2 reduce only to FeO. It may simply be due to differences between crystallographic orientations of the iron oxide or due to the morphological differences between very thin films ($\approx$ 2nm) and particles.

Although the chemical reduction of iron in Fe_2O_3 (or Fe_3O_4) to FeO has been reported previously in the literature, the chemical reduction of iron to Fe^{2+} in cobalt ferrite is less understood. Thermodynamic calculations under the same conditions conducive to the formation of FeO in the iron oxide system predict the formation of metallic Co and Fe in cobalt ferrites. In fact, we could not find any conditions where a thermodynamically stable phase of Fe^{2+} exists when chemically reducing cobalt ferrite with a mixture of H_2, CO, and CO_2. As predicted, the formation of Fe^{2+} was not observed for $Co_{0.85}Fe_{2.15}O_4$ synthesized via ALD. Rather, after the introduction of the reducing gas there is a rapid transition from the magnetite structure (30^o) to a CoFe alloy (44.5^o), as seen in Figure 5-10. For the duration of the reaction, the intensity of the alloy slowly increases, but the majority of the conversion occurs almost immediately after the reducing gases are delivered.

With guidance from the results of our in situ HT-XRD experiments, the subsequent water splitting chemistry of reduced iron oxide and cobalt ferrite ALD thin films was investigated. Chemical reduction was achieved in an ambient of 1 vol.-% H_2, 1 vol.-% CO, and 2 vol.-% CO_2 in He at 75 Torr for 600 s at 600 ^{o}C. The CO_2 signal was monitored with the mass spectrometer in order to determine a point at which full reduction was achieved. Oxidation was performed at 75 Torr and 12.5% H_2O.

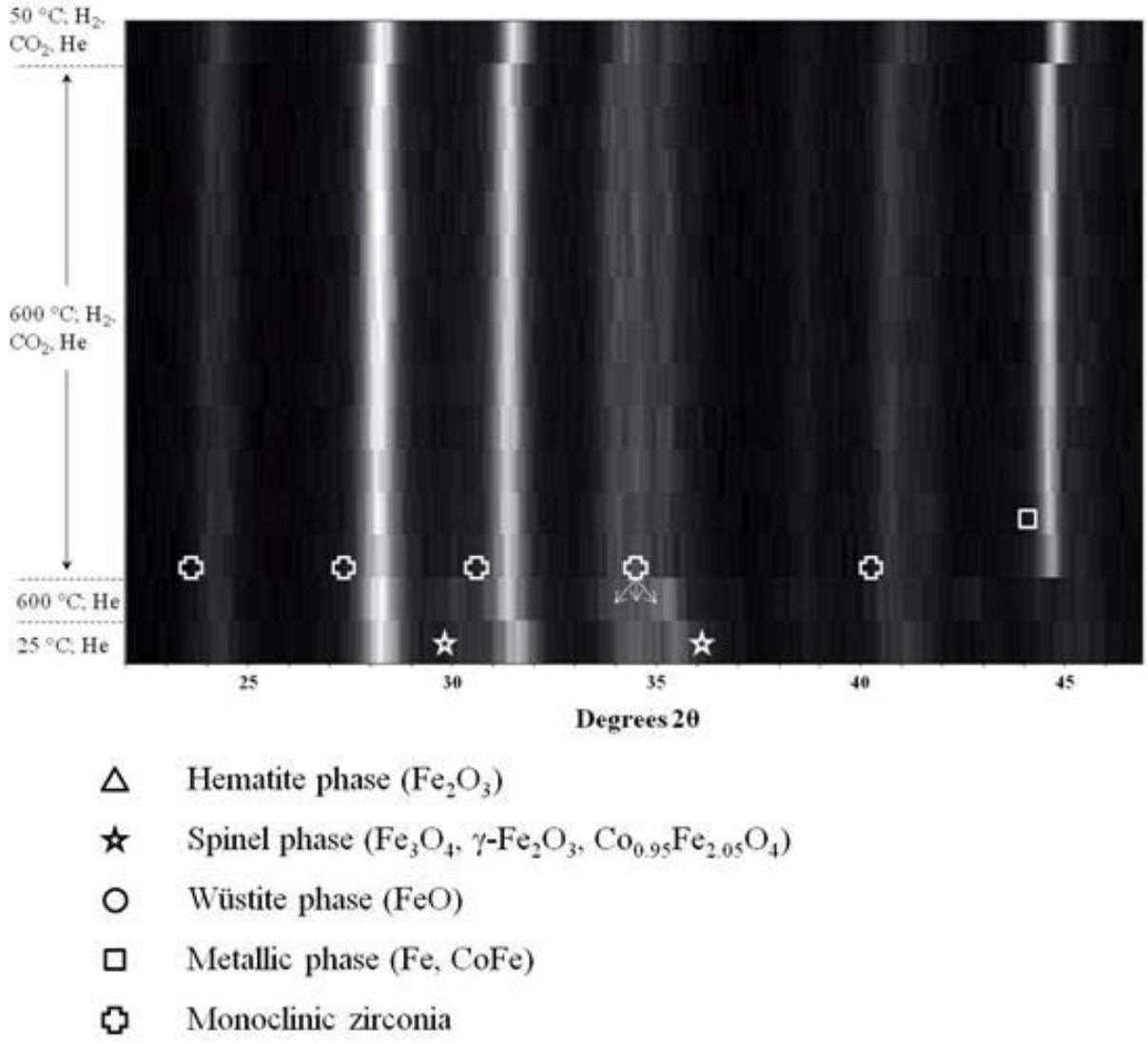

Figure 5-10: In situ XRD spectra of $Co_{0.85}Fe_{2.15}O_4$ on m-ZrO_2 (ALD/19% mass loading) reduced in 1% H_2 / 1% CO_2 in He (500 sccm total) at 600 ^oC

5.4.3 Water splitting in the stagnation flow reactor

Temporal water oxidation behavior at 600 ^oC is remarkably different for each of the materials. Both Fe_2O_3 (ALD/20.2% mass loading) and $Co_{0.85}Fe_{2.5}O_4$ (ALD/19% mass loading) were characterized by an initial rapid peak rate, followed by an exponential decay. However, the

physically mixed Fe_2O_3/ZrO_2 powder (25% mass loading) was characterized by an almost constant H_2 rate until the reaction was exhausted. The cyclical behavior of Fe_2O_3 (ALD/20.2% mass loading) is characterized by slightly decreasing peak H_2 rates, and a decrease in the time required for H_2 to decline back to baseline, as shown in Figure 5-11a. From cycle #1 to cycle #5, this time decreases from about 100 s to 50 s, and peak rates decrease from 36.9 to 31.1 μmoles/s/g. We do not believe that this behavior is primarily due to sintering, because the peak rates do not decrease nearly as dramatically as the total H_2 production. Additionally, BET surface area measurements indicated only a small decrease in specific surface area. Rather, we attribute this to iron solubility in the ZrO_2 support, which is well documented at these temperatures[41].

The first five cycles of $Co_{0.85}Fe_{2.5}O_4$ (ALD/19% mass loading) are shown in Figure 5-11b, and it is clear that the H_2 rate is nearly identical from one cycle to the next. There is almost no variation in the H_2 rate at a given time from one cycle to the next. This is indication that the sample structure and morphology is not changing to a significant degree. Interestingly, even though this sample is reduced to metallic Co and Fe, it does not deactivate in the same manner as Fe_2O_3 when reduced to metallic Fe. We observed rapid deactivation when Fe_2O_3 was reduced to Fe metal (not shown). The differences may be a result of cobalt limiting the migration of iron, and hindering its ability to grow and sinter. It is also apparent that, unlike Fe_2O_3, the H_2 rate does not decrease back to zero for the reaction times that we explored. After 400s, the rate appears to plateau above zero. It is unclear whether this is due to extremely slow reaction rates at these times due to the oxidation of metallic Co. Another possibility is that we are catalytically producing small amounts H_2 from the catalytic decomposition of H_2O.

The temporal behavior of the physically mixed Fe_2O_3/ZrO_2 powder (25% mass loading) does not exhibit the exponential decay that is observed for both of the ALD materials. Rather, the H_2 increases to a plateau until the reaction apparently reaches completion, as seen in Figure 5-11c. As the number of cycles increases, the magnitude of the plateau decreases and the reaction time increases. The decrease in reaction rate is due to sintering and grain growth of the iron oxide, which is corroborated by BET surface area measurements showing that the initial surface area of 210 m^2/g decreases to 10 m^2/g after only five cycles. This temporal behavior is different from reaction rates for iron oxide powders reported in the literature [10, 42]. Generally, an exponential decay of H_2 is observed that is attributed to diffusion limitations through the product oxide layer on particles. Clearly, the behavior we observe is not consistent with a reaction limited by diffusion because the rate remains constant as a function of time. Instead, our data suggests that the rate is limited by water adsorption on the surface of the particles. This is not an artifact of our reactor configuration because this behavior is not observed with any of our ALD materials. Additionally, it is unlikely we are limited by diffusion through the bed of particles, as we do not have a packed bed of particles but rather a thin layer ($\approx$ 1mm) placed on top of a ZrO_2 holder. It is possible that the exponential decay observed in some of the literature is an artifact of the packed-beds that are used rather than the inherent kinetics of the reactants themselves.

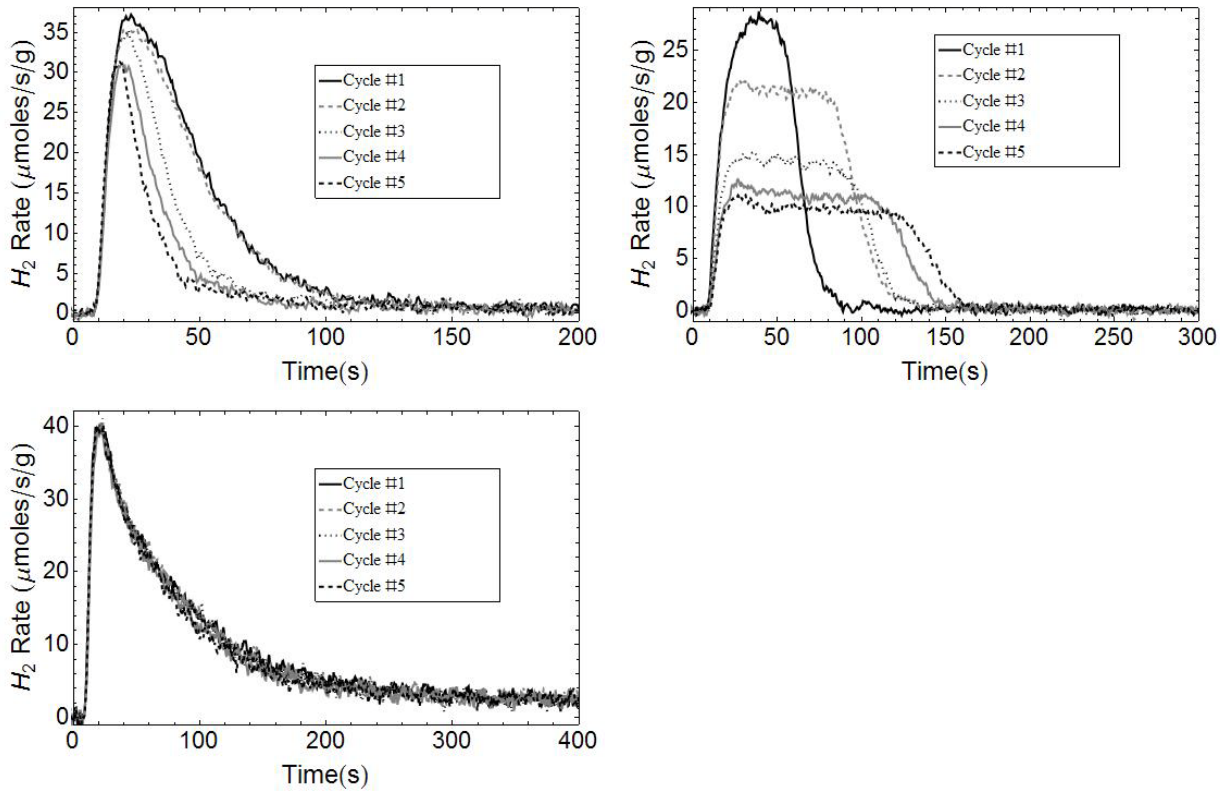

Figure 5-11: Temporal H_2 data for five cycles of samples reduced in 1% CO / 1% H_2 / 2% CO_2 in He (500 sccm total). a) Fe_2O_3 (ALD/20.2% mass loading) , b) $Co_{0.85}Fe_{2.15}O_4$ (ALD/19% mass loading) and c) physically mixed Fe_2O_3/ZrO_2 powder (25% mass loading)

Peak H_2 rates vary little with cycling, as shown in Figure 5-12a for seven cycles. The peak rate for Fe_2O_3 on ZrO_2 (ALD/20.2% mass loading) at 600 ^oC is 33.58 ± 3.1 μmoles/s/g, while for $Co_{0.85}Fe_{2.5}O_4$ (ALD/19% mass loading) the rate is 39.07 ± 1.2 μmoles/s/g. This behavior is remarkably better than when samples were chemically reduced without any oxidant present (not shown). We compared ALD materials to a physically mixed powder solution containing a 3:1 mass ratio of ZrO_2 to α-Fe_2O_3, and the peak rate of its first cycle is comparable to the ALD ferrite samples. However, subsequent cycling resulted in a gradual decrease in the peak rates, which is caused by grain growth that decreases specific surface area. BET measurements confirmed that the surface area of the powder had decreased from 210 m^2/g to 10

m^2/g after 5 redox cycles. The surface area of the ALD materials decreased slightly as well, but not nearly to the extent of the physically mixed powder. Fe_2O_3 on ZrO_2 (ALD/20.2% mass loading) decreased from a surface area of 39 m^2/g to 27 m^2/g and $Co_{0.85}Fe_{2.5}O_4$ (ALD/19% mass loading) decreased from 41m^2/g to 31.5 m^2/g when cycled at 600 ^oC. However, we did observed a decrease in surface area of Fe_2O_3 on ZrO_2 (ALD/20.2% mass loading) to 8.5 m^2/g when cycled at 700 ^oC.

The H_2 yield of $Co_{0.85}Fe_{2.5}O_4$ (ALD/19% mass loading) was greater than ALD synthesized and Fe_2O_3 powder for up to 7 redox cycles, as shown in Figure 5-12b. The initial yield of cobalt ferrite was 4100 μmoles H_2/g, whereas the yield for ALD iron oxide was 1200 μmoles H_2/g. The yield of the cobalt ferrite remained stable for all 7 cycles; however the yield of ALD iron oxide cycled at 600 ^oC decreased to 800 μmoles H_2/g by the 5^{th} cycle, and remained stable upon further cycling. We hypothesize that the yield for Fe_2O_3 ALD samples is less than cobalt ferrite for two reasons. Firstly, the potential extent of oxidation of the cobalt ferrite is greater because it was reduced all the way to metallic Co and Fe, as determined by *in situ* HT-XRD (Figure 5-10). The iron oxide, however, was only reduced to FeO. Secondly, Fe^{3+} is highly soluble in ZrO_2 at these temperatures, which may reduce the amount of iron that is available to participate in the redox reaction[41]. Although Fe^{3+} is present in the cobalt ferrite as well, the presence of metallic cobalt or CoO may inhibit the solubility of iron if it preferentially forms a solution with it.

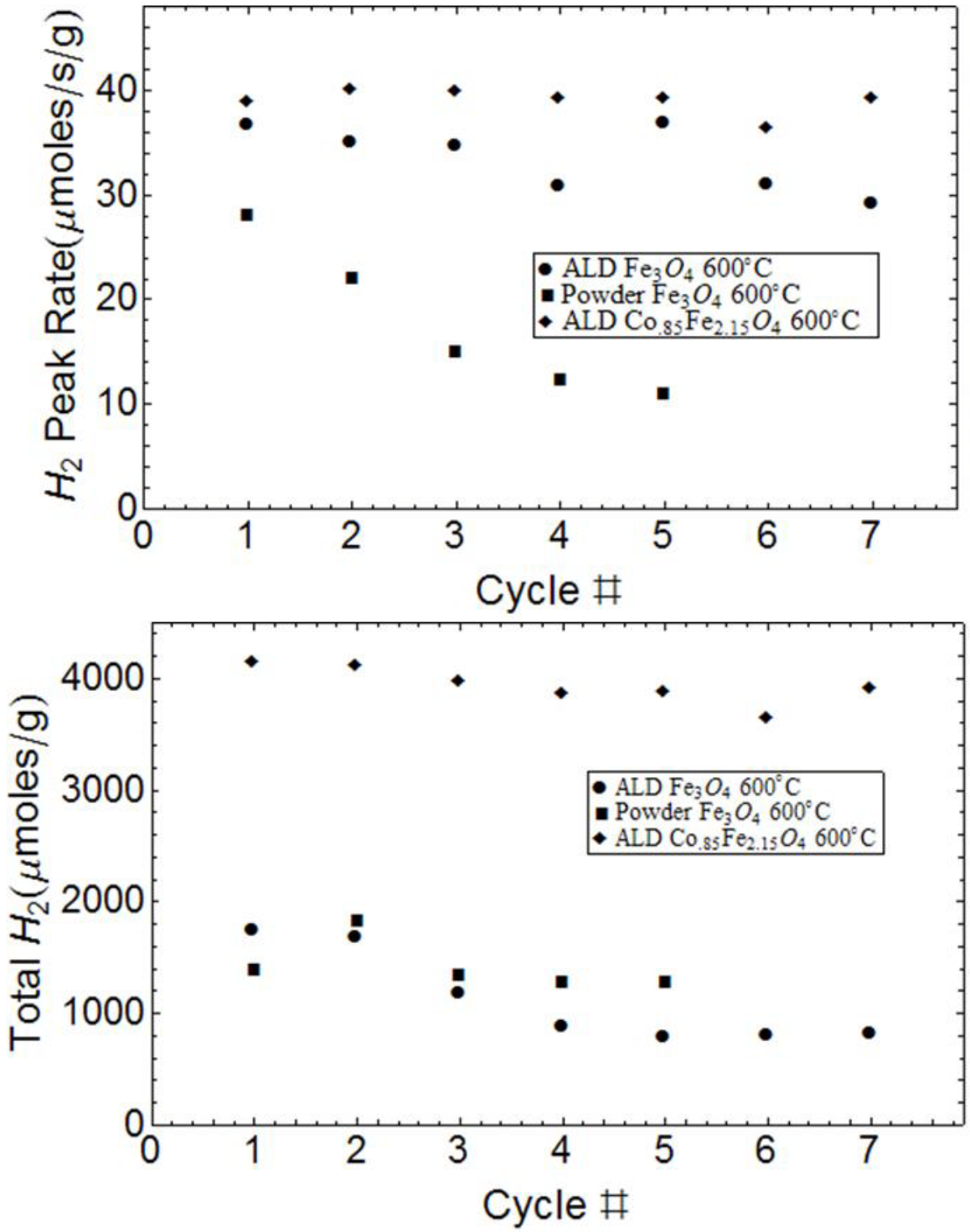

Figure 5-12: a)Peak H_2 rates for various samples after reduction in 1% CO / 1% H_2 / 2% CO_2 in He (500 sccm total) and b) corresponding total H2 yields

5.5 Conclusion

Conformal films of maghemite (γ-Fe_2O_3) and spinel cobalt oxides ($Co_xFe_{3-x}O_4$) were deposited on porous m-ZrO_2 supports by ALD using ferrocene and cobaltocene as the iron and cobalt sources and O_2 as the oxidant. These materials are shown to be highly active in a chemical looping process to split water for the production of H_2. ALD Fe_2O_3 samples reduced in a $CO/H_2/He$ mixture without the presence of an oxidant rapidly deactivated due to the formation of metallic Fe, likely resulting in growth and sintering. However, samples that were reduced with the addition of CO_2 exhibited remarkably better behavior. *In situ* XRD results indicated that ALD samples of Fe_2O_3 were reduced to Fe^{2+}, while $Co_{0.85}Fe_{2.5}O_4$ was reduced to a Co/Fe alloy. Also, Fe_2O_3/ZrO_2 powders reduced in the same manner reduced to Fe^{2+} for short times, but for longer times, metallic Fe was observed. ALD Fe_2O_3 samples reduced in this manner still exhibited signs of deactivation due to a loss of active iron resulting from its incorporation into the ZrO_2 support. Peak rates decreased slightly, but H_2 yields decreased by about 50% after 7 cycles. Cobalt ferrites are advantages compared to Fe_2O_3 samples for several reasons. When cobalt was substituted for iron, the material was reduced to metallic Co and Fe, rather than Fe^{2+}, resulting in much greater H_2 yields (about 4x). Additionally, there were no signs of deactivation. The H_2 reaction rates and yields were nearly identical for 7 redox cycles. When physically mixed Fe_2O_3/ZrO_2 powders were cycled in the same manner as the ALD materials, reaction rates became progressively slower as they were cycled due to sintering and grain growth.

These results suggest that thin films of cobalt ferrites perform remarkably better than their iron oxide analogs and iron oxide powders at producing repeatable and large amounts of hydrogen via chemical looping processes. Additionally, they provide motivation for studying the efficacy of using these materials in other analogous gas-splitting cycles, such as thermal redox

cycles to produce H_2 or CO via H_2O and CO_2 splitting. Further experimental investigation of the mechanism of material sintering and reduction/oxidation chemical kinetics must be performed to understand why these materials are superior to other analogous materials, but nevertheless, the impetus for future work is provided.

5.6 References

[1] Fino D, Russo N, Saracco G, Specchia V. Catalytic removal of NOx and diesel soot over nanostructure spinel-type oxides. Journal of Catalysis 2006;242:38.

[2] Simonsen VLE, Find D, Lilliedal M, Petersen R, Kammer K. Spinels as cathodes for the electrochemical reduction of O-2 and NO. Topics in Catalysis 2007;45:143.

[3] Silva JB, Diniz CF, Lago RM, Mohallem NDS. Catalytic properties of nanocomposites based on cobalt ferrites dispersed in sol-gel silica. Journal of Non-Crystalline Solids 2004;348:201.

[4] Yang Q, Choi H, Al-Abed SR, Dionysiou DD. Iron-cobalt mixed oxide nanocatalysts: Heterogeneous peroxymonosulfate activation, cobalt leaching, and ferromagnetic properties for environmental applications. Applied Catalysis B-Environmental 2009;88:462.

[5] Uddin MA, Tsuda H, Wu SJ, Sasaoka E. Catalytic decomposition of biomass tars with iron oxide catalysts. Fuel 2008;87:451.

[6] Lee JY, Lee DW, Lee KY, Wang Y. Cr-free Fe-based metal oxide catalysts for high temperature water gas shift reaction of fuel processor using LPG. Catalysis Today 2009;146:260.

[7] Baldychev I, Vohs JM, Gorte RJ. The effect of thermodynamic properties of zirconia-supported Fe3O4 on water-gas shift activity. Applied Catalysis a-General 2009;356:225.

[8] Yoon TJ, Lee W, Oh YS, Lee JK. Magnetic nanoparticles as a catalyst vehicle for simple and easy recycling. New Journal of Chemistry 2003;27:227.

[9] Jin H, Okamoto T, Ishida M. Development of a novel chemical-looping combustion: Synthesis of a looping material with a double metal oxide of CoO-NiO. Energy & Fuels 1998;12:1272.

[10] Bohn CD, Muller CR, Cleeton JP, Hayhurst AN, Davidson JF, Scott SA, Dennis JS. Production of Very Pure Hydrogen with Simultaneous Capture of Carbon Dioxide using the Redox Reactions of Iron Oxides in Packed Beds. Industrial & Engineering Chemistry Research 2008;47:7623.

[11] Miller JE, Allendorf MD, Diver RB, Evans LR, Siegel NP, Stuecker JN. Metal oxide composites and structures for ultra-high temperature solar thermochemical cycles. Journal of Materials Science 2008;43:4714.

[12] Gokon N, Murayama H, Umeda J, Hatamachi T, Kodama T. Monoclinic zirconia-supported Fe3O4 for the two-step water-splitting thermochemical cycle at high thermal reduction temperatures of 1400-1600 degrees C. International Journal of Hydrogen Energy 2009;34:1208.

[13] Kodama T, Kondoh Y, Yamamoto R, Andou H, Satou N. Thermochemical hydrogen production by a redox system of ZrO2-supported Co(II)-ferrite. Solar Energy 2005;78:623.

[14] Bleeker MF, Kersten SRA, Veringa HJ. Pure hydrogen from pyrolysis oil using the steam-iron process. Catalysis Today 2007;127:278.

[15] Bleeker MF, Veringa HJ, Kersten SRA. Deactivation of iron oxide used in the steam-iron process to produce hydrogen. Applied Catalysis a-General 2009;357:5.

[16] Loutzenhiser PG, Galvez ME, Hischier I, Stamatiou A, Frei A, Steinfeld A. CO2 Splitting via Two-Step Solar Thermochemical Cycles with Zn/ZnO and FeO/Fe3O4 Redox Reactions II: Kinetic Analysis. Energy & Fuels 2009;23:2832.

[17] Weidenkaff A, Nuesch P, Wokaun A, Reller A. Mechanistic studies of the water-splitting reaction for producing solar hydrogen. Solid State Ionics 1997;101:915.

[18] Huang W, Zhou LX, Zeng HZ, Wei XH, Zhu J, Zhang Y, Li YR. Epitaxial growth of the CoFe2O4 film on SrTiO3 and its characterization. Journal of Crystal Growth 2007;300:426.

[19] Echigoya J, Asano W, Yamaguchi A. Microstructure of sputtered CoFe2O4 film. Physica Status Solidi a-Applied Research 2002;191:359.

[20] Bahlawane N, Ngamou PHT, Vannier V, Kottke T, Heberle J, Kohse-Hoinghaus K. Tailoring the properties and the reactivity of the spinel cobalt oxide. Physical Chemistry Chemical Physics 2009;11:9224.

[21] Lie M, Klepper KB, Nilsen O, Fjellvag H, Kjekshus A. Growth of iron cobalt oxides by atomic layer deposition. Dalton Transactions 2008:253.

[22] Hossain MM, Lopez D, Herrera J, de Lasa HI. Nickel on lanthanum-modified gamma-Al2O3 oxygen carrier for CLC: Reactivity and stability. Catalysis Today 2009;143:179.

[23] Zafar Q, Mattisson T, Gevert B. Redox investigation of some oxides of transition-state metals Ni, Cu, Fe, and Mn supported on SiO2 and MgAl2O4. Energy & Fuels 2006;20:34.

[24] Lim BS, Rahtu A, Gordon RG. Atomic layer deposition of transition metals. Nature Materials 2003;2:749.

[25] Rooth M, Lindahl E, Harsta A. Atomic layer deposition of Co3O4 thin films using a CoI2/O-2 precursor combination. Chemical Vapor Deposition 2006;12:209.

[26] Klepper KB, Nilsen O, Fjellvag H. Epitaxial growth of cobalt oxide by atomic layer deposition. Journal of Crystal Growth 2007;307:457.

[27] Klepper KB, Nilsen O, Fjellvag H. Growth of thin films of Co3O4 by atomic layer deposition. Thin Solid Films 2007;515:7772.

[28] de Ridder M, van de Ven PC, van Welzenis RG, Brongersma HH, Helfensteyn S, Creemers C, Van Der Voort P, Baltes M, Mathieu M, Vansant EF. Growth of iron oxide on yttria-stabilized zirconia by atomic layer deposition. Journal of Physical Chemistry B 2002;106:13146.

[29] Nilsen O, Lie M, Foss S, Fjellvag H, Kjekshus A. Effect of magnetic field on the growth of alpha-Fe2O3 thin films by atomic layer deposition. Applied Surface Science 2004;227:40.

[30] Lie M, Fjellvag H, Kjekshus A. Growth of Fe2O3 thin films by atomic layer deposition. Thin Solid Films 2005;488:74.

[31] Bachmann J, Jing J, Knez M, Barth S, Shen H, Mathur S, Gosele U, Nielsch K. Ordered iron oxide nanotube arrays of controlled geometry and tunable magnetism by atomic layer deposition. Journal of the American Chemical Society 2007;129:9554.

[32] Rooth M, Johansson A, Kukli K, Aarik J, Boman M, Harsta A. Atomic layer deposition of iron oxide thin films and nanotubes using ferrocene and oxygen as precursors. Chemical Vapor Deposition 2008;14:67.

[33] Scheffe JR, Frances A, King DM, Liang XH, Branch BA, Cavanagh AS, George SM, Weimer AW. Atomic layer deposition of iron(III) oxide on zirconia nanoparticles in a fluidized bed reactor using ferrocene and oxygen. Thin Solid Films 2009;517:1874.

[34] King DM, Spencer JA, Liang X, Hakim LF, Weimer AW. Atomic layer deposition on particles using a fluidized bed reactor with in situ mass spectrometry. Surface & Coatings Technology 2007;201:9163.

[35] Leskela M, Ritala M. Atomic layer deposition (ALD): from precursors to thin film structures. Thin Solid Films 2002;409:138.

[36] Chernyshova IV, Hochella MF, Madden AS. Size-dependent structural transformations of hematite nanoparticles. 1. Phase transition. Physical Chemistry Chemical Physics 2007;9:1736.

[37] Gehring AU, Fischer H, Louvel M, Kunze K, Weidler PG. High temperature stability of natural maghemite: a magnetic and spectroscopic study. Geophysical Journal International 2009;179:1361.

[38] Navrotsky A, Mazeina L, Majzlan J. Size-driven structural and thermodynamic complexity in iron oxides. Science 2008;319:1635.

[39] Sakurai S, Namai A, Hashimoto K, Ohkoshi S. First Observation of Phase Transformation of All Four Fe2O3 Phases (gamma -> epsilon -> beta -> alpha-Phase). Journal of the American Chemical Society 2009;131:18299.

[40] Jacintho GVM, Brolo AG, Corio P, Suarez PAZ, Rubim JC. Structural Investigation of MFe2O4 (M = Fe, Co) Magnetic Fluids. Journal of Physical Chemistry C 2009;113:7684.

[41] Garcia FL, de Resende VG, De Grave E, Peigney A, Barnabe A, Laurent C. Iron-stabilized nanocrystalline ZrO2 solid solutions: Synthesis by combustion and thermal stability. Materials Research Bulletin 2009;44:1301.

[42] Galvita V, Sundmacher K. Cyclic water gas shift reactor(CWGS) for carbon monoxide removal from hydrogen feed gas for PEM fuel cells. Chemical Engineering Journal 2007;134:168.

CHAPTER 6 A SPINEL FERRITE/HERCYNITE WATER-SPLITTING REDOX CYCLE

6.1 Abstract

Cobalt ferrites are deposited on Al_2O_3 substrates via atomic layer deposition, and the efficacy of using these in a ferrite water splitting redox cycle to produce H_2 is studied. Experimental results are coupled with thermodynamic modeling, and results indicate that $CoFe_2O_4$ deposited on Al_2O_3 is capable of being reduced at lower temperatures than $CoFe_2O_4$ (200^oC-300^oC) due to a reaction between the ferrite and substrate to form $FeAl_2O_4$. Although the reaction of $FeAl_2O_4$ and H_2O is not as thermodynamically favorable as that of FeO and H_2O, it is shown to be capable of splitting H_2O to produce H_2 if non-equilibrium conditions are maintained. Significant quantities of H_2 are produced at reduction temperatures of only 1200 ^oC, whereas, $CoFe_2O_4$ produced little or no H_2 until reduction temperatures of 1400 ^oC. $CoFe_2O_4/Al_2O_3$ was capable of being cycled at 1200 ^oC reduction/1000 ^oC oxidation with no obvious deactivation.

6.2 Introduction

Solar thermal water splitting to produce hydrogen is a particularly promising technology as it has theoretical maximum system efficiencies of between 65-80% and solar to hydrogen efficiencies of about 20% [1, 2]. Additionally, hydrogen is an ideal energy carrier as it has the highest specific energy density of all conventional fuels and can be generated from renewable sources[3]. One process for renewable hydrogen generation is solar water splitting using metal oxide redox cycles[4-6]. Ferrites of the form $M_xFe_{3-x}O_4$ (where M is generally Co[7, 8], Ni[9-11], Mn[12-14], Zn[15-17], or Fe[9, 18-20]) have been shown to be capable of splitting water to generate hydrogen using solar thermal energy according to the redox reaction shown below:

$$M_xFe_{3-x}O_4 + \ thermal\ energy \rightarrow (3-x)FeO + xMO + \frac{1}{2}O_2 \quad \{T > 1673\ K\} \qquad \mathbf{6-1})$$

$$H_2O + (3-x)FeO + xMO \rightarrow M_xFe_{3-x}O_4 + \ H_2 \quad \{T < 1673\ K\} \qquad \mathbf{6-2})$$

The ferrite is thermally reduced in the first, high temperature step (1400 – 1600 ^{o}C), and oxygen is evolved. In the second lower temperature step (900 – 1100 ^{o}C), the reduced ferrite is reacted with steam to generate H_2 and re-oxidize the ferrite to its original state. Thus, the only net inputs are H_2O and thermal energy, and the only net outputs are H_2 and O_2. This process is advantageous to direct water splitting as it operates at much lower temperatures and O_2 and H_2 are generated in separate steps, eliminating the need for high temperature separation of product gases[5]. Cobalt and nickel ferrites are especially promising as they have favorable thermodynamic properties (i.e. low decomposition temperatures (>1400 ^{o}C) and high melting points (≈ 1550 ^{o}C) [21], and have been effectively utilized experimentally by several researchers [7-9, 11].

These cycles have been studied using bulk powders that were synthesized by solid state synthesis[12, 22-24], coprecipitation[8], or other analogous processes. However, it has been observed that it is not feasible to cycle bulk powders due to high temperature sintering which results in a loss of active surface area[11, 25]. Therefore, synthesis techniques have been employed in which ferrites were deposited on substrates such as ZrO_2[9, 11], YSZ[8, 18], and SiC[13, 14], with the idea being that surface area would remain unchanged through the high temperature cycling. This has been an effective means of maintaining cyclical stability of the ferrites. Kodama *et. al.* has observed greater cyclical stability and more H_2 production when depositing Ni, Co, and Fe ferrites on ZrO_2 and YSZ supports [7, 11, 18]. They observed that Fe^{2+} forms a solid solution with the substrate during thermal reduction and could be subsequently oxidized to reform the ferrite. Additionally, x and M in $M_xFe_{3-x}O_4$ affected the reported conversions.

One substrate that has yet to be studied in detail is Al_2O_3, because it is known that iron oxide reacts with Al_2O_3 to form hercynite ($FeAl_2O_4$) at elevated temperatures [26, 27]. As a result, it has been deemed undesirable to deposit ferrites on Al_2O_3 because it was thought that this would deactivate the ferrite due to undesired products being formed. However, the reaction of Al_2O_3 with $M_xFe_{3-x}O_4$ results in the evolution of O_2 from the reduction of Fe^{3+} to Fe^{2+}. According to the literature, this reaction occurs in air with Fe_3O_4 at temperatures as low as 1320 ^oC, which is lower than temperatures at which iron reduction occurs in $M_xFe_{3-x}O_4$ in inert atmospheres[21, 26]. Thermal reduction in air is more difficult than in an inert environment because an inert environment dilutes the reaction products (O_2), forcing the equilibrium to the right[21]. Therefore, it would be expected that the reduction of a ferrite in the presence of Al_2O_3 in an inert environment would occur at even lower temperatures than when in air, and much lower than reduction of a ferrite not exposed to Al_2O_3.

In light of this evidence, we deposit cobalt ferrites ($CoFe_2O_4$) on Al_2O_3 supports via atomic layer deposition (ALD) to study the feasibility of using these materials in a new two-step thermochemical water splitting cycle. This cycle is illustrated in the redox reaction shown below:

$$CoFe_2O_4 + 3\,Al_2O_3 + Thermal\ Energy \rightarrow CoAl_2O_4 + 2\,FeAl_2O_4 + 0.5\,O_2 \qquad \mathbf{6-3})$$

$$CoAl_2O_4 + 2FeAl_2O_4 + H_2O \rightarrow CoFe_2O_4 + 3Al_2O_3 + H_2 \qquad \mathbf{6-4})$$

We observe significantly lower decomposition temperatures (200 ^oC to 300 ^oC) for ferrites deposited on Al_2O_3 compared to bulk coprecipitated powders. Additionally, we successfully generate H_2 with these materials at upper operating temperatures of 1200 ^oC, whereas negligible H_2 is formed using ferrites that are not supported on Al_2O_3 at these temperatures. We couple experimental results with thermodynamic modeling performed using FactSage, and find that thermodynamics agrees very well with our experimental results.

6.3 Materials and Methods

6.3.1 ALD Synthesis

Multilayers of iron(III) oxide and cobalt(II) oxide are deposited onto porous Al_2O_3 substrates via ALD in alternating doses. Iron(III) oxide deposition consists of dosing ferrocene (99% purity acquired from Alfa Aesar®) and high purity oxygen (99.9%) in alternate doses into the reactor at 450 ^oC. Cobalt(II) oxide deposition is performed in an identical manner to that of iron(III) oxide, with the exception that cobaltocene, rather than ferrocene, is used. Details of the reactor configuration have been described elsewhere [28]. The ALD chemistries are measured in situ via mass spectrometry.

6.3.2 Porous Al_2O_3 Synthesis

Porous Al_2O_3 supports were synthesized by combining a 1:1 volume ratio of poly(methyl methacrylate) (PMMA) and Al_2O_3 nanoparticles (Sigma Aldrich®,<50nm). The mixture is ball-milled using ZrO_2 milling media for 24 hours in order to ensure homogeneous mixing. The resulting mixture is then hard-pressed at 20000 pounds. It is then heated to 700 ^oC in air in a ZrO_2 crucible for 60 minutes to burn out the PMMA, leaving a porous structure, and finally heated to 1400 ^oC in N_2 for two hours.

6.3.3 Co-Precipitation Synthesis

The cobalt ferrite precursor was precipitated from appropriate molar amounts of iron and cobalt nitrates by addition to NH_4OH at 60 ^oC. The solid was then washed and dried and calcined at 1100 ^oC in air. Once calcined, the powder was mixed with ZrO_2 in a 1:3 mass ratio of ferrite to ZrO_2.

6.3.4 Thermal Cycling

Samples were cycled in a high temperature horizontal tube furnace (CM furnace, model 1630) as shown in Supplemental Figure 6-13. The sample is placed in a ZrO_2 boat within a ¾ inch inner diameter

alumina reaction tube. High purity N_2 is delivered into the reactor at a flowrate of 200 sccm using electronic mass flow controllers in conjunction with Labview®. Water is delivered at a flowrate of 0.5 ml/min using a syringe pump. The end of the capillary is placed in a vaporizer at 200 ^oC in order to generate steam. A cold trap is placed at the outlet of the reactor in order to condense any vaporous H_2O. All outlet gases are monitored after the cold trap using a Stanford Research Systems QMS 100 series residual gas analyzer. The mass spectrometer is calibrated by flowing various mixtures of high purity H_2 and O_2 (1% in N_2) calibration gases in conjunction with high purity N_2. Reduction consists of purging the furnace of air and then heating the sample to the desired temperature (1200 ^oC-1500 ^oC) at 20 ^oC/minute in N_2. Oxidation consists of reducing the temperature to 1000 ^oC after thermal reduction, and flowing H_2O and N_2 for 60 minutes.

6.3.5 Thermodynamic Analysis

Thermodynamic calculations are performed using the thermodynamics software package, FactSage version 6.0. This was shown to be an effective method for predicting phases and H_2 generation by Allendorf et. al., as modeling calculations agreed well with their experimental results and in the literature[21]. The inclusion of solution phases with species was shown to have a significant impact upon the results. In these calculations, we are including the species and solution phases shown in Table 6-1. All of the calculations are performed at 1 atm. Thermal reduction calculations are performed with a dilution of 10000 moles of Ar, and unless specified otherwise, 10000 moles H_2O are used in H_2O oxidation calculations. Because experiments occur under non-equilibrium conditions, this dilution was chosen in order to represent these conditions as best we could. Higher dilutions drive the chemical equilibrium of the reaction to occur at lower temperatures, and therefore, if a higher dilution factor is chosen, the calculated decomposition temperature is expected to decrease.

Table 6-1: Species Included in Thermodynamic Calculations

Gases	Pure Liquids	Pure Solids	Solution Phases
Ar	Al_2O_3	Al_2O_3	spinel
O_2	FeO	$FeAl_2O_4$	-$M_xFe_{3-x}O_4$
O	CoO	FeO (wustite)	-$M_xCo_{3-x}O_4$
Co	Fe_3O_4	CoO	-$M_xAl_{3-x}O_4$
FeO	Co	$Al_2Fe_2O_6$	-MO_4
Fe	Fe	Fe_3O_4 (magnetite)	
AlO	Al	Fe_2O_3 (hematite)	metal oxides (MeO)
AlO_2	CoAl	Co	-FeO, Fe_2O_3, Al_2O_3, CoO
O_3		(CoO)(Fe_2O_3)	
Al		Fe	slag
$(AlO)_2$		Co_3O_4	- FeO, Fe_2O_3, Al_2O_3, CoO
Al_2O		CoAl	
Al_2		Al	corundum (M_2O_3)
		$CoAl_3$	-Fe_2O_3, Al_2O_3
		$FeAl_3$	
		Co_2Al_5	M = Fe, Co, or Al

6.3.6 Material Characterization

Visual inspection of the films is carried out using a 200 kV JEOL 2010F Schottky field emission high resolution transmission electron microscope (HRTEM). Film composition is determined via energy dispersive x-ray (EDX) analysis, X-ray diffraction (XRD, Scintag PAD5 Powder Diffractometer, CuKα radiation, λ = 1.5406Å), and induced coupled plasma – atomic emission spectroscopy (ICP-AES). XRD analysis is performed using a scan rate of 2 degrees/minute and step size of 0.2 degrees. ICP-AES is used as a means to quantify the mass loading and relative molar amounts of Co and Fe in $Co_xFe_{3-x}O_4$.

6.4 Results and Discussion

6.4.1 Material Characterization

ALD is governed by self limiting chemistry, and as a result nano-scale films are capable of being synthesized with relative ease [29-33]. This is observed in the STEM image shown in Figure 6-1a. The

bright layers surrounding the larger, darker areas are the cobalt ferrite ALD film, as verified by EDX analysis. It appears that the film is uniform around the Al_2O_3 core, and is on the order of 5nm. EDX analysis of the bulk structure, shown in Figure 6-1b, indicates that the predominant element present is Al. Co and Fe have x-ray counts that are an order of magnitude less than Al. However, EDX analysis of the surface, shown in Figure 6-1c, confirms that it is composed of a much higher concentration of Fe and Co than the bulk, as their x-ray counts are nearly on the order of Al. This is confirmation that a thin film composed of Fe and Co is deposited on the surface of the Al_2O_3 support. Powder XRD analysis confirms that the as-deposited film had a spinel structure, indicative of $Co_xFe_{3-x}O_4$, as shown in Supplemental Figure 6-14.

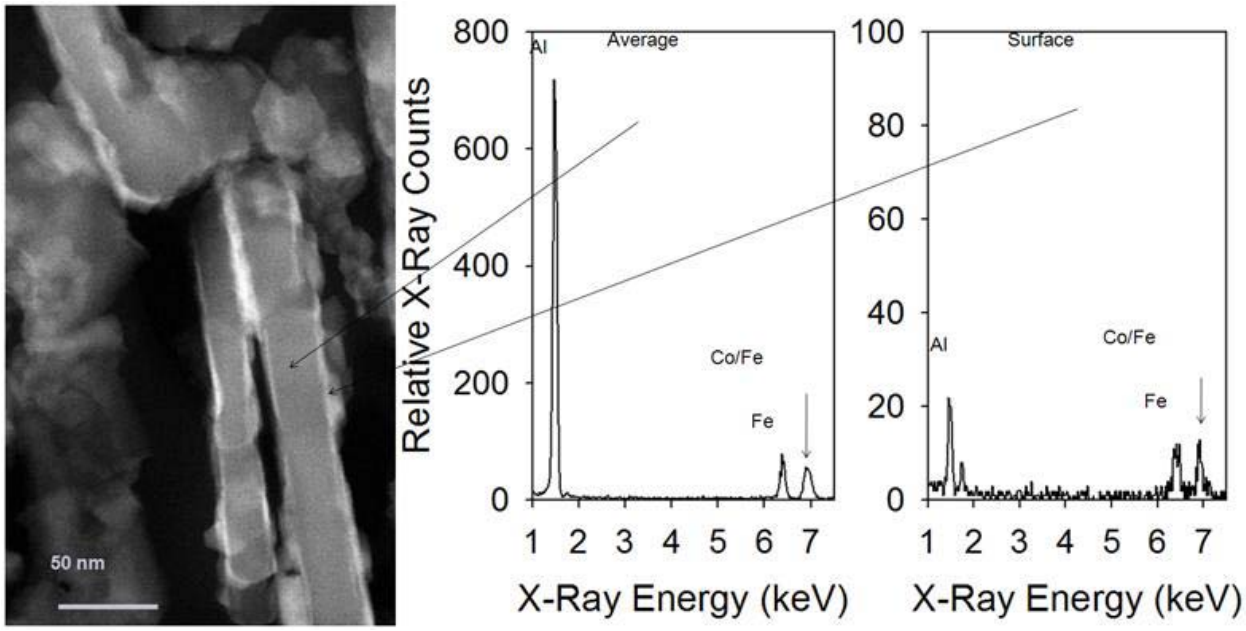

Figure 6-1: a) STEM image of as-deposited $CoFe_2O_4$ ALD film on Al_2O_3, and b) EDX analysis of the bulk (left) and surface (right).

6.4.2 Thermal Reduction

Previous literature has indicated that Fe^{3+}, in Fe_3O_4, is reduced at temperatures of 1320 ^oC in air in the presence of Al_2O_3, which is lower than traditional ferrite cycles [26]. Thermodynamic modeling is

performed in order to understand how these materials reduce in an inert environment, and the influence that Co has in $Co_xFe_{3-x}O_4$. Modeling is also performed using traditional ferrites without Al_2O_3, in a manner analogous to Allendorf, *et. al.* [21]. Experiments were then conducted in order to directly compare experimental results with thermodynamic modeling. Thermodynamic modeling showing O_2 evolution as a function of temperature for Fe_3O_4 and $CoFe_2O_4$, both with and without the presence of Al_2O_3, is shown in Figure 6-2. $CoFe_2O_4$ + 5 Al_2O_3 is predicted to begin reducing at temperatures below 800 ^oC, and after 1000 ^oC, the degree of reduction is expected to increase greatly. This is in contrast to $CoFe_2O_4$, in which O_2 does not begin to evolve to a significant extent until after 1200 ^oC.

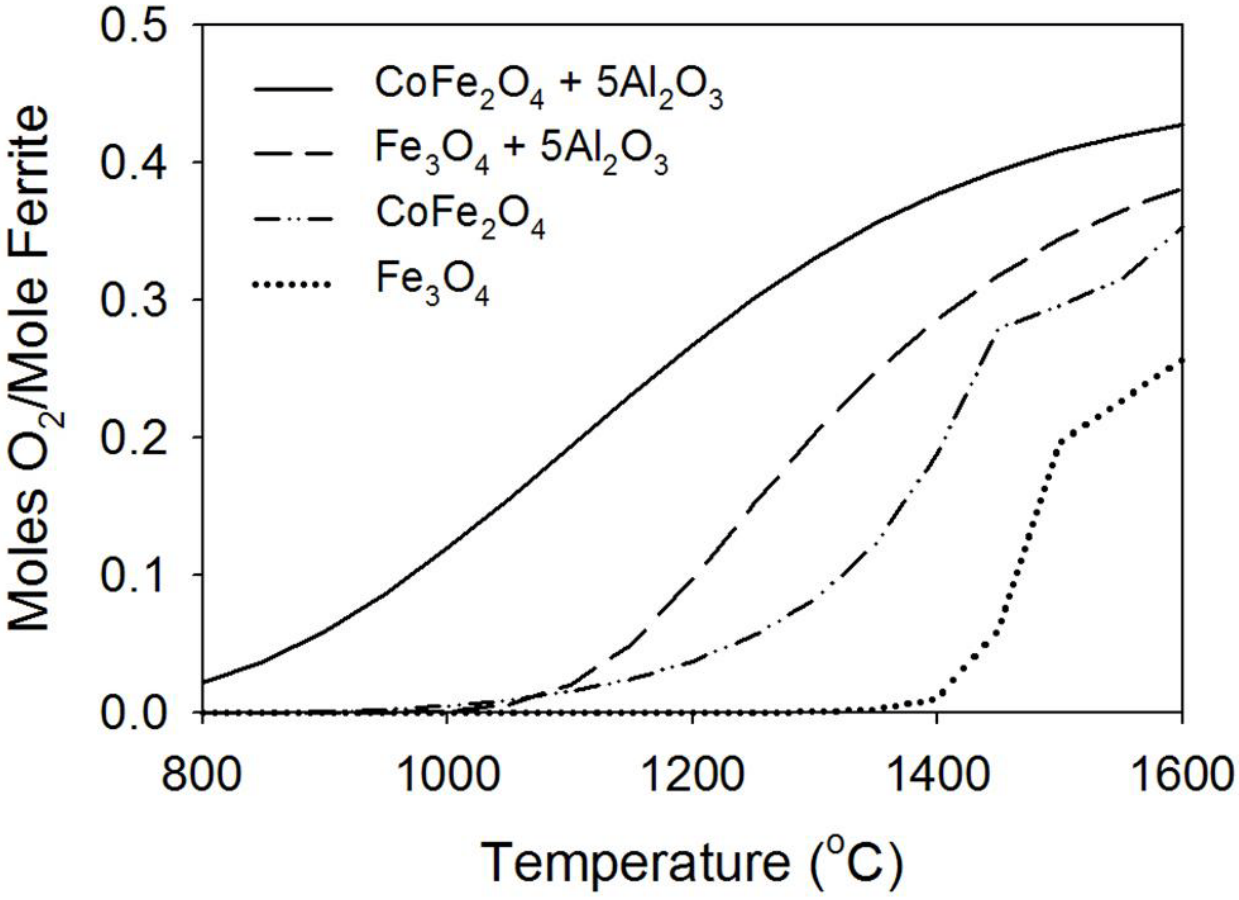

Figure 6-2: Total O_2 evolved per mole of ferrite as a function of temperature - equilibrium calculations

Additionally, Fe_3O_4 + 5 Al_2O_3 begins to evolve O_2 around 1100 ^oC, whereas Fe_3O_4 does not until 1400 ^oC. Based on these results, it is clear that the trend in reduction temperature is as follows: $CoFe_2O_4$ + $5Al_2O_3$< Fe_3O_4 + $5Al_2O_3$< $CoFe_2O_4$<Fe_3O_4. Experimental results corroborate these observations, and indicate that $CoFe_2O_4$ on Al_2O_3 reduces at a lower temperature than $CoFe_2O_4$ deposited on ZrO_2, as seen in Figure 6-3. O_2 begins to evolve at 950 ^oC for $CoFe_2O_4/Al_2O_3$ and a total of 0.17 moles is evolved. In contrast, $CoFe_2O_4/ZrO_2$ begins to reduce at 1200 ^oC, and only releases 0.105 moles O_2. In both cases, less O_2 is evolved than thermodynamically predicted at 1400 ^oC. This is likely due to kinetic limitations, as O_2 is still evolving from both samples after 10000s. These results confirm that cobalt ferrites deposited on Al_2O_3 are capable of being reduced at lower temperatures than those deposited on ZrO_2.

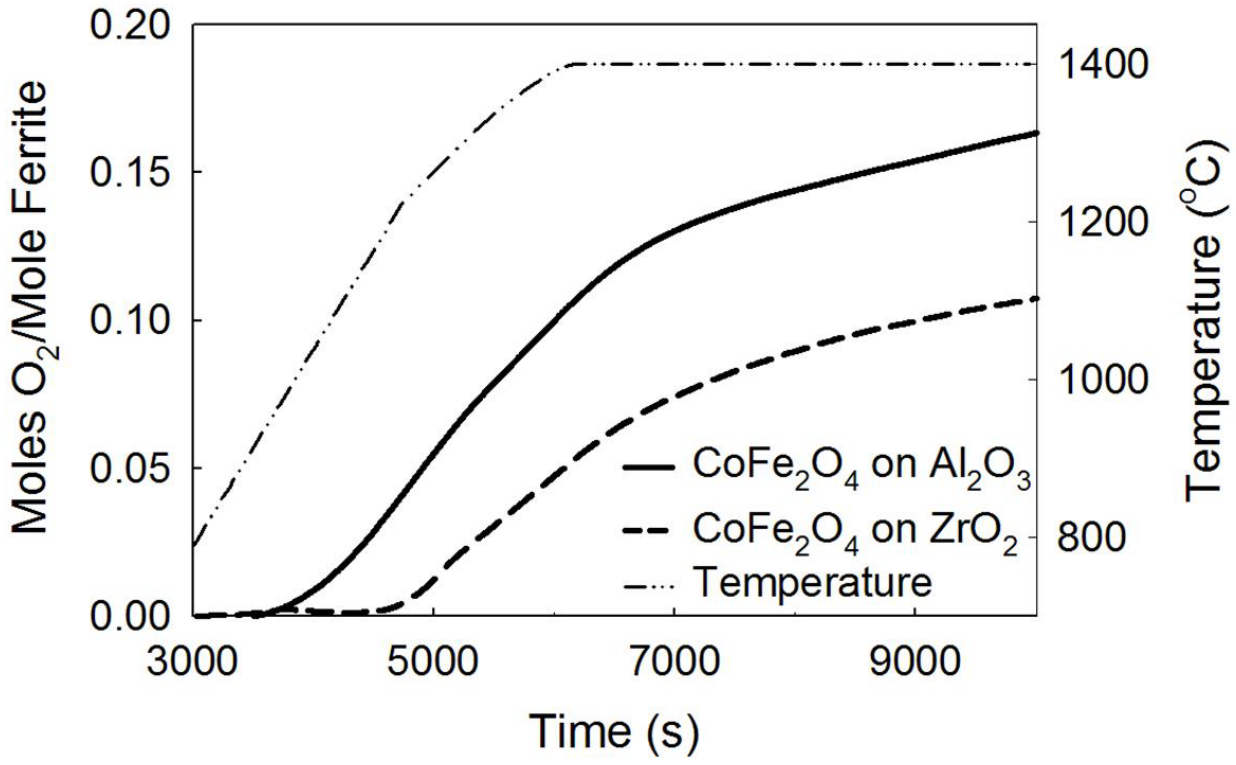

Figure 6-3: Total O_2 evolved per mole of ferrite as a function of temperature - experimental results.

The predominant species formed after the reduction of $CoFe_2O_4$ is a metal oxide solid solution (MeO) of FeO, CoO and a small amount of Fe_2O_3, as shown in Figure 6-4. $CoFe_2O_4$ actually exists as a

solid solution of various spinels (Fe_3O_4, $CoFe_2O_4$, $FeCo_2O_4$) under the temperature range considered, and is represented by Spinel in Figure 6-4. It is clear that as the temperature increases past 1200 ^oC, the Spinel phase decreases until it reaches zero moles at 1450 ^oC. At the same time, FeO, CoO and Fe_2O_3 begin to increase and eventually reach a maximum when the Spinel phase is fully decomposed. It should be noted that a significant amount of Fe_2O_3 (Fe^{3+}) is expected to be present under these conditions, which would have a negative impact on the amount of H_2 capable of being generated since less oxidizible iron (Fe^{2+}) is present. Additionally, the decrease in the MeO species after 1500 ^oC results from the presence of a Slag phase. This should be avoided experimentally, as this will result in a significant decrease in active surface area which would result in less H_2 production.

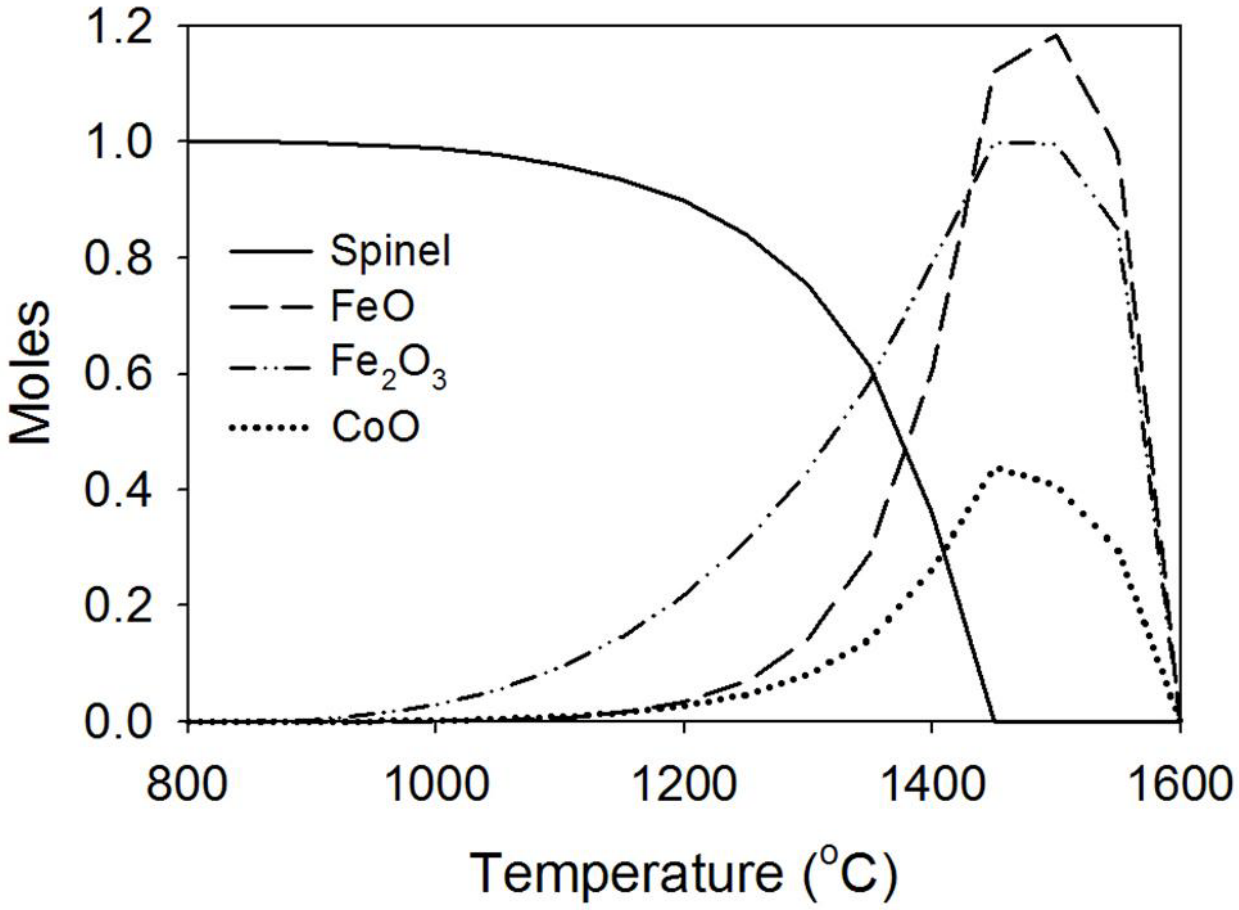

Figure 6-4: Thermodynamic predictions of species present as a function of reduction temperature for $CoFe_2O_4$.

When considering the Spinel solution with $CoFe_2O_4$ and $5Al_2O_3$, it is more complex than only $CoFe_2O_4$. This is because there are other possible species present such as $FeAl_2O_4$, $AlFe_2O_4$, $CoAl_2O_4$, and $AlCo_2O_4$, in addition to the species listed above. Rather than MeO species resulting from thermal decomposition of $CoFe_2O_4$, the reduction species are part of the Spinel solution. Therefore the major components of the Spinel solution are plotted in Figure 6-5, rather than only the total Spinel solution as was done in Figure 6-4.

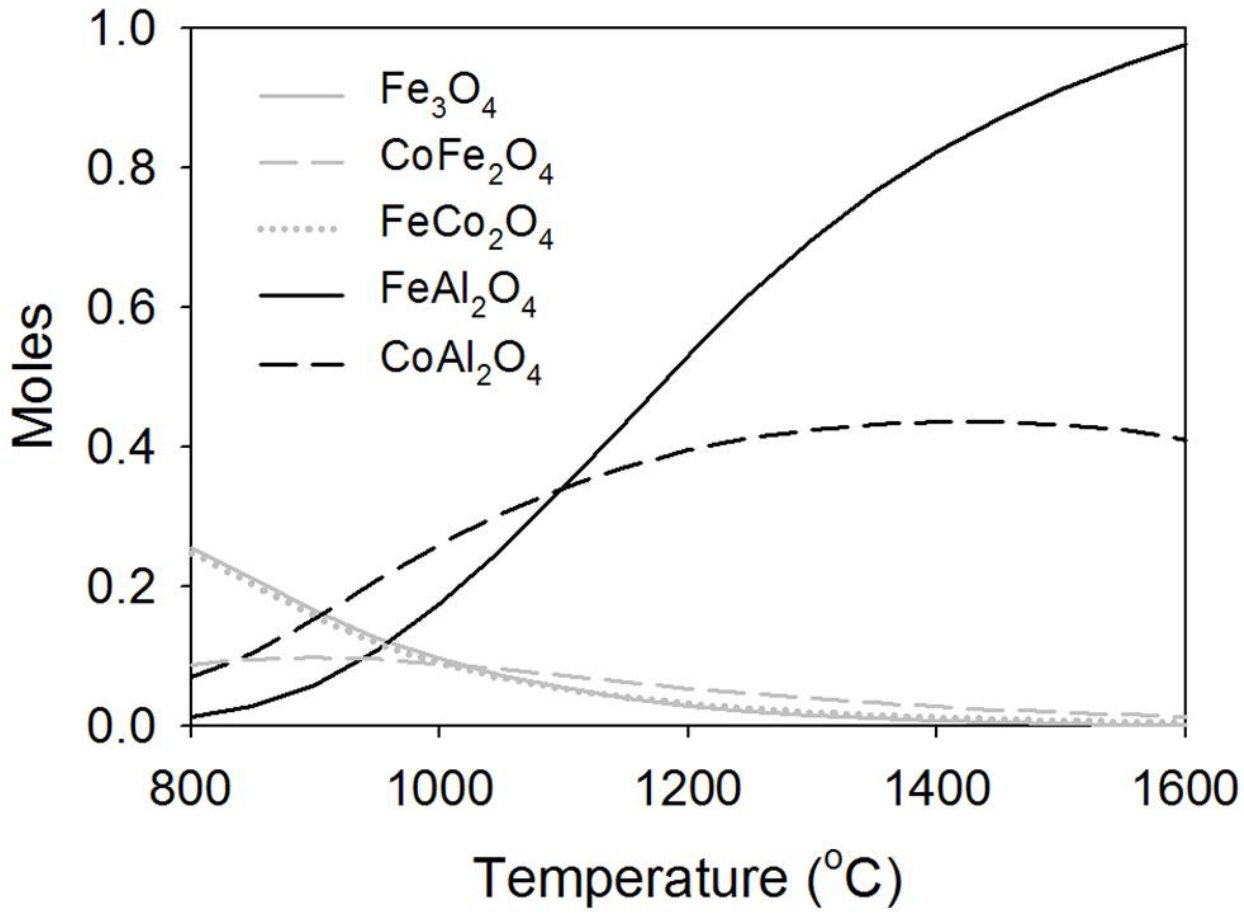

Figure 6-5: Thermodynamic predictions of species present as a function of reduction temperature for $CoFe_3O_4 + 5Al_2O_3$.

As can be seen, the two major components forming as a result of thermal decomposition beginning at 900 ^oC are $FeAl_2O_4$ and $CoAl_2O_4$. These can be thought of as the analogs of the MeO species during $CoFe_2O_4$ decomposition, FeO and CoO, as they are both in the 2+ reduced states. Also, there are no slag phases

that are formed during thermal reduction up to 1600 ^{o}C, as there were with $CoFe_2O_4$ decomposition. *Therefore, high temperature sintering should be less of a problem with ferrites supported on Al_2O_3, as the sintering temperature is generally proportional to the melting temperature.* This is significant, as high temperature sintering occurs frequently in traditional ferrite cycles and has a negative impact on H_2 generation due to a decrease in active surface area. Additionally, material considerations for high temperature solar reactors would be more flexible if the upper operating temperature could be reduced by 200 ^{o}C [34]. These factors make this cycle an attractive alternative to traditional ferrite water splitting thermochemical cycles. However, much is dependent on the capability of this material to split H_2O effectively which will be discussed in the following section.

We have studied the effect of the reduction temperature over the temperature range of 1200 ^{o}C to 1500 ^{o}C. Powder XRD results confirm that at temperatures as low as 1200 ^{o}C the predominant species present is $FeAl_2O_4$, as seen in Figure 6-6a. As the reduction temperature is increased to 1500 ^{o}C, the peak representative of $FeAl_2O_4$ is steadily shifted to a higher 2θ value. We hypothesize that the peak at 1200 ^{o}C is actually representative of a solid solution of $CoFe_2O_4$ and $FeAl_2O_4$, which is predicted thermodynamically at this temperature. As the temperature is increased, the relative percentage of $CoFe_2O_4$ decreases, resulting in the $FeAl_2O_4$ peak shifting to the right. This would be expected, as the standard peak for $FeAl_2O_4$ actually should fall to the right of where it is shown here. The fact that $CoFe_2O_4$ influences the peak position of $FeAl_2O_4$ is not surprising because the peaks fall very close together, as observed from the $CoFe_2O_4$ peak shown in Figure 6-6a. Qualitative evidence that $FeAl_2O_4$ has been formed after thermal reduction at 1200 ^{o}C can be seen from the change in color from black to green, shown in Figure 6-6b. The green color is indicative of $FeAl_2O_4$, indicating that a phase change has occurred from $CoFe_2O_4$ to $FeAl_2O_4$.

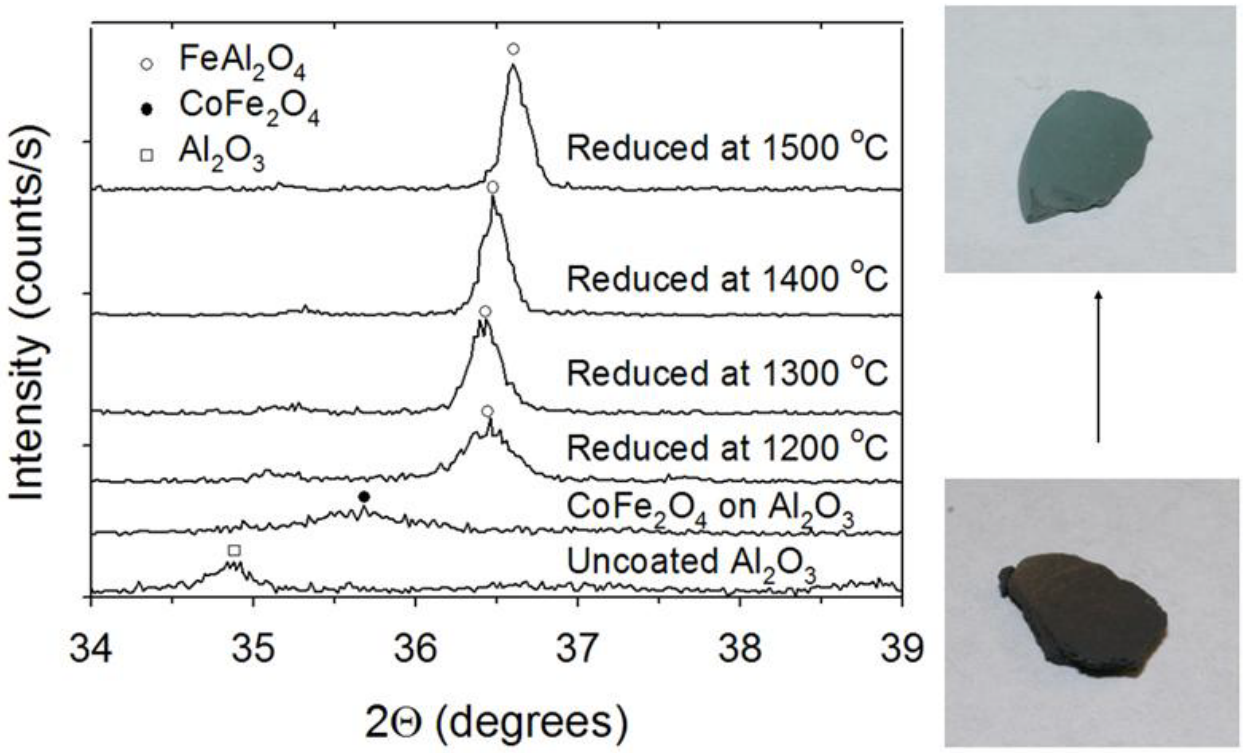

Figure 6-6: a) Powder XRD results of $CoFe_2O_4$ deposited on Al_2O_3 as a function of reduction temperature. b) Color change after reducing sample at 1200 ^oC.

6.4.3 Water Oxidation

Thermodynamic calculations were performed in which the reduction species at 1450 ^oC of both $CoFe_2O_4$ and $CoFe_2O_4/5Al_2O_3$ were exposed to steam. A Gibbs free energy minimization for the H_2O oxidation of FeO and $FeAl_2O_4$ over the temperature range of 700 ^oC to 1200 ^oC indicates that water oxidation with FeO is more favorable than with $FeAl_2O_4$, as shown in Supplemental Figure 6-15. These species were included because they are the reduced species that are oxidized in the water oxidation reaction. In fact, H_2O oxidation of FeO is spontaneous at temperatures below 700 ^oC, whereas it is not spontaneous under any temperatures for $FeAl_2O_4$. Even though oxidation is spontaneous below 700 ^oC, oxidation of FeO is commonly performed at temperatures much greater than 700 ^oC due to enhanced reaction kinetics. These reactions are capable of proceeding at elevated temperatures because the

experiments are not conducted at equilibrium, as it was in the case of the Gibbs free energy minimization calculation. Experimentally, the reactant gases are flowing over the solid reactants and sweep away the product species (H_2), driving the equilibrium of the reaction to the right. This behavior can be seen in Figure 6-7, in which a calculation is performed for the water oxidation of reduced $CoFe_2O_4$ (MeO) and $CoFe_2O_4/5Al_2O_3$ (Spinel/M_2O_3) at 1450 ^oC using two different concentrations of H_2O. When 100 moles H_2O are reacted with MeO, the amount of H_2 generated decreases as the temperature is increased, because the ΔG of the reaction is increasing. When the H_2O is increased to 1000 moles, it has little effect at lower temperatures, because the reaction is thermodynamically spontaneous. Its effect on the amount of H_2 predicted to form does not become noticeable until higher temperatures, due to the fact that the product species (H_2) is more diluted. More equilibrium H_2 is predicted at higher temperatures for 1000 moles H_2O compared to 100 moles.

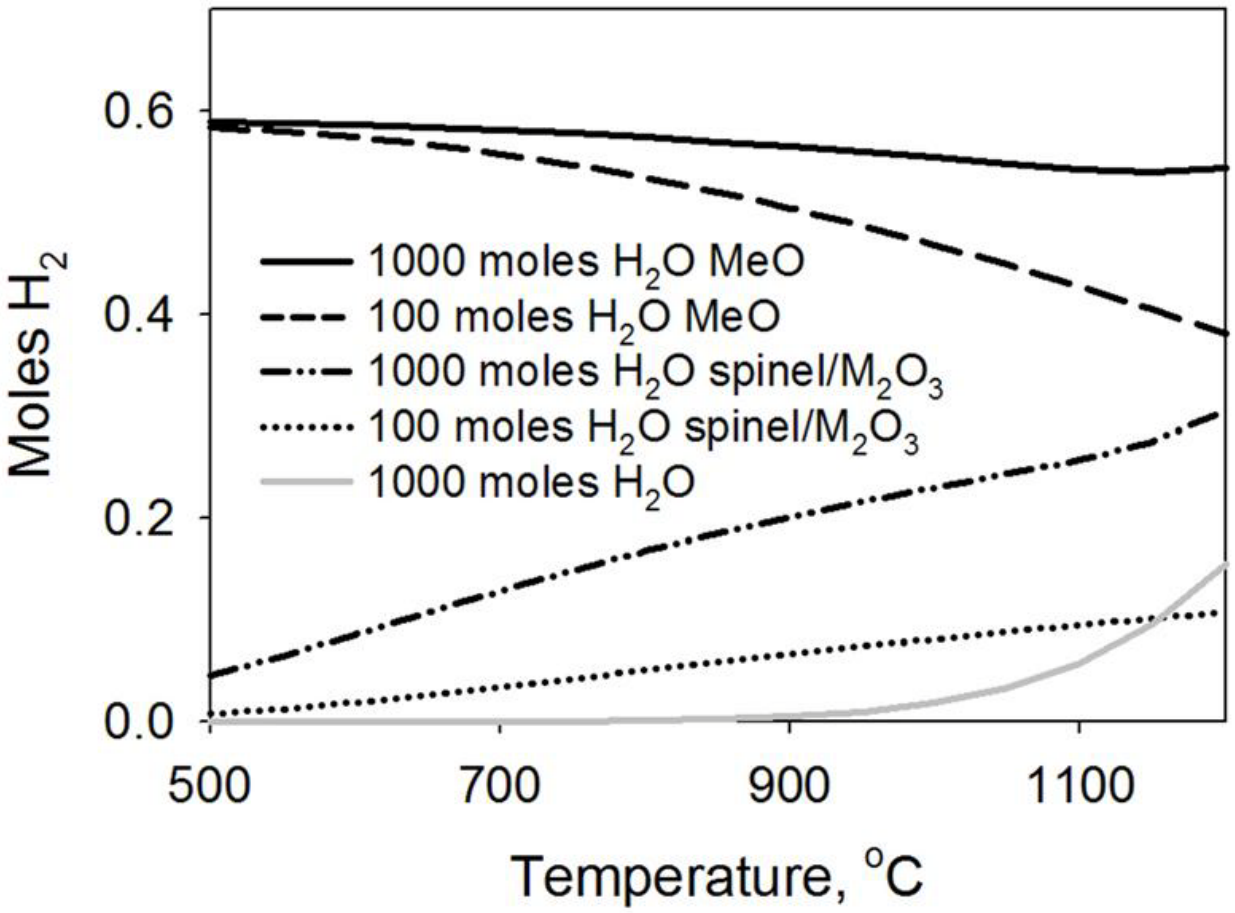

Figure 6-7: Effect of H_2O concentration on the H_2 production as a function of temperature for reduced $CoFe_2O_4$ (black) and reduced $CoFe_2O_4$ + 5 Al_2O_3 (red).

The water concentration has a much greater effect on the reaction of Spinel/M_2O_3 + H_2O, however because the reaction is not thermodynamically spontaneous over any of the temperatures explored. As the concentration is increased from 100 moles to 1000 moles, more H_2 is generated over all temperatures observed, and H_2 increases as a function of temperature. These results indicate that, although water oxidation of $FeAl_2O_4$ is not thermodynamically spontaneous, it is capable of splitting water if the reaction is carried out under non-equilibrium conditions. It should be noted that a small amount of H_2O is expected to be decomposed at temperatures greater than 900 °C, which has an effect on the amount of H_2 observed for each of the curves shown in the Figure 6-7. Therefore, the amount of H_2 generated due to H_2O

reacting with Spinel/M_2O_3 begins to decrease after about 1000 ^oC when accounting for H_2 that is due to water thermally decomposing. *Based on these calculations, it is thermodynamically favorable to perform this reaction near 1000 ^oC with high concentrations of water.*

Water oxidation experiments are conducted using $CoFe_2O_4$ deposited on Al_2O_3 and a coprecipitated $CoFe_2O_4/ZrO_2$ mixture (3:1 mass percent ZrO_2). ZrO_2 is added to alleviate high temperature sintering of the cobalt ferrite. Each of the samples is reduced at temperatures ranging from 1200 ^{o}C to 1500 ^{o}C and subsequently oxidized with steam at 1000 ^{o}C. Reduction and oxidation cycles are carried out in the following order for both samples: 1400 ^{o}C, 1200 ^{o}C, 1300 ^{o}C, 1500 ^{o}C. Samples are not removed from the furnace from one cycle to the next. As seen in Figure 6-8, the amount of H_2 generated increases as the reduction temperature increases for $CoFe_2O_4$ deposited on Al_2O_3. However, there is still a significant amount of H_2 generated at the lowest reduction temperature of 1200 ^{o}C. This is expected, as results from Figure 6-2 predict a significant amount of reduction to occur by 1200 ^{o}C and remain uncompleted even as the temperature surpasses 1500 ^{o}C. Powder XRD results did not confirm the presence of $CoFe_2O_4$ after oxidation, as seen in Supplemental Figure 6-16. However, the peak that is representative of $FeAl_2O_4$ is shifted to the left which is consistent with the powder XRD results of thermally reduced samples in which the peak is shifted to the right at higher reduction temperatures. We hypothesize that this shift is indicative of changes in the concentrations of $CoFe_2O_4$ and $FeAl_2O_4$ in the spinel solution.

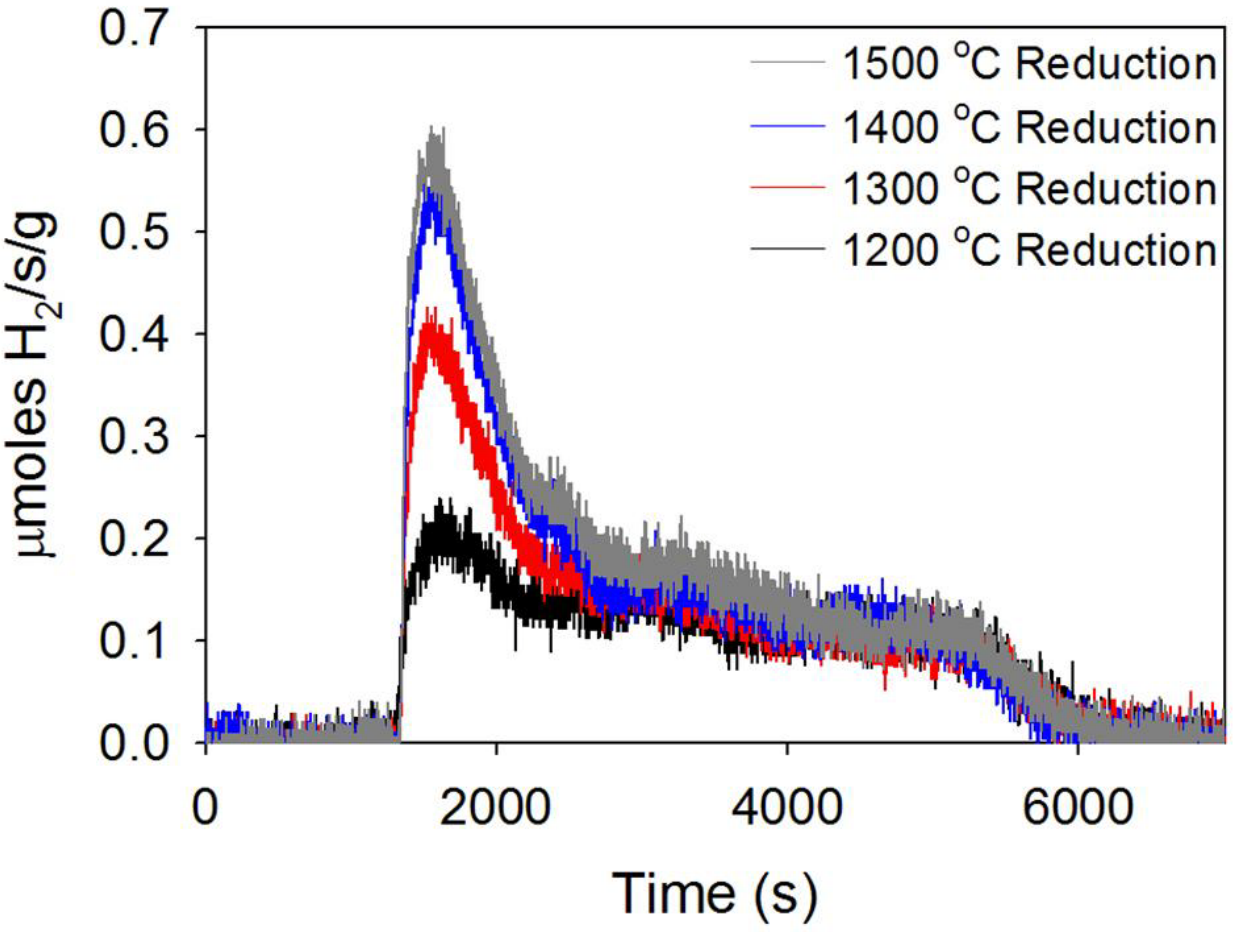

Figure 6-8: H_2 reaction rate as a function of reduction temperature for $CoFe_2O_4$ deposited on Al_2O_3.

The reduction temperature is shown to have a much larger impact on the amount of H_2 produced using the $CoFe_2O_4/ZrO_2$ mixture, as seen in Figure 6- 9. At 1200 ^oC and 1300 ^oC, there is very little H_2 produced. At 1400 ^oC the amount of H_2 generated increases, and finally at 1500 ^oC much more H_2 is produced. It is likely that the amounts of H_2 observed at 1200 and 1300 ^oC were simply due to the reduction at 1400 ^oC because they increase only to the value of its oxidation tail (about 0.05 µmoles H_2/s/g). This behavior is consistent with the thermodynamic results seen in Figure 6-4. At 1400 ^oC, the reduction is only expected to be partially complete, and by 1500 ^oC, all of the $CoFe_2O_4$ is expected to be reduced, resulting in more H_2 generated in the water oxidation step. This observation also agrees very well with Kodama *et. al.* 's

cobalt and nickel ferrite results in which very little H_2 was generated at reduction temperatures of 1300 ^oC, but about 4 times more was generated at 1400 ^oC reduction [11]. Based on these results, it is concluded that the reduced species of $CoFe_2O_4$ on Al_2O_3 (Spinel/ M_2O_3) is capable of reacting with H_2O to produce H_2 at lower reduction temperatures than the reduced species of $CoFe_2O_4$ (MeO).

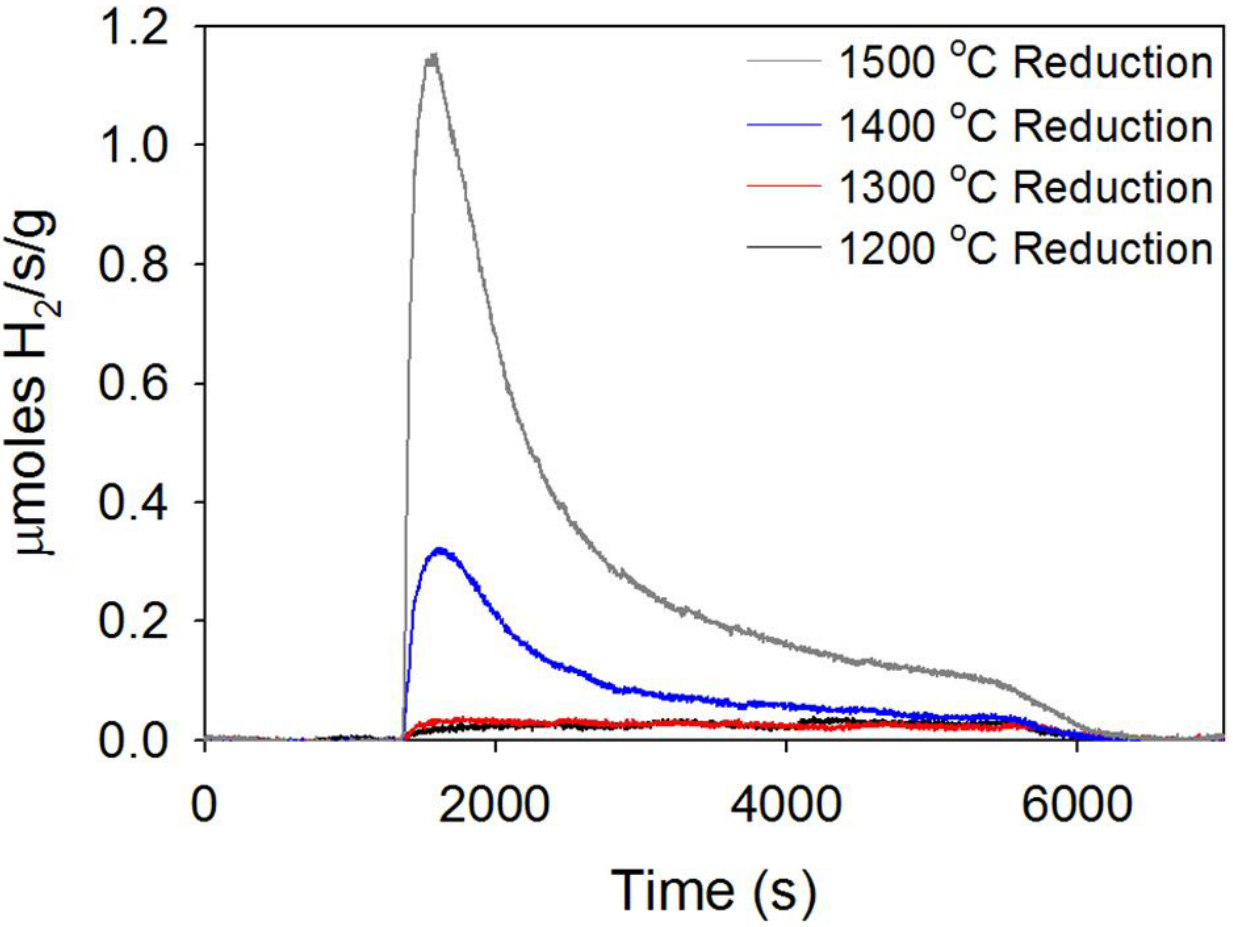

Figure 6-9: H_2 reaction rate as a function of reduction temperature for physically mixed $CoFe_2O_4/ZrO_2$.

Thermodynamic calculations of predicted H_2 production for $CoFe_2O_4/Al_2O_3$ and $CoFe_2O_4$ are consistent with experimental results. Equilibrium species of $CoFe_2O_4/5Al_2O_3$ and $CoFe_2O_4$ are calculated at 1200-1500 ^oC. These species, Spinel/M_2O_3 and MeO respectively, are then exposed to 10000 moles H_2O and the H_2 produced is shown in Figure 6-10. There is a small amount of H_2 produced due to direct

water splitting at this temperature (<0.02 moles per 10000 mole H_2O), and this is accounted for by subtracting this from the amount at equilibrium. As seen in Figure 6-10, 0.0005 moles H_2 is expected to be generated at a reduction temperature of 1200 ^oC for $CoFe_2O_4/Al_2O_3$, and this value increases to 0.0012 moles H_2 at a reduction temperature of 1500 ^oC. $CoFe_2O_4$ on the other hand is expected to produce almost no H_2 at 1200 ^oC and 1300 ^oC. At 1400 ^oC 0.0007 moles H_2 are produced and at 1500 ^oC, 0.00175 moles H_2.

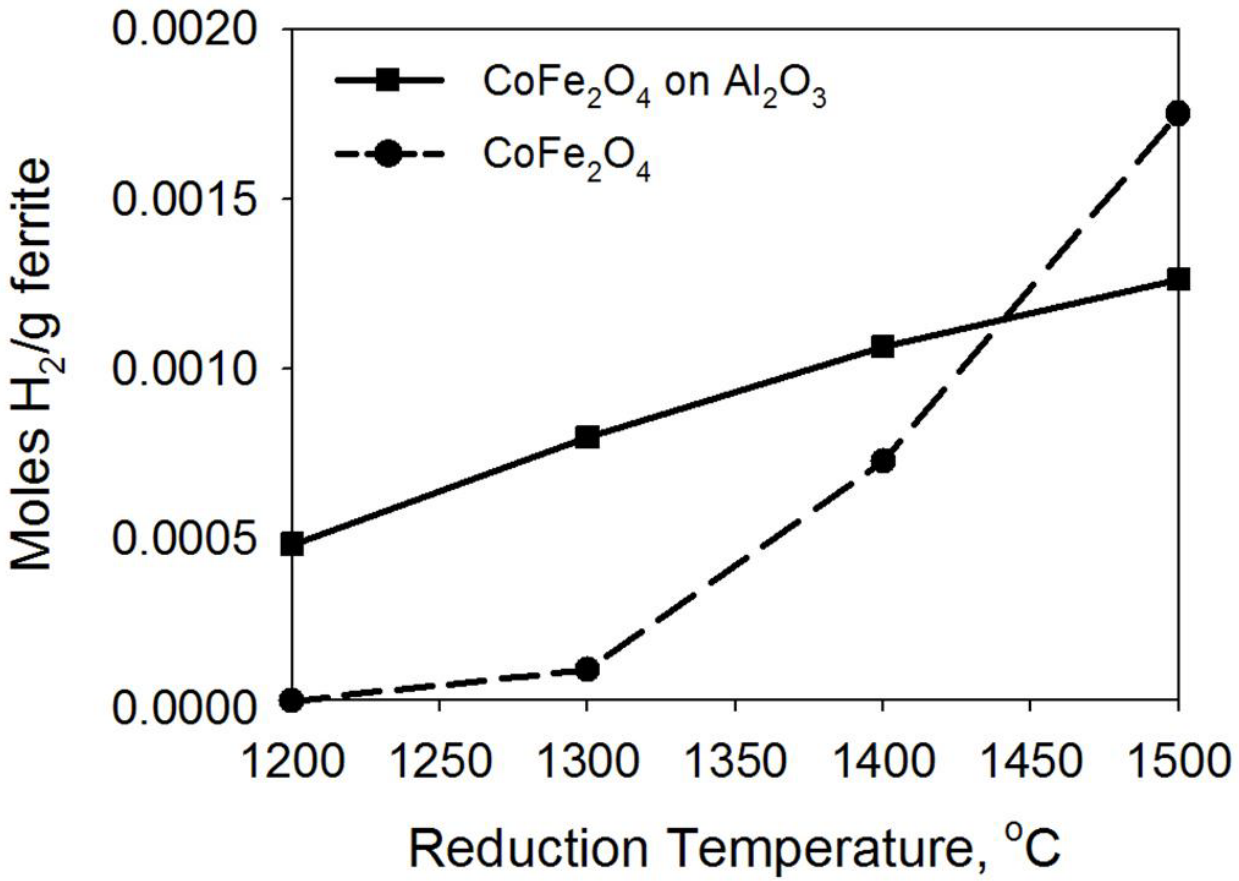

Figure 6-10: Total H_2 produced as a function of reduction temperature - equilibrium calculations.

When compared to experimental data shown in Figure 6-11, the trend is the same. The data in Figure 6-11 are calculated by computing the area of the H_2 production curves in Figure 6-8 and 6-9. A significant amount of H_2 is produced at 1200 ^oC with the $CoFe_2O_4/Al_2O_3$ sample, whereas very little is produced at

up to 1300 °C for only $CoFe_2O_4$. Only at 1500 °C does $CoFe_2O_4$ produce more H_2 than the $CoFe_2O_4/Al_2O_3$ sample.

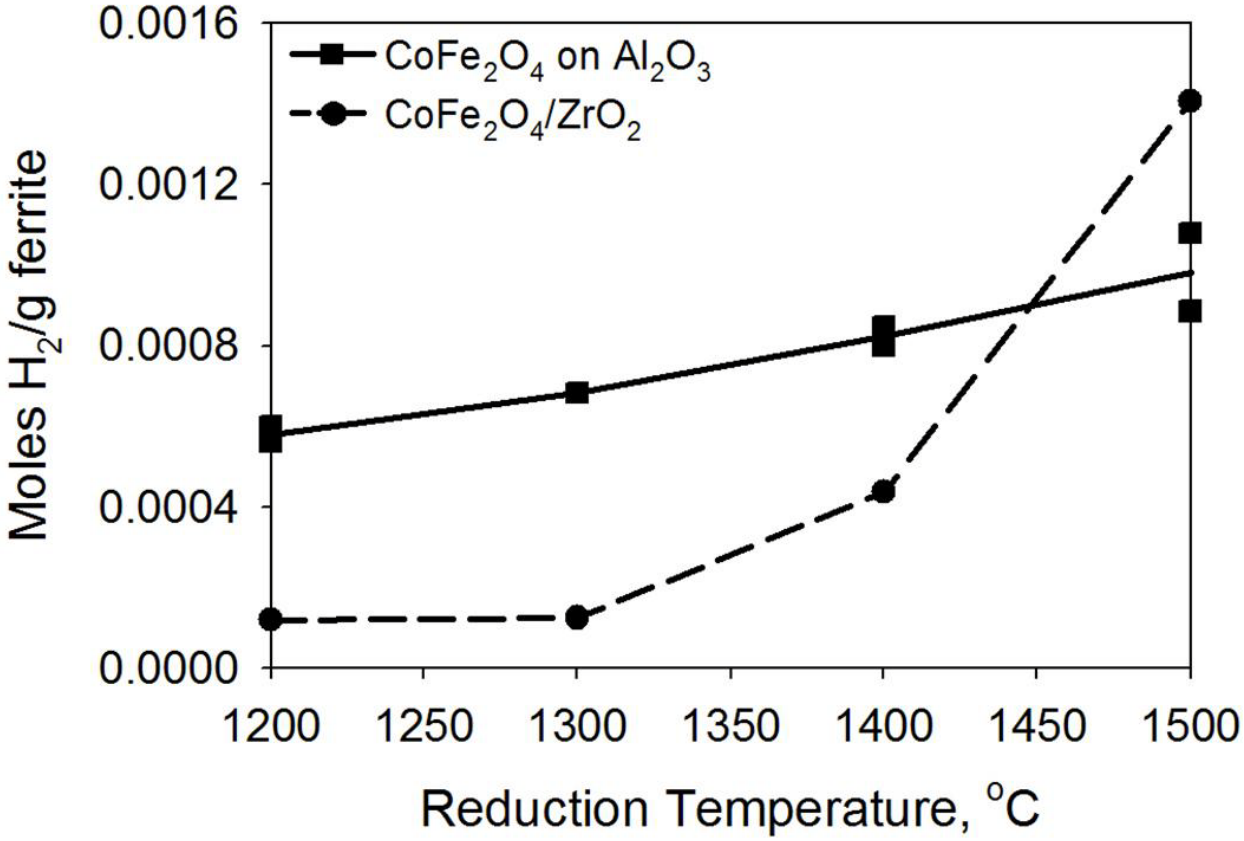

Figure 6-11: Total H_2 produced as a function of reduction temperature - experimental results.

In light of the fact that we were able to thermally reduce $CoFe_2O_4/Al_2O_3$ at temperatures as low as 1200 °C, and subsequently oxidize it with water at 1000 °C, we attempted to thermally cycle it under these conditions to evaluate its thermal stability. The H_2 reaction rates and associated conversions after 1200 °C reductions are shown in Figure 6-12. Conversions were calculated by assuming that 100% conversion is achieved when all of the Fe^{3+} is reduced to Fe^{2+} during thermal reduction, and then all of the Fe^{2+} is reoxidized to Fe^{3+} during water oxidation. The conversion ranges from 14.2% (.000591 moles H_2/g) to 18.7% (.000777 moles H_2/g), with no obvious trend either up or down. Obviously, more cycles need to be performed to determine the efficacy of these materials over hundreds, or even thousands of

cycles. However, these data do provide compelling evidence that these materials can produce significant quantities of H_2 at 1200 ^oC without obvious deactivation. This is 200 ^oC to 300 ^oC lower than where ferrite redox cycles are typically performed.

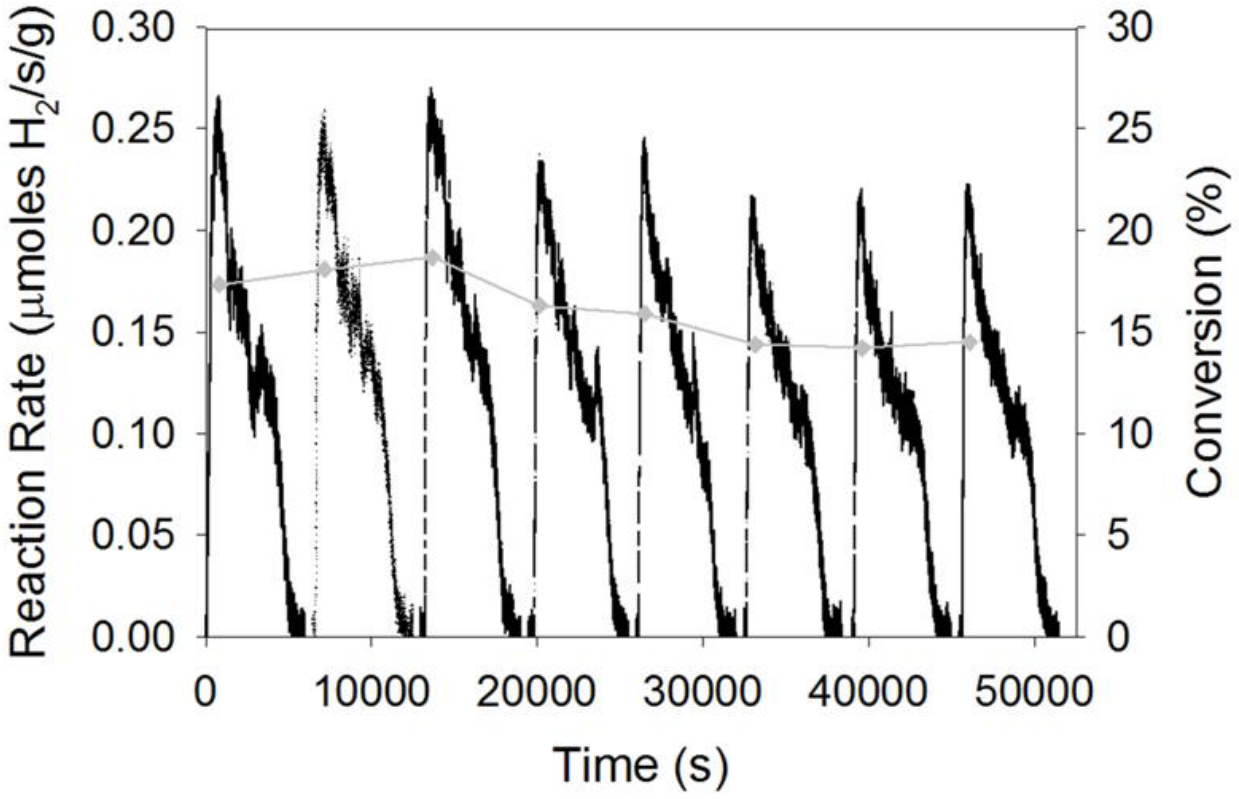

Figure 6-12: H_2 production rate of $CoFe_2O_4$ deposited on Al_2O_3 during water oxidation at 1000 ^oC over the course of eight redox cycles. The sample was thermally reduced at 1200 ^oC.

6.5 Conclusions

The efficacy of using $CoFe_2O_4$ deposited on Al_2O_3 substrates to split H_2O was studied experimentally and in conjunction with thermodynamic modeling. We observed very low decomposition temperatures (200 ^oC lower than $CoFe_2O_4$) due to a reaction between the ferrite and Al_2O_3, resulting in $FeAl_2O_4$. This behavior has been corroborated with thermodynamic modeling. Although the reaction of $FeAl_2O_4$ with H_2O is not as favorable as that of FeO, it is shown that under non-equilibrium conditions it is capable of splitting water to produce H_2 at 1000 ^oC. Significant quantities of H_2 are generated at

reduction temperatures of only 1200 ^{o}C, whereas little or no H_2 was generated using $CoFe_2O_4$ until 1400 ^{o}C. Additionally, $CoFe_2O_4/Al_2O_3$ is capable of being cycled at 1200 ^{o}C reduction/1000 ^{o}C oxidation with no obvious changes in H_2 conversion. These results certainly warrant further exploration of this cycle and provide compelling evidence that ferrites may be cycled with Al_2O_3 to produce H_2 at much lower temperatures than traditional ferrite redox cycles.

6.6 References

[1] Kodama T. High-temperature solar chemistry for converting solar heat to chemical fuels. Progress in Energy and Combustion Science 2003;29:567.

[2] Perkins C, Weimer AW. Solar-Thermal Production of Renewable Hydrogen. Aiche Journal 2009;55:286.

[3] Balat M. Political, economic and environmental impacts of biomass-based hydrogen. International Journal of Hydrogen Energy 2009;34:3589.

[4] Kodama T, Gokon N. Thermochernical cycles for high-temperature solar hydrogen production. Chemical Reviews 2007;107:4048.

[5] Perkins C, Weimer AW. Likely near-term solar-thermal water splitting technologies. International Journal of Hydrogen Energy 2004;29:1587.

[6] Steinfeld A. Solar thermochemical production of hydrogen - a review. Solar Energy 2005;78:603.

[7] Kodama T, Kondoh Y, Yamamoto R, Andou H, Satou N. Thermochemical hydrogen production by a redox system of ZrO_2-supported Co(II)-ferrite. Solar Energy 2005;78:623.

[8] Miller JE, Allendorf MD, Diver RB, Evans LR, Siegel NP, Stuecker JN. Metal oxide composites and structures for ultra-high temperature solar thermochemical cycles. Journal of Materials Science 2008. p.4714.

[9] Gokon N, Murayama H, Nagasaki A, Kodama T. Thermochemical two-step water splitting cycles by monoclinic ZrO_2-supported $NiFe_2O_4$ and Fe_3O_4 powders and ceramic foam devices. Solar Energy 2009;83:527.

[10] Hwang GJ, Park CS, Lee SH, Seo IT, Kim JW. Ni-ferrite-based thermochemical cycle for solar hydrogen production. Journal of Industrial and Engineering Chemistry 2004;10:889.

[11] Kodama T, Gokon N, Yamamoto R. Thermochemical two-step water splitting by ZrO_2-supported $NixFe_{3-x}O_4$ for solar hydrogen production. Solar Energy 2008;82:73.

[12] Agrafiotis C, Roeb M, Konstandopoulos AG, Nalbandian L, Zaspalis VT, Sattler C, Stobbe P, Steele AM. Solar water splitting for hydrogen production with monolithic reactors. 2005. p.409.

[13] Alvani C, La Barbera A, Ennas G, Padella F, Varsano F. Hydrogen production by using manganese ferrite: Evidences and benefits of a multi-step reaction mechanism. International Journal of Hydrogen Energy 2006;31:2217.

[14] Roeb M, Sattler C, Kluser R, Monnerie N, de Oliveira L, Konstandopoulos AG, Agrafiotis C, Zaspalis VT, Nalbandian L, Steele A, Stobbe P. Solar hydrogen production by a two-step cycle based on mixed iron oxides. Journal of Solar Energy Engineering-Transactions of the Asme 2006;128:125.

[15] Aoki H, Kaneko H, Hasegawa N, Ishihara H, Suzuki A, Tamaura Y. The $ZnFe_2O_4/(ZnO+Fe_3O_4)$ system for H-2 production using concentrated solar energy. Solid State Ionics 2004;172:113.

[16] Tamaura Y, Kaneko H. Oxygen-releasing step of $ZnFe_2O_4/(ZnO+Fe_3O_4)$-system in air using concentrated solar energy for solar hydrogen production. Solar Energy 2005;78:616.

[17] Kaneko H, Kojima N, Hasegawa N, Inoue M, Uehara R, Gokon N, Tamaura Y, Sano T. Reaction mechanism of H-2 generation for $H_2O/Zn/Fe_3O_4$ system. International Journal of Hydrogen Energy 2002;27:1023.

[18] Kodama T, Nakamuro Y, Mizuno T. A two-step thermochemical water splitting by iron-oxide on stabilized zirconia. Journal of Solar Energy Engineering 2006;128:3.

[19] Gokon N, Murayama H, Umeda J, Hatamachi T, Kodama T. Monoclinic zirconia-supported Fe_3O_4 for the two-step water-splitting thermochemical cycle at high thermal reduction temperatures of 1400-1600 degrees C. International Journal of Hydrogen Energy 2009;34:1208.

[20] Charvin P, Abanades S, Flamant G, Lemort F. Two-step water splitting thermochemical cycle based on iron oxide redox pair for solar hydrogen production. Energy 2007;32:1124.

[21] Allendorf MD. Two-Step Water Splitting Using Mixed-Metal Ferrites: Thermodynamic Analysis and Characterization of Synthesized Materials. Energy & Fuels 2008;22:4115.

[22] Han SB, Kang TB, Joo OS, Jung KD. Water splitting for hydrogen production with ferrites. Solar Energy 2007;81:623.

[23] Tamaura Y, Steinfeld A, Kuhn P, Ehrensberger K. Production Of Solar Hydrogen By A Novel, 2-Step, Water-Splitting Thermochemical Cycle. Energy 1995;20:325.

[24] Tamaura Y, Ueda Y, Matsunami J, Hasegawa N, Nezuka M, Sano T, Tsuji M. Solar hydrogen production by using ferrites. Solar Energy 1999;65:55.

[25] Gokon N, Takahashi S, Yamamoto H, Kodama T. Thermochemical two-step water-splitting reactor with internally circulating fluidized bed for thermal reduction of ferrite particles. International Journal of Hydrogen Energy 2008;33:2189.

[26] Fujimura T, Tanaka SL. In-situ high temperature X-ray diffraction study of Fe/Al_2O_3 interface reactions. Journal of Materials Science 1999;34:425.

[27] Trumble KP. Thermodynamic analysis of aluminate formation at Fe/Al_2O_3 and Cu/Al_2O_3 interfaces. Acta metallurgica et materialia 1992;40:S105.

[28] Scheffe JR, Frances A, King DM, Liang XH, Branch BA, Cavanagh AS, George SM, Weimer AW. Atomic layer deposition of iron(III) oxide on zirconia nanoparticles in a fluidized bed reactor using ferrocene and oxygen. Thin Solid Films 2009;517:1874.

[29] Hakim LF, George SM, Weimer AW. Conformal nanocoating of zirconia nanoparticles by atomic layer deposition in a fluidized bed reactor. Nanotechnology 2005;16:S375.

[30] King DM, Spencer JA, Liang X, Hakim LF, Weimer AW. Atomic layer deposition on particles using a fluidized bed reactor with in situ mass spectrometry. Surface & Coatings Technology 2007;201:9163.

[31] Wank JR, George SM, Weimer AW. Coating fine nickel particles with Al_2O_3 utilizing an atomic layer deposition-fluidized bed reactor (ALD-FBR). Journal of the American Ceramic Society 2004;87:762.

[32] Ferguson JD, Weimer AW, George SM. Surface chemistry and infrared absorbance changes during ZnO atomic layer deposition on ZrO_2 and $BaTiO_3$ particles. Journal of Vacuum Science & Technology A 2005;23:118.

[33] Hakim LF, McCormick JA, Zhan GD, Weimer AW, Li P, George SM. Surface modification of titania nanoparticles using ultrathin ceramic films. Journal of the American Ceramic Society 2006;89:3070.

[34] Lichty P PC, Woodruff B, Bingham C, Weimer A. High Temperature Solar Thermal Biomass Gasification in a Prototype Cavity Reactor. Journal of Solar Energy Engineering-Transactions of the Asme 2009.

6.7 Supplemental Figures

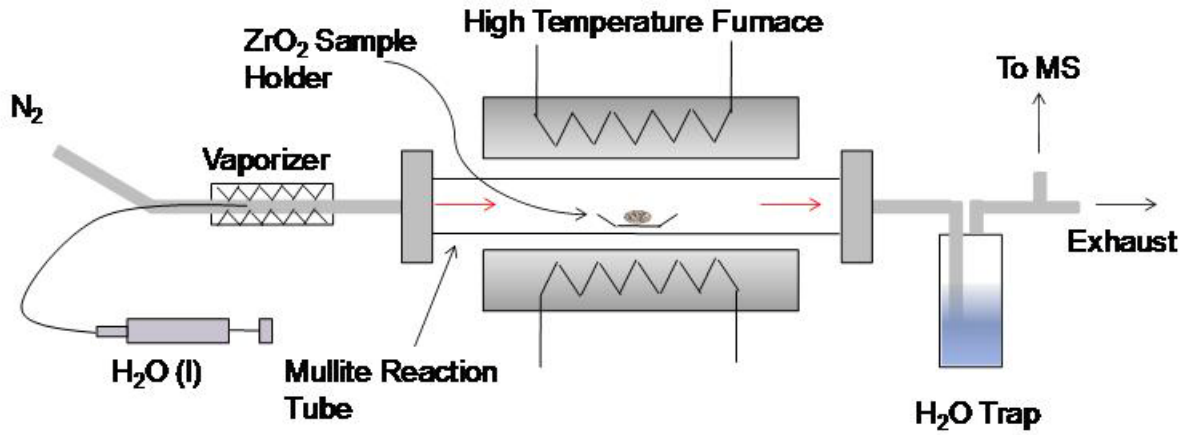

Supplemental Figure 6-13: Schematic representation of the water splitting reactor.

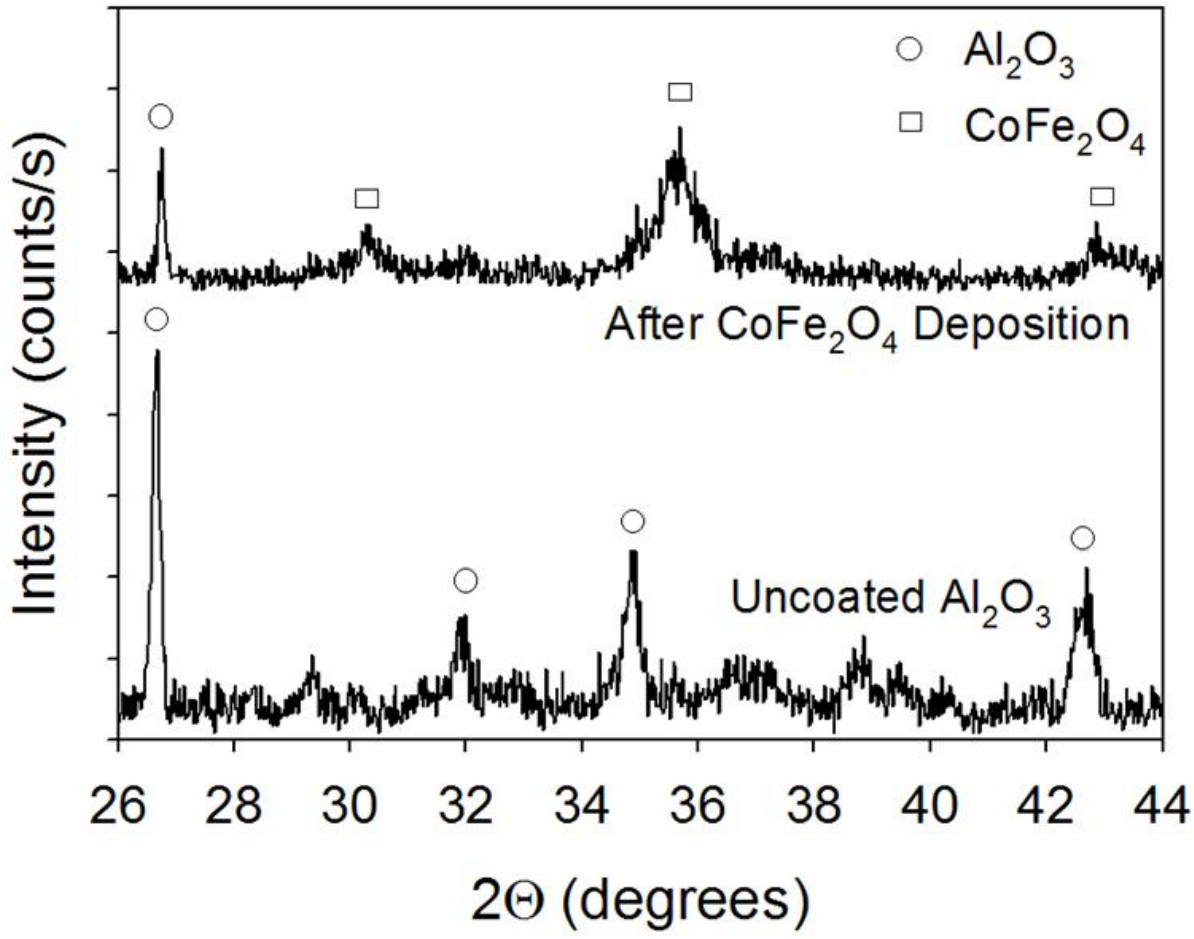

Supplemental Figure 6-14: Powder XRD results of uncoated Al_2O_3 and after $CoFe_2O_4$ deposition.

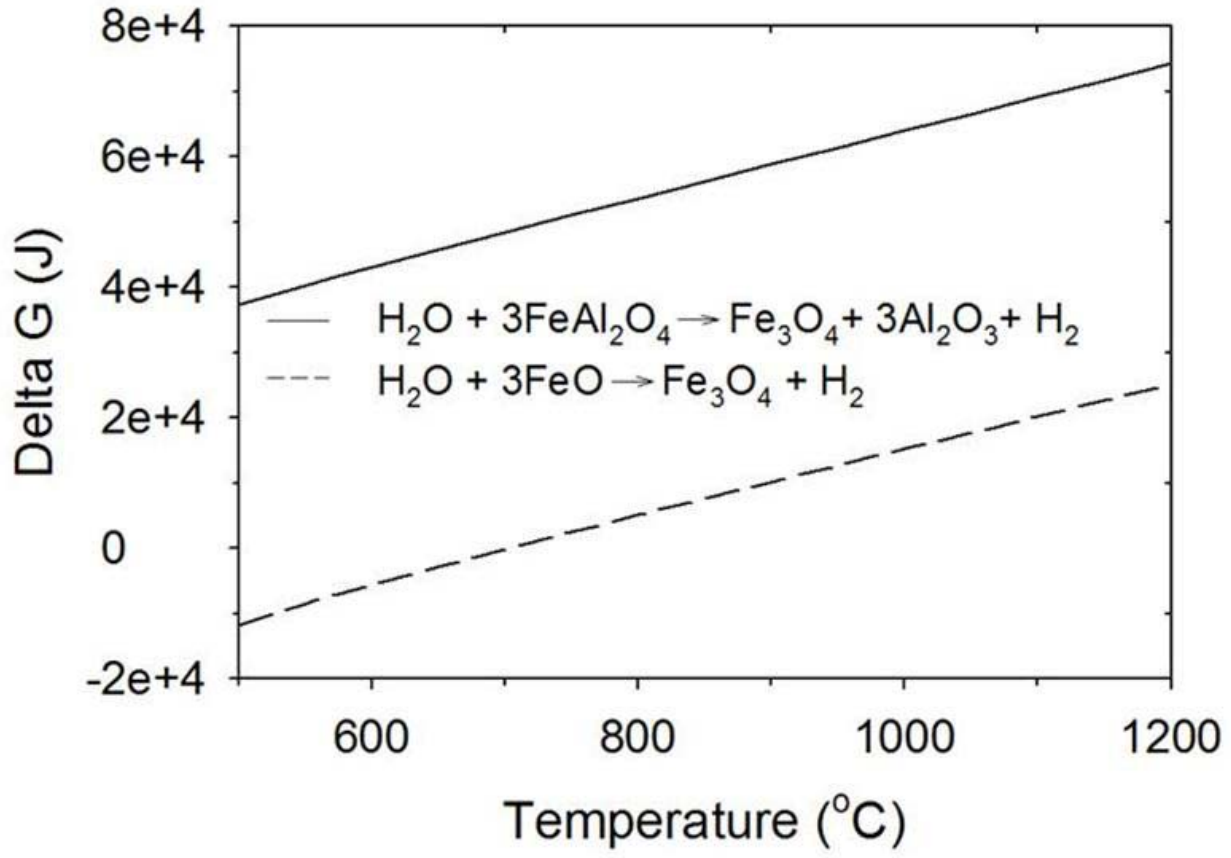

Supplemental Figure 6-15: Gibbs free energy minimization for the reaction of $H_2O + 3FeAl_2O_4 \rightarrow Fe_3O_4 + 3Al_2O_3 + H_2$ and $H_2O + 3FeO \rightarrow Fe_3O_4 + H_2$.

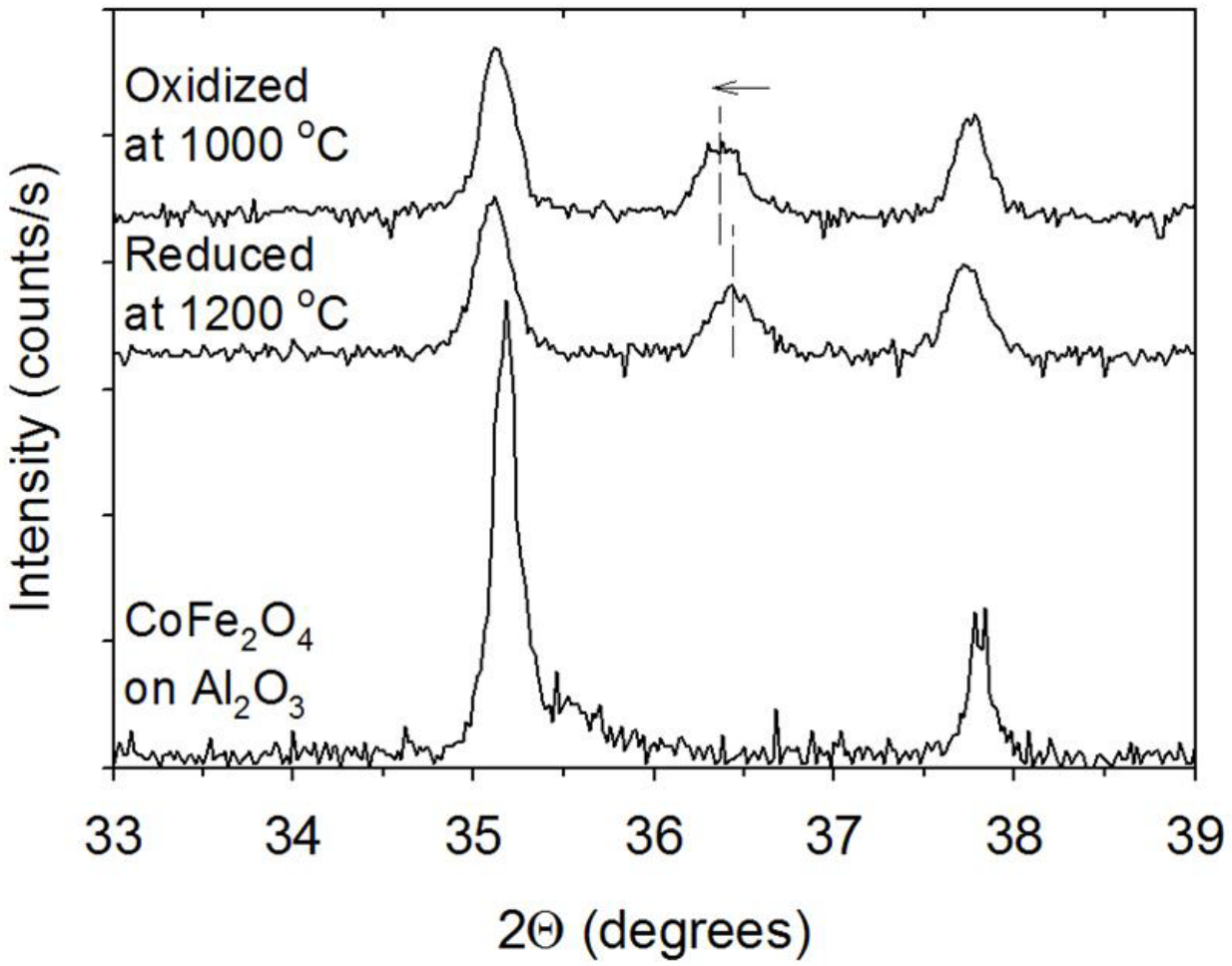

Supplemental Figure 6-16: Powder XRD results of $CoFe_2O_4$ on Al_2O_3 before thermal reduction, after 1200 ^oC reduction, and after H_2O oxidation at 1000 ^oC.

CHAPTER 7 INVESTIGATION OF THE KINETICS OF THERMOCHEMICAL FERRITE WATER SPLITTING CYCLES USING COBALT-IRON SPINEL OXIDES

7.1 Abstract

Cobalt ferrite ($Co_{0.9}Fe_{2.1}O_4$) and iron oxide (Fe_3O_4) thin films were deposited via atomic layer deposition on m-ZrO_2 supports and utilized in a high temperature water splitting redox cycle to produce H_2. Both materials were thermally reduced at 1450 ^oC and oxidized with H_2O (20-40%) at temperatures between 900 ^oC and 1400 ^oC in a stagnation flow reactor. Oxidation of iron oxide was more rapid than the cobalt ferrite, and the rates of both materials increased with temperature, even up to 1400 ^oC. At elevated oxidation temperatures (T > 1250 ^oC) we observed simultaneous production of H_2 and O_2, due to both thermal reduction and water oxidation operating in equilibrium. We produced H_2 under these conditions for an indefinite period of time, at temperatures much lower than those required for water thermolysis. A kinetic model was developed for the oxidation of cobalt ferrite from 900 ^oC to 1100 ^oC, in which there was an initial reaction order limited regime, followed by a slower diffusion limited regime characterized well by the parabolic rate law. The activation energy and H_2O reaction order during the reaction order regime were 119.76 ± 8.81 kJ/mole and 0.70 ± 0.32, respectively, and the activation energy during the diffusion limited regime was 191 ± 19.8 kJ/mol.

7.2 Introduction and Background

Spinel ferrites of the form $M_xFe_{3-x}O_4$, where M generally represents Ni, Zn, Co, Mn, or other transition metals, have been shown to be capable of splitting water according to the two step cycle shown below:

$$M_xFe_{3-x}O_4 + solar\ thermal\ energy \rightarrow xMO + (3-x)FeO + 0.5O_2 \qquad \mathbf{7-1})$$

$$xMO + (3-x)FeO + H_2O \rightarrow M_xFe_{3-x}O_4 + 2H_2 \qquad \mathbf{7-2})$$

This is an inherently clean and sustainable process, as the only net inputs are solar energy and water, and the net outputs are hydrogen and oxygen. The first, thermal reduction step generally operates at temperatures between 1400 ^oC and 1500 ^oC, which is lower than many other analogous high temperature metal oxide cycles, such as the ZnO/Zn and Mn_2O_3/MnO cycles. [1, 2]. As a result, radiation losses are decreased significantly because they increase as the fourth power of temperature, and material considerations for reactor design should be more flexible. Cycle repeatability has also been demonstrated with relative ease because the ferrites do not undergo any phase changes (i.e. solid to liquid) [3-6]. However, the theoretical amount of hydrogen generated is less than other higher temperature thermochemical cycles due to the fact that only Fe^{3+} is capable of being reduced to Fe^{2+} at the temperatures of interest[6]. Additionally, hydrolysis kinetics are relatively slow due to diffusion or surface area limitations created by near surface oxidation [6, 7]. This problem is exacerbated by high temperature sintering which occurs during thermal reduction. This often leads to increasing the water oxidation temperature (Step 2) in order to increase reaction rates (generally T > 1000 ^oC), resulting in oxidation temperatures

that are much higher than other analogous cycles [6, 8, 9]. Furthermore, vaporization of metals can lead to extensive metal loss over time.

Currently, little is understood about the factors that control the reaction rates and conversion efficiencies of ferrite water splitting cycles. To date, most literature has dealt with the effects of the substituted metals in $M_xFe_{3-x}O_4$ and their stoichiometry [3, 4], synthesis methods[4, 10, 11], and various substrates[3, 6] on the total amount of H_2 produced and their ability to be cycled a number of times. For example, Allendorf *et. al.* recently reported on the thermodynamic effects of Fe, Co, Ni, and Zn substitution in $M_xFe_{3-x}O_4$, and observed that x and M greatly influence the equilibrium of this reaction for a given reduction temperature [12]. Co and Ni ferrites were both reduced to a greater extent at temperatures of interest (~1400 ^oC), and it was shown that Fe_3O_4 does not fully reduce until after the melting temperature of wustite. Kodama *et. al.* has observed greater cyclical stability and more H_2 production when depositing Ni, Co, and Fe ferrites on ZrO_2 and YSZ supports [3-5]. They observed that Fe^{2+} forms a solid solution with the substrate during thermal reduction and could be subsequently oxidized to reform the ferrite. Additionally, x and M in $M_xFe_{3-x}O_4$ affected the reported conversions.

Though thermodynamics and the aforementioned factors have been studied, the kinetics and mechanisms of these reactions have yet to be explored in detail. Rapid hydrolysis kinetics are desired in order to facilitate high throughput of H_2 [6, 7]. Charvin *et. al.* observed a strong dependence of Fe_3O_4 particle size on the H_2 reaction rate during water oxidation experiments [13]. As the particle size was increased, slower rates were observed. It was hypothesized that this was due to an oxide barrier formed on the surface of the particles, hindering further oxidation of the bulk. Similar behavior has been observed for CO_2 splitting on chemically reduced $CoFe_2O_4$ nanoparticles [14]. Though it was hypothesized that this phenomena was due to bulk diffusion

limitations, there was no evidence that it was not more dependent on surface area. Go *et. al.* has studied the water oxidation of various ferrite powders after chemical reduction, and concluded that the reactions were diffusion limited processes[15]. Pitz-Paal *et. al.* have studied the water oxidation of zinc ferrite on SiC honeycomb supports and determined that the kinetics agreed well with the shrinking core model. The relevant kinetic paramaters were calculated based on peak H_2 rates, and the activation energy was determined to be 110 kJ/mol[16]. Ultimately, the economic viability of this thermochemical cycle is dependent on relatively fast kinetics.

Various methods are used to synthesize ferrites used in these cycles, including solid state synthesis (SSS) [10, 17-19], coprecipitation[6], aerial oxidation method[4], aerosol spray pyrolysis[10], and self-propagating high-temperature synthesis[10]. SSS is perhaps the simplest of these techniques, but it can be difficult to control particle sizes due to high temperature sintering that occurs during synthesis. This can result in decreased activity of the ferrites, possibly due to the fact that specific surface area plays an important role in either the reduction or oxidation steps [3-5]. Both coprecipitation and aerial oxidation have been used to successfully deposit ferrites on supports, such as ZrO_2 and YSZ, and were shown to increase the reactivity of the ferrites over several cycles [3, 6]. This was attributed to a reduction in high temperature sintering. Though these methods have helped improve cycle efficiencies and stability, it can be difficult to control some of their properties such as film thickness, specific surface area, and particle size. Because of these difficulties, this makes many of these synthesis techniques a poor platter for studying kinetics, in which a well characterized and homogeneous material would be ideal.

Atomic layer deposition (ALD), a technique capable of depositing highly conformal films one atomic layer at a time, is able to precisely control all of the aforementioned properties [20-

23], even on high surface area primary nanoparticles [24-27]. Operating conditions are controlled in such a manner that the precursors of one half-reaction react only on the surface with intermediate functional groups generated by the other precursor. This ensures atomic level control, since at most one sub-monolayer is deposited per half-reaction. Cobalt oxide thin films have been grown on a wide array of surfaces using precursors such as bis(N,N-diisopropylacetamidinato)cobalt(II) [28], CoI_2 [29], $Co(thd)_2$ [30, 31]. Additionally, iron oxide films have been deposited using bis(N,N-diisopropylacetamidinato)iron(II) [28], $Fe(acac)_3$ [32], $Fe(thd)_2$ [33], $Fe(thd)_3$ [34], iron(III) tert-butoxide [35], and ferrocene [36, 37]. By combining these chemistries in alternating doses it is possible to deposit films of $Co_xFe_{3-x}O_4$ [38]. This process is ideal for studying ferrite reaction kinetics as it is capable of synthesizing well-defined and homogeneous films. Additionally, due to the self limiting nature of the process, the cobalt and iron stoichiometry in $Co_xFe_{3-x}O_4$ can be controlled with a high level of precision.

We have prepared two different ferrite stoichiometries by ALD ($Co_{0.9}Fe_{2.1}O_4$ and Fe_3O_4) to study the efficacy of utilizing them in a thermochemical redox cycle to produce H_2. Of particular importance to us is gaining an understanding of the rate limiting mechanisms of the water oxidation reaction. Finally, we hope to be able to incorporate the rate limiting reaction mechanisms with relevant kinetic parameters to derive a global rate expression capable of describing the oxidation reaction rates over a wide range of conditions.

7.3 Experimental Details

7.3.1 ALD Synthesis

Multilayers of iron(III) oxide and cobalt(II) oxide were deposited onto porous ZrO_2 substrates (BET surface area = 50, Alfa Aesar®) via ALD in alternating doses. Iron(III) oxide

deposition consisted of dosing ferrocene (99% purity acquired from Alfa Aesar®) and high purity oxygen (99.9%) in alternate doses into the reactor at 450 ^{o}C. Details of the reactor configuration have been described elsewhere [37]. Ferrocene was delivered into the reactor using a 200cc bubbler (Precision Fabricators Ltd.) heated to 60 ^{o}C. The reactor was then purged with nitrogen in order to remove any excess ferrocene and by-products. Once purged, oxygen was dosed, followed by another nitrogen purge. Cobalt(II) oxide deposition was performed in an identical manner to that of iron(III) oxide, with the exception that cobaltocene, rather than ferrocene, was used. The ALD chemistries were measured in situ via mass spectrometry and all lines were heated to 65 ^{o}C in order to prevent any ferrocene or cobaltocene vapor from condensing. Induced coupled plasma – atomic emission spectroscopy (ICP-AES) was used to verify both cobalt stoichiometry (x, in $Co_xFe_{3-x}O_4$) and mass loadings of the films.

7.3.2Thermal Cycling: Stagnation Flow Reactor

Water oxidation and thermal reduction experiments were conducted in a vertically oriented stagnation flow reactor (SFR) at 75 Torr, which has been described in Chapter 5. Two gas lines were used concurrently, line 1 and line 2, and switched from the reactor to a bypass orientation depending on the gas species desired. 500 sccm of helium was flowed through line 1 and used as a purge gas. Line 2 contained a mixture of H_2O and He, with the total flow equaling 500 sccm. Water was delivered using a non-porous nafion membrane provided by RASIRC™ at 70 ^{o}C and 350 Torr. The flowrate was controlled by varying the inlet gas flow, and was calculated according to the equation 7-3 shown below,

$$F_r = F_m P_r / (P_o - P_r) \qquad \mathbf{7-3})$$

where F_r is the H_2O flowrate in sccm, F_m is the flowrate of inert gas through the membrane, P_r is the vapor pressure of H_2O at the membrane temperature, and P_o is the pressure of the membrane.

Thermal reduction consisted of heating the sample to 1450 ^oC at 15 ^oC/minute while flowing 500 sccm He. Once the setpoint was achieved, the furnace temperature was held for an additional 75 minutes. Following reduction, the temperature was reduced at 15 ^oC/minute to the desired oxidation set point while continuing to flow He. Once achieved, the steam/He mixture was delivered into the reactor for 600s. Both O_2 and H_2 were measured at the outlet of the reactor by a modulated beam mass spectrometer, and calibration was achieved by delivering various known concentrations of O_2 and H_2 in He. The sample was placed in a YSZ holder fabricated by Zircar Zirconia, Inc.

7.3.3 Material Characterization

Visual inspection of the films was carried out using a JEOL 7600F field-emission scanning electron microscope (FESEM) operating at 4kV and 15kV to examine surface morphology and local chemical variation. Here, samples were mounted on conductive tape and sputtered with carbon. Film composition was determined via induced coupled plasma – atomic emission spectroscopy (ICP-AES).

7.4 Results

7.4.1 Temporal Behavior/Cycling

Two representative ferrite samples, $Co_{0.9}Fe_{2.1}O_4$ and Fe_3O_4, were synthesized and investigated and are described in Table 7-1. After deposition the cobalt ferrite surface area was

29 m^2/g with a mass loading of 45%, and iron oxide surface area was of 27 m^2/g with a mass loading of 36%. Extensive characterization was conducted and described in Chapter 5, and indicated that these films were deposited homogeneously on the surface of the m-ZrO_2 supports. Film stoichiometry was verified by ICP-AES analysis, and raman spectroscopy. The water oxidation of $Co_{0.9}Fe_{2.1}O_4$ was studied at oxidation temperatures between 900 and 1400 ^oC and mole fractions of water from 0.2 to 0.4 at 75 Torr. Oxidation experiments using Fe_3O_4 were not as exhaustive as $Co_{0.9}Fe_{2.1}O_4$, but were conducted over the same range of conditions. All experiments were conducted by cycling the same sample repetitively, rather than separate samples for each experiment. The samples were never tampered with between cycles and remained in the reactor for the duration of their experiments.

Table 7-1: Physical characteristics of synthesized ferrites

	Stoichiometry (ICP-AES)	Initial ZrO_2 SA (BET)	Final SA After Deposition (BET)	Mass (%) Loading (ICP-AES)
Sample 1	$Co_{0.9}Fe_{2.1}O_4$	51 m^2/g	29 m^2/g	45%
Sample 2	Fe_3O_4	51 m^2/g	27 m^2/g	36%

The temporal behavior of H_2 and O_2 evolution during water oxidation and thermal reduction are similar for both $Co_{0.9}Fe_{2.1}O_4$ and Fe_3O_4. Shown on the left half of Figures 7-1a and 7-1b are the water oxidation rates for both materials at 1100 ^oC and 30% H_2O. Both H_2 rates increase rapidly at the onset of the reaction, and exponentially decay as the reaction progresses. This behavior is very characteristic of, and similar to, other ferrite water splitting rates observed in the literature [6, 16]. Also, the rate of Fe_3O_4 oxidation is faster than the cobalt ferrite. It's peak H_2 rate of 8.8 μmoles/s/g is nearly double the peak rate of the cobalt ferrite (4.3 μmoles/s/g).

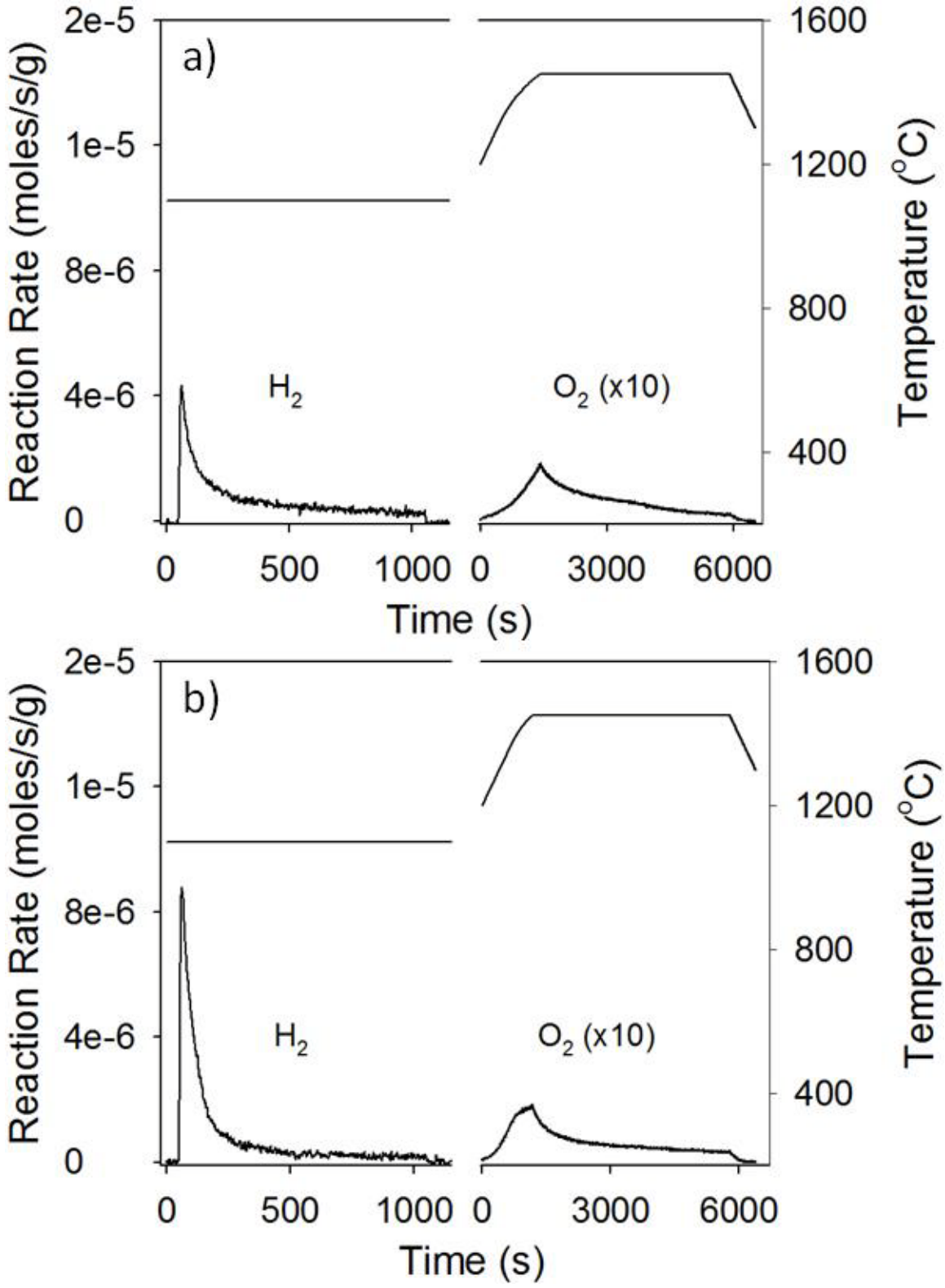

Figure 7-1: a) Temporal water oxidation rates (left) and O_2 evolution rates (right) for $Co_{0.9}Fe_{2.1}O_4$ and b) Fe_3O_4

The onset of O_2 evolution (right half of Figures 7-1a and 7-1b) for both samples occurs right after 1200 ^oC, and the O_2 yields for $Co_{0.9}Fe_{2.1}O_4$ (378 μmoles/g) and Fe_3O_4 (366 μmoles/g) are both similar. This was surprising because thermodynamics predicts the onset of thermal reduction to occur at lower temperatures for cobalt ferrites, as well as larger conversions[12]. The rate of O_2 evolution is also noticeably slower than H_2 evolution for both samples. Reduction was continued for 75 minutes after the set point of 1450 ^oC was achieved, yet the rates were still well above baseline after that length of time. The majority of both oxidation reactions occurred within the first 10 minutes. This is contrary to some previous literature reports in which these reaction rates are similar, or the water oxidation rates are even slower than thermal reduction[6]. However, it is likely that these rates are highly dependent on the size and morphology of the materials used.

Both materials were capable of being cycled without signs of deactivation. Continuous water oxidation cycles, after thermal reduction, of $Co_{0.9}Fe_{2.1}O_4$ and Fe_3O_4 , are shown in Figures 7-2a and 7-2b for increasing oxidation temperatures. The rates of both samples increase as the oxidation temperature is increased, even up to 1400 ^oC for the cobalt ferrite. This is significant because it is only 50 ^oC less than its thermal reduction upper operating temperature, suggesting that it is possible to drive the water oxidation reaction, rather than thermal reduction, simply by altering the gas composition. To the best of our knowledge, this is the first published report of this phenomenon. These results suggest that there is a competition between kinetics and thermodynamics as the temperature is increased. Thermodynamics predicts that the oxidation reaction for both materials is unfavorable ($\Delta G>0$) as the temperature is increased past about 750 ^oC [Supplemental Figure 7-11], yet the H_2 reaction rates and conversions continue to increase up to 1400 ^oC. This is clearly indicative of a kinetically limited reaction. Subsequent O_2 rates during

thermal reduction at 1450 ^{o}C are shown in Figure 7-2c, for $Co_{0.9}Fe_{2.1}O_4$. As expected, the O_2 yields increase as the degree of oxidation increases, corroborating that the extent of oxidation increased as the oxidation temperature was increased.

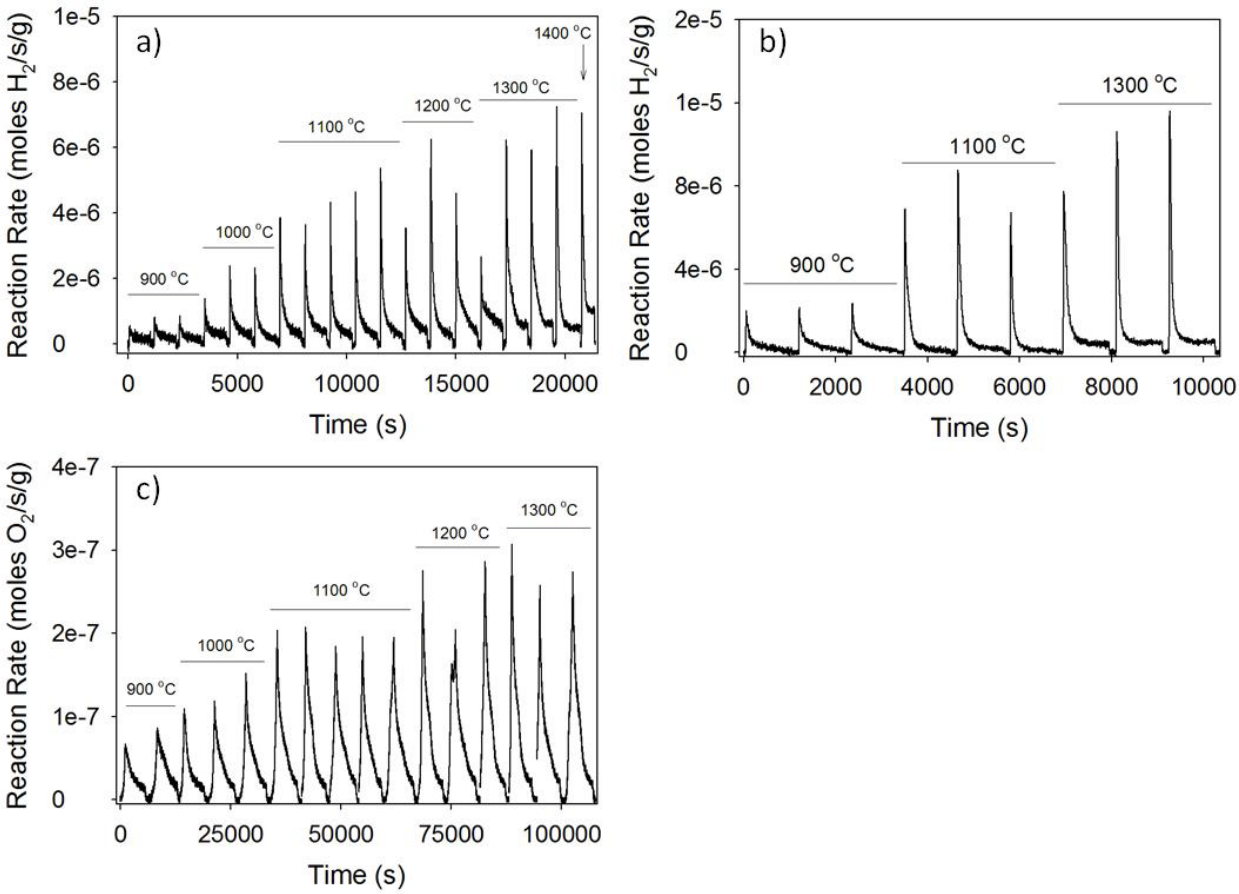

Figure 7-2: a) H_2 reaction rates for $Co_{0.9}Fe_{2.1}O_4$, b) Fe_3O_4 and c) subsequent O_2 evolution rates for $Co_{0.9}Fe_{2.1}O_4$

It is also apparent from Figure 7-2a, that the value of the H_2 plateau increases as the oxidation temperature is increased. The plateau is observed at long oxidation times where the rate of change of H_2 approaches zero. To determine the nature of this plateau, we performed experiments without samples to see if it was due to water thermolysis. We saw no evidence of any H_2 until 1400 ^{o}C, but even at that temperature the increase was very minimal and much less than the values of the H_2 plateaus observed in Figure 7-2a. Therefore, we performed extended

oxidation runs with $Co_{0.9}Fe_{2.1}O_4$ to see if the plateaus remain constant or eventually decreased to zero once the reaction was exhausted. This was initially attempted at 1300 ^oC / 40% H_2O. The initial reaction rate is very rapid and is preceded by an exponential decay to a plateau of 5e-7 moles/g/s, as shown in Figure 7-3. This rate stays constant for up to 1500 s without showing any sign of decreasing. After 2000 s at 1300 ^oC, we increased the temperature to 1350 ^oC, and finally 1400 ^oC, while continuing to flow steam.

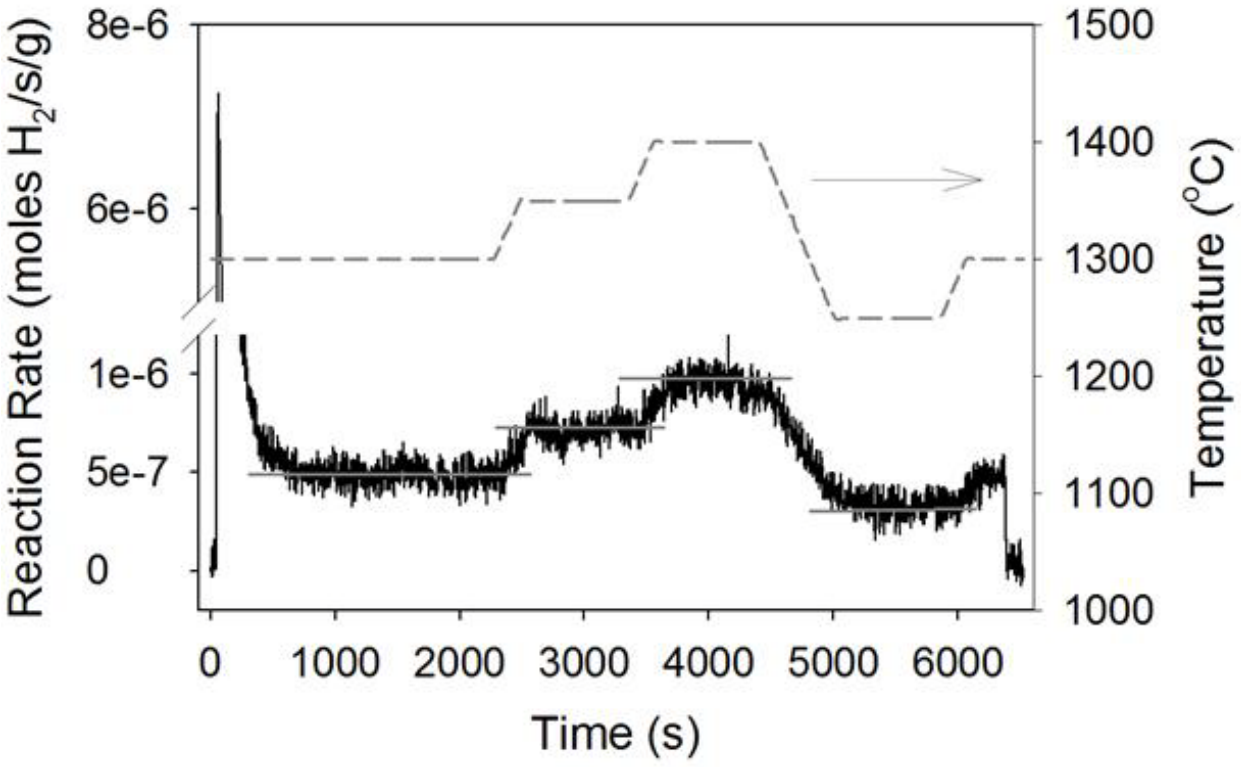

Figure 7-3: Extended H_2O oxidation of $Co_{0.9}Fe_{2.1}O_4$ while varying the temperature

There was a corresponding increase in the H_2 rate as the temperature was increased, and after continuing to oxidize the sample for 6000 s, the rate of change of H_2 was zero except for when the temperature was changed, indicating that this is an activated process. We do not believe that the extended H_2 rates are due to the slow oxidation of the sample because the amount of H_2 generated was 4332 μmoles/g, whereas the amount of O_2 generated during the subsequent

thermal reduction was only 407 μmoles/g. Clearly there is more H_2 generated than predicted based on a stoichiometric amount of H_2 and O_2 generated from H_2O (2:1). In fact, more H_2 is generated than is thermodynamically possible from a ferrite based two step water splitting process [12]. We believe that this phenomenon is due to both thermal reduction and water oxidation occurring simultaneously, without a net effect on the oxidation state of the ferrite. In addition to continued H_2 production, we observe the simultaneous evolution of oxygen. Without the presence of steam, thermal reduction is favorable under these conditions, and in fact, once the flow rate of steam is stopped a rapid increase in the O_2 evolution rate results. These results indicate that it is possible to split H_2O into H_2 and O_2 for an indefinite period of time, without going to extreme temperatures which are required for water thermolysis[39].

A stoichiometric amount of H_2 and O_2 is generated at low oxidation temperatures ($T \leq$ 1100 ^{o}C). A plot of O_2 verses H_2 yeilds for both the cobalt ferrite and iron oxide for all oxidation conditions is shown in Figure 7-4. The lower yields agree well with the predicted ratio of 2:1 (H_2:O_2, ideal line) expected from stoichiometric H_2O splitting. However, at higher H_2 conversions, the amount of O_2 evolved plateaus and the H_2:O_2 ratios begin to fall away from the ideal line. This phenomenon is attributed to the continued production of H_2 at elevated temperatures, as discussed previously. The data obtained for the extended oxidation (Figure 7-3) is indicated by the point on the extreme right of the figure, indicating the extent to which this varies from a stoichiometric reaction expected from a standard ferrite-based water splitting cycle.

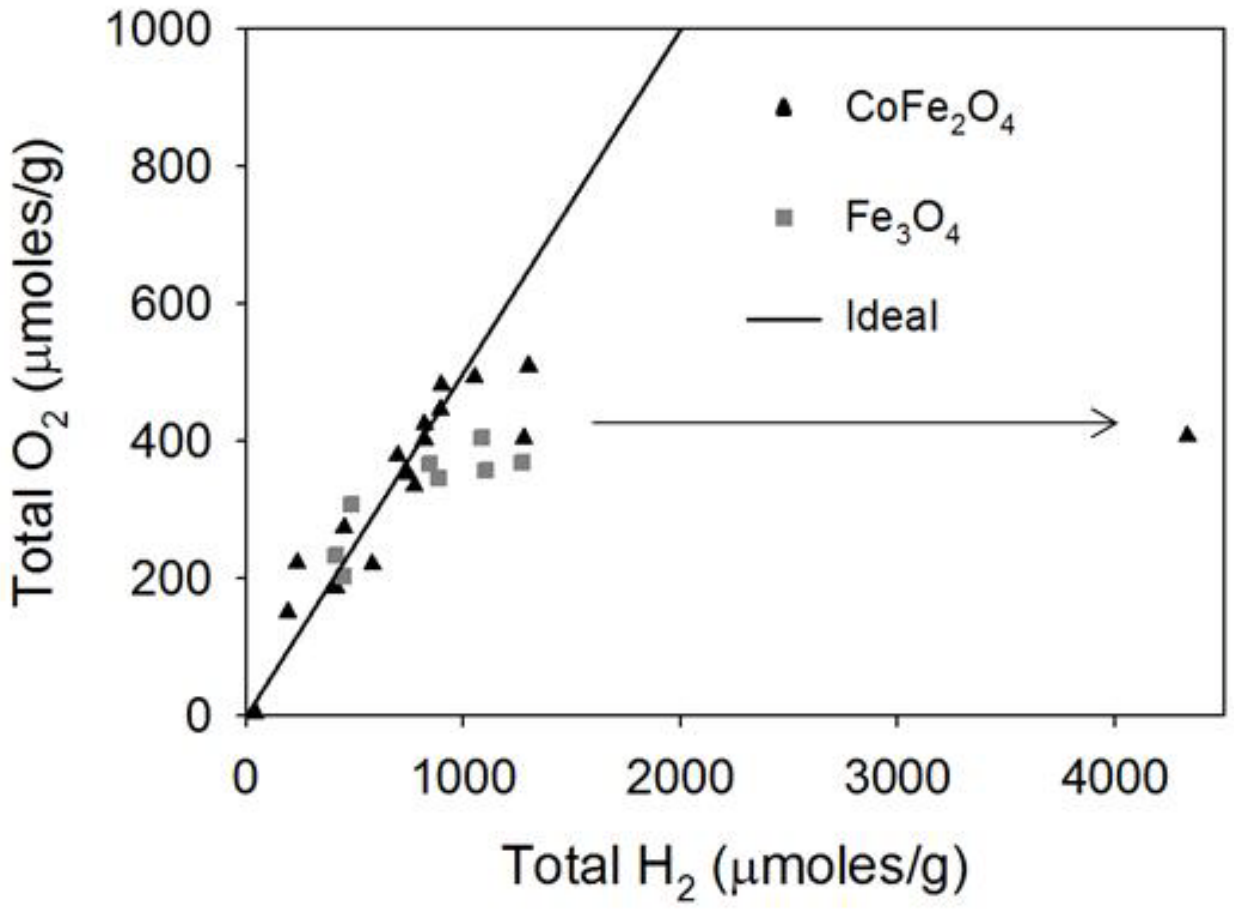

Figure 7-4: Total O_2 yields vs. H_2 yields for $CoFe_2O_4$ and Fe_3O_4

The O_2 yields of $Co_{0.9}Fe_{2.1}O_4$ range from 150 μmoles/g to 510 μmoles/g, depending on the oxidation conditions, and increase as the oxidation temperature is increased. These values are less than the original amount of O_2 evolved from the sample, which was 641 μmoles/g, and indicate that even at the highest H_2 conversions, the sample is not able to be completely oxidized. At low temperatures the sample is not capable of being oxidized completely due to kinetic limitations, and at higher oxidation temperatures the reaction is limited by thermodynamics ($\Delta G>0$). All of the relevant H_2 data for $Co_{0.9}Fe_{2.1}O_4$ and Fe_3O_4, is tabulated in Table 7-2. Conversions for both samples increase with increasing temperatures, and less noticeably with

increasing water concentration. ANOVA analysis of $Co_{0.9}Fe_{2.1}O_4$ data indicates that temperature has a statistical effect on the H_2 yield, O_2 yields, and H_2 peak rates (p-value $\leq$ .05), whereas the effect of H_2O concentration on these values is less significant, with p-values ranging from 0.042 to 0.10.

Table 7-2: Total H_2 yields as a function of reactive material, oxidation temperature and water concentration

	H_2O %	H_2 Yield (moles H_2/g) $Co_{0.9}Fe_{2.1}O_4$	H_2 Yield (moles H_2/g) Fe_3O_4
900 °C	20	.000194	0.000451
	30	.000252	0.000415
	40	.000236	0.000411
1000°C	20	.000416	
	30	.000580	
	40	.000452	
1100°C	20	.000740	0.000887
	30	.000736 ± 3.9E-05	0.000844
	40	.000820	0.000484
1200°C	20	.000821	
	30	.000900	
	40	.001053	
1300°C	20	.000895	0.001088
	30	.001280	0.001105
	40	.001302	0.001274

7.4.2 Kinetic discussion – Cobalt Ferrite

Water oxidation kinetic parameters based on the peak H_2 rate were calculated for $Co_{0.9}Fe_{2.1}O_4$, assuming Arrhenius type rate dependence according to the rate expression given by:

$$rH_2\left[\frac{mol}{g\times s}\right] = [y_{H_2O}]^n k_o e^{\frac{-E_a}{RT}} \qquad \mathbf{7-4})$$

where rH_2 is the peak H_2 production rate, y_{H_2O} is the H_2O mole fraction, n is the H_2O reaction order, k_o is the pre-exponential factor, E_a is the activation energy, R is the ideal gas constant, and T is the isothermal reaction temperature. A plot of the $\ln[rH_2]$ verses inverse temperature is shown in Figure 7-5, and indicates that there is a linear trend between temperatures ranging from 900 ^oC to 1100 ^oC. At higher temperatures the rates plateau which we attribute to thermodynamic limitations [Supplemental Figure 7-11]. The activation energy was calculated by estimating the slope of each linear portion of the figure, and was determined to be 119.76 ± 8.81 kJ/mole. There is limited literature data to compare this value to, but it is greater than previous reports for H_2O and CO_2 splitting for various ferrites. Go *et. al.* studied the water oxidation of Fe_2O_3, $MnFe_2O_4$, and $ZnFe_2O_4$ and calculated activation energies ranging from 57.4 to 109.7 kJ/mol[15]. However, all of their samples were reduced at lower temperatures (< 900 ^oC) in the presence of CH_4, whereas our experiments were thermally reduced at much high temperatures (1450 ^oC). Steinfeld *et.al.* have calculated the activation energy of FeO oxidation using CO_2, and calculated peak rate activation energies of 73.4 ± 8.5 and 69 kJ/mol for isothermal and dynamic thermogravimetric experiments, respectively[40]. Most recently Pitz-Paal *et. al.* calculated an activation energy of 110 ± 14 kJ/mol for the water oxidation of zinc ferrite. The H_2O reaction order was calculated by determining the slope of a plot of $\ln[rH_2]$ verses $\ln y_{H_2O}$, and is 0.70 ± 0.32. This is close to the value determined by Steinfeld *et.al.* for CO_2 decomposition on FeO (0.78), and none was reported by Go *et. al.* for H_2O decomposition because they assumed a zero order reaction dependence. Pitz-Paal *et. al.* did not see any dependence from 10-80% H_2O and therefore concluded that it's reaction order was zero. Tabulated values of all kinetic parameters based on peak H_2 reaction rates are shown in within Figure 7-5. The calculated data was

incorporated into the above Arrhenius kinetic expression and shown as the fitted data in Figure 7-5 and there is good agreement with the data and the fitted expression.

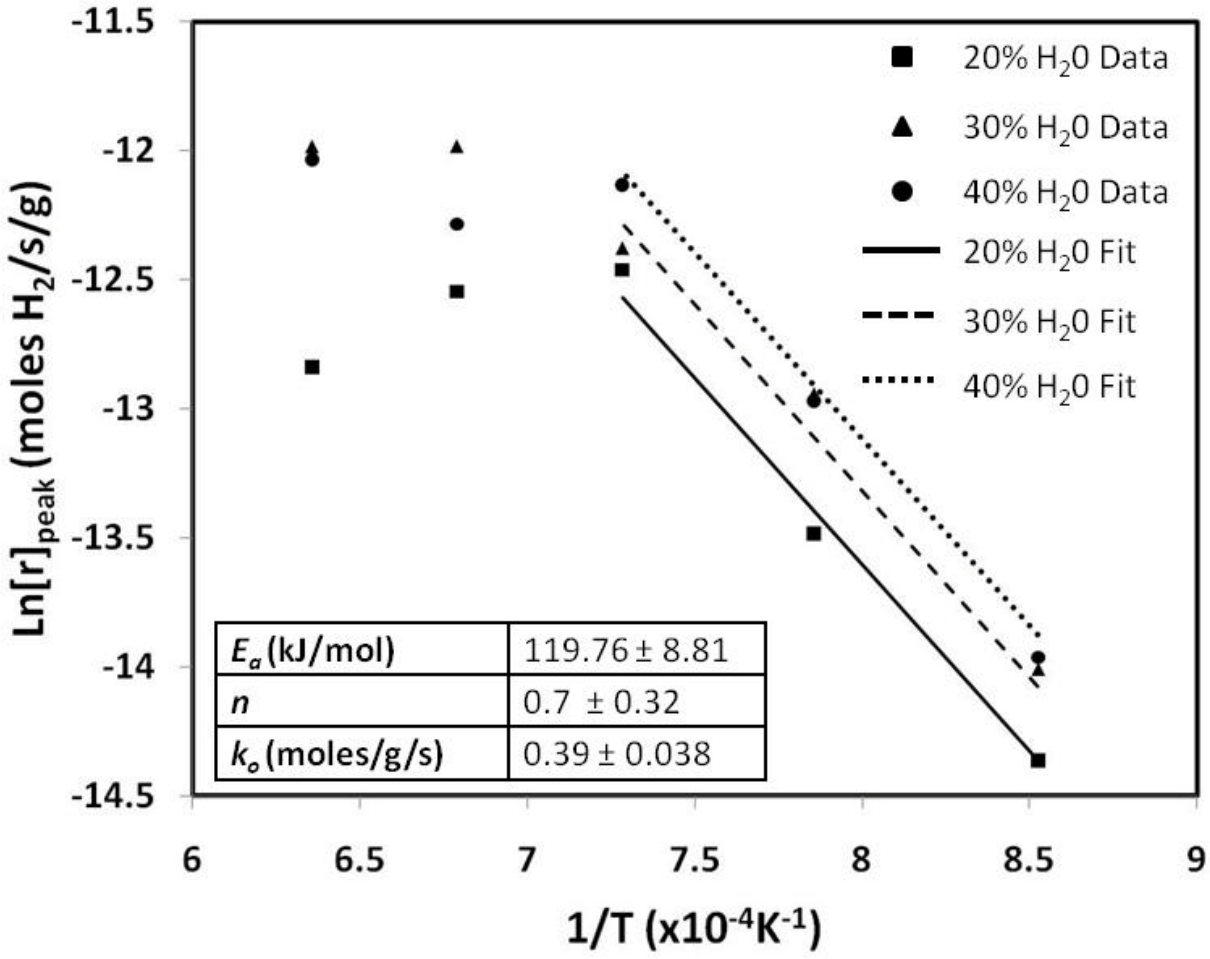

Figure 7-5: Arrhenius plots based on peak H_2 rates and corresponding kinetic parameters and fits.

While this simple Arrhenius expression is capable of describing the peak H_2 rate behavior, it is not necessarily valid for predicting all H_2 rates as a function of time. Therefore, we have implemented a master plot analysis technique which is capable of comparing our normalized rate data in differential form to functional forms of known solid state kinetic models [41]. The advantage of this analysis is that the curves are only dependent on the kinetic model and not on other kinetic parameters. Therefore individual sets of differential rate data can be

compared to various kinetic models in order to determine appropriate models characteristic of the reaction mechanism. The kinetic model, f(α), is a function which is capable of describing the mechanism of the process, and is implemented into the differential form of a generic Arrhenius expression shown below as:

$$\frac{d\alpha}{dt} = k \cdot f(\alpha) \qquad \mathbf{7-5})$$

where α is the reacted fraction at time *t* [42]. We have compared our experimental data to several common reaction models, as described in Table 7-3.

Table 7-3: Reaction models that were compared to experimental data

Model	Symbol	f(α)
Reaction Order	Fn	$(1-\alpha)^n$
Nucleation and Growth (Johnson-Mehl-Avrami equation)	An	$n(1-\alpha)[-\ln(1-\alpha)]^{1-\frac{1}{n}}$
Phase Boundary Controlled Reaction	R2	$2(1-\alpha)^{\frac{1}{2}}$
Phase Boundary Controlled Reaction	R3	$3(1-\alpha)^{\frac{2}{3}}$
One Dimensional Diffusion	D1	$\frac{2}{\alpha}$
Two Dimensional Diffusion	D2	$\frac{1}{-\ln(1-\alpha)}$
Three Dimensional Diffusion	D3	$\frac{3(1-\alpha)^{\frac{2}{3}}}{2[1-(1-\alpha)^{\frac{1}{3}}]}$

As shown in Figure 7-6, water oxidation at 1100 ^{o}C/30% H_2O is compared to several reaction models and no single model is identical to the experimental data over all conversions. However, after a fractional reaction of 0.3, the experimental data and D1 model agree very well. At lower conversions, the predicted rates are much faster than experimental rates, and the data is best represented by a second order reaction model (F2).

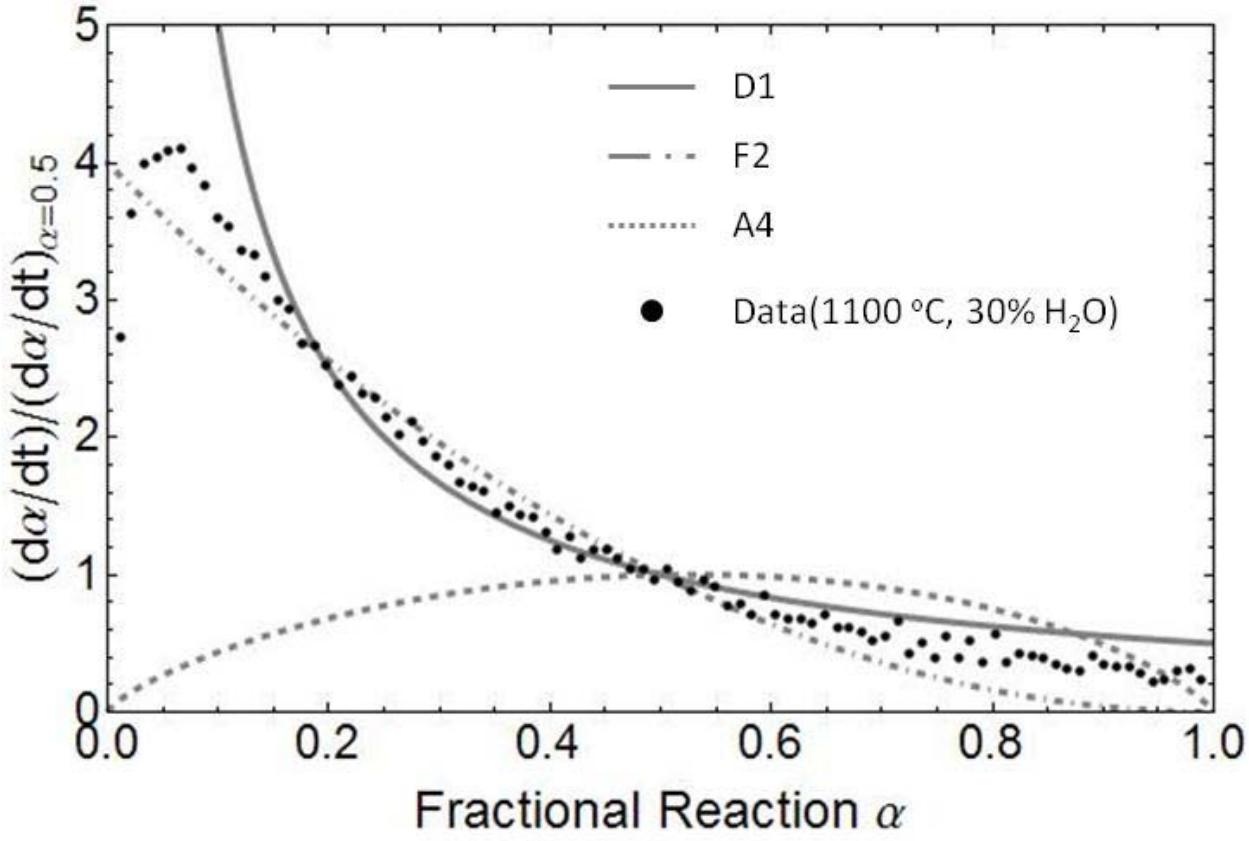

Figure 7-6: Master plot comparing experimental oxidation data at 1100 ^{o}C/30% H_2O to various reaction mechanisms.

This suggests that the reaction is limited by two different mechanisms, the first being a surface chemical reaction limitation described by the second order reaction model, and the second, a diffusion mechanism at longer reaction times. Steinfeld *et.al.* have observed similar behavior when oxidizing FeO particles to Fe_3O_4 using CO_2 [40]. However, given the thin nature of the

ALD cobalt ferrite films it is surprising that the oxidation data is represented well by a diffusion model. These models are commonly described by the oxidation of metals in which a growing oxide layer limits the reaction rate due to diffusion through the oxide layer [43]. However, our materials were synthesized with films that were about 2nm thick, and so diffusion limitations by that same mechanism would be unlikely unless the materials changed morphologically due to the high temperatures required for these redox cycles.

FESEM images and EDX analysis of samples before and after one complete redox cycle indicate that extensive sintering and metal phase segregation occurred during thermal cycling. As-synthesized $Co_{0.9}Fe_{2.1}O_4$ on the m-ZrO_2 support is shown in Figure 7-7a, and the ZrO_2 nanoparticles within the support are easily observed with average particle sizes of 50nm. Corresponding EDX maps are shown in Figures 7-7c and 7-7e, and it is clear that both zirconium and iron are distributed homogeneously, as shown by the evenly disbursed areas of gray and black. A cobalt EDX map is not shown because it looks identical to iron. This is clear indication that the ferrite film was dispersed evenly and throughout the porous support. However, after the first redox cycle the ZrO_2 nanoparticles can no longer be observed, and sintered grains with an average size of 1 μm result, as seen in Figure 7-7b. This resulted in a decrease of surface area from 29 m^2/g to less than 1 m^2/g, and is further confirmation of sintering and grain growth. Also accompanying sintering was extensive zirconium and iron phase segregation, observed in Figures 7-7d and 7-7f. There are high concentrations where only iron can be observed, and vice versa. These morphological changes clearly indicate that the ALD films no longer exist as they were originally synthesized, but rather as a sintered material with grain sizes much larger than the original film thickness. This change may explain why the oxidation rates appear to be limited by diffusion, which is common for the oxidation of bulk powder oxides and metals.

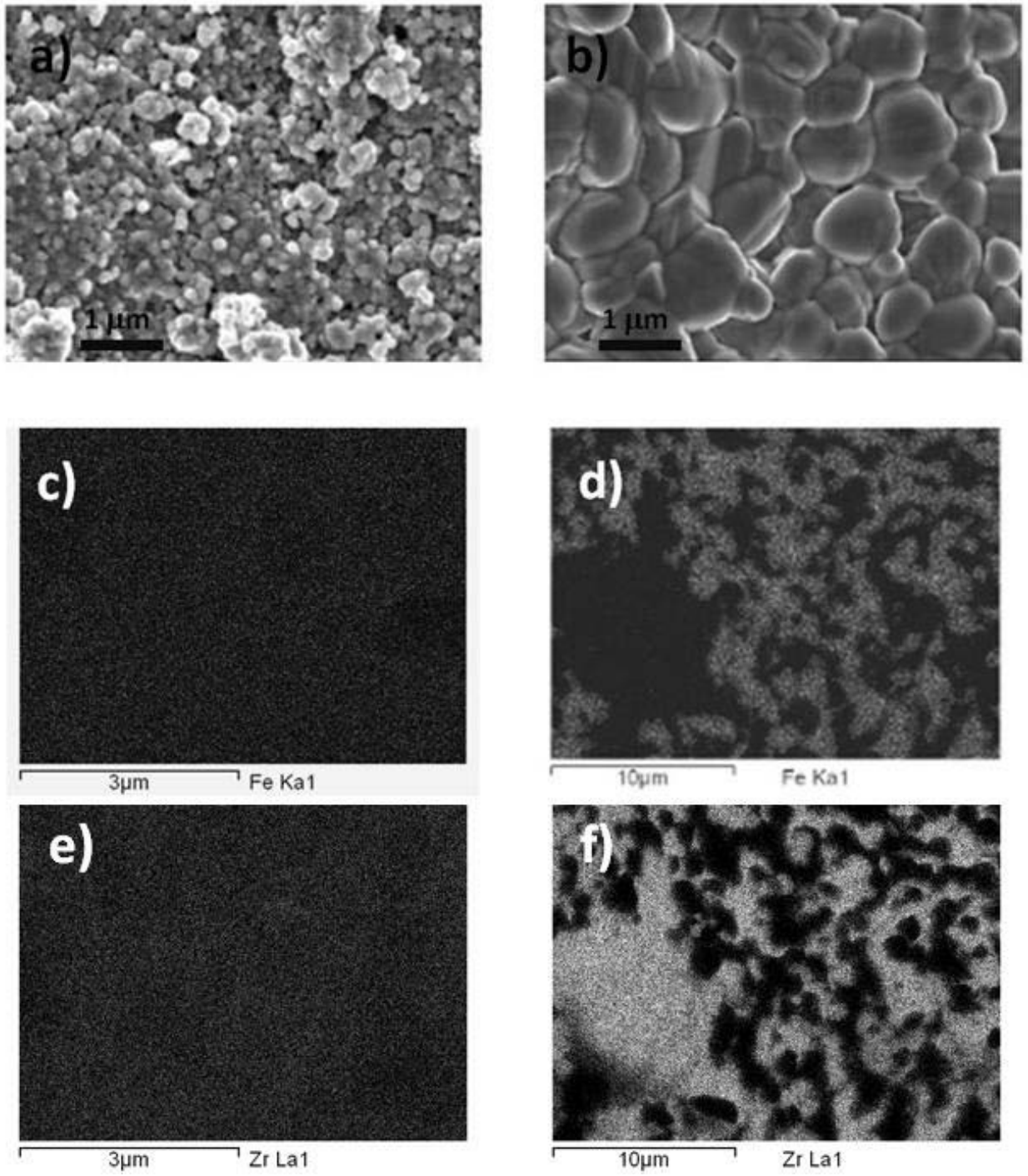

Figure 7-7: a)FESEM image of as synthesized cobalt ferrite, b) FESEM after 1st redox cycle, c) Fe EDS map of as synthesized cobalt ferrite, d) FE EDS map after 1st redox cycle, e) Zr EDS map of as synthesized cobalt ferrite, f) Zr EDS map after 1st redox cycle

To further investigate the role of diffusion in the water oxidation reaction, we have attempted to fit our data to the parabolic rate law which describes solid state reactions which are limited by diffusion of a reactant through a growing oxide film, as shown below:

$$\alpha^n = k_p \cdot t \qquad \mathbf{7-6})$$

where α is the reacted fraction at time *t*, k_p is the parabolic rate constant, *t* is time, and *n* is an empirically derived exponent[44]. The reacted fraction, α, is defined as:

$$\alpha = \frac{Total\ H_{2\ t}}{2 \cdot Total\ O_{2\ R1}} \qquad \mathbf{7-7})$$

where $Total\ H_{2\ t}$ is the total amount of H_2 generated at a given time, *t*, and $Total\ O_{2\ R1}$ is the total amount of oxygen that was evolved from the sample during the first thermal reduction. This is the true measure of the materials oxidation potential, because we cannot assume that all of the Fe^{3+} was reduced to Fe^{2+} due to incomplete reduction. Additionally, we cannot calculate this after every cycle because other O_2 yields are always less than the first thermal reduction this due to incomplete oxidation. According to Equation 7-6, data that can be characterized by the parabolic rate law would be linear when ln(α) is plotted verses ln(*t*) with a slope of 1/*n*. A plot of ln(α) verses ln(*t*) for all sets of data is shown in Figure 7-8, and the data is not linear for the entire length of the reactions. However, after the first 150 s of the reaction (ln[t] = 5) the data is approximately linear, and agrees well with the parabolic rate law, further confirming that the reaction is limited by diffusion for long reaction times. This also agrees with the master plot analysis discussed in Figure 7-6, in which the data only agreed well with the D1 diffusion model

after the reaction progressed to a conversion greater than 0.3. We were able to compute *n* for each data set from their respective slopes, and the average value is 1.94 ± 0.44, which is close to the value of 2 most commonly associated with the parabolic rate law. There was a large variation of *n* with respect to oxidation temperature; *n* was 1.54 ± 0.13 at 900 ^{o}C, 1.87 ± 0.39, and 2.41 ± 0.17 at 1100 ^{o}C.

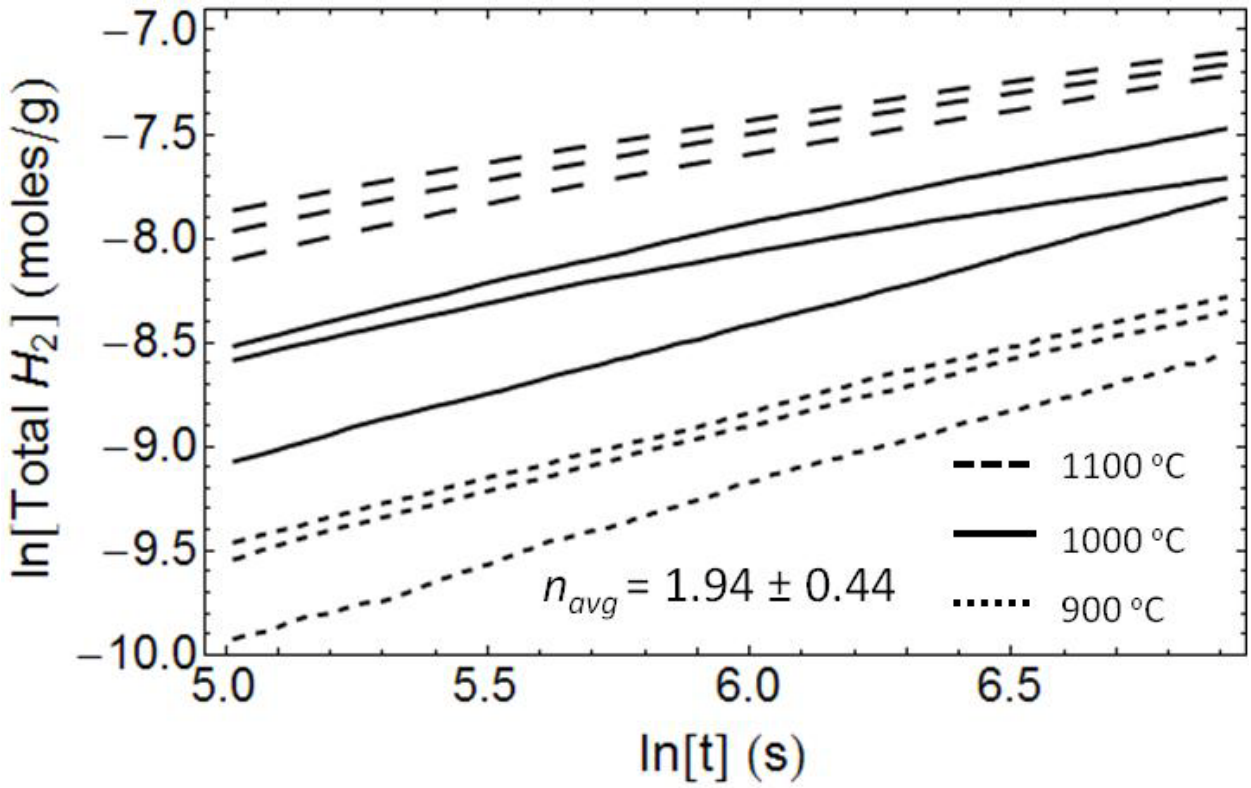

Figure 7-8: Calculation of *n* as defined by the parabolic rate law. Linear portions indicate good agreement with the model.

The calculated activation energy during the diffusion limited regime is higher than that of the activation energy calculated based on peak H_2 rates. Activation energy was calculated by plotting $\ln[\alpha] - (1/n)\ln[t]$ verses 1/T for t > 150s, and determining the slope, which is equal to Ea/R. These values are plotted for various water concentrations, as shown in Figure 7-9, and the

average activation energy is 191 ± 19.8 kJ/mol, compared to 119.76 ± 8.81 kJ/mole for the peak H_2 rates.

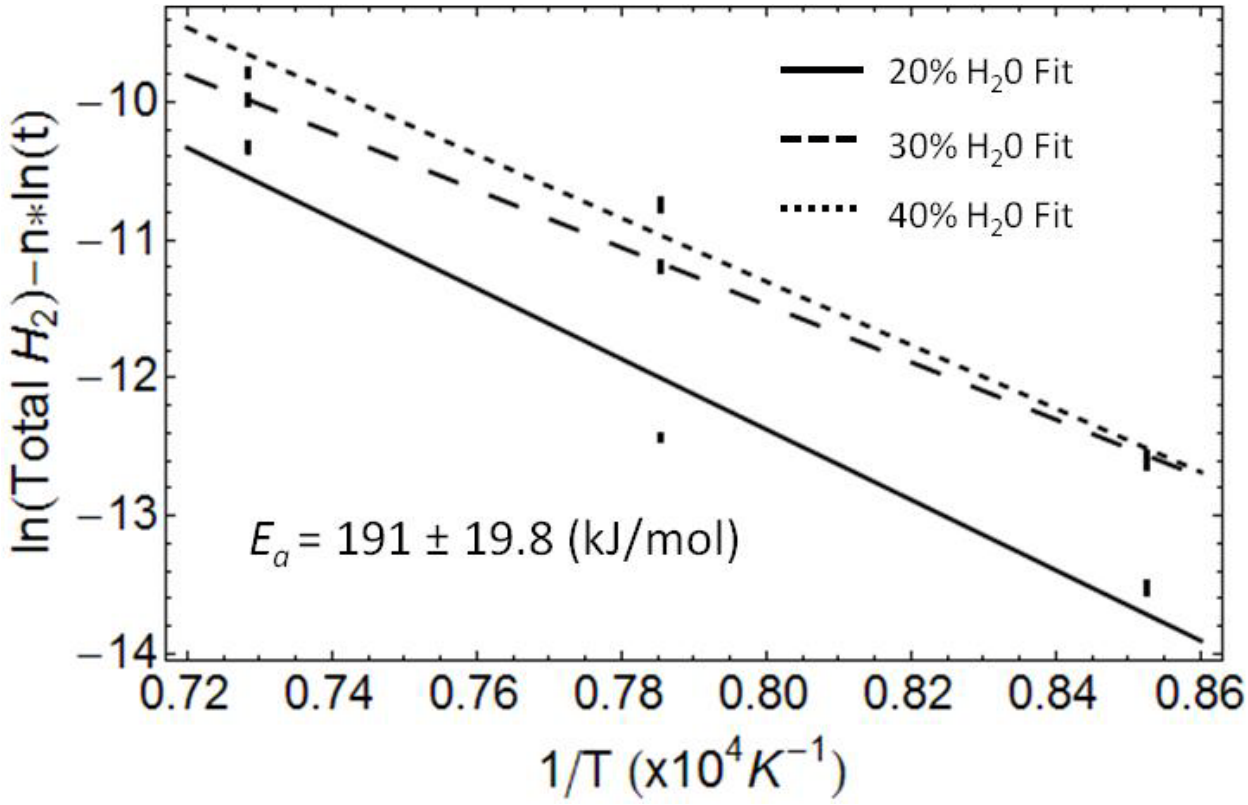

Figure 7-9: Arrhenius plot over all times where the data fits the parabolic rate law (t> 150s).

Calculated activation energies of Fe[43, 45] and FeO[15, 40] oxidation during diffusion limited regimes, and Fe diffusion in Fe_3O_4[46-48] generally range from about 100 to 160 kJ/mol. Iron diffusion through magnetite is the rate limiting step in these processes, and therefore activation energies calculated for Fe and FeO oxidation are usually equal to the activation energy of iron diffusion in magnetite [45]. We have not observed any reported activation energies for oxidation to cobalt ferrite, and therefore can only compare our data with reports of iron and iron oxide oxidation to magnetite. Our calculated activated energies in this regime are higher than for Fe and FeO oxidation. This is likely due to the presence of cobalt, because rather than Fe_3O_4 our

oxide layer consists of $Co_{0.9}Fe_{2.1}O_4$. It is unlikely that this process is limited by either Fe or O diffusion through the ZrO_2 support, as we saw no evidence that a significant amount of Fe was dissolved in the ZrO_2, and the activation energy for O diffusion in YSZ is much less than the activation energy we calculated [49]. Additionally, if we were limited by diffusion through the support, we would have expected to see similar rates for both Fe_3O_4 and $Co_{0.9}Fe_{2.1}O_4$. Therefore, we conclude that the activation energy of iron diffusion through cobalt ferrite is greater than the activation energy through magnetite. Further qualitative evidence of this can be observed when comparing the oxidation rates of Fe_3O_4 and $Co_{0.9}Fe_{2.1}O_4$, in which the rate of oxidation of magnetite is faster under all of the conditions that we investigated.

Following these results, we have derived a global rate expression capable of describing the temporal water oxidation behavior of $Co_{0.9}Fe_{2.1}O_4$ from 900 to 1100 ^oC. Because we are limited by two different mechanisms, namely a reaction order limitation initially followed by a diffusion limitation at longer reaction times, we have incorporated two different expressions with varying kinetic parameters. The initial reaction was capable of being described well by employing the Arrhenius expression based on peak H_2 rates, coupled with a second order reaction model, shown by:

$$rH_2\left[\frac{mol}{g \cdot s}\right] = \frac{d\alpha}{dt} = [y_{H_2O}]^n k_o e^{\frac{-E_a}{RT}}(1-\alpha)^2 \qquad \mathbf{7-8})$$

where the relevant kinetic parameters are the same as those discussed in Figure 7-5, with the exception of k_o. This was determined to be 0.32 moles/g/s rather than 0.39 moles/g/s to account for the addition of the reaction model. The diffusion limited regime could be described well by

an Arrhenius expression with no dependence on water concentration, coupled with a diffusion limited reaction model, shown by:

$$rH_2\left[\frac{mol}{g \cdot s}\right] = \frac{d\alpha}{dt} = k_o e^{\frac{-E_a}{RT}} f(\alpha) \qquad \mathbf{7-9})$$

where $f\ (\alpha)$ was derived from the parabolic rate law and is dependent on the empirically calculated *n*. As shown by the derivation below, $f\ (\alpha)$ can be derived from the parabolic rate law by differentiation and algebraic manipulation.

$$\alpha^n = k_p t \qquad \mathbf{7-10})$$

$$\frac{d\alpha}{dt} = \frac{k_p^{\frac{1}{n}}}{n} t^{\left(\frac{1}{n}-1\right)} \qquad \mathbf{7-11})$$

$$\frac{d\alpha}{dt} = \frac{k_p}{n} (\alpha^n)^{\left(\frac{1}{n}-1\right)} \qquad \mathbf{7-12})$$

$$k = \frac{k_p}{n}, \qquad f(\alpha) = (\alpha^{1-n}) \qquad \mathbf{7-13})$$

$$\frac{d\alpha}{dt} = kf(\alpha) \qquad \mathbf{7-14})$$

We have used the experimentally determined *n* value of 1.94. Water concentration was not included in this kinetic expression because we are limited only by Fe diffusion. Ea was the value calculated in Figure 7-9 and equals 191 ± 19.8 kJ/mol and k_o was derived empirically and determined to be 9 moles/g/s. The time at which the first mechanism transitions to the diffusion limited regime is dependent upon the extent of reaction, and therefore is different for each water concentration and temperature. We have defined this transition to occur when the conversion of a specific data set was equal to 20% of its maximum conversion. Plots of the integral form of the data from 900 ^{o}C to 1100 ^{o}C and fits are shown in Figure 7-10 for 20% H_2O. As expected, the rate of change of the conversions is faster as the temperature is increased, and the models agree well with the data. There is a clear inflection point observed for the fits at low conversions which is due to the transition from the reaction order mechanism to the diffusion limited mechanism. The data does not have such a sharp transition because it does not occur instantaneously, as it was modeled, but gradually over time. Without the inclusion of the initial reaction order model, the predicted diffusion model rates are much more rapid than the experimentally observed rates. Additionally, if we were to only include the reaction order model, the predicted rates eventually become much faster than the observed rates. By including both the reaction order model and the diffusion limited model we are able to capture both the initial rates and the longer-term parabolic rates fairly accurately. There is error that exists between some of the fits and experimental rates is due to the large degree of experimental error, as evidenced in the variability in Figure 7-2. Because we are using the same material and continuously thermally reducing/oxidizing, it is inherently a very complex system in which the reactive species may be changing morphologically depending on the number of cycles that is has withstood. Furthermore, in addition to just one reactive species such as iron, we also have cobalt and zirconia, all of which

are capable of interacting with each other and diffusing as the number of cycles is increased. This may result in dynamic concentration gradients which could have an effect on the oxidation behavior of Fe.

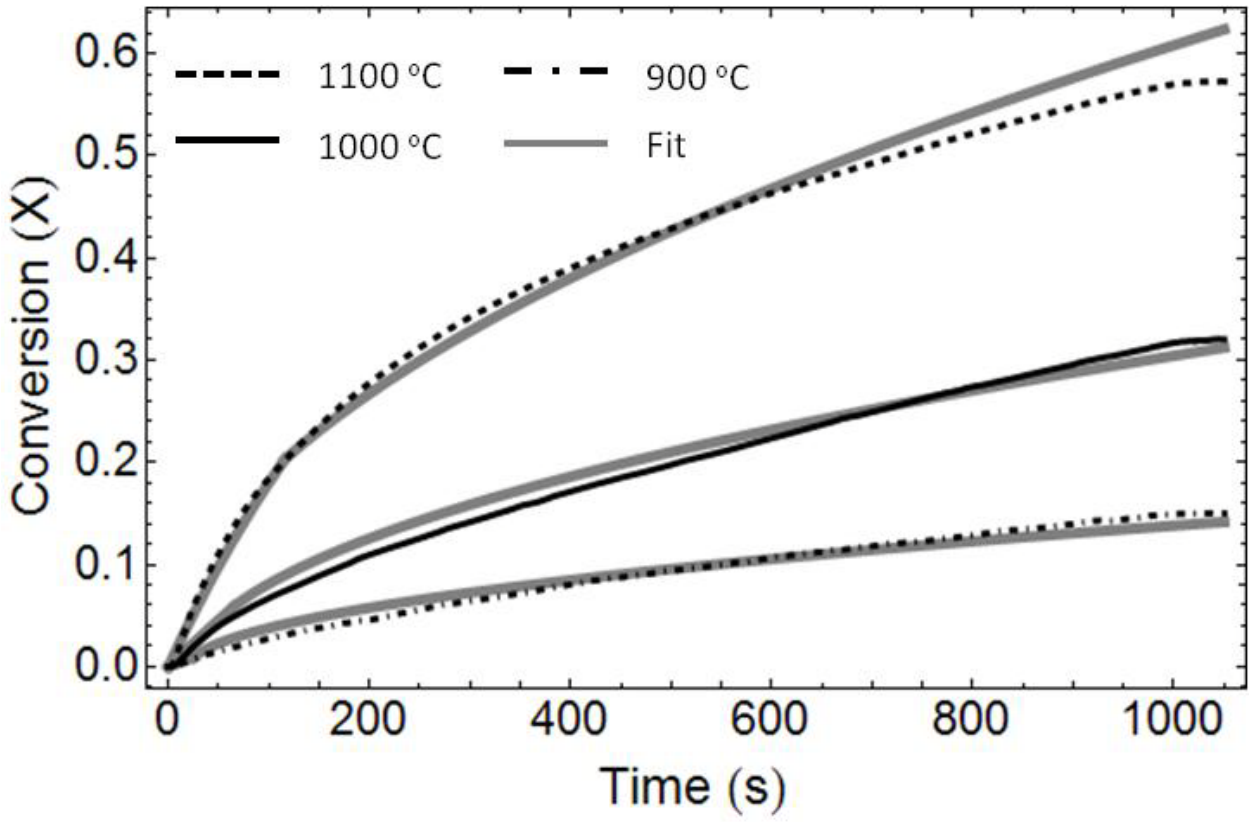

Figure 7-10: Comparison of experimental data to reaction models for 20% H_2O between 900 and 1100 ^oC.

In other less complex reactions, similar mechanistic behavior has been observed when oxidizing metals and metal oxides at high temperatures. For instance, Steinfeld *et. al.* observed a rapid interfacial reaction follow by a slower diffusion limited reaction when oxidizing FeO between 923 and 1473 K and Zn metal between 640 and 754 K with CO_2 [40]. Also, Fe oxidation by air or oxygen is generally characterized by a rapid reaction rate followed by longer term oxidation rate described well by the parabolic rate law. Although our system is more complex than any of these, they are similar in that our only reactive species with the oxidant is

FeO, and so conceptually it makes sense that we observe similar behavior. Additionally, the inclusion of an initial reaction order limited mechanism is more realistic than a diffusion-limited models over all times, because diffusion models are characterized by a nearly infinite reaction rate at a conversion of zero. This is because they are all based off of a functional form similar to $f(\alpha) = 1/\alpha$, and so for very small conversions the reaction rates are infinitely fast.

7.5 Conclusions

Cobalt ferrite ($Co_{0.9}Fe_{2.1}O_4$) and iron oxide (Fe_3O_4) thin films were both successfully utilized in a two step thermochemical water splitting cycle to produce H_2. H_2 conversions of both materials were comparable and increased as oxidation temperature was increased. This was surprising considering the thermodynamically predicted extent of reduction is expected to be greater for cobalt ferrite under these reduction conditions (1450 ^oC). The oxidation rates exhibited Arrhenius type behavior from 900 to 1100 ^oC, but H_2 was capable of being generated even at temperatures as high as 1400 ^oC. This is due to the occurrence of both oxidation and reduction reactions occuring, and results in simultaneous production of H_2 and O_2 for an indefinite amount of time. The temperature at which this reaction occurs ($T > 1250\ ^oC$) is much less than that required for water thermolysis.

Master plot analysis was utilized to compare the experimental data to various functional forms representative of reaction mechanisms, and it was determined that there are two distinct reaction limited regimes. Initially, the reaction is limited by a second order reaction mechanism, and the activation energy and H_2O reaction order during this regime were determined to be 119.76 ± 8.81 kJ/mole and 0.70 ± 0.32, respectively. Following this mechanism, the reaction was limited by diffusion, and agreed well with the parabolic rate law. This was accompanied by an

increase in the activation energy, which was determined to be 191 ± 19.8 kJ/mol. This activation energy is higher than all other published reports of Fe or FeO oxidation, or Fe diffusion through magnetite. As a result, we believe that the activation energy for Fe diffusion through cobalt ferrite is higher than magnetite, resulting in the observed slower reaction rates. By combining both reaction mechanisms into a single rate expression, we were able to derive a global rate expression capable of characterizing the temporal behavior of the oxidation of cobalt ferrite for temperatures between 900 and 1100 ^{o}C, and water concentrations from 20% to 40%.

7.6 References

[1] Perkins C, Weimer AW. Likely near-term solar-thermal water splitting technologies. International Journal Of Hydrogen Energy 2004;29:1587.

[2] Sturzenegger M, Nuesch P. Efficiency analysis for a manganese-oxide-based thermochemical cycle. Energy 1999;24:959.

[3] Kodama T, Gokon N, Yamamoto R. Thermochemical two-step water splitting by ZrO2-supported NixFe3-xO4 for solar hydrogen production. Solar Energy 2008;82:73.

[4] Kodama T, Kondoh Y, Yamamoto R, Andou H, Satou N. Thermochemical hydrogen production by a redox system of ZrO2-supported Co(II)-ferrite. Solar Energy 2005;78:623.

[5] Kodama T, Nakamuro Y, Mizuno T. A two-step thermochemical water splitting by iron-oxide on stabilized zirconia. Journal of Solar Energy Engineering-Transactions of the Asme 2006;128:3.

[6] Miller JE, Allendorf MD, Diver RB, Evans LR, Siegel NP, Stuecker JN. Metal oxide composites and structures for ultra-high temperature solar thermochemical cycles. Journal of Materials Science 2008;43:4714.

[7] Gokon N, Hasegawa T, Takahashi S, Kodama T. Thermochemical two-step water-splitting for hydrogen production using Fe-YSZ particles and a ceramic foam device. Energy 2008;33:1407.

[8] Ernst FO, Steinfeld A, Pratsinis SE. Hydrolysis rate of submicron Zn particles for solar H-2 synthesis. International Journal Of Hydrogen Energy 2009;34:1166.

[9] Ma XF, Zachariah MR. Size-resolved kinetics of Zn nanocrystal hydrolysis for hydrogen generation. International Journal Of Hydrogen Energy;35:2268.

[10] Agrafiotis C, Roeb M, Konstandopoulos AG, Nalbandian L, Zaspalis VT, Sattler C, Stobbe P, Steele AM. Solar water splitting for hydrogen production with monolithic reactors. Solar Energy 2005;79:409.

[11] Lorentzou S, Agrafiotis CC, Konstandopoulos AG. Aerosol spray pyrolysis synthesis of water-splitting ferrites for solar hydrogen production. Granular Matter 2008;10:113.

[12] Allendorf MD. Two-Step Water Splitting Using Mixed-Metal Ferrites: Thermodynamic Analysis and Characterization of Synthesized Materials. Energy & Fuels 2008;22:4115.

[13] Charvin P, Abanades S, Flamant G, Lemort F. Two-step water splitting thermochemical cycle based on iron oxide redox pair for solar hydrogen production. Energy 2007;32:1124.

[14] Khedr MH, Omar AA, Abdel-Moaty SA. Reduction of carbon dioxide into carbon by freshly reduced CoFe2O4 nanoparticles. Materials Science and Engineering a-Structural Materials Properties Microstructure and Processing 2006;432:26.

[15] Go KS, Son SR, Kim SD. Reaction kinetics of reduction and oxidation of metal oxides for hydrogen production. International Journal Of Hydrogen Energy 2008;33:5986.

[16] Neises M, Roeb M, Schmuker M, Sattler C, Pitz-Paal R. Kinetic investigations of the hydrogen production step of a thermochemical cycle using mixed iron oxides coated on ceramic substrates. International Journal of Energy Research;34:651.

[17] Tamaura Y, Steinfeld A, Kuhn P, Ehrensberger K. Production Of Solar Hydrogen By A Novel, 2-Step, Water-Splitting Thermochemical Cycle. Energy 1995;20:325.

[18] Tamaura Y, Ueda Y, Matsunami J, Hasegawa N, Nezuka M, Sano T, Tsuji M. Solar hydrogen production by using ferrites. 1999. p.55.

[19] Han SB, Kang TB, Joo OS, Jung KD. Water splitting for hydrogen production with ferrites. Solar Energy 2007;81:623.

[20] George SM, Ott AW, Klaus JW. Surface chemistry for atomic layer growth. Journal of Physical Chemistry 1996;100:13121.

[21] Hakim LF, Blackson J, George SM, Weimer AW. Nanocoating individual silica nanoparticles by atomic layer deposition in a fluidized bed reactor. Chemical Vapor Deposition 2005;11:420.

[22] Leskela M, Ritala M. Atomic layer deposition (ALD): from precursors to thin film structures. Thin Solid Films 2002;409:138.

[23] Niinisto L, Paivasaari J, Niinisto J, Putkonen M, Nieminen M. Advanced electronic and optoelectronic materials by Atomic Layer Deposition: An overview with special emphasis on recent progress in processing of high-k dielectrics and other oxide materials. Physica Status Solidi a-Applied Research 2004;201:1443.

[24] Ferguson JD, Weimer AW, George SM. Surface chemistry and infrared absorbance changes during ZnO atomic layer deposition on ZrO2 and BaTiO3 particles. Journal of Vacuum Science & Technology A 2005;23:118.

[25] Hakim LF, George SM, Weimer AW. Conformal nanocoating of zirconia nanoparticles by atomic layer deposition in a fluidized bed reactor. Nanotechnology 2005;16:S375.

[26] King DM, Spencer JA, Liang X, Hakim LF, Weimer AW. Atomic layer deposition on particles using a fluidized bed reactor with in situ mass spectrometry. Surface & Coatings Technology 2007;201:9163.

[27] Wank JR, George SM, Weimer AW. Coating fine nickel particles with Al2O3 utilizing an atomic layer deposition-fluidized bed reactor (ALD-FBR). Journal of the American Ceramic Society 2004;87:762.

[28] Lim BS, Rahtu A, Gordon RG. Atomic layer deposition of transition metals. Nature Materials 2003;2:749.

[29] Rooth M, Lindahl E, Harsta A. Atomic layer deposition of Co3O4 thin films using a CoI2/O-2 precursor combination. Chemical Vapor Deposition 2006;12:209.

[30] Klepper KB, Nilsen O, Fjellvag H. Epitaxial growth of cobalt oxide by atomic layer deposition. Journal of Crystal Growth 2007;307:457.

[31] Klepper KB, Nilsen O, Fjellvag H. Growth of thin films of Co3O4 by atomic layer deposition. Thin Solid Films 2007;515:7772.

[32] de Ridder M, van de Ven PC, van Welzenis RG, Brongersma HH, Helfensteyn S, Creemers C, Van Der Voort P, Baltes M, Mathieu M, Vansant EF. Growth of iron oxide on yttria-stabilized zirconia by atomic layer deposition. Journal of Physical Chemistry B 2002;106:13146.

[33] Nilsen O, Lie M, Foss S, Fjellvag H, Kjekshus A. Effect of magnetic field on the growth of alpha-Fe2O3 thin films by atomic layer deposition. Applied Surface Science 2004;227:40.

[34] Lie M, Fjellvag H, Kjekshus A. Growth of Fe2O3 thin films by atomic layer deposition. Thin Solid Films 2005;488:74.

[35] Bachmann J, Jing J, Knez M, Barth S, Shen H, Mathur S, Gosele U, Nielsch K. Ordered iron oxide nanotube arrays of controlled geometry and tunable magnetism by atomic layer deposition. Journal of the American Chemical Society 2007;129:9554.

[36] Rooth M, Johansson A, Kukli K, Aarik J, Boman M, Harsta A. Atomic layer deposition of iron oxide thin films and nanotubes using ferrocene and oxygen as precursors. Chemical Vapor Deposition 2008;14:67.

[37] Scheffe JR, Frances A, King DM, Liang XH, Branch BA, Cavanagh AS, George SM, Weimer AW. Atomic layer deposition of iron(III) oxide on zirconia nanoparticles in a fluidized bed reactor using ferrocene and oxygen. Thin Solid Films 2009;517:1874.

[38] Lie M, Klepper KB, Nilsen O, Fjellvag H, Kjekshus A. Growth of iron cobalt oxides by atomic layer deposition. Dalton Transactions 2008:253.

[39] Etievant C. SOLAR HIGH-TEMPERATURE DIRECT WATER SPLITTING - A REVIEW OF EXPERIMENTS IN FRANCE. Solar Energy Materials 1991;24:413.

[40] Loutzenhiser PG, Galvez ME, Hischier I, Stamatiou A, Frei A, Steinfeld A. CO2 Splitting via Two-Step Solar Thermochemical Cycles with Zn/ZnO and FeO/Fe3O4 Redox Reactions II: Kinetic Analysis. Energy & Fuels 2009;23:2832.

[41] Gotor FJ, Criado JM, Malek J, Koga N. Kinetic analysis of solid-state reactions: The universality of master plots for analyzing isothermal and nonisothermal experiments. Journal of Physical Chemistry A 2000;104:10777.

[42] Perez-Maqueda LA, Criado JM, Gotor FJ, Malek J. Advantages of combined kinetic analysis of experimental data obtained under any heating profile. Journal of Physical Chemistry A 2002;106:2862.

[43] del Campo L, Perez-Saez RB, Tello MJ. Iron oxidation kinetics study by using infrared spectral emissivity measurements below 570 degrees C. Corrosion Science 2008;50:194.

[44] Cabrera N, Mott NF. THEORY OF THE OXIDATION OF METALS. Reports on Progress in Physics 1948;12:163.

[45] Chen RY, Yuen WYD. Review of the high-temperature oxidation of iron and carbon steels in air or oxygen. Oxidation of Metals 2003;59:433.

[46] Dieckmann R, Schmalzried H. POINT-DEFECTS AND CATION DIFFUSION IN MAGNETITE. Zeitschrift Fur Physikalische Chemie-Frankfurt 1975;96:331.

[47] Dieckmann R, Schmalzried H. DEFECTS AND CATION DIFFUSION IN MAGNETITE .1. Berichte Der Bunsen-Gesellschaft-Physical Chemistry Chemical Physics 1977;81:344.

[48] Hendy SC, Laycock NJ, Ryan MP. Atomistic modeling of cation transport in the passive film on iron and implications for models of growth kinetics. Journal of the Electrochemical Society 2005;152:B271.

[49] Kilo M, Argirusis C, Borchardt G, Jackson RA. Oxygen diffusion in yttria stabilised zirconia - experimental results and molecular dynamics calculations. Physical Chemistry Chemical Physics 2003;5:2219.

7.7 Supplemental Figures

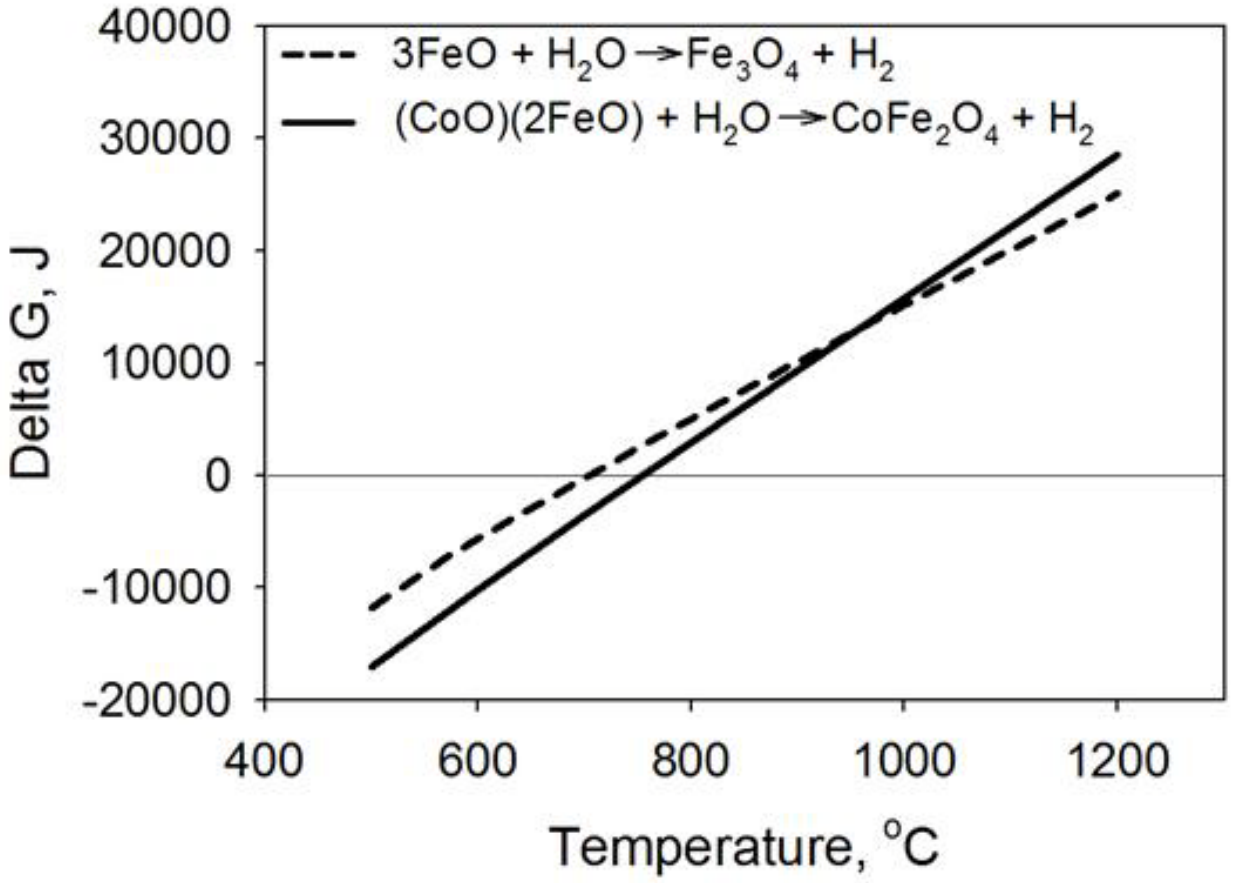

Supplemental Figure 7-11: ΔG verses temperature for cobalt ferrite and iron oxide oxidation reactions.

CHAPTER 8 KINETIC ANALYSIS OF COMMERCIALLY AVAILABLE CEO_2 FELTS FOR SOLAR THERMOCHEMICAL H_2 PRODUCTION

8.1 Abstract

The feasibility of using commercially available, un-doped, ceria (CeO_2) felts in a thermochemical redox cycle to produce H_2 has been explored, and a detailed kinetic analysis of the oxidation reaction is discussed. Reduction is achieved at 1450 ^oC, and the subsequent H_2 producing step is studied from 700 to 1200 ^oC and H_2O mole fractions of 0.04 to 0.32. The O_2 and H_2 equilibrium compositions remain constant for up to 30 redox cycles, and sintering appears to be abated by microscopy analysis. The average amount of H_2 produced is 280.9 ± 45.8 μmoles/g CeO_2. The re-oxidation rates are faster on a per mass basis than similar ferrite based-cycles because the surface area is largely unaffected by thermal cycling.

The oxidation reaction is governed by a first order reaction mechanism $(1-\alpha)$ at low temperatures and conversions, but at higher temperatures the mechanism transitions to a second order reaction $(1-\alpha)^2$. This is attributed to the onset of the thermodynamically favored reverse reaction at elevated temperatures. In fact, the reaction rates decrease above oxidation temperatures of 1000 ^oC, due to this competition. The activation energy is calculated between 700 and 900 ^oC from $0.2<\alpha<0.5$, and determined to be 35.5 ± 13.3 kJ/mol. An Arrhenius expression, coupled with a first order reaction mechanism is used to model the experimentally observed reaction rates where the forward reaction was predominant.

8.2 Introduction

Ceria (CeO_2) and metal doped ceria have received a tremendous amount of interest recently as "high temperature" solar thermochemical water splitting candidates for renewable hydrogen production. They are capable of splitting water using solar energy according to the generic two step redox cycle shown below, where the only net inputs are solar energy and water and the outputs are O_2 and H_2.

$$CeO_2 + Solar\ Thermal\ Energy \rightarrow CeO_{2-\delta} + \frac{\delta}{2} O_2 \qquad \mathbf{8-1})$$

$$CeO_{2-\delta} + \delta H_2O \rightarrow CeO_2 + \delta H_2 \qquad \mathbf{8-2})$$

The first step proceeds via the thermal decomposition of CeO_2, usually to a non-stoichiometric state, and O_2 is evolved. The reduced ceria is then re-oxidized in the second lower temperature step using steam to produce H_2. The degree of reduction (Ce^{4+} to Ce^{3+}) is highly dependent on temperature, and complete reduction to Ce_2O_3 is only achieved at very high temperatures (≈2000 ^oC) [1]. Under these conditions most ceramic reactor construction materials become unstable and radiation heat losses are considerable because of their fourth order temperature dependence. Therefore, reduction at lower temperatures (≈1400 - 1500 ^oC) is more common, resulting in reduction to a non-stoichiometric state where the ceria's fluorite structure is maintained [2, 3].

Ceria has some distinct advantages over analogous ferrite gas splitting cycles. Generally, ferrite gas splitting cycles have upper operating temperatures that are very close to their melting temperatures, and as a result extensive sintering is observed [4-6]. Ceria, on the other hand, has a much higher melting temperature (2300 ^oC) but has upper operating temperatures that are comparable to ferrite cycles [7]. Because of this, the degree of sintering is less than ferrites and

they are able to maintain their surface area more effectively, resulting in observed oxidation rates that are generally faster than ferrites [1, 2, 6]. It has also been suggested that the oxidation rates may not be limited by bulk diffusion through an oxide scale because of high oxygen diffusivities and a fixed crystal structure [2]. Ceria and ferrites are both capable of being cycled with relative ease compared to other high temperature cycles, such as the ZnO/Zn and sodium manganese cycles, because they remain as solids through the redox cycle rather than undergoing phase transformations [8-10]. On the other hand, because ceria is reduced to a non-stoichimetric state, the degree of reduction is less than other high temperature thermochemical cycles, resulting in less H_2 produced per mole of material. Also, ceria is highly reactive with most materials and has a significant vapor pressure at the operating temperatures of interest, so maintaining its chemical state proves to be challenging.

It is well understood that dopants have an effect on the thermodynamics of ceria reduction [11-13]. The addition of ceria dopants ($Ce_{1-x}M_xO_{2-\delta,}$ where M is commonly Gd or Sm), has been widely studied for enhancing the conductivity of solid oxide fuel cells, which is directly related to the degree of oxygen vacancies [11, 12]. The introduction of dopants has been shown to increase the degree of reduction at low oxygen partial pressures compared to un-doped ceria. Therefore, the addition of dopants such as zirconium [3] and samarium [2] and metal oxides ($MO_{x,}$ M = Mn, Ni, Fe, Cu) [14, 15] is being explored as a means to increase the thermodynamic driving force of reduction at lower temperatures for uses in solar thermochemical redox cycles.

Abanades *et.al.* were the first to study the thermal decomposition of CeO_2 to Ce_2O_3 at temperatures as high as 2000 ^oC in a solar reactor. The reduced ceria was capable of reacting with steam at temperatures between 400-600 ^oC to re-oxidize the ceria and produce H_2 in less than five minutes, which is considerably faster than the rate of ferrite oxidation. However, the

upper operating temperatures are much higher and at these conditions reactor construction materials are expected to be a concern. More recently, they investigated doping ceria with as much as 50% zirconium ($Ce_{1-x}Zr_xO_2$) to increase the thermodynamic driving force for reduction at lower temperatures [3]. Thermogravimetric analysis indicated the mass loss due to thermal decomposition at 1500 ^oC could be increased from 0.4% to 2% by increasing the Zr content from 0% to 50%. The reduced material was still capable of reacting with water to produce H_2 at temperatures between 800 and 1000 ^oC, but this temperature is higher than that required for the oxidation of undoped ceria.

Samerian doped ceria CO_2/H_2O splitting for the production of syngas and methane has been studied by Haile *et.al.*[2]. The Sm-doped ceria (15% Sm) was chemically reduced at 800 ^oC with a mixture of H_2, H_2O and Ar to an oxidation state that would be expected at 1500 ^oC via thermal reduction. The reduced ceria was then exposed to steam, CO_2, or a combination thereof at temperatures between 500 ^oC and 700 ^oC to produce H_2 and/or CO. The activation energy and reaction order for CO_2 splitting (0.8 eV and 0.77) was higher than H_2O splitting (0.52 eV and 0.54), and a ratio of $H_2/CO = 2$ was achievable by flowing a 2:1 ratio of H_2O to CO_2: the addition of a nickel catalyst to the surface of the ceria resulted in producing CH_4 in addition to CO and H_2. This reaction was favorable at lower temperatures (T = 400 ^oC) because of the thermodynamic driving force at lower temperatures to form carbon rather than CO_2. Kaneko *et.al.* have studied the feasibility of using solid solutions of ceria and various metal oxides (MO_x, M = Mn, Ni, Fe, Cu) to split water for hydrogen production [14, 15]. They observed an increase in the degree of reduction when using solid solutions of ceria and NiO or MnO. The materials were capable of being reduced at temperatures between 1400 ^oC and 1500 ^oC, and oxidized to produce H_2 at 1000 ^oC.

We are interested in studying the water splitting reactions of un-doped commercially available ceria felts, which are being considered as potential reactive intermediates in Sandia National Laboratory's counter-rotating-ring receiver/reactor/recuperator (CR5) reactor [16], as part of their Sunshine to Petrol ("S2P") program [17]. The goal is to determine the optimal conditions for both reduction and oxidation reactions and to baseline the materials for comparison to other potential water splitting candidates, including other metal-doped ceria samples, and ferrites. From these experiments, we hope to provide some mechanistic insight into the oxidation reactions and determine relevant kinetic parameters that can be incorporated into future reactor and material designs.

8.3 Experimental Methods

Ceria (CeO_2) felts (CeF-100) were purchased from Zircar Zirconia, Inc. Samples are greater than 99% pure with slight impurities of Al_2O_3, SiO_2, and Fe_2O_3. The surface area was measured to be 5.4 ± 0.035 m^2/g by BET analysis. Surface area measurements were made with a Micrometrics Gemini V BET surface area analyzer. Scanning electron microscopy (SEM) and energy-dispersive spectroscopy (EDS) were performed on a in a Zeiss scanning electron microscope at 15 kV. Samples were sputtered with a thin layer of palladium before analysis to prevent charging

Oxidation and thermal reduction experiments were conducted in a vertically oriented stagnation flow reactor (SFR) at 75 Torr, which has been described in Chapter 5. Gases exiting the flow reactor were sampled using a differentially pumped, modulated effusive beam mass spectrometer (Extrell C50, 500 amu). Upon expansion into the second of three pumping stages, the molecular beam is chopped by a resonant modulator driven at 200 Hz and ionized by electron impact at 30 eV. Modulated ion current from the electron multiplier is routed through a lock-in

amplifier and discriminated against DC background. This increases detector sensitivity and digitally filters out ion current resulting from gases that persist in the ionization volume thus enabling real-time baseline correction and a higher degree of precision for quantifying component partial pressures. A mixture of 5 vol.-% H_2 in He was used to calibrate the detector.

Mass flow controllers were used to meter all gas feed rates. The reactor exhaust was throttled, allowing for feedback control of the reactor pressure to any desired setpoint within the range 1 to 760 Torr. Water was delivered through an evaporator fed by micro-syringe pump. H_2O/He concentrations were calculated by assuming steam behaves as an ideal gas at 75 Torr. Liquid nitrogen traps were used to condense H_2O prior to sampling the reactor effluent with the mass spectrometer. Between 100 and 200 mg of sample material were placed in the reactor on a YSZ holder fabricated by Zircar Zirconia, Inc.

Thermal reduction consisted of heating the sample to 1450 ^oC at 15 ^oC/minute and dwelling for 35 minutes while flowing 500 sccm He. Following reduction, the temperature was reduced at 15 ^oC/minute to the desired oxidation set point while continuing to flow He. Once achieved, a steam/He mixture was delivered into the reactor for 600s. Oxidation experiments were conducted at temperatures ranging from 700 to 1200 ^oC, and mole fractions of H_2O from 0.04 to 0.32.

All thermodynamic values were obtained from the thermodynamic software package, FactSage version 6.0.

8.4 Results

8.4.1 Temporal Behavior/Cycling

The onset of O_2 evolution during thermal reduction begins around 1200 ^oC, and reaches a maximum rate near 1400 ^oC, as seen in Figure 8-1. The decomposition rate is characterized by an

initial acceleration which eventually plateaus near 1400 ^{o}C, and begins to decrease once the set point of 1450 ^{o}C is achieved. The rate then decelerates and eventually plateaus to a rate that is above the baseline. This behavior is similar to that observed for the decomposition of other ceria and ferrite based powders [3, 7]. We have performed experiments at temperatures as high as 1500 ^{o}C, but did not observe a substantial improvement in the degree of reduction to justify operating at temperatures this high.

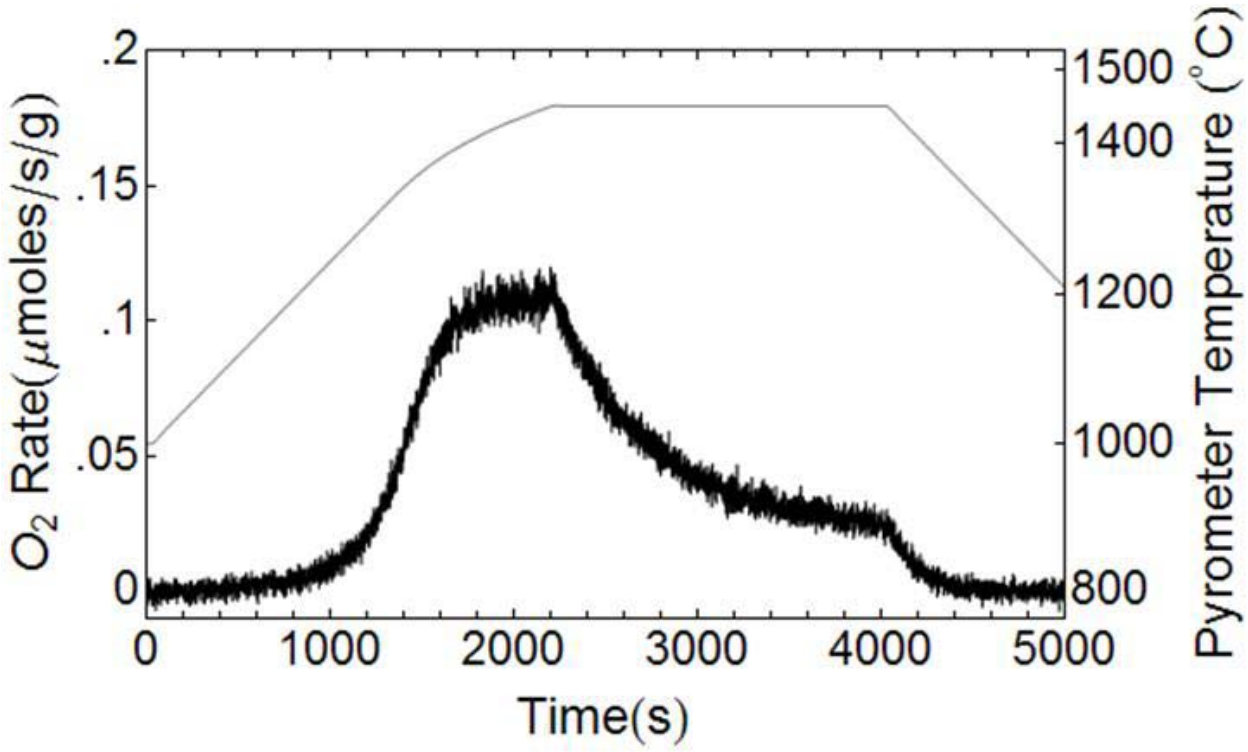

Figure 8-1: Temporal O_2 evolution during thermal decomposition at 1450 ^{o}C.

It is not clear what the rate limiting mechanism is that results in the asymptotic behavior for long reduction times. Clearly, the reaction is not thermodynamically limited because the reaction is still progressing, but a more detailed kinetic analysis of the decomposition must be performed to understand what limits the rate of the reaction. Also of interest is the observation that the ceria's performance improved remarkably after the first redox cycle. The first attempt at reduction did

not begin until much higher temperatures than the data shown in Figure 8-1, and less total O_2 was evolved. However, subsequent reductions resulted in behavior more characteristic of the decomposition discussed above. It is not clear whether this behavior is due to inherent impurities in the ceria leaching out over time, or because of a reaction between the YSZ sample holder and the ceria. It is well documented that the introduction of dopants such as Zr, lead to lower decomposition temperatures by stabilizing the oxygen deficient fluorite structure at lower temperatures than un-doped ceria [3].

Temporal oxidation rates are characterized by a rapid increase in H_2 production, followed by a deceleration back to baseline. The rate of H_2 production increases with temperature from 700 ^{o}C to 1000 ^{o}C, and decreases as the temperature is increased beyond this point. This is observed in Figures 8-2a and 8-2b, where the H_2 production rates for all oxidation temperatures are shown while flowing 16% H_2O. From 700 to 900 ^{o}C, the peak rates increase from 2.5 μmoles/g/s to 5 μmoles/g/s and from 1000 to 1200 ^{o}C decrease from 6.5 μmoles/g/s to 3 μmoles/g/s. Obviously, the Ea is not negative above 1000 C, but rather the reverse reaction likely becomes more favorable as the temperature is increased, resulting in slower observed reaction rates. Thermodynamic calculations have indicated that the reaction of fully reduced ceria (Ce_2O_3) and steam become unfavorable at temperatures greater than 700 K, based on Gibbs free energy minimization calculations [18].

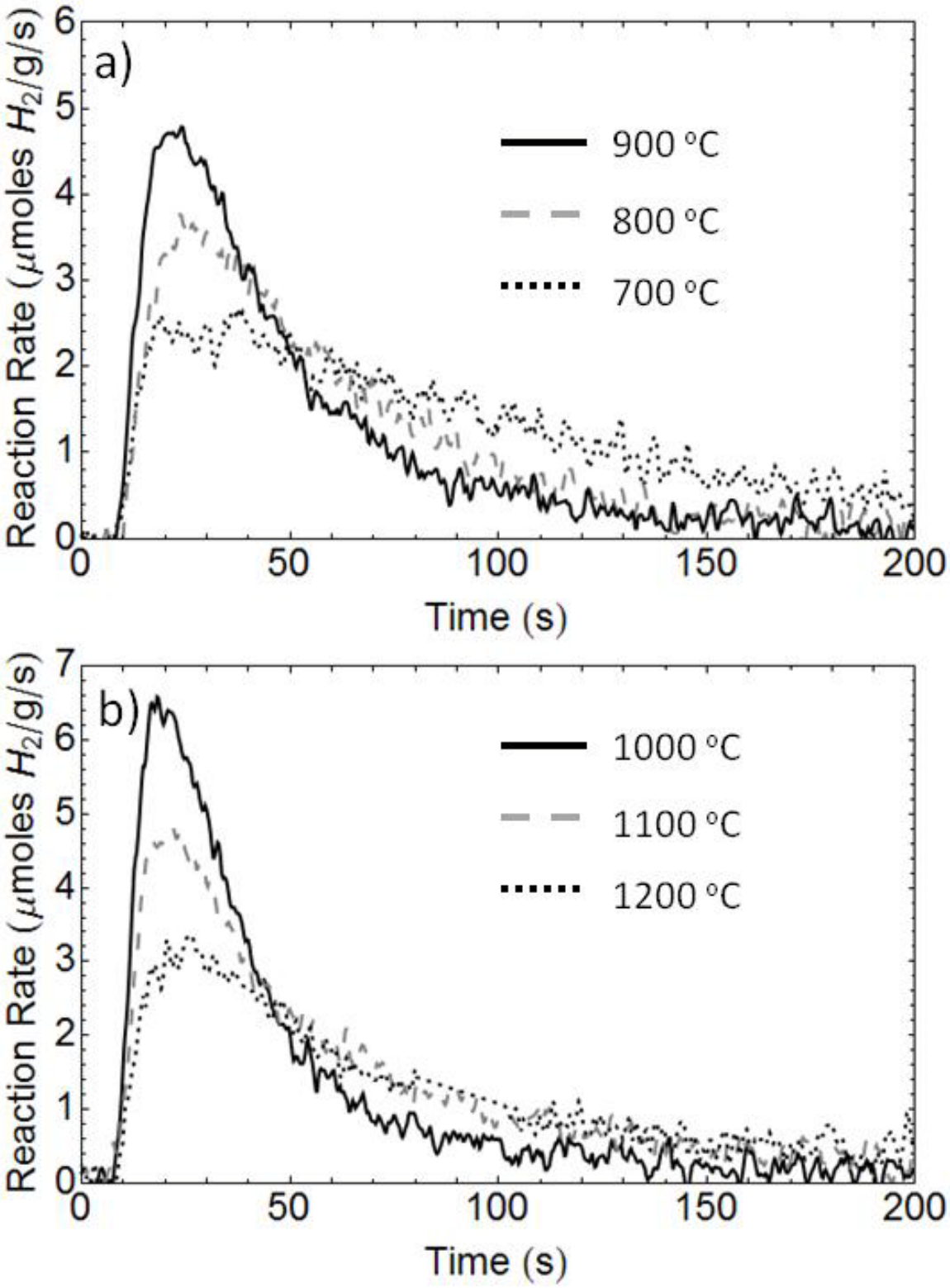

Figure 8-2: Temporal H_2 evolution from 700-900°C (a) and 1000-1200 °C (b). Mole fraction H_2O = 0.16.

The observed reaction rates are due to contributions from the forward and reverse reactions, and are related to each other by their equilibrium constant, *K*. This is related to the Gibbs free energy change of the reaction by the following equation,

$$RTlnK = -\Delta G_{rxn} \qquad \mathbf{8-3})$$

where *R* is the ideal gas constant, *T* is the absolute temperature and ΔG_{rxn} is the Gibbs free energy for standard conditions (p_{gas} = 1 atm). When the equilibrium constant is greater than one, the ΔG_{rxn} is negative, and the forward reaction is more thermodynamically favorable than the reverse. For values less than one, the reverse reaction is more favorable than the forward. Knowledge of this value alone is not enough to make any predictions about the observed reaction rates, but it can give some insight into the temperature range where a given reaction is expected to be favorable. The observed peak H_2 rates for all experimental conditions are shown in the Arrhenius plot shown in Figure 8-3. Also included are the ΔG_{rxn} values of the following idealized reversible reaction.

$$Ce_6O_{11} + H_2O \leftrightarrow 6CeO_2 + H_2 \qquad \mathbf{8-4})$$

The peak rates increase linearly from 700 to 900 ^{o}C, and climax somewhere between 900 and 1000 ^{o}C. After this point, the rates decrease with temperature, due to competition with the reverse reaction as suggested by the equilibrium calculations. At temperatures greater than 900 ^{o}C, $\Delta G_{rxn} > 0$, and the reverse reaction is more thermodynamically favored than the forward, which results in slower observed H_2 production rates. Although the decrease in peak reaction

rates as a function of temperature can be explained by equilibrium calculations, there are several factors which could contribute to disagreements between the observed reaction rates and thermodynamic predictions. For example, kinetic limitations could result in conditions where the forward reaction proceeds, even at temperatures where thermodynamics predicts the reverse reaction is more favorable.

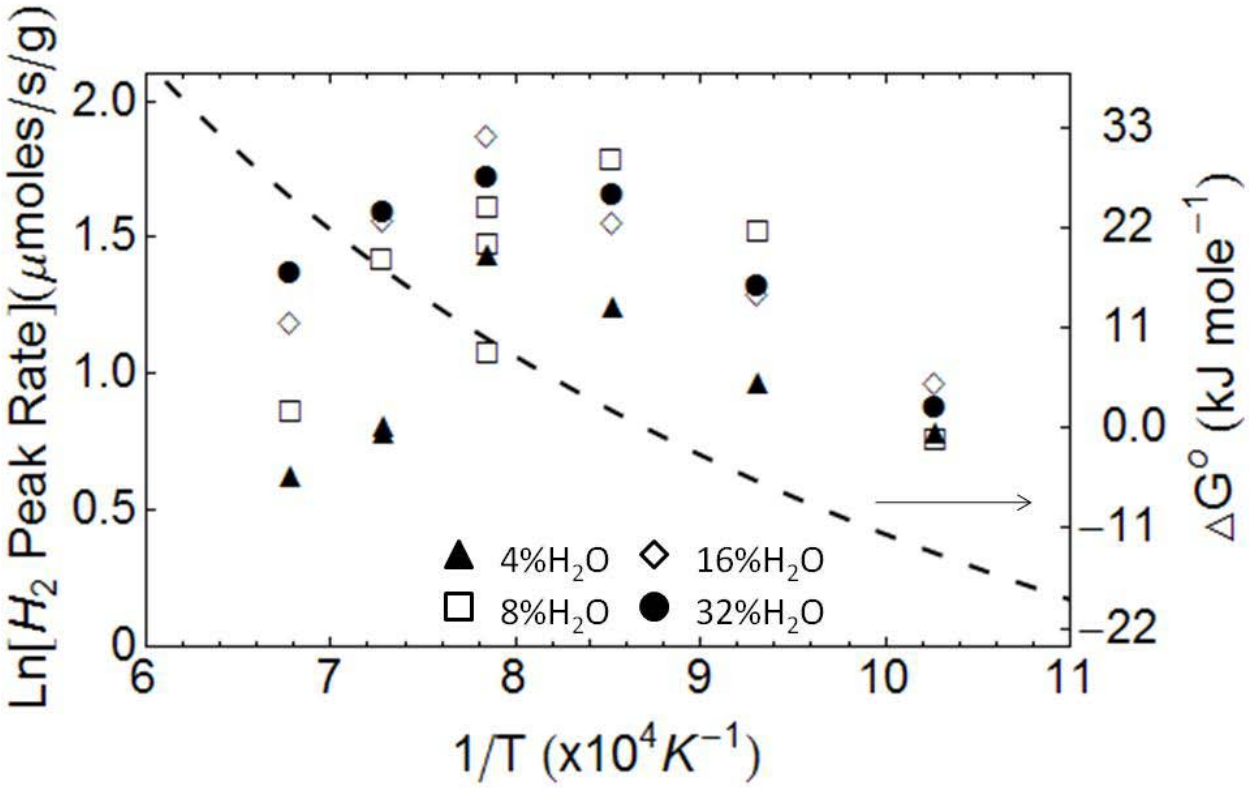

Figure 8-3: Arrhenius plot of peak H_2 rates for all experimental conditions shown with DG^{o}_{rxn}.

Behavior similar to this has been observed experimentally in ferrite-based water oxidation studies [7]. Water oxidation rates of most ferrites continue to increase well above temperatures where thermodynamics would predict because the reaction is limited by diffusion through their bulk. Additionally, oxidation conditions of thermochemical redox cycles are generally not operated close to equilibrium. The solid samples are usually stationary, while a sweeping gas

carries the reaction products away from their surface. However, based on these thermodynamic calculations and the observed decrease in reaction rates at elevated temperatures, it is clear that the reverse reaction is competing with the forward.

The ability of ceria to produce consistent amounts of hydrogen repetitively is vital for large scale operations. Ideally, it would remain chemically active for thousands or even millions of cycles. Because we are constrained by relatively slow heating and cooling times it is not feasible to cycle the ceria thousands of times in our current configuration, but we have monitored changes in the samples equilibrium H_2 and O_2 productivity over 30 redox cycles and do not observe a noticeable decline in performance. The total H_2 and O_2 produced as a function or redox cycles is shown in Figure 8-4. There is a large amount of variability, especially in the H_2 production, which is mainly caused by experimental variation and poor signal to noise. Also, each of the data points shown are for experiments that were conducted under varying conditions (i.e. H_2O mole fraction and oxidation temperature). However, there is not a systematic trend that would indicate sample degradation due to a loss of surface area or other chemical transformations. These results are different than those observed by Haile *et.al.*, who observed a decrease in equilibrium H_2 and O_2 production for the first 100 cycles using Sm-doped ceria powders. The differences may lie in the morphological differences between the samples. The ceria used in this study was a web-like support with 5 to 10 μm thick threads about 100 μm long (see Supplemental Figure 8-8). Therefore, there is less active surface area available to sinter than powder materials, resulting in more stable H_2 production. Ideally, the ratio of H_2 to O_2 produced for a given redox cycle would be 2:1, assuming that water is decomposed stoichiometrically. We observe slightly more O_2 than would be expected for a stoichiometric reaction (280.9 ± 45.8

μmoles H_2/g vs. 185.4 ± 38.9 μmoles O_2/g), which is attributed to small air leaks within the reactor or O_2 impurities within the reactant gases.

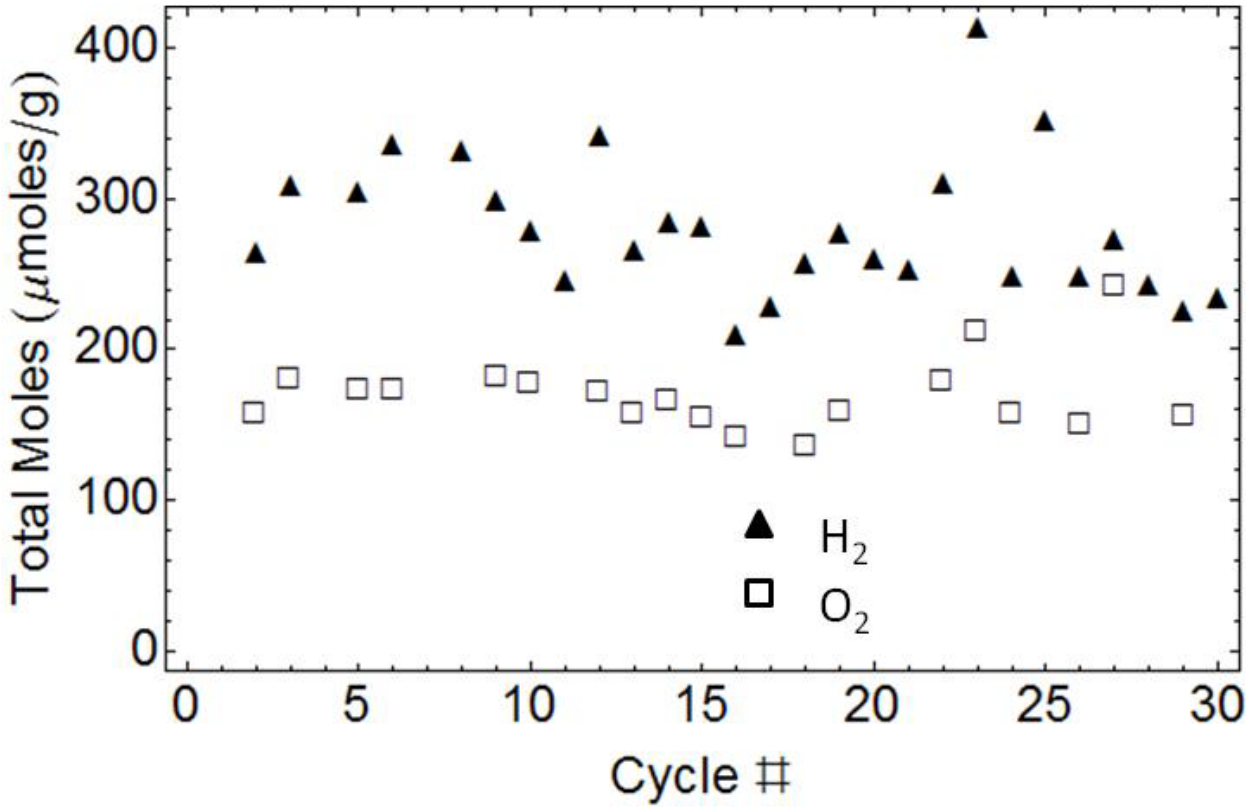

Figure 8-4: Total H_2 and O_2 generated over the course of 30 redox cycles. Experimental conditions range from 700 to 1200 ^oC, and 0.04 to 0.32 mole fraction H_2O.

8.4.2 Kinetic Investigation

Previous investigations of ceria oxidation for high-temperature gas splitting processes have suggested that reaction rates are not limited by diffusion, but this has largely been based on circumstantial evidence. Calculated characteristic diffusion times were sufficiently fast compared to measured reaction rates that diffusion was ruled out as a rate limiting mechanism [18]. For this study, a rigorous kinetic analysis has been employed to determine the governing rate limiting mechanisms. Specifically, measured differential rate data has been compared to various

functional forms of known solid state kinetic models using master plot methods [19], which have been used extensively in solid state thermal analysis [20-22]. The advantage of this analysis is that the data is capable of being normalized in such a way that it is only dependent on the governing kinetic model and not other kinetic variables. Therefore, individual sets of differential rate data can be compared to known kinetic models to determine those that are characteristic of measured data without any knowledge of kinetic parameters. The kinetic model, f(α), is a function which is capable of describing the mechanism of a solid state reaction, and is incorporated into the differential form of a generic Arrhenius rate expression, as shown below

$$\frac{d\alpha}{dt} = kf(\alpha) \qquad \mathbf{8-5})$$

where $d\alpha/dt$ is the measured differential rate data, k is the kinetic rate constant and α is the reacted fraction at time t. For isothermal experiments, this equation can be simplified to show that

$$\frac{d\alpha/dt}{(d\alpha/dt)_{\alpha=0.5}} = \frac{f(\alpha)}{f(\alpha)_{\alpha=0.5}} \qquad \mathbf{8-6})$$

where the left and right hand sides are the normalized rate data and kinetic models, respectively. Therefore, if the normalized rate data agrees well with a given kinetic model, a plot of $(d\alpha/dt)/(d\alpha/dt)_{\alpha=0.5}$verses α and $f(\alpha)/f(\alpha)_{\alpha=0.5}$ verses α should be equivalent. The fractional conversion, α, is defined as

$$\alpha = \frac{Total\ H_2(t)}{Total\ H_2} \qquad \mathbf{8-7})$$

The normalized rate data from have been compared to several kinetic models which are described in Table 8-1. Plots of the data from 700 to 1200 ^{o}C and an H_2O mole fraction of 0.16 compared to these models are shown in Figure 8-5.

Table 8-1: Solid state reaction models and corresponding differential forms, *f(α)*

Model	Symbol	f(α)
Reaction Order	Fn	$(1-\alpha)^n$
Nucleation and Growth (Johnson-Mehl-Avrami equation)	An	$n(1-\alpha)[-\ln(1-\alpha)]^{1-\frac{1}{n}}$
Phase Boundary Controlled Reaction	R2	$2(1-\alpha)^{\frac{1}{2}}$
Phase Boundary Controlled Reaction	R3	$3(1-\alpha)^{\frac{2}{3}}$
One Dimensional Diffusion	D1	$\frac{2}{\alpha}$
Two Dimensional Diffusion	D2	$\frac{1}{-\ln(1-\alpha)}$
Three Dimensional Diffusion	D3	$\frac{3(1-\alpha)^{\frac{2}{3}}}{2[1-(1-\alpha)^{\frac{1}{3}}]}$

The data agrees well with a first order reaction model at 700 ^{o}C, but transitions to a second order model at higher temperatures. For $\alpha<0.5$ and temperatures from 700 to 900 ^{o}C, the data agrees well with a first order reaction mechanism, but larger conversions above 700 ^{o}C, the reaction transitions to a second order model. From 1000-1200 ^{o}C, the normalized rate data agrees best with a second order model for all conversions.

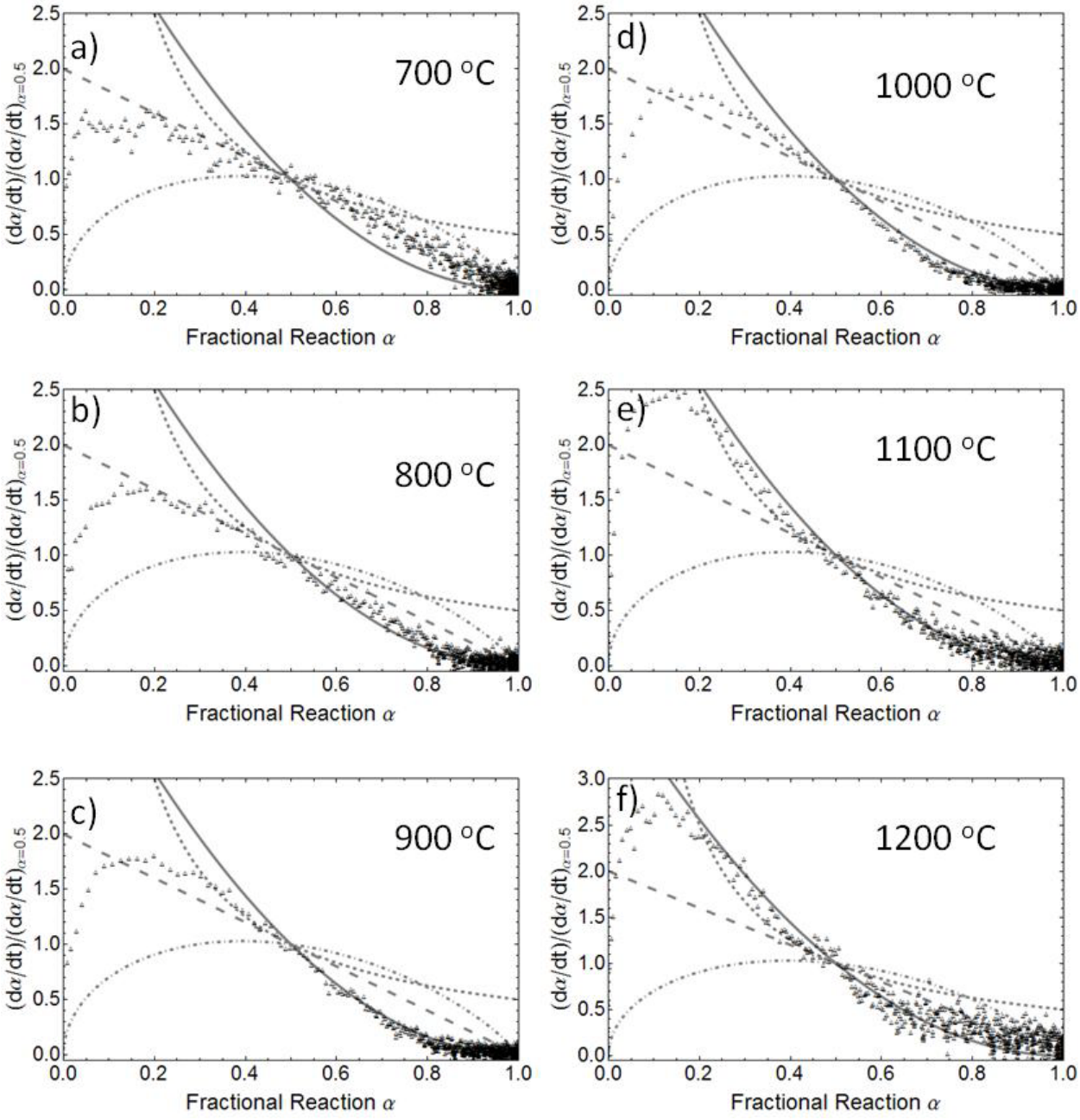

Figure 8-5: Normalized rate data compared to various solid state reaction models. a) 700 ^{o}C, b) 800 ^{o}C, c) 900 ^{o}C, d) 1000 ^{o}C, e) 1100 ^{o}C and f) 1200 ^{o}C. H_2O mole fraction = 0.16. (– – F1), (—— F2), (– · –A2), (··· D1), (Δ16% H_2O)

The transition from a first to second order reaction model is likely due to the contribution of the reverse reaction to the observed rates, which was shown to be thermodynamically more

favorable than the forward reaction above 900 ^{o}C (see Figure 8-3). It is also clear that the observed reaction rates are not limited by nucleation and growth or diffusion mechanisms, and agrees well with Haile *et.al.*'s observations that the characteristic diffusion time is much less than observed oxidation rates [18]. The initial rise in the normalized rate data for low conversions is attributed to a delay in the time that H_2 is produced to the time it is sampled in the mass spectrometer and the time required for steam concentrations to equilibrate.

With knowledge of the appropriate reaction model, the activation energy can be calculated for all conversions where the mechanism is valid. The reaction rate was assumed to have Arrhenius dependence according to the equation shown below,

$$rate_{H_2} = \frac{d\alpha}{dt} = [H_2O]^n k_o \exp\left(-\frac{\mathrm{E_a}}{\mathrm{RT}}\right)(1-\alpha), \qquad 0.2 < \alpha < 0.5 \qquad \mathbf{8-8})$$

where $[H_2O]$ is the mole fraction of steam, n is the steam reaction order, k_o is the pre-exponential factor, E_a is the activation energy, R is the ideal gas constant, and T is the absolute temperature. The activation energy can be obtained by taking the natural logarithm of both sides of the Arrhenius equation and determining the slope ($-E_a/R$) of $\ln \frac{d\alpha}{dt}/(1-\alpha)$ verses $1/T$, as illustrated below.

$$\ln \frac{d\alpha}{dt}/(1-\alpha) = n \ln[H_2O] - \left(\frac{E_a}{R}\right)\left(\frac{1}{T}\right) \qquad \mathbf{8-9})$$

If the correct reaction mechanism, f(α), is applied, then $\ln \frac{d\alpha}{dt}/(1-\alpha)$ for all α's of a given experimental data set should be equal [21]. Inappropriate mechanisms would result in randomly

scattered data. Calculation of the apparent E_a in this manner is more accurate than a simple peak rate analysis because a larger spectrum of the fractional conversion is included. Additionally, the reaction model is incorporated into the calculation, whereas a peak rate analysis is generally calculated independently of the fractional conversion. Arrhenius plots from $0.2<\alpha<0.5$ are shown in Figures 8-6a-d for all H_2O mole fractions investigated.

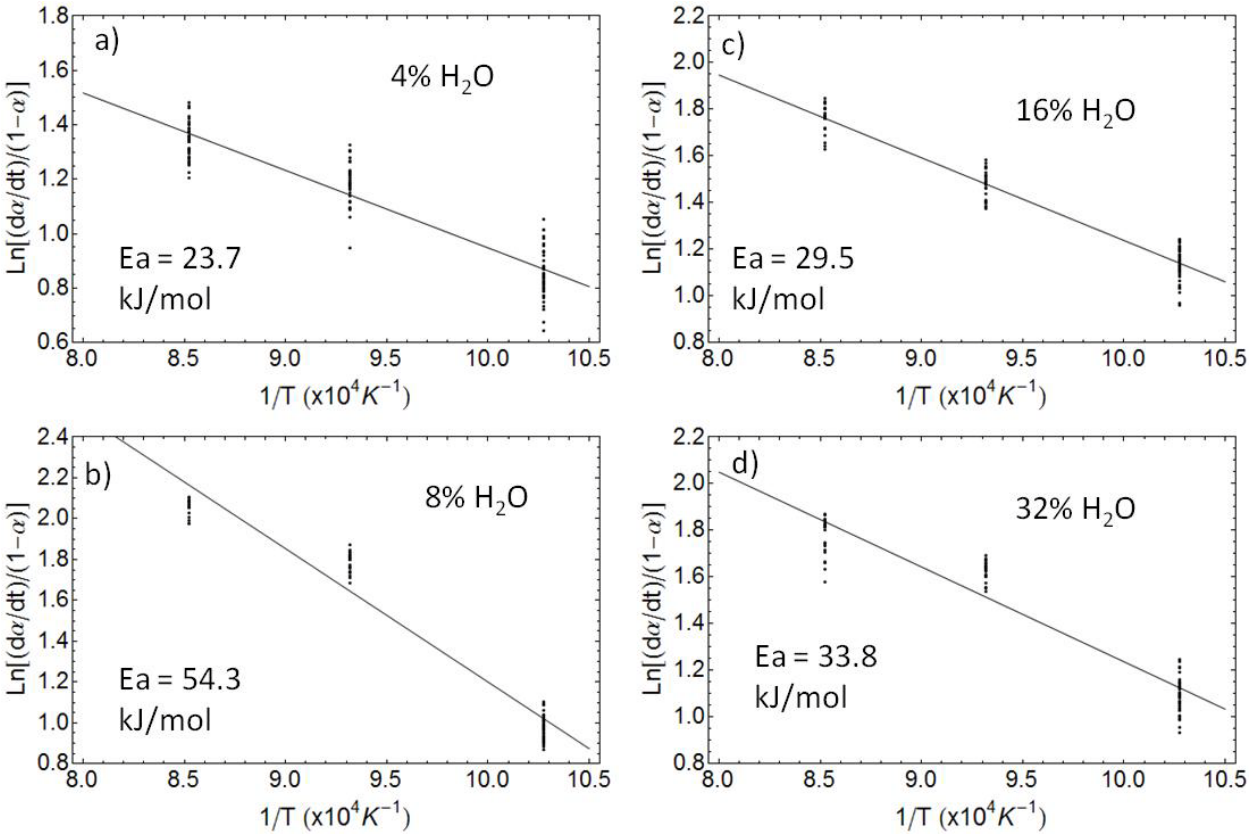

Figure 8-6: Arrhenius plots between 700 and 900 ^{o}C for H_2O mole fractions of a) 0.04 , b) 0.08, c) 0.16, d) 0.32. The apparent activation energy, E_a = 35.5 ± 13.3 kJ/mol.

The apparent E_a between 700 and 900 ^{o}C was determined to be 35.5 ± 13.3 kJ/mol. Between these temperatures, a linear dependence was observed between $\ln\frac{d\alpha}{dt}/(1-\alpha)$ and $1/T$, as expected for Arrhenius type behavior, but for greater temperatures the rates began to decrease due to contributions from the reverse reaction. The large degree in variability arises from the

inherent signal to noise of the mass spectrometer, the large number of data points included, and experimental variability. Haile *et.al.* calculated a larger activation energy of 50 kJ/mol for H_2O splitting on chemically reduced Sm-doped ceria between 400 and 700 ^oC. However, this is not surprising because the role of dopants, like samarium, is to induce more oxygen vacancies at lower temperatures than un-doped ceria. As a result, doped ceria is thermodynamically more stable with higher oxygen vacancy concentrations than undoped, resulting in a larger energy barrier that needs to be overcome for re-oxidation. The H_2O reaction order, *n*, was calculated by determining the slope of $\ln \frac{d\alpha}{dt}/(1-\alpha)$ verses $\ln[H_2O]$, from $0.2<\alpha<0.5$. This was observed to be 0.17 ± 0.03, indicating a weak dependence of water concentration on the observed reaction rates.

We have coupled the calculated kinetic parameters E_a, *n* and $f(\alpha)$, which are summarized in Table 8-2, with the Arrhenius expression shown in equation 8-8 to compare this kinetic model to the experimentally observed reaction rates. The pre-exponential factor, k_o, was determined empirically to be 1.0.

Table 8-2: Summary of calculated kinetic parameters.

$f(\alpha)$	(1-α)
Ea (kJ/mol)	35.5 13.3
k_o	1.0
n	0.17 0.03

The integrated form of the rate equation with corresponding experimental data sets is shown in Figure 8-7a-c for an H_2O mole fraction of 0.16. As seen in Figure 8-7a, the data and kinetic model agree well over all conversions at 700 ^oC. As the temperature increases to 800 and 900 ^oC,

however, the fits become progressively worse for large conversions. After conversions of 0.8 at 800 ^{o}C, and 0.6 at 900 ^{o}C, the rates predicted by the first order reaction model are faster than the observed. This is due to the transition from a first order to a second order reaction model, which was evident from the master plot analysis discussed in Figure 8-5.

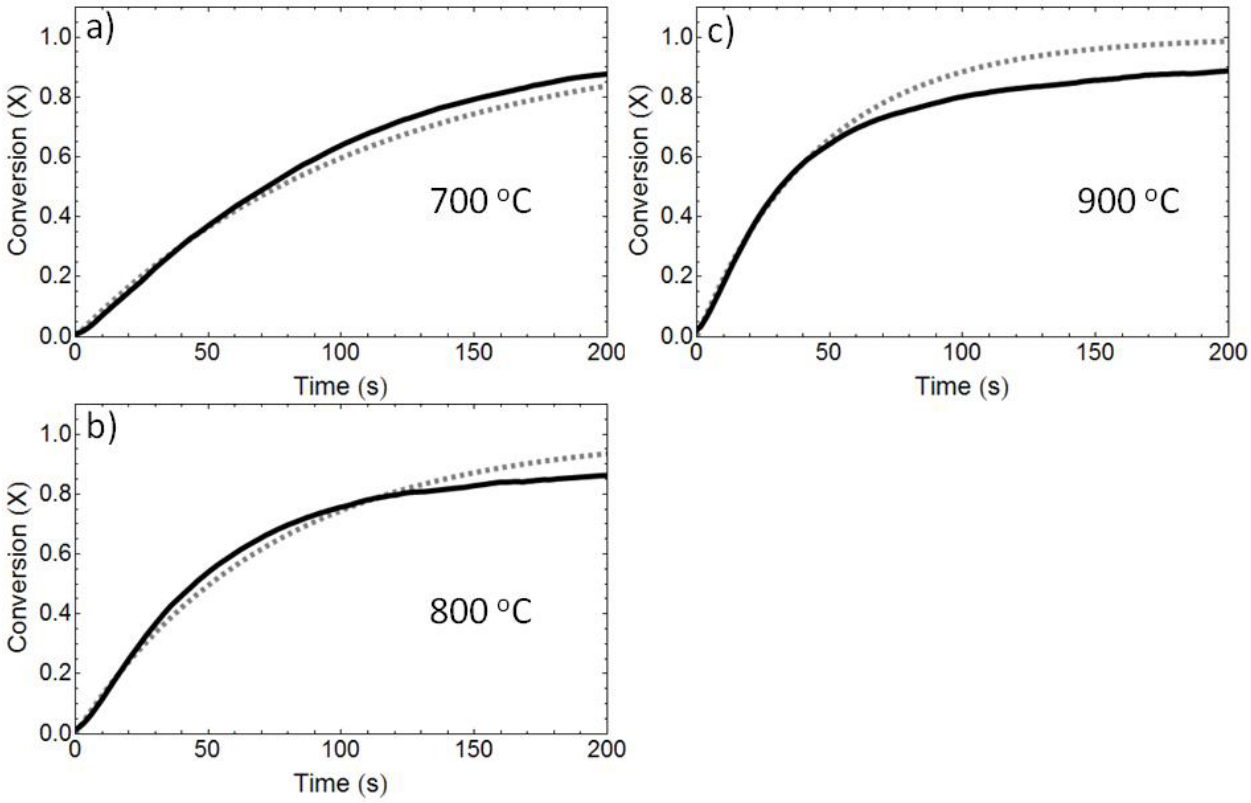

Figure 8-7: Experimental data (—) and corresponding kinetic model (···). a) 700 ^{o}C, b) 800 ^{o}C, c) 900 ^{o}C, H_2O mole fraction = 0.16.

It is hypothesized that this transition results from a competition between the forward and reverse reactions. Incorporating the reverse reaction into the overall kinetic expression would be optimal, but is beyond the scope of this work. To do this, a separate comprehensive kinetic study of the reverse reaction would be required. Additionally, there would be complications incorporating both the forward and reverse rates into a kinetic expression for our experimental apparatus

because we are not operating under equilibrium conditions. Nevertheless, for a commercial or large scale process such as the CR5 reactor [16], reactions will likely not be carried out to maximum conversions because their slow rates will have a negative impact on overall fuel production rates.

8.5 Conclusions

Commercially available ceria (CeO_2) felts were thermally cycled up to 30 times under various re-oxidation conditions with minimal effects on its H_2 fuel production. The onset of thermal decomposition was near 1200 ^oC, and reaches a maximum rate at 1450 ^oC, which is comparable to ferrite based water splitting cycles. Additionally, the oxidation rates were faster on a per mass bases than those we have observed for analogous ferrite cycles because sintering is abated. However, the amount of H_2 produced was less than comparable ferrite cycles because the ceria is only capable of being reduced to a non-stoichiometric state.

The water oxidation reaction was not limited by diffusion, as it is in other similar thermal water splitting cycles [23, 24], but rather by first and second order reaction mechanisms. At low temperatures (700 ^oC) the reaction is limited by a first order reaction, but as the temperature increase to 1200 ^oC, the mechanism changes to a second order reaction. We attribute this transition to the increased presence of the reverse reaction, which is thermodynamically more favorable than the forward reaction at temperatures greater than 900 ^oC. The reverse reaction is also evidenced experimentally at temperatures greater than 1000 ^oC, resulting in decreasing H_2 reaction rates as a function of temperature. The maximum H_2 rates were observed between 900 and 1000 ^oC.

The activation energy was calculated between conversions of 0.2 and 0.5 and temperatures of 700 to 900 ^oC, and determined to be 35.5 ± 13.3 kJ/mol. This is similar to, but

lower than, the activation energy of 50 kJ/mol calculated by Haile *et.al* for water oxidation of Sm-doped ceria. Finally, an Arrhenius kinetic expression coupled with a first order reaction model, (1-α), was capable of describing the temporal data well for conversions less than α=0.6. At 700 ^{o}C, the model fit the data for all conversions, but became progressively worse as the reaction order transitioned from a first to second order model at higher temperatures and conversions.

8.6 References

[1] Abanades S, Flamant G. Thermochemical hydrogen production from a two-step solar-driven water-splitting cycle based on cerium oxides. Solar Energy 2006;80:1611.

[2] Chueh WC, Haile SM. Ceria as a Thermochemical Reaction Medium for Selectively Generating Syngas or Methane from H2O and CO2. Chemsuschem 2009;2:735.

[3] Abanades S, Legal A, Cordier A, Peraudeau G, Flamant G, Julbe A. Investigation of reactive cerium-based oxides for H-2 production by thermochemical two-step water-splitting. Journal of Materials Science;45:4163.

[4] Allendorf MD. Two-Step Water Splitting Using Mixed-Metal Ferrites: Thermodynamic Analysis and Characterization of Synthesized Materials. Energy & Fuels 2008;22:4115.

[5] Kodama T, Kondoh Y, Yamamoto R, Andou H, Satou N. Thermochemical hydrogen production by a redox system of ZrO2-supported Co(II)-ferrite. Solar Energy 2005;78:623.

[6] Neises M, Roeb M, Schmuker M, Sattler C, Pitz-Paal R. Kinetic investigations of the hydrogen production step of a thermochemical cycle using mixed iron oxides coated on ceramic substrates. International Journal of Energy Research;34:651.

[7] Miller JE, Allendorf MD, Diver RB, Evans LR, Siegel NP, Stuecker JN. Metal oxide composites and structures for ultra-high temperature solar thermochemical cycles. Journal of Materials Science 2008;43:4714.

[8] Francis TM, Lichty PR, Weimer AW. Manganese oxide dissociation kinetics for the Mn2O3 thermochemical water-splitting cycle. Part 1: Experimental. Chemical Engineering Science;65:3709.

[9] Perkins C, Lichty PR, Weimer AW. Thermal ZnO dissociation in a rapid aerosol reactor as part of a solar hydrogen production cycle. International Journal of Hydrogen Energy 2008;33:499.

[10] Steinfeld A. Solar hydrogen production via a two-step water-splitting thermochemical cycle based on Zn/ZnO redox reactions. International Journal of Hydrogen Energy 2002;27:611.

[11] Andersson DA, Simak SI, Skorodumova NV, Abrikosov IA, Johansson B. Optimization of ionic conductivity in doped ceria. Proceedings of the National Academy of Sciences of the United States of America 2006;103:3518.

[12] Kharton VV, Figueiredo FM, Navarro L, Naumovich EN, Kovalevsky AV, Yaremchenko AA, Viskup AP, Carneiro A, Marques FMB, Frade JR. Ceria-based materials for solid oxide fuel cells. Journal of Materials Science 2001;36:1105.

[13] Nakayama M, Martin M. First-principles study on defect chemistry and migration of oxide ions in ceria doped with rare-earth cations. Physical Chemistry Chemical Physics 2009;11:3241.

[14] Kaneko H, Miura T, Ishihara H, Taku S, Yokoyama T, Nakajima H, Tamaura Y. Reactive ceramics of CeO2-MOx (M = Mn, Fe, Ni, Cu) for H-2 generation by two-step water splitting using concentrated solar thermal energy. Energy 2007;32:656.

[15] Kaneko H, Tamaura Y. Reactivity and XAFS study on (1-x)CeO2-xNiO (x=0.025-0.3) system in the two-step water-splitting reaction for solar H-2 production. Journal of Physics and Chemistry of Solids 2009;70:1008.

[16] Diver RB, Miller JE, Allendorf MD, Siegel NP, Hogan RE. Solar thermochemical water-splitting ferrite-cycle heat engines. Journal of Solar Energy Engineering-Transactions of the Asme 2008;130.

[17] Service RF. Sunlight in Your Tank. Science 2009;326:1472.

[18] Chueh WC, Haile SM. A thermochemical study of ceria: exploiting an old material for new modes of energy conversion and CO2 mitigation. Philosophical Transactions of the Royal Society a-Mathematical Physical and Engineering Sciences;368:3269.

[19] Gotor FJ, Criado JM, Malek J, Koga N. Kinetic analysis of solid-state reactions: The universality of master plots for analyzing isothermal and nonisothermal experiments. Journal of Physical Chemistry A 2000;104:10777.

[20] Jankovic B, Mentus S, Jelic D. A kinetic study of non-isothermal decomposition process of anhydrous nickel nitrate under air atmosphere. Physica B-Condensed Matter 2009;404:2263.

[21] Perez-Maqueda LA, Criado JM, Gotor FJ, Malek J. Advantages of combined kinetic analysis of experimental data obtained under any heating profile. Journal of Physical Chemistry A 2002;106:2862.

[22] Yang HC, Eun HC, Cho YZ, Lee HS, Kim IT. Kinetic analysis of dechlorination and oxidation of PrOCl by using a non-isothermal TG method. Thermochimica Acta 2009;484:77.

[23] Funke HH, Diaz H, Liang XH, Carney CS, Weimer AW, Li P. Hydrogen generation by hydrolysis of zinc powder aerosol. International Journal of Hydrogen Energy 2008;33:1127.

[24] Loutzenhiser PG, Galvez ME, Hischier I, Stamatiou A, Frei A, Steinfeld A. CO2 Splitting via Two-Step Solar Thermochemical Cycles with Zn/ZnO and FeO/Fe3O4 Redox Reactions II: Kinetic Analysis. Energy & Fuels 2009;23:2832.

8.7 Supplemental Figures

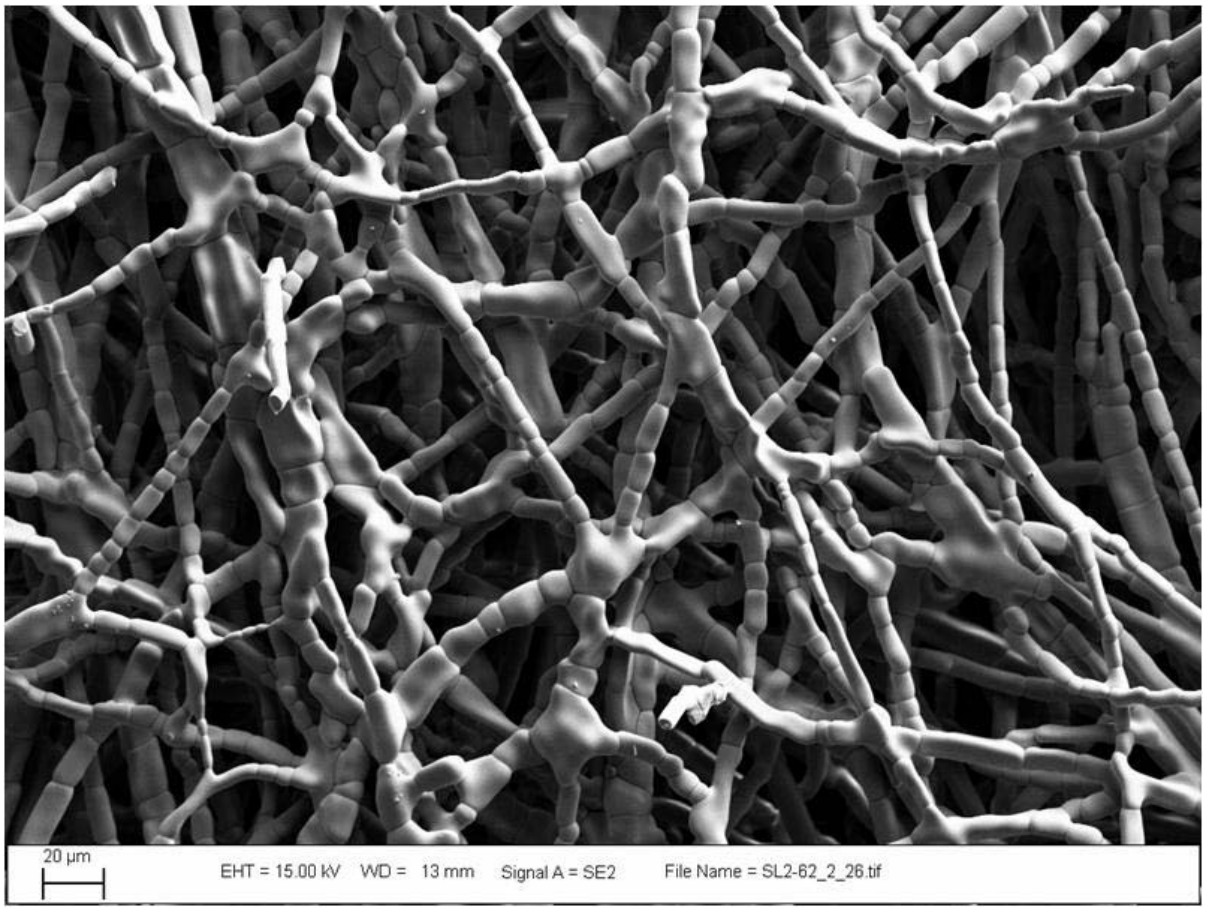

Supplemental Figure 8-8: SEM image of ceria felt before thermal cycling.

CHAPTER 9 CONCLUSIONS AND FUTURE OUTLOOK

9.1 Conclusions

Thermochemical redox cycles using metal oxides as intermediates, specifically ferrites and ceria, has shown to be a practical means of producing renewable H_2 using concentrated solar energy. We have considered the use of these materials in thermochemical redox cycles from both a thermodynamic and kinetic perspective, and focused on the effect of different synthesis procedures and substrates.

Equilibrium calculations have shown that the thermal reduction of metal substituted ferrites, such as Co and Ni, occurs at lower temperatures than un-substituted Fe_3O_4. Both are expected to decompose completely by 1450 ^oC, while Fe_3O_4 does not decompose completely until its slag phase is expected to occur. Additionally, the decomposition temperature is directly related to the amount of inert gas present which acts to dilute the gas phase reaction products (O_2). As a result, the decomposition temperature can be manipulated experimentally by diluting the reactants with a sweep gas, or operating under vacuum. Also, the reduction temperature decreases as the amount of cobalt in $Co_xFe_{3-x}O_4$ is increased. The maximum amount of hydrogen is expected to be produced using $CoFe_2O_4$ reduced at temperatures greater than 1450 ^oC, and oxidized at temperatures less than 1100 ^oC. Below 1450 ^oC, ferrites with higher cobalt concentrations are expected to produce more H_2. Ceria is expected to decompose at higher temperatures than cobalt ferrites, unless doped with metals such as Sm or Zr. Additionally, complete reduction to Ce_2O_3 is not achievable until very high temperatures ($\approx$ 2000 ^oC), resulting in reduction to a non-stoichiometric state that has less potential for H_2 production than the complete decomposition of metal substituted ferrites.

ALD chemistry that combined ferrocene and oxygen as precursors was used to deposit ultrathin amorphous iron oxide layers on zirconia nanoparticles in a fluidized bed reactor. Self-limiting chemistry, characteristic of ALD, was observed via in situ mass spectrometry and ICP-AES studies. HRTEM images were used to show the conformal and uniform nature of the films on individual nanoparticles. XRD and XPS analyses established that essentially all of the iron oxide that was deposited was amorphous and in the +3 oxidation state. After heat treatment at 850 ^{o}C, it was shown that the films could be crystallized to form α-Fe_2O_3, even on the high radius of curvature substrates used here.

Conformal films of maghemite (γ-Fe_2O_3) and spinel cobalt oxides ($Co_xFe_{3-x}O_4$) were deposited on porous m-ZrO_2 supports by ALD using ferrocene and cobaltocene as the iron and cobalt sources and O_2 as the oxidant. These materials are shown to be highly active in a chemical looping process to split water for the production of H_2. ALD Fe_2O_3 samples reduced in a CO/H_2/He mixture without the presence of an oxidant rapidly deactivated due to the formation of metallic Fe, likely resulting in growth and sintering. However, samples that were reduced with the addition of CO_2 exhibited remarkably better behavior. *In situ* XRD results indicated that ALD samples of Fe_2O_3 were reduced to Fe^{2+}, while $Co_{0.85}Fe_{2.5}O_4$ was reduced to a Co/Fe alloy. Also, Fe_2O_3/ZrO_2 powders reduced in the same manner reduced to Fe^{2+} for short times, but for longer times, metallic Fe was observed. ALD Fe_2O_3 samples reduced in this manner still exhibited signs of deactivation due to a loss of active iron resulting from its incorporation into the ZrO_2 support. Peak rates decreased slightly, but H_2 yields decreased by about 50% after 7 cycles. Cobalt ferrites are advantages compared to Fe_2O_3 samples for several reasons. When cobalt was substituted for iron, the material was reduced to metallic Co and Fe, rather than Fe^{2+}, resulting in much greater H_2 yields (about 4x). Additionally, there were no signs of deactivation.

The H_2 reaction rates and yields were nearly identical for 7 redox cycles. When physically mixed Fe_2O_3/ZrO_2 powders were cycled in the same manner as the ALD materials, reaction rates became progressively slower as they were cycled due to sintering and grain growth.

These results suggest that thin films of cobalt ferrites perform remarkably better than their iron oxide analogs and iron oxide powders at producing repeatable and large amounts of hydrogen via chemical looping processes. Additionally, they provide motivation for studying the efficacy of using these materials in other analogous gas-splitting cycles, such as thermal redox cycles to produce H_2 or CO via H_2O and CO_2 splitting. Further experimental investigation of the mechanism of material sintering and reduction/oxidation chemical kinetics must be performed to understand why these materials are superior to other analogous materials, but nevertheless, the impetus for future work is provided.

The efficacy of using $CoFe_2O_4$ deposited on Al_2O_3 substrates to split H_2O was studied experimentally and in conjunction with thermodynamic modeling. We observed very low decomposition temperatures (200 ^oC lower than $CoFe_2O_4$) due to a reaction between the ferrite and Al_2O_3, resulting in $FeAl_2O_4$. This behavior has been corroborated with thermodynamic modeling. Although the reaction of $FeAl_2O_4$ with H_2O is not as favorable as that of FeO, it is shown that under non-equilibrium conditions it is capable of splitting water to produced H_2 at 1000 ^oC. Significant quantities of H_2 are generated at reduction temperatures of only 1200 ^oC, whereas little or no H_2 was generated using $CoFe_2O_4$ until 1400 ^oC. Additionally, $CoFe_2O_4/Al_2O_3$ is capable of being cycled at 1200 ^oC reduction/1000 ^oC oxidation with no obvious changes in H_2 conversion. These results certainly warrant further exploration of this cycle and provide compelling evidence that ferrites may be cycled with Al_2O_3 to produce H_2 at much lower temperatures than traditional ferrite redox cycles.

Cobalt ferrite ($Co_{0.9}Fe_{2.1}O_4$) and iron oxide (Fe_3O_4) thin films were both successfully utilized in a two step thermochemical water splitting cycle to produce H_2. H_2 conversions of both

materials were comparable and increased as oxidation temperature was increased. This was surprising considering the thermodynamically predicted extent of reduction is expected to be greater for cobalt ferrite under these reduction conditions (1450 ^{o}C). The oxidation rates exhibited Arrhenius type behavior from 900 to 1100 ^{o}C, but H_2 was capable of being generated even at temperatures as high as 1400 ^{o}C. This is due to the occurrence of both oxidation and reduction reactions occuring, and results in simultaneous production of H_2 and O_2 for an indefinite amount of time. The temperature at which this reaction occurs (T > 1250 ^{o}C) is much less than that required for water thermolysis.

Master plot analysis was utilized to compare the experimental data to various functional forms representative of reaction mechanisms, and it was determined that there are two distinct reaction limited regimes. Initially, the reaction is limited by a second order reaction mechanism, and the activation energy and H_2O reaction order during this regime were determined to be 119.76 ± 8.81 kJ/mole and 0.70 ± 0.32, respectively. Following this mechanism, the reaction was limited by diffusion, and agreed well with the parabolic rate law. This was accompanied by an increase in the activation energy, which was determined to be 191 ± 19.8 kJ/mol. This activation energy is higher than all other published reports of Fe or FeO oxidation, or Fe diffusion through magnetite. As a result, we believe that the activation energy for Fe diffusion through cobalt ferrite is higher than magnetite, resulting in the observed slower reaction rates. By combining both reaction mechanisms into a single rate expression, we were able to derive a global rate expression capable of characterizing the temporal behavior of the oxidation of cobalt ferrite for temperatures between 900 and 1100 ^{o}C, and water concentrations from 20% to 40%.

Commercially available ceria (CeO_2) felts were thermally cycled up to 30 times under various re-oxidation conditions with minimal effects on its H_2 fuel production. The onset of

thermal decomposition was near 1200 ^{o}C, and reaches a maximum rate at 1450 ^{o}C, which is comparable to ferrite based water splitting cycles. Additionally, the oxidation rates were faster on a per mass bases than those we have observed for analogous ferrite cycles because sintering is abated. However, the amount of H_2 produced was less than comparable ferrite cycles because the ceria is only capable of being reduced to a non-stoichiometric state.

The water oxidation reaction was not limited by diffusion, as it is in other similar thermal water splitting cycles [23, 24], but rather by first and second order reaction mechanisms. At low temperatures (700 ^{o}C) the reaction is limited by a first order reaction, but as the temperature increase to 1200 ^{o}C, the mechanism changes to a second order reaction. We attribute this transition to the increased presence of the reverse reaction, which is thermodynamically more favorable than the forward reaction at temperatures greater than 900 ^{o}C. The reverse reaction is also evidenced experimentally at temperature greater than 1000 ^{o}C, resulting in decreasing H_2 reaction rates as a function of temperature. The maximum H_2 rates were observed between 900 and 1000 ^{o}C.

The activation energy was calculated between conversions of 0.2 and 0.5 and temperatures of 700 to 900 ^{o}C, and determined to be 35.5 ± 13.3 kJ/mol. This is similar to, but lower than, the activation energy of 50 kJ/mol calculated by Haile *et.al* for water oxidation of Sm-doped ceria. Finally, an Arrhenius kinetic expression coupled with a first order reaction model, $(1-\alpha)$, was capable of describing the temporal data well for conversions less than $\alpha=0.6$. At 700 ^{o}C, the model fit the data for all conversions, but became progressively worse as the reaction order transitioned from a first to second order model at higher temperatures and conversions.

9.2 Outlook

Ultimately, these materials will be used in a large scale process to produce solar H_2, and their ability to efficiently do so will be scrupulously considered. The efficiency of the process, in terms of dollars per kilogram of H_2, is dependent upon a given materials production cost, its ability to be cycled thousands or even millions of times repeatedly, the rate of its H_2 and O_2 production, its equilibrium H_2 and O_2 production, and the temperature that it operates. Based on these factors, an argument could be made that supports further investigation of all of the materials considered in this thesis. Each material was capable of being cycled repeatedly, and was successfully shown to produce H_2 at reasonable temperatures. Following is an analysis of considered each materials advantages, disadvantages, and approaches which may positively impact their performance, based on the results of this work.

9.2.1 Ferrites

The main advantage of ferrites, specifically metal substituted ferrites, lies in their ability to produce large amounts of H_2 at equilibrium. The effect of substitution is well understood, based on thermodynamic calculations and experimental evidence, and improvements in this area are not expected. However, the kinetics of H_2 and O_2 production were limited by diffusion, suggesting that improved kinetics could result by improvements in material design. This was attempted experimentally, by depositing thin films onto inert substrates, but because of sintering the observed effect was negligible. However, when we proceeded to chemically reduce the ferrites via syngas reduction, the integrity of the films remained and reaction rates were remarkably faster. This suggests that depositing thin films of ferrites onto substrates that are more stable than the m-ZrO_2 support that we investigated would limit sintering and improve

reaction rates. Therefore, it may be beneficial to observe the effect of depositing ferrites onto felts, similar to the ceria felt discussed in Chapter 8. Because of their thin, woven, rod-like structure they may maintain their integrity better and suppress sintering. It would be worth looking not only at the effect of ZrO_2 felts, but also CeO_2 felts. Based on the microsopy results from Chapter 8, we know that sintering is suppressed. From the literature we also know that the ferrite reacts with ceria, but still remains active at producing H_2. If excess ferrite were deposited onto the ceria, this may result in a ferrite/ceria hybrid in which both species contribute to H_2 production. The advantage of this would be twofold. First, the support would be utilized in the cycle, whereas with ZrO_2 it is an energy sink. Secondly, the high surface area of the ferrite would be maintained, resulting in improved reaction rates.

9.2.2 Ceria

Unlike the ferrites, the advantage of ceria lies in its ability to be quickly cycled. Sintering was not an issue like it was with the ferrite-based cycle, and as a result the kinetics were faster on a per mass basis. However, its main disadvantage was a result of thermodynamic limitations, rather than material limitations, which negatively affected the amount of equilibrium H_2 and O_2 produced. Therefore, investigating the role of dopants to increase the degree of reduction at moderate temperatures will prove to be important. An investigation of Sm and Zr doped ceria, as well as various transition metal oxides, has already been performed by other researchers. However, there are several other dopants which may result in better performance, and have already been investigated by the solid oxide fuel cell community for other applications. Therefore, a thorough investigation of the literature would be beneficial, and may provide insight other dopants whose effect on reduction has already been well characterized. The economic

feasibility of this cycle is dependent upon improving the thermodynamics of the reduction reaction, either by decreasing the temperature requirements sufficiently or increasing the amount of equilibrium H_2 it is capable of generating.

9.2.3 Hercynite

The hercynite redox cycle's main advantage is its ability to be cycled at upper operating temperatures that are 250 ^{o}C lower than ferrite or ceria-based cycles. This is important because the biggest capital cost of large scale solar thermochemical H_2 production are heliostats, which concentrate solar energy to achieve the high temperatures which are required. A cycle's temperature requirements are directly related to the number of heliostats that are needed, and therefore, for lower temperatures cycles such as hercynite, less heliostats are required and capital costs are reduced. However, much less is known about the limitations of the hercynite cycle compared to the ferrite and ceria cycles. The total amount of H_2 generated is comparable to ferrite cycles, but the kinetics and of the reaction are less understood. A comprehensive kinetic study, along careful morphological characterization as it is cycled, would be beneficial to understand the limitations associated with this reaction.

9.3 Future Work

In addition to using these materials in a thermochemical cycle to produce H_2, there are other similar cycles which should be explored. Feedstocks such as CO_2, or CO_2 in conjunction with H_2O, also have the potential to produce useable solar-derived fuels. For example, when CO_2 is substituted for H_2O in the two-step redox cycle, the end product is CO rather than H_2. This can easily be converted into H_2 via the water gas shift reaction, or used in a syngas mixture to

produce carbon based fuels. Also, by using CO_2 and H_2O at the same time, it is possible to generate a syngas mixture of CO and H_2, without the water gas shift reaction. We have demonstrated the efficacy of using both ferrites and ceria felts to split CO_2 to produce CO, as seen in Figures 9-1 and 9-2, respectively.

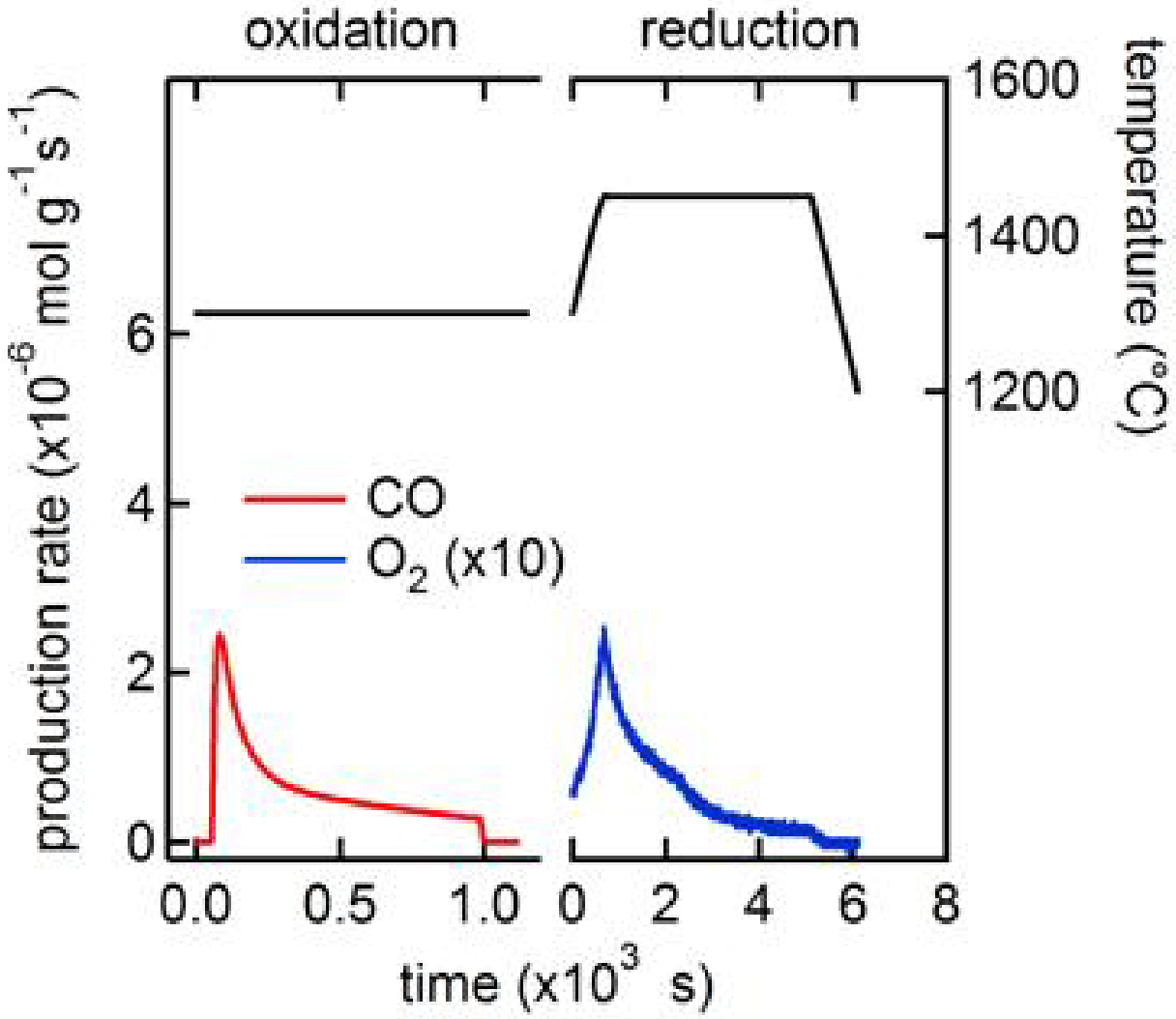

Figure 9-1: CO_2 splitting redox cycle using $Co_{0.9}Fe_{2.1}O_4$ deposited on ZrO_2.

CO_2 splitting using ferrites proceed successfully at the same conditions as water splitting with similar results, namely at oxidation temperatures between 900 and 1300 ^oC, and thermal

reduction temperatures of 1450 ^{o}C. Ceria CO_2 splitting experiments were also successful for up to 30 redox cycles under similar conditions to H_2O splitting. Results were similar to H_2O splitting, except for the dependence on CO_2 concentration, as shown in Figure 9-2. CO rates were highly dependent upon CO_2 concentration, whereas H_2 rates were only weakly dependent on H_2O concentrations under the conditions explored.

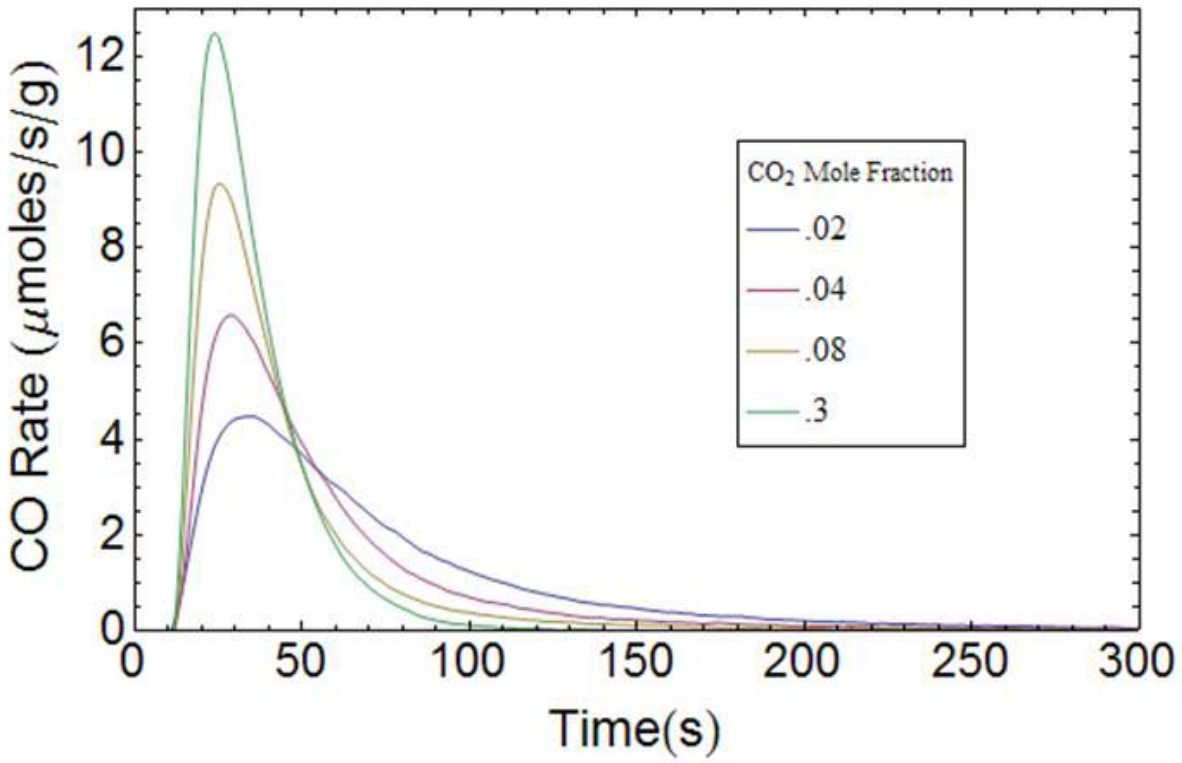

Figure 9-2: CO rates as a function of CO_2 mole fraction measured at 75 Torr and 800 ^{o}C, with a total gas flow of 500 sccm (CO_2 + He).

Additionally, the kinetics of decomposition of ferrites and ceria has largely remained uninvestigated. However, knowledge of this redox step will prove to be every bit as crucial as the oxidation step, which has been considered in this thesis. The next logical step for these materials is a small scale demonstration to study the feasibility of using them on-sun, in a solar reactor.

The design of this reactor will be dependent upon the kinetics of both the thermal decomposition and oxidation steps, and therefore, a thorough investigation of the decomposition reaction of each of the materials will prove to be essential.

CHAPTER 10 BIBLIOGRAPHY

(2007). IPCC Fourth Assessment Report, Intergovernmental Panel on Climate Change.

Aaltonen, T. (2005). Atomic Layer Deposition of Noble Metal Thin Films. Department of Chemistry. Helsinki, University of Helsinki: 71.

Abanades, S. and G. Flamant (2006). "Thermochemical hydrogen production from a two-step solar-driven water-splitting cycle based on cerium oxides." Solar Energy 80(12): 1611-1623.

Abanades, S., A. Legal, et al. "Investigation of reactive cerium-based oxides for H-2 production by thermochemical two-step water-splitting." Journal of Materials Science 45(15): 4163-4173.

Agrafiotis, C., M. Roeb, et al. (2005). Solar water splitting for hydrogen production with monolithic reactors.

Agrafiotis, C., M. Roeb, et al. (2005). "Solar water splitting for hydrogen production with monolithic reactors." Solar Energy 79(4): 409-421.

Allendorf, M. D. (2008). "Two-Step Water Splitting Using Mixed-Metal Ferrites: Thermodynamic Analysis and Characterization of Synthesized Materials." Energy & Fuels 22(6): 4115-4124.

Alvani, C., A. La Barbera, et al. (2006). "Hydrogen production by using manganese ferrite: Evidences and benefits of a multi-step reaction mechanism." International Journal of Hydrogen Energy 31(15): 2217-2222.

Andersson, D. A., S. I. Simak, et al. (2006). "Optimization of ionic conductivity in doped ceria." Proceedings of the National Academy of Sciences of the United States of America 103(10): 3518-3521.

Aoki, H., H. Kaneko, et al. (2004). "The ZnFe2O4/(ZnO+Fe3O4) system for H-2 production using concentrated solar energy." Solid State Ionics 172: 113-116.

Bachmann, J., J. Jing, et al. (2007). "Ordered iron oxide nanotube arrays of controlled geometry and tunable magnetism by atomic layer deposition." Journal of the American Chemical Society 129(31): 9554-+.

Bahlawane, N., P. H. T. Ngamou, et al. (2009). "Tailoring the properties and the reactivity of the spinel cobalt oxide." Physical Chemistry Chemical Physics 11(40): 9224-9232.

Balat, M. (2009). "Political, economic and environmental impacts of biomass-based hydrogen." International Journal of Hydrogen Energy 34(9): 3589-3603.

Balat, M. (2009). "Possible Methods for Hydrogen Production." Energy Sources Part a-Recovery Utilization and Environmental Effects 31(1): 39-50.

Balat, M. and E. Kirtay "Major Technical Barriers to a "Hydrogen Economy"." Energy Sources Part a-Recovery Utilization and Environmental Effects 32(9): 863-876.

Baldychev, I., J. M. Vohs, et al. (2009). "The effect of thermodynamic properties of zirconia-supported Fe3O4 on water-gas shift activity." Applied Catalysis a-General 356(2): 225-230.

Barber, Z. H. (2006). "The control of thin film deposition and recent developments in oxide film growth." Journal of Materials Chemistry 16(4): 334-344.

Baykara, S. Z. (2004). "Experimental solar water thermolysis." International Journal of Hydrogen Energy 29(14): 1459-1469.

Bishop, J. K. B. (2006). "Surface Solar Irradiance from ISCCP data." from http://www-ocean.lbl.gov/seawifs.html.

Bleeker, M. F., S. R. A. Kersten, et al. (2007). "Pure hydrogen from pyrolysis oil using the steam-iron process." Catalysis Today 127(1-4): 278-290.

Bleeker, M. F., H. J. Veringa, et al. (2009). "Deactivation of iron oxide used in the steam-iron process to produce hydrogen." Applied Catalysis a-General 357(1): 5-17.

Bohn, C. D., C. R. Muller, et al. (2008). "Production of Very Pure Hydrogen with Simultaneous Capture of Carbon Dioxide using the Redox Reactions of Iron Oxides in Packed Beds." Industrial & Engineering Chemistry Research 47(20): 7623-7630.

Cabrera, N. and N. F. Mott (1948). "THEORY OF THE OXIDATION OF METALS." Reports on Progress in Physics 12: 163-184.

Cerri, G., C. Salvini, et al. "Sulfur-Iodine plant for large scale hydrogen production by nuclear power." International Journal of Hydrogen Energy 35(9): 4002-4014.

Charvin, P., S. Abanades, et al. (2007). "Two-step water splitting thermochemical cycle based on iron oxide redox pair for solar hydrogen production." Energy 32(7): 1124-1133.

Chavez-Galan, J. and R. Almanza (2007). "Solar filters based on iron oxides used as efficient windows for energy savings." Solar Energy 81(1): 13-19.

Chen, R. Y. and W. Y. D. Yuen (2003). "Review of the high-temperature oxidation of iron and carbon steels in air or oxygen." Oxidation of Metals 59(5-6): 433-468.

Chernyshova, I. V., M. F. Hochella, et al. (2007). "Size-dependent structural transformations of hematite nanoparticles. 1. Phase transition." Physical Chemistry Chemical Physics 9(14): 1736-1750.

Chueh, W. C. and S. M. Haile "A thermochemical study of ceria: exploiting an old material for new modes of energy conversion and CO2 mitigation." Philosophical Transactions of the Royal Society a-Mathematical Physical and Engineering Sciences 368(1923): 3269-3294.

Chueh, W. C. and S. M. Haile (2009). "Ceria as a Thermochemical Reaction Medium for Selectively Generating Syngas or Methane from H2O and CO2." Chemsuschem 2(8): 735-739.

Dahl, J. K., J. Tamburini, et al. (2001). "Solar-thermal processing of methane to produce hydrogen and syngas." Energy & Fuels 15(5): 1227-1232.

de Ridder, M., P. C. van de Ven, et al. (2002). "Growth of iron oxide on yttria-stabilized zirconia by atomic layer deposition." Journal of Physical Chemistry B 106(51): 13146-13153.

del Campo, L., R. B. Perez-Saez, et al. (2008). "Iron oxidation kinetics study by using infrared spectral emissivity measurements below 570 degrees C." Corrosion Science 50(1): 194-199.

Dghoughi, L., B. Elidrissi, et al. (2006). "Physico-chemical, optical and electrochemical properties of iron oxide thin films prepared by spray pyrolysis." Applied Surface Science 253(4): 1823-1829.

Dieckmann, R. and H. Schmalzried (1975). "POINT-DEFECTS AND CATION DIFFUSION IN MAGNETITE." Zeitschrift Fur Physikalische Chemie-Frankfurt 96(4-6): 331-333.

Dieckmann, R. and H. Schmalzried (1977). "DEFECTS AND CATION DIFFUSION IN MAGNETITE .1." Berichte Der Bunsen-Gesellschaft-Physical Chemistry Chemical Physics 81(3): 344-347.

Diver, R. B., J. E. Miller, et al. (2008). "Solar thermochemical water-splitting ferrite-cycle heat engines." Journal of Solar Energy Engineering-Transactions of the Asme 130(4).

Dokiya, M., K. Fukuda, et al. (1977). "STUDY OF THERMOCHEMICAL HYDROGEN PREPARATION .2. ELECTROCHEMICAL HYBRID CYCLE USING SULFUR-IODINE SYSTEM." Denki Kagaku 45(3): 139-143.

Echigoya, J., W. Asano, et al. (2002). "Microstructure of sputtered CoFe2O4 film." Physica Status Solidi a-Applied Research 191(2): 359-369.

EIA (2008). Annual Energy Review 2008, United States Department of Energy.

Ekins, P. and N. Hughes (2009). "The prospects for a hydrogen economy (1): hydrogen futures." Technology Analysis & Strategic Management 21(7): 783-803.

Ernst, F. O., A. Steinfeld, et al. (2009). "Hydrolysis rate of submicron Zn particles for solar H-2 synthesis." International Journal Of Hydrogen Energy 34(3): 1166-1175.

Etievant, C. (1991). "SOLAR HIGH-TEMPERATURE DIRECT WATER SPLITTING - A REVIEW OF EXPERIMENTS IN FRANCE." Solar Energy Materials 24(1-4): 413-440.

Fahlman, B. D. (2006). "Recent advances in chemical vapor deposition." Current Organic Chemistry 10(9): 1021-1033.

Ferguson, J. D., A. W. Weimer, et al. (2005). "Surface chemistry and infrared absorbance changes during ZnO atomic layer deposition on ZrO2 and BaTiO3 particles." Journal of Vacuum Science & Technology A 23(1): 118-125.

Fino, D., N. Russo, et al. (2006). "Catalytic removal of NOx and diesel soot over nanostructure spinel-type oxides." Journal of Catalysis 242(1): 38-47.

Francis, T. M., P. R. Lichty, et al. "Manganese oxide dissociation kinetics for the Mn2O3 thermochemical water-splitting cycle. Part 1: Experimental." Chemical Engineering Science 65(12): 3709-3717.

Fujimura, T. and S. L. Tanaka (1999). "In-situ high temperature X-ray diffraction study of Fe/Al2O3 interface reactions." Journal of Materials Science 34(3): 425-429.

Funke, H. H., H. Diaz, et al. (2008). "Hydrogen generation by hydrolysis of zinc powder aerosol." International Journal of Hydrogen Energy 33(4): 1127-1134.

Galvita, V. and K. Sundmacher (2007). "Cyclic water gas shift reactor(CWGS) for carbon monoxide removal from hydrogen feed gas for PEM fuel cells." Chemical Engineering Journal 134(1-3): 168-174.

Garcia, F. L., V. G. de Resende, et al. (2009). "Iron-stabilized nanocrystalline ZrO2 solid solutions: Synthesis by combustion and thermal stability." Materials Research Bulletin 44(6): 1301-1311.

Gehring, A. U., H. Fischer, et al. (2009). "High temperature stability of natural maghemite: a magnetic and spectroscopic study." Geophysical Journal International 179(3): 1361-1371.

George, S. M., A. W. Ott, et al. (1996). "Surface chemistry for atomic layer growth." Journal of Physical Chemistry 100(31): 13121-13131.

Getoff, N. (1990). "PHOTOELECTROCHEMICAL AND PHOTOCATALYTIC METHODS OF HYDROGEN-PRODUCTION - A SHORT REVIEW." International Journal of Hydrogen Energy 15(6): 407-417.

Glasscock, J. A., P. R. F. Barnes, et al. (2008). "Structural, optical and electrical properties of undoped polycrystalline hematite thin films produced using filtered arc deposition." Thin Solid Films 516(8): 1716-1724.

Go, K. S., S. R. Son, et al. (2008). "Reaction kinetics of reduction and oxidation of metal oxides for hydrogen production." International Journal Of Hydrogen Energy 33(21): 5986-5995.

Gokon, N., T. Hasegawa, et al. (2008). "Thermochemical two-step water-splitting for hydrogen production using Fe-YSZ particles and a ceramic foam device." Energy 33(9): 1407-1416.

Gokon, N., H. Murayama, et al. (2009). "Thermochemical two-step water splitting cycles by monoclinic ZrO2-supported NiFe2O4 and Fe3O4 powders and ceramic foam devices." Solar Energy 83(4): 527-537.

Gokon, N., H. Murayama, et al. (2009). "Monoclinic zirconia-supported Fe3O4 for the two-step water-splitting thermochemical cycle at high thermal reduction temperatures of 1400-1600 degrees C." International Journal of Hydrogen Energy 34(3): 1208-1217.

Gokon, N., S. Takahashi, et al. (2008). "Thermochemical two-step water-splitting reactor with internally circulating fluidized bed for thermal reduction of ferrite particles." International Journal of Hydrogen Energy 33(9): 2189-2199.

Gotor, F. J., J. M. Criado, et al. (2000). "Kinetic analysis of solid-state reactions: The universality of master plots for analyzing isothermal and nonisothermal experiments." Journal of Physical Chemistry A 104(46): 10777-10782.

Hakim, L. F., J. Blackson, et al. (2005). "Nanocoating individual silica nanoparticles by atomic layer deposition in a fluidized bed reactor." Chemical Vapor Deposition 11(10): 420-425.

Hakim, L. F., S. M. George, et al. (2005). "Conformal nanocoating of zirconia nanoparticles by atomic layer deposition in a fluidized bed reactor." Nanotechnology 16(7): S375-S381.

Hakim, L. F., J. A. McCormick, et al. (2006). "Surface modification of titania nanoparticles using ultrathin ceramic films." Journal of the American Ceramic Society 89(10): 3070-3075.

Hakim, L. F., J. L. Portman, et al. (2005). "Aggregation behavior of nanoparticles in fluidized beds." Powder Technology 160(3): 149-160.

Han, J. H., G. L. Gao, et al. (2004). "A quantum chemical study of ZrO2 atomic layer deposition growth reactions on the SiO2 surface." Surface Science 550(1-3): 199-212.

Han, S. B., T. B. Kang, et al. (2007). "Water splitting for hydrogen production with ferrites." Solar Energy 81(5): 623-628.

Hauch, A., S. D. Ebbesen, et al. (2008). "Highly efficient high temperature electrolysis." Journal of Materials Chemistry 18(20): 2331-2340.

Hendy, S. C., N. J. Laycock, et al. (2005). "Atomistic modeling of cation transport in the passive film on iron and implications for models of growth kinetics." Journal of the Electrochemical Society 152(8): B271-B276.

Hertwich, E. G. and X. P. Zhang (2009). "Concentrating-Solar Biomass Gasification Process for a 3rd Generation Biofuel." Environmental Science & Technology 43(11): 4207-4212.

Hohn, K. L. and Y. C. Lin (2009). "Catalytic Partial Oxidation of Methanol and Ethanol for Hydrogen Generation." Chemsuschem 2(10): 927-940.

Hossain, M. M., D. Lopez, et al. (2009). "Nickel on lanthanum-modified gamma-Al2O3 oxygen carrier for CLC: Reactivity and stability." Catalysis Today 143(1-2): 179-186.

Huang, W., L. X. Zhou, et al. (2007). "Epitaxial growth of the CoFe2O4 film on SrTiO3 and its characterization." Journal of Crystal Growth 300(2): 426-430.

Huang, W. X., W. Ranke, et al. (2005). "Molecular-level understanding of the catalytic cycle of dehydrogenation of ethylbenzene to styrene over iron oxide-based catalyst." Journal of Physical Chemistry B 109(19): 9202-9204.

Huang, Y., J. Lin, et al. (2007). "Coating carbon nanotubes with iron oxide using methanol-thermal reaction." Materials Letters 61(3): 697-700.

Hwang, G. J., C. S. Park, et al. (2004). "Ni-ferrite-based thermochemical cycle for solar hydrogen production." Journal of Industrial and Engineering Chemistry 10(6): 889-893.

Ingler, J. W. B. and S. U. M. Khan (2005). "Photoresponse of spray pyrolytically synthesized copper-doped p-Fe2O3 thin film electrodes in water splitting." International Journal of Hydrogen Energy 30(8): 821-827.

Jacintho, G. V. M., A. G. Brolo, et al. (2009). "Structural Investigation of MFe2O4 (M = Fe, Co) Magnetic Fluids." Journal of Physical Chemistry C 113(18): 7684-7691.

Jankovic, B., S. Mentus, et al. (2009). "A kinetic study of non-isothermal decomposition process of anhydrous nickel nitrate under air atmosphere." Physica B-Condensed Matter 404(16): 2263-2269.

Jin, H., T. Okamoto, et al. (1998). "Development of a novel chemical-looping combustion: Synthesis of a looping material with a double metal oxide of CoO-NiO." Energy & Fuels 12(6): 1272-1277.

Kaneko, H., H. Ishihara, et al. (2008). "Cerium ion redox system in CeO2-xFe(2)O(3) solid solution at high temperatures (1,273-1,673 K) in the two-step water-splitting reaction for solar H-2 generation." Journal of Materials Science 43(9): 3153-3161.

Kaneko, H., T. Kodama, et al. (2004). "Decomposition of Zn-ferrite for O-2 generation by concentrated solar radiation." Solar Energy 76(1-3): 317-322.

Kaneko, H., N. Kojima, et al. (2002). "Reaction mechanism of H-2 generation for H2O/Zn/Fe3O4 system." International Journal of Hydrogen Energy 27(10): 1023-1028.

Kaneko, H., T. Miura, et al. (2007). "Reactive ceramics of CeO2-MOx (M = Mn, Fe, Ni, Cu) for H-2 generation by two-step water splitting using concentrated solar thermal energy." Energy 32(5): 656-663.

Kaneko, H. and Y. Tamaura (2009). "Reactivity and XAFS study on (1-x)CeO2-xNiO (x=0.025-0.3) system in the two-step water-splitting reaction for solar H-2 production." Journal of Physics and Chemistry of Solids 70(6): 1008-1014.

Kester, E. and B. Gillot (1998). "Cation distribution, thermodynamic and kinetics considerations in nanoscaled copper ferrite spinels. New experimental approach by XPS and new results both in the bulk and on the grain boundary." Journal of Physics and Chemistry of Solids 59(8): 1259-1269.

Kharton, V. V., F. M. Figueiredo, et al. (2001). "Ceria-based materials for solid oxide fuel cells." Journal of Materials Science 36(5): 1105-1117.

Khedr, M. H., A. A. Omar, et al. (2006). "Reduction of carbon dioxide into carbon by freshly reduced CoFe2O4 nanoparticles." Materials Science and Engineering a-Structural Materials Properties Microstructure and Processing 432(1-2): 26-33.

Kilo, M., C. Argirusis, et al. (2003). "Oxygen diffusion in yttria stabilised zirconia - experimental results and molecular dynamics calculations." Physical Chemistry Chemical Physics 5(11): 2219-2224.

King, D. M., J. A. Spencer, et al. (2007). "Atomic layer deposition on particles using a fluidized bed reactor with in situ mass spectrometry." Surface & Coatings Technology 201(22-23): 9163-9171.

Klepper, K. B., O. Nilsen, et al. (2007). "Epitaxial growth of cobalt oxide by atomic layer deposition." Journal of Crystal Growth 307(2): 457-465.

Klepper, K. B., O. Nilsen, et al. (2007). "Growth of thin films of Co3O4 by atomic layer deposition." Thin Solid Films 515(20-21): 7772-7781.

Kodama, T. (2003). "High-temperature solar chemistry for converting solar heat to chemical fuels." Progress in Energy and Combustion Science 29(6): 567-597.

Kodama, T. and N. Gokon (2007). "Thermochernical cycles for high-temperature solar hydrogen production." Chemical Reviews 107(10): 4048-4077.

Kodama, T., N. Gokon, et al. (2008). "Thermochemical two-step water splitting by ZrO2-supported NixFe3-xO4 for solar hydrogen production." Solar Energy 82(1): 73-79.

Kodama, T., Y. Kondoh, et al. (2005). "Thermochemical hydrogen production by a redox system of ZrO2-supported Co(II)-ferrite." Solar Energy 78(5): 623-631.

Kodama, T., Y. Nakamuro, et al. (2006). "A two-step thermochemical water splitting by iron-oxide on stabilized zirconia." Journal of Solar Energy Engineering-Transactions of the Asme 128(1): 3-7.

Kodama, T., Y. Nakamuro, et al. (2006). "A two-step thermochemical water splitting by iron-oxide on stabilized zirconia." Journal of Solar Energy Engineering 128: 3-7.

Kolb, G. J., R. B. Diver, et al. (2007). "Central-station solar hydrogen power plant." Journal of Solar Energy Engineering-Transactions of the Asme 129(2): 179-183.

Lee, J. Y., D. W. Lee, et al. (2009). "Cr-free Fe-based metal oxide catalysts for high temperature water gas shift reaction of fuel processor using LPG." Catalysis Today 146(1-2): 260-264.

Lee, Y. J., K. W. Jun, et al. (2008). "A simple chemical route for the synthesis of gamma-Fe2O3 nano-particles dispersed in organic solvents via an iron-hydroxy oleate precursor." Journal of Industrial and Engineering Chemistry 14(1): 38-44.

Lemus, R. G. and J. M. M. Duart "Updated hydrogen production costs and parities for conventional and renewable technologies." International Journal of Hydrogen Energy 35(9): 3929-3936.

Leskela, M. and M. Ritala (2002). "Atomic layer deposition (ALD): from precursors to thin film structures." Thin Solid Films 409(1): 138-146.

Li, S. Z., S. Krishnamoorthy, et al. (2002). "Promoted iron-based catalysts for the Fischer-Tropsch synthesis: Design, synthesis, site densities, and catalytic properties." Journal of Catalysis 206(2): 202-217.

Li, T. Z., Y. Yang, et al. (2007). "Effect of manganese on an iron-based Fischer-Tropsch synthesis catalyst prepared from ferrous sulfate." Fuel 86(7-8): 921-928.

Li, Z. W., A. Rahtu, et al. (2006). "Atomic layer deposition of ultrathin copper metal films from a liquid copper(I) amidinate precursor." Journal of the Electrochemical Society 153(11): C787-C794.

Lichty P, P. C., Woodruff B, Bingham C, Weimer A (2009). "High Temperature Solar Thermal Biomass Gasification in a Prototype Cavity Reactor." Journal of Solar Energy Engineering-Transactions of the Asme.

Lichty, P., C. Perkins, et al. "Rapid High Temperature Solar Thermal Biomass Gasification in a Prototype Cavity Reactor." Journal of Solar Energy Engineering-Transactions of the Asme 132(1).

Lie, M., H. Fjellvag, et al. (2005). "Growth of Fe2O3 thin films by atomic layer deposition." Thin Solid Films 488(1-2): 74-81.

Lie, M., K. B. Klepper, et al. (2008). "Growth of iron cobalt oxides by atomic layer deposition." Dalton Transactions(2): 253-259.

Lim, B. S., A. Rahtu, et al. (2003). "Atomic layer deposition of transition metals." Nature Materials 2(11): 749-754.

Lorentzou, S., C. C. Agrafiotis, et al. (2008). "Aerosol spray pyrolysis synthesis of water-splitting ferrites for solar hydrogen production." Granular Matter 10(2): 113-122.

Loutzenhiser, P. G., M. E. Galvez, et al. (2009). "CO2 Splitting via Two-Step Solar Thermochemical Cycles with Zn/ZnO and FeO/Fe3O4 Redox Reactions II: Kinetic Analysis." Energy & Fuels 23: 2832-2839.

Ma, X. F. and M. R. Zachariah "Size-resolved kinetics of Zn nanocrystal hydrolysis for hydrogen generation." International Journal Of Hydrogen Energy 35(6): 2268-2277.

Marban, G. and T. Vales-Solis (2007). "Towards the hydrogen economy?" International Journal of Hydrogen Energy 32(12): 1625-1637.

Mauvernay, B., L. Presmanes, et al. (2007). "Elaboration and characterization of Fe1-xO thin films sputter deposited from magnetite target." Thin Solid Films 515(16): 6532-6536.

McQuillan, B. W., G. E. Besenbruch, et al. (2007). Meal sulfate water splitting thermochemical hydrogen production cycles. The Second International Workshop on Hydrogen, Ghardaïa.

Meille, V. (2006). "Review on methods to deposit catalysts on structured surfaces." Applied Catalysis a-General 315: 1-17.

Melchior, T., C. Perkins, et al. (2009). "Solar-driven biochar gasification in a particle-flow reactor." Chemical Engineering and Processing 48(8): 1279-1287.

Miller, J. E., M. D. Allendorf, et al. (2008). "Metal oxide composites and structures for ultra-high temperature solar thermochemical cycles." Journal of Materials Science 43(14): 4714-4728.

Miller, J. E., M. D. Allendorf, et al. (2008). Metal oxide composites and structures for ultra-high temperature solar thermochemical cycles.

Mufson, S. (2008). This Time, It's Different: Global Pressures Have Converged to Forge a New Oil Reality. The Washington Post. Washington DC.

Nakajima, H., K. Ikenoya, et al. (1998). "Closed-cycle continuous hydrogen production test by thermochemical IS process." Kagaku Kogaku Ronbunshu 24(2): 352-355.

Nakamura, T. (1977). "HYDROGEN PRODUCTION FROM WATER UTILIZING SOLAR HEAT AT HIGH-TEMPERATURES." Solar Energy 19(5): 467-475.

Nakayama, M. and M. Martin (2009). "First-principles study on defect chemistry and migration of oxide ions in ceria doped with rare-earth cations." Physical Chemistry Chemical Physics 11(17): 3241-3249.

Naterer, G. F., K. Gabriel, et al. (2008). "Thermochemical hydrogen production with a copper-chlorine cycle. I: oxygen release from copper oxychloride decomposition." International Journal of Hydrogen Energy 33(20): 5439-5450.

Navrotsky, A., L. Mazeina, et al. (2008). "Size-driven structural and thermodynamic complexity in iron oxides." Science 319(5870): 1635-1638.

Neftel, A., H. Friedli, et al. (1994). Historical Carbon Dioxide Record from the Siple Station Ice Core, Carbon Dioxide Information Analysis Center Oak Ridge National Laboratory.

Neises, M., M. Roeb, et al. "Kinetic investigations of the hydrogen production step of a thermochemical cycle using mixed iron oxides coated on ceramic substrates." International Journal of Energy Research 34(8): 651-661.

Niinisto, L., J. Paivasaari, et al. (2004). "Advanced electronic and optoelectronic materials by Atomic Layer Deposition: An overview with special emphasis on recent progress in processing of high-k dielectrics and other oxide materials." Physica Status Solidi a-Applied Research 201(7): 1443-1452.

Nilsen, O., M. Lie, et al. (2004). "Effect of magnetic field on the growth of alpha-Fe2O3 thin films by atomic layer deposition." Applied Surface Science 227(1-4): 40-47.

Park, C. D., D. Magana, et al. (2007). "High-quality Fe and gamma-Fe2O3 magnetic thin films from an epoxide-catalyzed sol-gel process." Chemistry of Materials 19(4): 677-683.

Park, S., S. Lim, et al. (2006). "Chemical vapor deposition of iron and iron oxide thin films from Fe(II) dihydride complexes." Chemistry of Materials 18(22): 5150-5152.

Pasternak, A. D. (2000). Global Energy Futures and Human Development: A Framework for Analysis, United States Department of Energy. UCRL-ID-140773.

Perez-Maqueda, L. A., J. M. Criado, et al. (2002). "Advantages of combined kinetic analysis of experimental data obtained under any heating profile." Journal of Physical Chemistry A 106(12): 2862-2868.

Perkins, C., P. Lichty, et al. (2007). "Determination of aerosol kinetics of thermal ZnO dissociation by thermogravimetry." Chemical Engineering Science 62(21): 5952-5962.

Perkins, C., P. R. Lichty, et al. (2008). "Thermal ZnO dissociation in a rapid aerosol reactor as part of a solar hydrogen production cycle." International Journal of Hydrogen Energy 33(2): 499-510.

Perkins, C. and A. W. Weimer (2004). "Likely near-term solar-thermal water splitting technologies." International Journal of Hydrogen Energy 29(15): 1587-1599.

Perkins, C. and A. W. Weimer (2009). "Solar-Thermal Production of Renewable Hydrogen." Aiche Journal 55(2): 286-293.

Piatkowski, N. and A. Steinfeld "Reaction kinetics of the combined pyrolysis and steam-gasification of carbonaceous waste materials." Fuel 89(5): 1133-1140.

Piatkowski, N. and A. Steinfeld (2008). "Solar-driven coal gasification in a thermally irradiated packed-bed reactor." Energy & Fuels 22(3): 2043-2052.

Revelle, R. (1976). "ENERGY USE IN RURAL INDIA." Science 192(4243): 969-975.

Rhodes, M. (2006). Introduction to Particle Technology, John Wiley and Sons.

Roeb, M., C. Sattler, et al. (2006). "Solar hydrogen production by a two-step cycle based on mixed iron oxides." Journal of Solar Energy Engineering-Transactions of the Asme 128(2): 125-133.

Rooth, M., A. Johansson, et al. (2008). "Atomic layer deposition of iron oxide thin films and nanotubes using ferrocene and oxygen as precursors." Chemical Vapor Deposition 14(3-4): 67-70.

Rooth, M., E. Lindahl, et al. (2006). "Atomic layer deposition of Co3O4 thin films using a CoI2/O-2 precursor combination." Chemical Vapor Deposition 12(4): 209-213.

Sakurai, S., A. Namai, et al. (2009). "First Observation of Phase Transformation of All Four Fe2O3 Phases (gamma -> epsilon -> beta -> alpha-Phase)." Journal of the American Chemical Society 131(51): 18299-18303.

Salameh, M. G. (2003). "The new frontiers for the United States energy security in the 21st century." Applied Energy 76(1-3): 135-144.

Satsangi, V. R., S. Kumari, et al. (2008). "Nanostructured hematite for photoelectrochemical generation of hydrogen." International Journal of Hydrogen Energy 33(1): 312-318.

Scheffe, J. R., A. Frances, et al. (2009). "Atomic layer deposition of iron(III) oxide on zirconia nanoparticles in a fluidized bed reactor using ferrocene and oxygen." Thin Solid Films 517(6): 1874-1879.

Schule, A., U. Nieken, et al. (2007). "Styrene synthesis over iron oxide catalysts: from single crystal model system to real catalysts." Physical Chemistry Chemical Physics 9(27): 3619-3634.

Schunk, L. O., P. Haeberling, et al. (2008). "A receiver-reactor for the solar thermal dissociation of zinc oxide." Journal of Solar Energy Engineering-Transactions of the Asme 130(2).

Service, R. F. (2009). "Sunlight in Your Tank." Science 326(5959): 1472-1475.

Silva, J. B., C. F. Diniz, et al. (2004). "Catalytic properties of nanocomposites based on cobalt ferrites dispersed in sol-gel silica." Journal of Non-Crystalline Solids 348: 201-204.

Simonsen, V. L. E., D. Find, et al. (2007). "Spinels as cathodes for the electrochemical reduction of O-2 and NO." Topics in Catalysis 45(1-4): 143-148.

Steinfeld, A. (2002). "Solar hydrogen production via a two-step water-splitting thermochemical cycle based on Zn/ZnO redox reactions." International Journal of Hydrogen Energy 27(6): 611-619.

Steinfeld, A. (2005). "Solar thermochemical production of hydrogen - a review." Solar Energy 78(5): 603-615.

Stiegel, G. J. and M. Ramezan (2006). "Hydrogen from coal gasification: An economical pathway to a sustainable energy future." International Journal of Coal Geology 65(3-4): 173-190.

Sturzenegger, M., J. Ganz, et al. (1999). "Solar hydrogen from a manganese oxide based thermochemical cycle." Journal De Physique Iv 9(P3): 331-335.

Sturzenegger, M. and P. Nuesch (1999). "Efficiency analysis for a manganese-oxide-based thermochemical cycle." Energy 24(11): 959-970.

Tamaura, Y. and H. Kaneko (2005). "Oxygen-releasing step of ZnFe2O4/(ZnO+Fe3O4)-system in air using concentrated solar energy for solar hydrogen production." Solar Energy 78(5): 616-622.

Tamaura, Y., A. Steinfeld, et al. (1995). "Production Of Solar Hydrogen By A Novel, 2-Step, Water-Splitting Thermochemical Cycle." Energy 20(4): 325-330.

Tamaura, Y., Y. Ueda, et al. (1999). "Solar hydrogen production by using ferrites." Solar Energy 65: 55-57.

Tamaura, Y., Y. Ueda, et al. (1999). Solar hydrogen production by using ferrites.

Trommer, D., F. Noembrini, et al. (2005). "Hydrogen production by steam-gasification of petroleum coke using concentrated solar power - I. Thermodynamic and kinetic analyses." International Journal of Hydrogen Energy 30(6): 605-618.

Trumble, K. P. (1992). "THERMODYNAMIC ANALYSIS OF ALUMINATE FORMATION AT FE/AL2O3 AND CU/AL2O3 INTERFACES." Acta metallurgica et materialia 40: S105-S110.

Turner, J., G. Sverdrup, et al. (2008). "Renewable hydrogen production." International Journal of Energy Research 32(5): 379-407.

Uddin, M. A., H. Tsuda, et al. (2008). "Catalytic decomposition of biomass tars with iron oxide catalysts." Fuel 87(4-5): 451-459.

Wandelt, K. (1982). "Photoemission studies of adsorbed oxygen and oxide layers." Surface Science Reports 2(1): 1-121.

Wank, J. R., S. M. George, et al. (2004). "Coating fine nickel particles with Al2O3 utilizing an atomic layer deposition-fluidized bed reactor (ALD-FBR)." Journal of the American Ceramic Society 87(4): 762-765.

Weidenkaff, A., P. Nuesch, et al. (1997). "Mechanistic studies of the water-splitting reaction for producing solar hydrogen." Solid State Ionics 101: 915-922.

Weiss, R. J., H. C. Ly, et al. (2005). "H-2 production by Zn hydrolysis in a hot-wall aerosol reactor." Aiche Journal 51(7): 1966-1970.

Weiss, W. and W. Ranke (2002). "Surface chemistry and catalysis on well-defined epitaxial iron-oxide layers." Progress in Surface Science 70(1-3): 1-151.

Weiss, W., D. Zscherpel, et al. (1998). "On the nature of the active site for the ethylbenzene dehydrogenation over iron oxide catalysts." Catalysis Letters 52(3-4): 215-220.

Welipitiya, D., P. A. Dowben, et al. (1996). "The adsorption and desorption of ferrocene on Ag(100)." Surface Science 367(1): 20-32.

Wong, B., R. T. Buckingham, et al. (2007). "Construction materials development in sulfur-iodine thermochemical water-splitting process for hydrogen production." International Journal of Hydrogen Energy 32(4): 497-504.

Wood, J. H., G. R. Long, et al. (2004). Long-Term World Oil Supply Scenarios: The Future Is Neither as Bleak or Rosy as Some Assert, EIA, United States Department of Energy.

Yamashita, T. and P. Hayes (2006). "Effect of curve fitting parameters on quantitative analysis of Fe0.94O and Fe2O3 using XPS." Journal of Electron Spectroscopy and Related Phenomena 152(1-2): 6-11.

Yamashita, T. and P. Hayes (2008). "Analysis of XPS spectra of Fe2+ and Fe3+ ions in oxide materials." Applied Surface Science 254(8): 2441-2449.

Yang, H. C., H. C. Eun, et al. (2009). "Kinetic analysis of dechlorination and oxidation of PrOCl by using a non-isothermal TG method." Thermochimica Acta 484(1-2): 77-81.

Yang, Q., H. Choi, et al. (2009). "Iron-cobalt mixed oxide nanocatalysts: Heterogeneous peroxymonosulfate activation, cobalt leaching, and ferromagnetic properties for environmental applications." Applied Catalysis B-Environmental 88(3-4): 462-469.

Yoon, T. J., W. Lee, et al. (2003). "Magnetic nanoparticles as a catalyst vehicle for simple and easy recycling." New Journal of Chemistry 27(2): 227-229.

Yoshida, K. and H. Kameyama (1979). "THERMOCHEMICAL HYDROGEN PRODUCTION BY THE BR-CA-FE UT-3 CYCLE." Abstracts of Papers of the American Chemical Society(APR): 21-21.

Zafar, Q., T. Mattisson, et al. (2006). "Redox investigation of some oxides of transition-state metals Ni, Cu, Fe, and Mn supported on SiO2 and MgAl2O4." Energy & Fuels 20(1): 34-44.

Zhou, M., T. Chen, et al. (2007). "Effect of pretreatment of TaN substrates on atomic layer deposition growth of Ru thin films." Chinese Physics Letters 24(5): 1400-1402.